Assessment of Hip Fracture Risk in Astronauts Exposed to Long-term Weightlessness

by

Grant Schaffner

B.S., Aeronautics and Astronautics
Massachusetts Institute of Technology
1989

M.S., Aeronautics and Astronautics
Massachusetts Institute of Technology
1995

Submitted to the Harvard University – Massachusetts Institute of Technology
Division of Health Sciences and Technology
in Partial Fulfillment of the Requirements for the Degree of
Doctor of Philosophy
in Medical Engineering
at the
Massachusetts Institute of Technology

August, 1999

Author _____

Harvard-MIT Division of Health Sciences and Technology

Certified by _____

Dava J. Newman, Ph.D.
Associate Professor of Aeronautics and Astronautics
Thesis Supervisor

Accepted by _____

Martha L. Gray, Ph.D.
J.W. Kieckhefer Professor of Electrical Engineering
Co-Director, Division of Health Sciences and Technology

Assessment of Hip Fracture Risk in Astronauts Exposed to Long-term Weightlessness

by

Grant Schaffner

Submitted to the Harvard University – Massachusetts Institute of Technology
Division of Health Sciences and Technology
in Partial Fulfillment of the Requirements for the Degree of
Doctor of Philosophy in Medical Engineering

Abstract

Background: A human exploration mission to Mars could take place within 10 years. During the 6 to 12 month journey astronauts would likely lose bone mineral density (BMD) at a mean rate of 1–2 percent per month in weight-bearing areas, approximately 10 times the rate associated with normal ageing. There exists an important need to quantify the fracture risk associated with this loss. Methods: Using computational modeling, the factor of risk for hip fracture (applied load divided by failure load) was assessed following 0, 6, and 12 months of weightlessness for: 1) the mid-stance phase of gait, and 2) a fall to the side impacting the greater trochanter. Peak applied loading was calculated for Earth and Mars gravity levels using the equations of motion for three-segment models representing locomotion and falls. Mars simulations included extravehicular activity (EVA, with spacesuit) and intravehicular activity (IVA). The structural properties of the femur were analyzed using a three-dimensional finite element model derived from quantitative computed tomography scans of a representative cadaveric femur. Space flight associated changes in density, geometry, and muscle strength were incorporated. Results: Peak applied joint contact force ranges for mid-stance were: 1.2–2.5 kN (Earth), 0.9–1.8 kN (Mars IVA), and 1.5–2.4 kN (Mars EVA). Peak applied joint contact forces for fall impact were: 4.2-8.0 kN (Earth), 2.7-5.1 kN (Mars IVA), and 3.1–5.0 kN (Mars EVA). Femoral strength in mid-stance decreased from 5.9–6.1 kN (0 months) to 5.1–5.4 kN (12 months), while femoral strength in fall impact decreased from 4.2–4.4 kN (0 months) to 3.8–4.0 kN (12 months). Typically, the factor of risk for hip fracture was highest for falls in Earth gravity following 12 months of weightlessness (1.12–2.08), and lowest for IVA locomotion in Mars gravity (0.26–0.49). All fall conditions yielded a high likelihood of fracture. Astronauts are advised to take precautions against falling following long duration space flight and could benefit from the temporary use of hip pads.

Thesis Supervisor: Dava J. Newman

Title: Associate Professor of Aeronautics and Astronautics

Thesis Committee

Dava J. Newman, Ph.D. (Chair / Thesis Supervisor)
Associate Professor of Aeronautics and Astronautics

Z. Maria Oden, Ph.D.
Assistant Professor, Department of Orthopaedics
University of Texas – Houston Medical School

Roger D. Kamm, Ph.D.
Professor of Mechanical Engineering and Bioengineering

Mary L. Bouxsein, Ph.D.
Instructor, Department of Orthopaedic Surgery
Harvard Medical School and Beth Israel Deaconess Medical Center

Acknowledgements

This research was sponsored by a grant from the National Space Biomedical Research Institute (NSBRI).

First of all, I would like to thank my thesis committee: Dava Newman, Maria Oden, Roger Kamm and Mary Bouxsein. I am greatly indebted to them for all the time they devoted to editing this thesis. Their patience and accommodation during the hectic finishing-up period, in particular, went way above and beyond the call of duty. I quite honestly could not have wished for a better committee. I would especially like to thank Dava for all the time and care she put into editing the thesis so thoroughly, and also for all her support and encouragement throughout the six years of graduate school. I am thankful also to Maria for the tremendous amount of help she gave me with the finite element analysis, even spending time on the phone with me while she was on vacation.

Much gratitude goes out also to Dr. Tom Beck and Dr. Chris Ruff of the Johns Hopkins University School of Medicine. Their guidance in establishing my research plan was crucial.

I would like to thank everyone at the Orthopaedics Biomechanics Laboratory at Beth Israel Deaconess Medical Center. Their support, encouragement, and friendship made graduate school a whole lot more enjoyable. In particular, I would like to thank Adolfo and Ara for their devoted and ungrumbling systems administration support. They saw me through many a dark hour. Also Jeanine and Paula, for their help with all things administrative, social, and otherwise.

For my many wonderful friends, I am extremely grateful. They know who they are, and they know how their kindness, thoughtfulness, and humour, made the grad school years go by a whole lot quicker than they might of.

To my darling wife, Candace, I devote my love and enduring thankfulness for her support, her kindness, and especially her patience during this last tough year. I must also not forget Chelsey (our Brittany Spaniel), for without her taking me for walks and playing ball with me in the lab hallways during the many allnighters of this last month, I might well have lost my sense of humour. Finally, I can not thank my parents enough, for their love, their support, and their unfailing confidence and encouragement throughout the many years of schooling.

In Memory of

Dr. Derek J. Gray

and

Prof. Thomas A. McMahon.

Two fine gentlemen whom I was greatly blessed to have had as mentors.

Table of Contents

List of Figures

List of Tables

Abbreviations

AMG	automatic mesh generation
BMD	bone mineral density
BW	body weight
c.g.	center of gravity
CSMI	cross-sectional moment of inertia
CT	computed tomography
DXA	dual-energy x-ray absorptiometry
EVA	extravehicular activity
FEA	finite element analysis
FEM	finite element method
G	gravity (usually Earth-normal)
ISS	International Space Station
IVA	intravehicular activity
PLSS	portable life support system
PPD	proportional plus derivative (control)
QCT	quantitative computed tomography
pQCT	peripheral quantitative computed tomography
ULLS	unilateral lower limb suspension

CHAPTER 1 *Introduction*

We choose to go to the Moon in this decade and do the other things, not because they are easy, but because they are hard.
— John F. Kennedy

Given the right political motivation and an appropriate investment of resources, astronauts could be exploring the surface of Mars as early as 10 years from now. During the 6 to 12 month journey the astronauts will experience physiological adaptations that are not yet fully understood. Some of the major systems affected include the musculoskeletal, cardiovascular, immune, hematologic, and neurovestibular systems. The changes that occur in these systems, while representing a natural adaptation to weightlessness, could have serious consequences to the individual upon return to a gravitational environment, either on Earth or on Mars. The purpose of the body of work described in this thesis is to gain insight into the risks imposed by changes in one of these physiological systems, namely, the musculoskeletal system.

1.1 Background

1.1.1 Measurement of bone mineral density

The parameter that is most often used to describe loss of bone mass, stiffness, and strength, is bone mineral density (BMD). This is not a "density" in the traditional engineering

sense, that is, total mass divided by volume (gm/cm^3), but is instead an "areal density" of mineral mass (gm/cm^2). Its value is derived from dual-energy X-ray absorptiometry (DXA), in which a two-dimensional projection of a bone is divided up into regions in which the bone-mineral content (BMC, calculated from the amount of X-ray absorptance) is divided by the projected area of the region to yield the BMD value for that region. This technique has several limitations in terms of assessing the strength of bone. Specifically, by collapsing the bone to two dimensions, information about its three dimensional geometry, and three dimensional density distribution are lost. It is thus difficult to reconstruct an engineering model of the bone that takes into account these three-dimensional attributes. To date, all of the measurements of bone mineral loss in the proximal femora of astronauts (and subjects in Earth-based space flight simulations) have used DXA as the sole imaging technique. To assess strength, the BMD values obtained from DXA are correlated with *in vitro* mechanical tests of cadaveric femora. Applying more accurate techniques of assessing bone strength, such as the three-dimensional finite element analysis described in this thesis, is greatly hindered in the case of space flight studies due to the absense of three dimensional bone information, such as can be obtained by computed tomography (CT), for instance. Many of the limitations of the work described in this thesis stem directly from this lack of three-dimensional data and it is hoped that future space flight bone studies will fill this information gap.

1.1.2 Bone Loss in Spaceflight and Earth-based Analogs

During space flights lasting longer than one month, astronauts undergo significant losses of bone mass and bone mineral density in the weight bearing areas of the skeleton, particularly the spine and lower limbs, as a result of the unloading produced by weightlessness in the microgravity environment (LeBlanc *et al.*, 1998; Holick, 1998; Vico *et al.*, 1998). Due to the

relatively small number of human subjects who have flown in space, the limited duration of missions to date, and the inaccuracy of early measurement techniques, the problem of bone loss during weightlessness is not yet well quantified or well understood. Enough evidence has been gained, however, to raise concern about the risk of fracture, particularly in the hip, during skeletal loading following return to Earth (1 G), during activities on the surface of Mars (3/8 G), or even during strenuous activities performed in weightlessness, such as extravehicular (EVA) construction of the International Space Station (ISS).

The results of studies conducted during the space flights of the 1960's and early 1970's are highly variable due to poor measurement techniques employed in some cases. Following the Gemini 4, 5, and 7 missions, lasting from 4 to 14 days, investigators noticed a distinct increase in calcium excretion (Lutwak, 1966; Whedon *et al.*, 1967) and initially thought that the astronauts had experienced a dramatic 10-20% loss in calcaneus and metacarpal bone density (Mack and Lachance, 1966; Mack *et al.*, 1967). However, through reevaluation, these losses were reduced to about 2-4% for five astronauts and 9% for one astronaut (Vose, 1974). The 18-day Soyuz 9 mission produced a 8-10% decrease in heel bone density for both cosmonauts (Birykov and Krasnykh, 1970). Bone density measurement techniques were improved during the three-man Apollo flights, lasting up to 13 days, but in only one of these flights were investigators able to measure a significant amount of bone loss from the heel (Rambaut *et al.*, 1975).

Studies conducted during the longer-term Skylab, Salyut and Mir space station missions allowed for better measurement of calcium homeostasis and bone density, but were confounded by other factors such as variable compliance with prescribed exercise countermeasures intended to minimize bone loss. Skylab metabolic data indicate that over a three month period, the total negative calcium balance from excess urine and fecal excretion is as much as

25 grams (Rambaut *et al.*, 1979b; Rambaut *et al.*, 1979a), but later estimates reduced this value to 12.8 grams or 1% of the 1250 grams in the average skeleton (Cann, 1993). Reduced losses during the Skylab 4 mission have been attributed to increased exercise by the astronauts. Both US and Soviet investigations estimated that the average bone loss from the calcaneus was 1% per month (Stupakov *et al.*, 1984). A combined US / USSR study of long-term spaceflight, in which quantitative computed tomography (QCT) scans were taken of the spine found no significant loss of density in the vertebral bodies (Oganov *et al.*, 1990), apparently validating the exercise countermeasures. Closer inspection, however, revealed that there was an 8% loss of density in the posterior elements of the vertebrae, which correlated with a 4% loss of volume in the attached muscles, perhaps demonstrating the limited effectiveness of exercise countermeasures in space. Further evidence of this limitation came from QCT scans of one cosmonaut after a 366-day Mir mission, which showed a 10% loss of trabecular bone mass in L1, L2, and L3 vertebrae (Grigoriev *et al.*, 1991). When investigators started looking at other regions in the body, they found even more distressing losses. Most significantly, a quantitative digital radiography (QDR, equivalent to DXA) study of cosmonauts after 4.5–6 month long missions on Mir found bone mineral density (BMD) losses of as much as 14% in the femoral neck and greater trochanter of the hip (Oganov *et al.*, 1992). A study of US astronauts found that even in relatively short flights (1 to 2 weeks), the vertebrae L2-4 could lose as much as 3% of baseline BMD (Miyamoto *et al.*, 1998).

The seriousness of the losses in BMD during spaceflight is evident when compared with the losses attributed to aging. On average, the rate of BMD loss for the proximal femur and lumbar vertebrae in men and women over 55 years of age has been estimated to be around 0.5–1% per year (Burger *et al.*, 1998; Greenspan *et al.*, 1996; Ensrud *et al.*, 1995; Jones *et al.*, 1994). These rates of loss are believed to increase the risk of hip fracture in elderly individuals

at the rate of about 4% per year and beyond age 75 the risk of hip fracture increases exponentially. As mentioned above, the rates of loss from the same skeletal areas during spaceflight are about 1 - 2% per month, 10 or more times greater than the rate occurring in normal aging. From another perspective, an estimated loss of 20% in femoral neck BMD during a year of spaceflight would correspond to the average BMD loss in the femoral neck of a woman aging from 50 years to almost 80 years (Looker *et al.*, 1995). While the mechanisms responsible for bone loss in ageing and spaceflight are probably different (LeBlanc and Schneider, 1991), the similarities in the observed changes may be of mutual benefit to the study of either case (Hughes-Fulford, 1991).

Some investigators have used bed rest as an analog for the skeletal unloading experienced in spaceflight. One early study put 90 healthy young men through 5-36 weeks of bed rest and found that not only was there an average 5% loss of calcaneal mineral each month, but that mechanical and biochemical countermeasures were unsuccessful at preventing this loss (Schneider and McDonald, 1984). During another 17 week bed rest study, subjects lost an average of 0.21 +/- 0.05% per week of bone mineral density in the femoral neck, and 0.27 +/- 0.05% per week in the trochanteric area (LeBlanc *et al.*, 1990). Other studies have shown similar mineral losses, slowing of mineralization, and limitations of countermeasures. Some studies have also encountered contradictory results demonstrating the difficulties of bed rest as an analog for spaceflight (Vico *et al.*, 1987; Zaichick and Morukov, 1998). The combined results of space flight and bed rest studies, in terms of measured BMD loss, are summarized in Table 1.1. The last column is a normalized parameter indicating the actual or projected BMD loss per year.

Results from animal studies of bone mineral loss in spaceflight and immobilization have been highly variable due to differences in study design, duration, and measurement tech-

Table 1.1 Summary of space flight and bed rest studies of bone loss.

Study	Duration	BMD loss	Region	BMD loss per month
Birykov & Krasnykh, 1970	18 d	8-10%	Calcaneus	5%
Rambaut *et al.*, 1979b Stupakov *et al.*, 1984	1 mth	1%	Calcaneus	1%
Grigoriev *et al.*, 1991	366 d	10%	Lum. Vertebrae	0.8%
Oganov *et al.*, 1992	4.5-6 mth	14%	Femoral neck	2.3-3.1%
Miyamoto *et al.*, 1998	1-2 wk	3%	Lum. Vertebrae	6-12%
Schneider & McDonald, 1984	1 mth	5%	Calcaneus	5%
LeBlanc *et al.*, 1990	17 wk	3.6% 4.6%	Femoral neck Trochanteric	0.9% 1.2%

niques. In addition, much of the variability may be due to the age of the animals, since many of the early studies were carried out on rats that were still growing (less than 5-6 months old). Rats were flown on eight Russian Cosmos biosatellite missions, lasting from 5 days to 22 days, as well as on the US Spacelab 3 mission (7 days). Juvenile male rhesus monkeys were flown on five Cosmos missions and an adult nemestria macaque monkey was flown on an early US mission (Biosatellite 3). Additional studies were carried out on rats and monkeys in various forms of suspension and hypokinesia. Bone formation was found to be reduced in the metaphyses of long bones during the first Cosmos mission (Yagodovsky *et al.*, 1976). The Cosmos 782 and 936 missions resulted in a 40% reduction in the length of the primary spongiosa (Asling, 1978) and a 30% decrease in the femoral breaking strength (Spector *et al.*, 1983). In addition, these missions revealed that an arrest line separating normal bone from defective and hypomineralized bone formed during spaceflight (Turner *et al.*, 1985) and that osteoblast differentiation in *non*-weight bearing bones was suppressed during weightlessness (Roberts *et al.*, 1981), thus yielding evidence that other bones in the body might be affected in long term flight. Rats flown for 5 days aboard the Cosmos 1514 biologic satellite incurred no measurable change in bone mass (Vico *et al.*, 1987), while calcium excretion studies on mon-

keys on the same flight showed evidence of increased resorption (Cann *et al.*, 1986). After the slightly longer Cosmos 1667 mission, the flight rats showed a greater loss of trabecular bone in the proximal metaphyses of the tibia than rats undergoing tail suspension for the same duration on earth (Kaplansky *et al.*, 1987; Vico *et al.*, 1991). Rats undergoing tail suspension of their hindlimbs for 15 days showed reductions in calcium content to 86.2 ± 2.5% for the tibia, and 75.5 ± 3.5% for vertebrae (Globus *et al.*, 1984), while those exposed to hypokinesia and head-down suspension for periods of 35 to 60 days exhibited osteoporosis in the tibial and vertebral spongiosa (Durnova *et al.*, 1986). Other tail suspension studies revealed a reduction of osteoblast number and growth and mineralization rates in the unloaded bones (Morey-Holton and Globus, 1998). Rhesus monkeys flown for 13 days on Cosmos 1887 and 2044, and 11.5 days aboard Cosmos 2229, showed reduced bone mineralization and growth and a significant decrease in whole body bone mineral content (BMC), with only partial recovery by one month post-flight (Cann *et al.*, 1990; Zerath *et al.*, 1996). In addition, during the Cosmos 2044 mission it was shown that the fracture repair process was impaired in rats (Kaplansky *et al.*, 1991).

1.1.3 Summary of findings from spaceflight and immobilization studies

The findings of these spaceflight and immobilization studies, conducted over the past 35 years, may be summarized as follows:

- Significant bone loss occurs in humans and animals exposed to weightlessness during spaceflight
- Urine and fecal calcium excretion is increased resulting in a negative calcium balance
  - Calcium resorption from bone is increased and absorption from gut is decreased
- Bone mineral density decreases

- Critical weight-bearing areas lose density most rapidly and the rate of loss is approximately 1-2% per month
- Non-weight-bearing areas are affected in the long term

- Osteoblast proliferation and activity are reduced while osteoclast activity either remains the same or increases slightly
- Bone growth is slowed
- Fracture repair is impaired
- Bone strength is reduced

1.2 Significance

Several conclusions may be drawn regarding the significance of these skeletal changes in terms of human spaceflight.

- Astronauts and cosmonauts spending a significant period in weightlessness (> 1 month) will experience a loss of bone strength and a subsequent increase in fracture risk during:
  - Activities on Earth (walking / running, falls)
  - Intravehicular / extravehicular activity (IVA / EVA) on Mars or in weightlessness
- A fracture occurring on Mars (3/8 G) has serious consequences to the individual and crew due to:
  - remoteness (limited medical resources)
  - possible inhibition of fracture repair and immune respones associated with weightlessness
  - loss of functionality in terms of the crew member's skills and duties (increased workload on remaining crew members)

To date, hip fracture has risk has generally been estimated based on correlations between bone mineral density (BMD) and failure load for a given loading condition (usually associated with an specific activity, including traumatic activities such as falls). In the vast majority of

cases, the failure load in this context is obtained through mechanical testing of cadaveric femora. Thus, while BMD correlates reasonably well with bone strength *in vitro*, actual fracture risk is harder to calculate due to *in vivo* factors (e.g. body mass). Consequently, there exists a need to better assess the *in vivo* fracture risk for astronauts performing normal and traumatic activities following a significant period of weightlessness (i.e., more than a month).

1.3 Research Aims

The goals of this thesis may be summarized according to the following aims:

Primary Aim:

To improve the assessment of hip fracture risk in astronauts exposed to long-term weightlessness.

Specific Aim 1:

To estimate the loading applied to the proximal femur during locomotion and falls, both in Earth gravity and Mars gravity.

Specific Aim 2:

To estimate the failure load of the proximal femur during locomotion and falls.

Specific Aim 3:

To model the changes in geometry, bone mineral density and muscle forces related to the proximal femur due to weightlessness, and to account for sex differences.

Specific Aim 4:

To estimate the risk of hip fracture during locomotion and falls in Earth gravity and Mars gravity.

1.4 Outline of Thesis

A diagram of the overall research plan for this thesis is presented in Figure 1.1. There were two main components to the plan, one aimed at determining the failure load for the proximal femur, the other aimed at determining the applied load. The applied loading was calculated by means of dynamic simulations of human locomotion and falls using three-segment models. The equations of motion for these simulations were derived using both a Lagrangian formulation and Kane's method. The failure load was determined through the use of an adjustable finite element model that served as a representation of the proximal femur for an average male or female adult of the approximate age expected of an astronaut. The model was derived directly from quantitative computerized tomography (QCT) scans of the right femur from a deceased 36 year-old male. The QCT images weer used to derive both geometric information and bone density data. When the applied load (estimated in the dynamics analysis) was divided by the failure load (calculated in the finite element analysis), it yielded the factor of risk for hip fracture ("fracture risk") under the given loading condition (locomotion or fall). The analysis was repeated as the model was adjusted to account for changes in geometry and density due to spaceflight and sex differences. In addition, differences in gravity level (Earth vs Mars) were taken into account during the dynamic simulation.

This work is described in the remaining chapters of this thesis in the following manner:

Chapter 2: This chapter describes the formulation of equations of motion for three-segment dynamic models used to assess the applied loading in the hip during locomotion and falls. Environments simulated include Earth (1 G) and Mars (3/8 G), as well as both intravehicular activity (IVA) and extravehicular activity (EVA). The applied loads calculated were later used in Chapter 5 to determine the factor of risk for fracture.

Chapter 3: The construction and analysis of a three-dimensional finite element model of the proximal femur are discussed. The model was analyzed in configurations simulating both locomotion (mid-stance) and a fall to the side impacting the greater trochanter. Failure analysis was carried out through a user subroutine employing maximum and minimum principle strain failure criteria.

Chapter 4: The finite element model described in Chapter 3 was modified to account for changes in femoral geometry and bone mineral density that are associated with space flight and gender differences.

Chapter 5: The values calculated for applied loading (Chapter 1) were combined with the corresponding failure load values (Chapters 3 and 4) to arrive at values for factor of risk for hip fracture associated with the various loading cases considered. Conclusion of thesis.

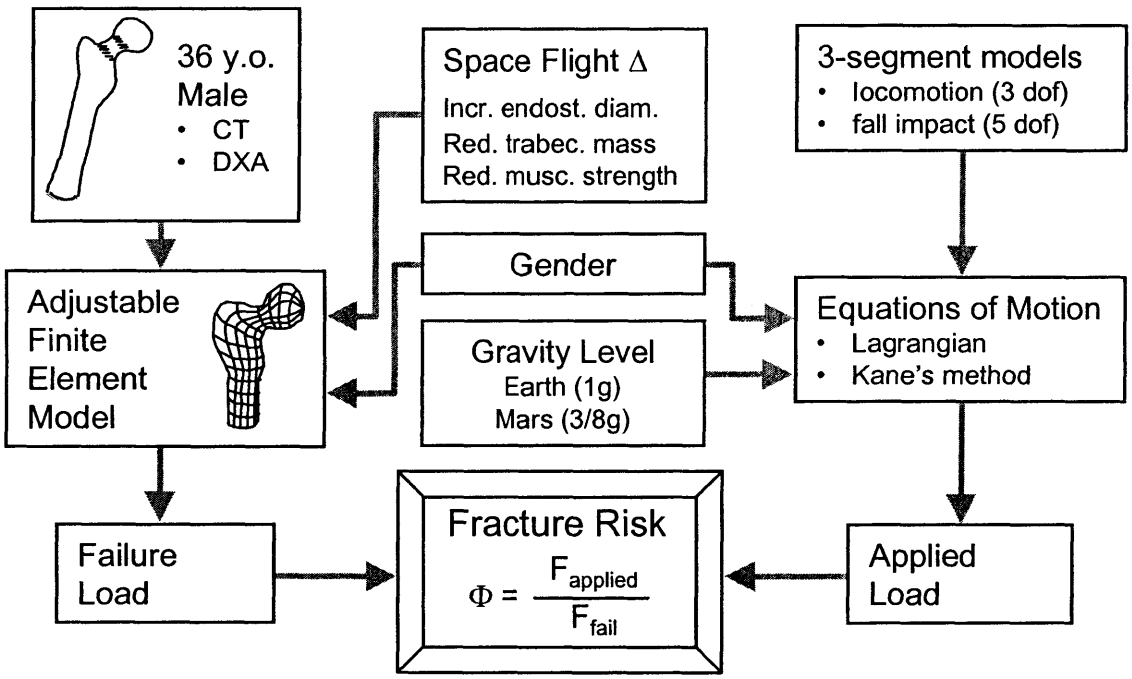

Figure 1.1: Diagram of overall research plan for thesis.

1.5 References

Asling, C.W., *Histological studies on tibial bone of rats in the 1975 Cosmos 782 flight*, in *Final reports of U.S experiments flown on the Soviet satellite Cosmos 782*, S.N. Rosenzweig and K.A. Souza, Editors. 1978, NASA TM-78525. p. 276-307.

Birykov, N. and Krasnykh, I.G., *[Changes in optical density of bone tissue and calcium metabolism in the cosmonauts].* Kosm Biol Med, 1970. **4**: p. 42-45.

Burger, H., de Laet, C.E., van Daele, P.L., Weel, A.E., Witteman, J.C., Hofman, A. and Pols, H.A., *Risk factors for increased bone loss in an elderly population: the Rotterdam study.* Am J Epidemiol, 1998. **147**(9): p. 871-879.

Cann, C.E., *Adaptations of the skeletal system to spaceflight*, in *Introduction to space life science*, S. Churchill, Editor. 1993.

Cann, C.E., *Calcium metabolism and correlated endocrine measurements in primates during Cosmos '83*, in *Final reports of U.S. monkey and rat experiments flown on the Soviet satellite Cosmos 1514*, R.C. Mains and E.W. Gomersall, Editors. 1986, NASA TM-88223. p. 129-144.

Cann, C.E., Rakhmanov, A. and Oganov, V., *Radiographic studies of skeletal growth in primates in Cosmos 1887*, in *Final reports of the U.S. experiments flown on the Soviet biosatellite Cosmos 1887*, J.P. Connolly, R.E. Grindeland, and R.W. Ballard, Editors. 1990, NASA TM-102254.

Durnova, G.N., Sakharova, Z.F., Kaplanskii, A.S., Ivanov, V.M. and Khaidakov, M.S., *[Quantitative study of osteoblasts and osteoclasts in the bones of rats during the simulation of weightlessness].* Kosm Biol Aviakosm Med, 1986. **20**(6): p. 37-41.

Ensrud, K.E., Palermo, L., Black, D.M., Cauley, J., Jergas, M., Orwoll, E.S., Nevitt, M.C., Fox, K.M. and Cummings, S.R., *Hip and calcaneal bone loss increase with advancing age: longitudinal results from the study of osteoporotic fractures.* J Bone Miner Res, 1995. **10**(11): p. 1778-1787.

Greenspan, S. L., Maitland-Ramsey, L., and Myers, E. (1996). "Classification of osteoporosis in the elderly is dependent on site-specific analysis." *Calcif Tissue Int*, 58(6), 409-14.

Globus, R.K., Bikle, D.D., and Morey-Holton, E., *Effects of simulated weightlessness on bone mineral metabolism.* Endocrinology, 1984. **114**(6): p. 2264-2270.

Grigoriev, A.I., Bugrov, S.A., Bogomolov, V.V., Egorov, A.D., Kozlovskaya, I.B., Pestov I.D., Polyakov, V.V., Tarasov, I.K., *Medical results of the Mir year-long mission.* Physiologist, 1991. **34**(Suppl): p. S44-S48.

Holick, M.F., *Perspective on the impact of weightlessness on calcium and bone metabolism.* Bone, 1998. **22**(5 Suppl): p. 105S-111S.

Hughes-Fulford, M., *Altered cell function in microgravity.* Exp Gerontol, 1991. **26**(2-3): p. 247-256.

Jones, G., Nguyen, T., Sambrook, P., Kelly, P.J. and Eisman, J.A., *Progressive loss of bone in the femoral neck in elderly people: longitudinal findings from the Dubbo osteoporosis epidemiology study.* BMJ, 1994. **309**(6956): p. 691-695.

Kaplansky, A.S., Durnova, G.N., Burkovskaya, T.E. and Vorotnikova, E.V., *The effect of microgravity on bone fracture healing in rats flown on Cosmos 2044.* Physiologist, 1991. **34**(Suppl): p. S196-S199.

Kaplansky, A.S., Durnova, G.N. and Sakharova, Z.F., *[Histomorphometric analysis of the bones of rats on board the Kosmos 1667 biosatellite].* Kosm Biol Aviakosm Med, 1987. **21**(5): p. 25-31.

LeBlanc, A. and Schneider, V., *Can the adult skeleton recover lost bone?* Exp Gerontol, 1991. **26**(2-3): p. 189-201.

LeBlanc, A., L. Shackleford, L. and Schneider, V., *Future human bone research in space.* Bone, 1998. **22**(5 Suppl): p. 113S-116S.

LeBlanc, A.D., Schneider, V.S., Evans, H.J., Engelbretson, D.A. and Krebs, J.M., *Bone mineral loss and recovery after 17 weeks of bed rest.* J Bone Min Res, 1990. **5**(8): p. 843-850.

Looker, A.C., Johnston, C.C., Jr, Wahner, H.W., Dunn, W.L., Calvo, M.S., Harris, T.B., Heyse, S.P., Lindsay, R.L., *Prevalence of low femoral bone density in older U.S. women from NHANES III.* J Bone Min Res, 1995. **10**(5): p. 796-802.

Lutwak, L., *Chemical analysis of diet, urine, feces and sweat parameters relating to the calcium and nitrogen balance studies during Gemini VII flight (Exp M7),* . 1966.

Mack, P.B. and Lachance, P.A.. *Effects of recumbence and space flight on bone density.* in *2nd Annual Biomedical Research Conference.* 1966. Houston, TX.

Mack, P.B., LaChance, P.A., Vose, G.P. and Vogt, F.B., *Bone demineralization of foot and hand of Gemini-Titan IV, V and VII astronauts during orbital flight.* Am J Roentgenol Rad Therapy Nucl Med, 1967. **100**: p. 503-511.

Miyamoto, A., Shigematsu, T., Fukunaga, T., Kawakami, K., Mukai, C. and Sekiguchi, C., *Medical baseline data collection on bone change with space flight.* Bone, 1998. **22**(5 Suppl): p. 79S-82S.

Morey-Holton, E.R. and Globus, R.K., *Hindlimb unloading of growing rats: a model for predicting skeletal changes during space flight.* Bone, 1998. **22**(5 Suppl): p. 83S-88S.

Oganov, V.S., Cann, C., Rakhmanov, A.S. and Ternovoi S.K., *[A computer tomographic investigation of the muskuloskeletal system of the spine in humans after long-term space flight].* Kosm Biol Aviakosm Med, 1990. **24**: p. 20-21.

Oganov, V.S., Grigor'ev, A.I., Voronin, L.I., Rakhmanov, A.S., Bakulin, A.V., Schneider, V.S. and LeBlanc, A.D., *[Bone mineral density in cosmonauts after flights lasting 4.5-6 months on the Mir orbital station].* Aviakosm Ekolog Med, 1992. **26**(5-6): p. 20-24.

Rambaut, P.C., *Skeletal response.*, in *Biomedical results of Apollo*, R.S. Johnston, L.F. Dietlin, and C.A. Berry, Editors. 1975, NASA SP-368: Washington, DC. p. 303-322.

Rambaut, P.C. and Johnston, R.S., *Prolonged weightlessness and calcium loss in man.* Acta Astronautica, 1979b. **6**: p. 1113-1122.

Rambaut, P.C., Leach, C.S. and Whedon, G.D., *A study of metabolic balance in crew members of Skylab IV.* Acta Astronautica, 1979a. **6**: p. 1313-1322.

Roberts, W.E., Mozsary, P.G. and Morey, E.R., *Suppression of osteoblast differentiation during weightlessness.* Physiologist, 1981. **24**(Suppl): p. S75-S76.

Schneider, V.S. and McDonald, J., *Skeletal calcium homeostasis and countermeasures to prevent disuse osteoporosis.* Calcif Tissue Int, 1984. **36**(Suppl 1): p. S144-S151.

Spector, M., *Arrested bone formation during space flight results in hypomineralized skeletal defect.* Physiologist, 1983. **26**(Suppl): p. S110-S111.

Stupakov, G.P., Kazeikin, V.S., Kozlovskii, A.P. and Korolev, V.V., *[Evaluation of changes in human axial skeletal bone structures during long-term space flights].* Kosm Biol Aviakosm Med, 1984. **18**: p. 33-37.

Turner, R.T., Bell, N.H., Duvall, P., Bobyn, J.D., Spector, M., Holton, E.M. and Baylink, D.J., *Spaceflight results in formation of defective bone.* Proc Soc Exp Biol Med, 1985. **180**(3): p. 544-549.

Vico, L., Chappard, D., Alexandre, C., Palle, S., Minaire, P., Riffat, G., Morukov, B. and Rakhmanov, S., *Effects of a 120 day period of bed-rest on bone mass and bone cell activities in man: attempts at countermeasure.* Bone Miner, 1987. **2**(5): p. 383-394.

Vico, L., Chappard, D., Alexandre, C., Palle, S., Minaire, P., Riffat, G., Novikov, V.E. and Bakulin, A.V., *Effects of weightlessness on bone mass and osteoclast number in pregnant rats after a five-day spaceflight (COSMOS 1514).* Bone, 1987. **8**(2): p. 95-103.

Vico, L., Lafage-Proust, M.H. and Alexandre, C., *Effects of gravitational changes on the bone system in vitro and in vivo.* Bone, 1998. **22**(5 Suppl): p. 95S-100S.

Vico, L., Novikov, V.E., Very, J.M. and Alexandre, C., *Bone histomorphometric comparison of rat tibial metaphysis after 7-day tail suspension vs. 7-day spaceflight.* Aviat Space Environ Med, 1991. **62**(1): p. 26-31.

Vose, G.P., *Review of roentgenographic bone demineralization studies of the Gemini space flights.* Am J Roentgenol Rad Therapy Nucl Med, 1974. **121**: p. 1-4.

Whedon, G.D., Lutwak, L. and Neuman, W., *Calcium and Nitrogen balance. In: A review of medical results of Gemini 7 and related flights*, . 1967, Kennedy Space Center, FL.

Yagodovsky, V.S., Trifaranidi, L.A., and Goroklova, G.P., *Space flight effects on skeletal bones of rats.* Aviat Space Environ Med, 1976. **47**: p. 734-738.

Zaichick, Y. and Morukov, B.V., *In vivo bone mineral studies on volunteers during a 370-day antiorthostatic hypokinesia test.* Appl Radiat Isot, 1998. **49**(5-6): p. 691-694.

Zerath, E., Novikov, V., Leblanc, A., Bakulin, A., Oganov, V. and Grynpas M., *Effects of spaceflight on bone mineralization in the rhesus monkey.* J Appl Physiol, 1996. **81**(1): p. 194-200.

CHAPTER 2

Hip Loading During Locomotion and Falls in Earth Gravity and Mars Gravity

Man walks the moon but his soul remains riveted to earth. Once upon a time it was the opposite.

— Elie Wiesel

As mentioned in the previous chapter, calculating the factor of risk for hip fracture requires the determination of two parameters: the force applied to the hip joint, and the failure load of the proximal femur. The principal purpose of the work described in this chapter is to determine the applied force for two distinct activities/conditions, namely, locomotion (running) and a fall to the side impacting the greater trochanter. Locomotion was chosen as one of the conditions since it represents a normal activity that could be performed soon after a space flight, either on arrival at Mars or after return to Earth. Fall impact was chosen as the second activity since it represents an abnormal, worst-case, condition; since it is widely believed that approximately 90% of hip fractures on Earth are the result of a fall (Hedlund and Lindgren, 1987; Cummings *et al.*, 1990); and since astronauts are believed to be at greater risk of fall following space flight due to neurovestibular (balance) compromise and orthostatic intolerance (susceptibility to fainting). The peak forces calculated in this chapter will be used in Chapter 5 as the expected applied force in calculating the factor of risk for fracture during the two activities.

Since we are concerned about the fracture risk following return to Earth after a long flight as well as during activity shortly after arrival on Mars, the simulations reported here were performed under conditions of both Earth and Mars gravity, and, in the case of a Mars mission, both during intravehicular activity (IVA) and extravehicular activity (EVA). The loadings are calculated by means of two distinct three-link dynamic systems representative of the human body, one used to analyze locomotion and one used to analyze falls. The systems are designed to achieve sufficient accuracy (within 20% of values presented elsewhere in the literature), while still being simple enough that the motion can be controlled without requiring very complex motor control schemes.

2.1 Background

A review of the literature on human locomotion and falls reveals that a significant body of information exists on the musculoskeletal loading experienced during these two activities. A new dynamics simulation study was deemed necessary, however, for two reasons. Firstly, there appears to be little or no information on hip loading during locomotion and falls in reduced gravity. Secondly, the forces reported from calculation and direct measurement in past studies do not have a high degree of consistency.

2.1.1 Terminology

To assist the reader with some of the terminology used in this chapter and other chapters in this thesis, two figures are presented in this section. The first, Figure 2.1, shows the three main stages of the stance phase of human gait. The work in this thesis is focussed on the mid-stance stage. The second, Figure 2.2, shows some of the main regions and anatomical landmarks that will be referred to repeatedly, especially in chapters 3 and 4. It is presented here

because the background text on hip loading makes use of some of the terms. Note in the figure

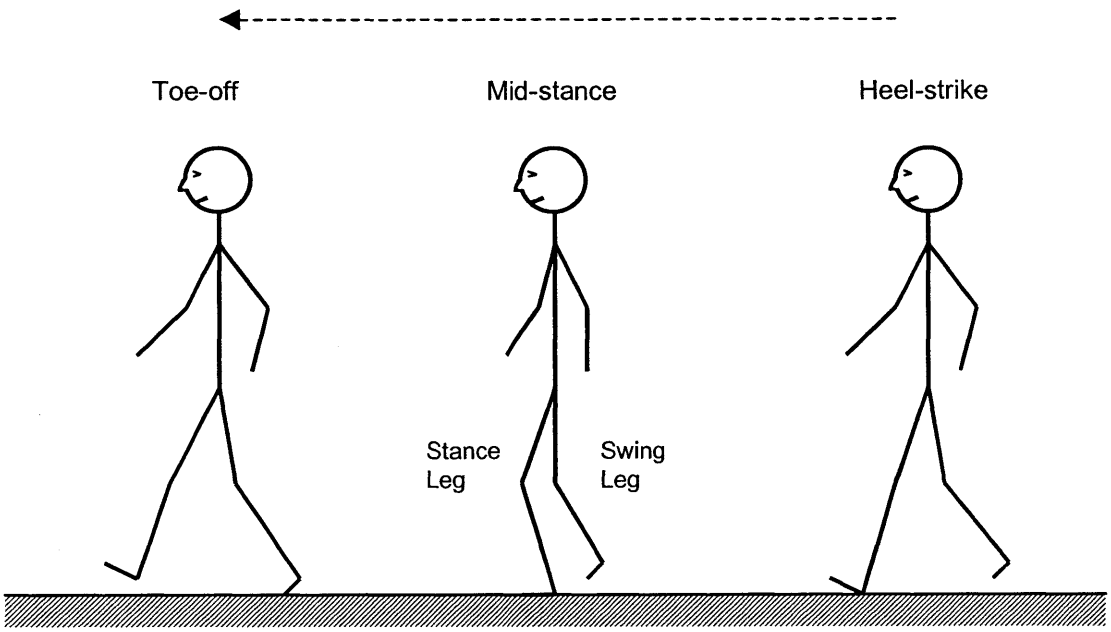

Figure 2.1: A few terms used to describe human gait.

that the trochanteric region is a combination of the "trochanteric" and "intertrochanteric" regions conventionally used in analysis of DXA scans.

2.1.2 Locomotion

A number of studies have been performed on the mechanics and energetics of locomotion in Earth gravity. In general, two types of approaches have been adopted: mathematical models that examine certain aspects of the mechanics or energetics of locomotion, and experimental studies that measure parameters of interest directly.

The majority of studies using mathematical models of locomotion have ranged in complexity from simple inverted pendulums, to multi-segment ballistic models, to lumped mass and spring models. Despite their relative simplicity, these models have been successful at capturing the most important determinants of gait, such as step lengths, swing-times, and ground reaction forces. Mochon and McMahon (1980) used a three-link mathematical model to

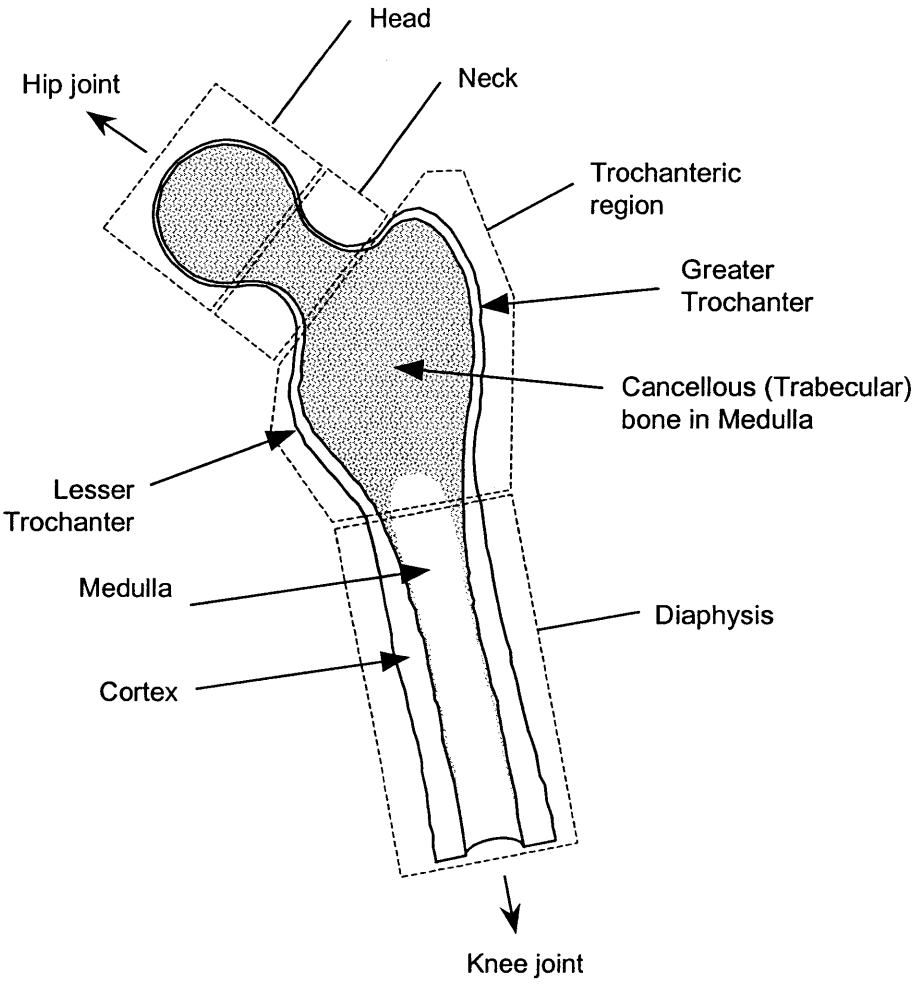

Figure 2.2: Principal regions, and anatomical landmarks of the proximal femur.

examine the swing phase of walking and obtained good correlation with experimental data for swing times, joint angles, and horizontal ground reaction force. Siegler *et al.* (1982) simulated the stance phase of human locomotion with a model consisting of a concentrated mass supported by two elastic and viscous straight legs. They obtained relatively good correspondence with experimental results, particularly for the vertical ground reaction force. Furthermore, the shape of the force time-history plots agreed well with force plate measurements. McMahon *et al.* (1987) further analyzed how changes in the effective vertical stiffness (i.e., the stiffness of the lower limb that serves to reverse the downward velocity of the body during one contact

period) of the body affect locomotion characteristics. They found that reducing the vertical stiffness, through running with bent knees, reduces transmission of mechanical shock from the foot to the upper body, but requires significantly greater energy utilization. A simple mass-spring model predicted the peak vertical ground reaction force with good accuracy for normal running, but with slightly reduced accuracy for bent-knee running (since the larger joint angles introduce more nonlinearity into vertical stiffness). McMahon and Cheng (1990) further explored the lumped mass and spring model by assuming that the leg acts as a linear spring, but taking into account the angle between the leg and the vertical. The model provided good predictions if the leg stiffness, k_{leg}, was assumed constant, while the effective vertical stiffness increased with increasing forward speed due to a required increase in the initial angle of the leg to the vertical (which results in greater compression of the leg spring). In support of the leg spring model, some studies have sought to characterize the stiffness of the leg spring through experimentation. Farley and Gonzalez (1996) used a treadmill-mounted force platform to derive leg spring stiffness in subjects running at 2.5 m/s. The leg spring stiffness was found to vary from 7.0 to 16.3 kN/m between the lowest and highest stride frequencies. Viale *et al.* (1998) also used force platform measurements in conjunction with a spring-mass model and obtained a leg spring stiffness of 13.0 kN/m for running.

Studies aimed at assessing the actual loading in the hip joint during walking, running, and other activities have generally used indirect approaches to determine the forces and moments present, either through inverse dynamics applied to experimental measurements, or through mathematical models. Crowninshield *et al.* (1978) generated kinematic data through photography of subjects performing movements and combined this with kinetic data from a force platform in an inverse dynamics analysis to determine the intersegmental forces and moments at the hip, knee, and ankle. They found that a 69 kg subject walking at 1.0 m/s experiences a

vertical joint contact force in the hip of 4.0 to 5.0 times body weight (BW). Recently, van den Bogert *et al.* (1999) found similar results using a slightly different approach, which measured acceleration of the upper body through a body-mounted accelerometer system in nine male subjects. Intersegmental force and moment at the hip joint during walking, running, and skiing were obtained through inverse dynamics. The peak joint contact force during walking at 1.5 m/s was 2.5 times BW, while running at 3.5 m/s produced a peak joint contact force of 5.2 times BW.

It was not until the introduction of instrumented hip prostheses, however, that actual measurements of *in vitro* hip loading could be obtained. Bergmann *et al.* (1993) measured hip forces and moments in two patients. In the first patient, they found that median peak forces increased with walking speed from 2.8 times body weight (BW) at 0.3 m/s (1 km/h) to about 4.8 times BW at 1.4 m/s (5 km/h). The forces increased to about 5.5 times BW during jogging and very fast walking. In the second patient, the median forces at 0.8 m/s (3 km/h) were about 4.1 times BW. Bassey *et al.* (1997) measured compressive axial force in an instrumented titanium implant during 'osteogenic' (encouraging bone formation) exercises (slow jumping, fast continuous jumping, or jogging). The implant forces (equivalent to the hip forces described by Bergmann *et al.*) were 2.5 to 4.0 times BW, and were also significantly related to muscle activity.

Studies of locomotion in reduced gravity are not nearly as numerous as those in Earth gravity conditions. Some of the early studies were conducted during the late 1960's in support of the Apollo moon landings (Margaria, 1966; Margaria and Cavagna, 1967; Hewes, 1968; Hewes, 1969). These studies were mainly concerned with gait strategies, energy requirements, and the feasibility of locomotion in a reduced gravity environment (the moon, 1/6 (0.17) Earth gravity) while wearing a pressurized space suit.

More recent studies have sought to understand the mechanics and energetics of reduced gravity locomotion in greater scientific detail. He *et al.* (1991) performed experiments in which subjects ran on a treadmill instrumented with a force platform while reduced gravity was simulated using a suspension device that applied a nearly constant vertical force to the subjects. Four subjects ran at speeds of 2.0–6.0 m/s in conditions of Earth gravity and at 3.0 m/s in six simulated fractions of Earth gravity, ranging from 0.2 to 0.7 G. A leg stiffness of 11.3 kN/m applied to their linear spring-mass model produced good agreement with experimental results. They found that leg stiffness and the vertical excursion of the center of mass during the flight phase of running did not change with increased forward speed or gravity. Furthermore, their model successfully predicted the decreasing peak force observed under conditions simulating reduced gravity. Newman *et al.* (1994) used an underwater treadmill with a ballasting harness to simulate partial gravity environments. They found that a loping gait was used over a wide range of speeds (1.5 m/s to 2.3 m/s). Furthermore, peak vertical force and stride frequency were significantly reduced as the gravity level was reduced, while ground contact time was independent of gravity.

Several studies have focussed more exclusively on the energetics of reduced gravity locomotion. Farley and McMahon (1992) found that reducing gravity decreases the energetic cost for running much more than for walking, with the result that running is actually more efficient than walking for low levels of gravity. The same partial gravity simulation system used by Newman *et al.* was used by Wickman and Luna (1996) to assess energy requirements imposed on astronauts when supporting the mass of a protective suit and portable life support system (PLSS). They found that energy expenditure, calculated from measured oxygen consumption, was positively correlated with gravity level, speed, and load size. They predicted that individuals in average physical condition could walk for 8 h on the Moon with up to 170% of their

body mass, and on Mars with up to 50% of their body mass for the same duration. They also predicted that added mass (i.e., for a space suit) could be beneficial for bone mass maintenance in reduced gravity environments, but that some supplemental bone mass maintenance measures would still be required for most individuals. Cavagna *et al.* (1998) employed an aircraft undergoing gravity-reducing flight profiles to investigate the mechanics of walking on Mars. The optimal walking speed on Mars was found to be 0.9 m/s (3.4 km/h), compared to 1.5 m/s (5.5 km/h) on Earth. Furthermore, the walk-run transition on Mars is predicted to occur near the optimal walking speed on Earth and the work done per unit distance to move the center of mass would be about half that on Earth, which agrees with the findings of Newman *et al.* (1994).

2.1.3 Falls

It has been well established that 90 percent of all hip fractures are the result of a fall (Anonymous, 1985). While less than 10 percent of falls result in hip fracture, susceptible patients can sustain a hip fracture even from mild trauma (Goh *et al.,* 1996). The factors associated with an increased risk of hip fracture during a fall are listed in Table 2.1 (Goh *et al.,* 1996; Greenspan *et al.*, 1998; Schwartz *et al.*, 1998).

Table 2.1 Factors associated with increased risk of hip fracture during a fall.

1) Reduced BMD in the proximal femur
2) Fall direction (to the side, versus any other direction)
3) Direct impact (without hitting knee first, or catching oneself with an outstretched arm)
4) Impairment in mobility
5) Reduced soft tissue covering the greater trochanter (thin vs obese patients)
6) Poor physical conditioning

Impact direction has also been shown to correlate with failure load. Ford *et al.* (1996) used a finite element model of the proximal femur to establish that a change in angle between the

line of action of the applied force and the axis of the femoral neck from 0 degrees (direct lateral impact) to 45 degrees (posterolateral impact) reduces structural capacity by 26%. Pinilla *et al.* (1996) validated this result with an experimental study that showed that the failure load decreased by 24% as the loading angle changed from 0 to 30 degrees.

Robinovitch *et al.* (1991, 1995b, 1997) performed a series of studies to characterize the force applied to the proximal femur during impact resulting from a fall. The first study involved a pelvis release experiment designed to measure the effective stiffness and damping of the body when a step change in force is applied to the lateral aspect of the hip. They found that for high impact loads (above 500 N), the stiffness (k) and damping (b) coefficients plateau at values of 71.1 kN/m and 561 N-s/m for females and at 90.4 kN/m and 756 N-s/m for males, respectively. Further, they concluded that increased soft tissue thickness over the hip and impacting the ground in a relaxed state can decrease peak impact forces. In the second study, they used an impact pendulum and surrogate human pelvis to apply impact forces to trochanteric soft tissue specimens harvested from cadavers of nine elderly individuals. Peak forces ranged from 4,050 N to 6,420 N and energy absorption (integrated force over displacement) from 8.4 to 81.6 J (with 140 J total applied energy). Although increased tissue thickness correlated strongly with decreased peak force and increased tissue energy absorption, they concluded that trochanteric soft tissue alone is insufficient to prevent fracture in an elderly person with low bone mass. In the third study, they again performed the pelvis release experiment, this time establishing that only 15% of total impact force is distributed to tissues peripheral to the femur. They also found that impacting with the trunk upright (at a larger angle to the horizontal) significantly increases peak force, while muscle contraction has little effect. In the fourth study, they evaluated four different single-degree-of-freedom models, each possessing a single mass, to determine which best characterized the step response of the surrogate

human pelvis / impact pendulum system. They found that measured peak impact forces were best predicted by the mass-spring, Maxwell, and standard linear solid models (errors within 3%), but with significantly less accuracy by the Voigt model (error of 10%).

Several studies have been performed to assess the effectiveness of various hip protectors (hip pads) in attenuating the force applied to the femur during a fall impact. Lauritzen *et al.* (1993, 1996, 1997) found that the rate of hip fracture in a randomized nursing home population was reduced by 50% with the use of hip protectors and that none of the hip fractures in the intervention group occurred during the time that the hip protector was being worn. Parkkari *et al.* (1995) found in one series of tests that a peak impact force of 6940 N was attenuated by trochanteric soft tissue to a force of 5590 N, and by a hip protector to a force of 1040 N. In the second series, the peak impact force was reduced from 13,130 N to 10,400 N and 1810 N by trochanteric soft tissue and a hip protector, respectively. They later reported that, when wearing a hip protector, the fall impact forces do not cause unacceptable pain to the hip region and that the forces entering the proximal femur remain below the fracture range for elderly individuals (Parkkari *et al.*, 1997). Robinovitch *et al.* (1995a) found that their hip padding system attenuated the femoral impact force by 65 percent. They further concluded that hip pads that shunt energy away from the femur are superior to those that rely on absorbing energy in the pad material. Similarly, Mills (1996) found that through load transfer to the thigh musculature and energy absorption, a hip protector could double the estimated fall distance before fracture.

Dynamic models of varying levels of complexity have been used to simulate certain aspects of falls. A particularly thorough study was performed by van den Kroonenberg *et al.* (1995) in which they used three different paradigms to simulate the dynamics of falling: 1) a falling point mass or a rigid bar pivoting at its base; 2) two-link models consisting of a leg

segment and a torso; and 3) three-link models including a knee. Forces during hip impact were calculated from a simple spring-mass system in each case. Predicted values for the peak force applied to the greater trochanter ranged from 2.90 to 9.99 kN. In a related study, a video system was used to obtain fall kinematics parameters for six healthy young athletes (van den Kroonenberg *et al.*, 1996). The mean value for vertical hip impact velocity was 2.75 m/s and the mean value for trunk angle (with respect to the vertical) was 17.3 degrees. They also found a 38% reduction in trunk angle at impact, and a 7% reduction in hip impact velocity for relaxed vs muscle-active falls.

A summary of peak hip force values reported in the literature is presented in Table 2.2.

Table 2.2 Summary of peak hip forces in locomotion and fall studies.

Study	Locomotion Peak hip force (BW*)	Fall impact Peak hip force (BW*)
Crowninshield *et al.*, 1978	4.0-5.0 (walking, 1 m/s)	
van den Bogert *et al.*, 1999	2.5 (walking, 1 m/s) 5.2 (running, 3.5 m/s)	
Bergmann *et al.*, 1993	2.8 (walking, 0.3 m/s) 4.1 (walking, 0.8 m/s) 4.8 (walking, 1.4 m/s) 5.5 (jogging)	
Bassey *et al.*, 1997	2.5–4.0 (jumping, jogging)	
Robinovitch *et al.*, 1995†		5.8–9.2
Parkkari *et al.*, 1995†		9.9–18.8
van den Kroonenberg et al., 1996†		4.1–14.3

* BW = Body Weight
† Converted from N assuming BW = 700 N

Based on the values in the table it may be expected that the modeling effort described in the remainder of the chapter should produce hip forces in the range of 2.5–5.5 BW for locomotion, and 5.8–18.8 for fall impact.

2.2 Methods

The peak hip forces for the activities considered (locomotion and falls) were arrived at, in both cases, through three-link dynamic systems. Since most of the body motions during locomotion and falls are carried out by the ankle, knee and hip joints, a three-link model that includes these joints seemed appropriate. Given the success achieved in other studies using simpler models, such as the lumped-mass and linear spring model used by McMahon *et al.* (1987), and given that van den Kroonenberg *et al.* (1995) found that their two and three-link distributed mass models provided more accurate results than their simpler point mass and one-link models, it was anticipated that three-segment models with distributed mass properties would offer the appropriate level of accuracy.

In the case of the locomotion simulation, the motion was restricted to a single plane and thus the system required only three degrees of freedom (p_1, p_2 and p_3 in Figure 2.3). Given this fact, it was practical to formulate the equations of motion for the system by hand. An advantage of doing this was that added insight could be gained into the dynamics of the system through an explicit knowledge of the governing equations. This insight then helped guide the choice of an appropriate human control scheme, and also facilitated interpretation of the simulation results. The fall simulation, while also using only three links in the system, allowed motion in three-dimensions, thus requiring a greater number of degrees of freedom (five: q_1, q_2, q_3, q_4, and q_5 in Figure 2.7). The greater complexity introduced by these added degrees of freedom prompted the use of a computational formulation of the equations of motion.

2.2.1 Locomotion

The three segment dynamic system used in the locomotion simulation is depicted in Figure 2.3. The first segment represented the lower leg between the ankle and knee joints on one side of the body, the second segment represented the upper leg between knee and hip joints on the same side of the body, and the third segment represented the combined mass and inertia of the rest of the body (trunk, arms, head, and opposite leg). The mass (m_i) and inertia (I_i) of each segment (i) was assumed to be fixed with respect to its body-fixed coordinate system (in this case, 'body' refers to a single segment). In reality, movement of the arms and opposite leg would likely alter the inertia of the third segment somewhat, but it was assumed that this alteration would not have a large enough impact on the forces and moments in the hip joint to warrant the much greater complexity that would be required in the model to account for this.

Since planar motion was assumed (in the sagittal plane), the ankle, knee and hip joints were represented by simple one degree-of-freedom pin (or hinge) joints, giving the system a total of three degrees of freedom. The joint angles (p_1, p_2 and p_3) and torques (τ_1, τ_2 and τ_3) were described in general coordinates (i.e., with respect to a fixed horizontal reference) since this simplified the formulation of the equations of motion. The geometry of each segment was described by the distance between joints (l_i), and the distance of the center of mass from the inboard (closer to ground/ankle) joint (l_{ci}). The center of mass of each segment was assumed to lie along the line connecting the joints or along the axis of symmetry (in the case of the third segment).

The equations of motion for the system were determined through a Lagrangian Formulation (Asada and Slotine, 1986). Note that in all equations given below, bold characters are

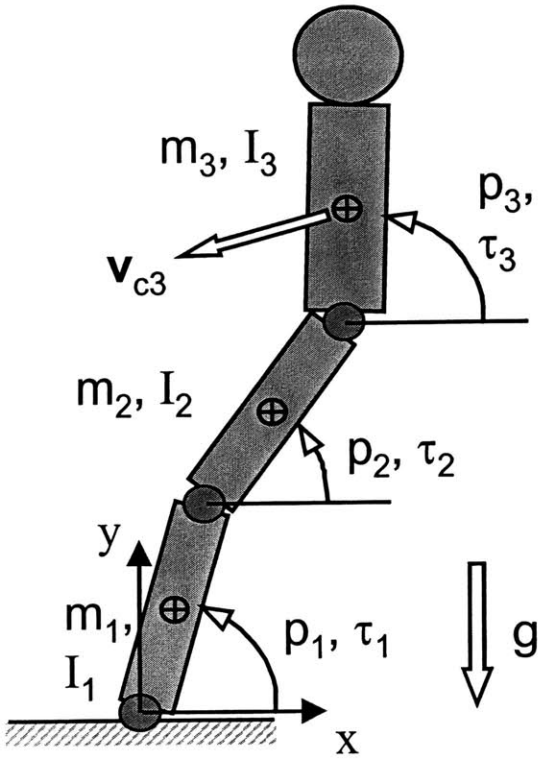

Figure 2.3: Three segment planar model used to simulate human locomotion.

used to represent vectors and matrices. The governing equation for this formulation, which has been simplified from its most general form by the use of generalized coordinates, is

$$\mathbf{H}\ddot{\mathbf{p}} + \mathbf{h}\dot{\mathbf{p}}_{sq} + \mathbf{G} = \mathbf{Q} \tag{2.1}$$

The first term on the left side represents the inertial coupling between segments. It consists of the system inertia tensor, $\mathbf{H}$, multiplied by the joint angular acceleration vector:

$$\ddot{\mathbf{p}} = \begin{bmatrix} \ddot{p}_1 \\ \ddot{p}_2 \\ \ddot{p}_3 \end{bmatrix} \tag{2.2}$$

The second term, which would generally account for torques arising due to centrifugal and Coriolis effects, in this case represents only centrifugal effects, since Coriolis terms were

eliminated by the choice of generalized coordinates. Consequently, only squared angular velocity terms appear in the vector:

$$\dot{\mathbf{p}}_{sq} = \begin{bmatrix} \dot{p}_1^2 \\ \dot{p}_2^2 \\ \dot{p}_3^2 \end{bmatrix} \tag{2.3}$$

The third term, $\mathbf{G}$, represents torques on the system due to gravity. Finally, the term on the right side, $\mathbf{Q}$, corresponds with the external torques placed on the system, including torques generated by the action of muscles.

More explicitly, the inertia tensor is given by:

$$\mathbf{H} = \begin{bmatrix} H_{11} & H_{12} & H_{13} \\ H_{21} & H_{22} & H_{23} \\ H_{31} & H_{32} & H_{33} \end{bmatrix} \tag{2.4}$$

where

$$\begin{aligned}
H_{11} &= m_1 l_{c1}^2 + I_1 + m_2 l_1^2 + m_3 l_1^2 \\
H_{12} &= (m_2 l_1 l_{c2} + m_3 l_1 l_2)\cos(p_1 - p_2) \\
H_{13} &= m_3 l_1 l_{c3}\cos(p_1 - p_3) \\
H_{21} &= H_{12} \\
H_{22} &= m_2 l_{c2}^2 + I_2 + m_3 l_2^2 \\
H_{23} &= m_3 l_2 l_{c3}\cos(p_2 - p_3) \\
H_{31} &= H_{13} \\
H_{32} &= H_{23} \\
H_{33} &= m_3 l_{c3}^2 + I_3
\end{aligned}$$

The length of each segment is denoted by l_i, and the distance from the inboard joint to the corresponding segment's center of mass is denoted by l_{ci}. The derivation of each of the terms in this matrix from the system Jacobians is given in Appendix A.

The coefficient matrix in the second term of Equation (2.1) contains nine entries:

$$\mathbf{h} = \begin{bmatrix} h_{111} & h_{122} & h_{133} \\ h_{211} & h_{222} & h_{233} \\ h_{311} & h_{322} & h_{333} \end{bmatrix} \tag{2.5}$$

The individual entries are derived from the system inertia tensor via the expression:

$$h_{ijk} = \frac{\partial H_{ij}}{\partial p_k} - \frac{1}{2}\frac{\partial H_{jk}}{\partial p_i} \qquad (i = 1, 2, 3), (j = 1, 2, 3), (k = 1, 2, 3) \tag{2.6}$$

Ordinarily, this expression would yield 27 terms, but the use of general coordinates eliminates terms where $j \neq k$. The nine remaining entries that fill the matrix in Equation (2.5) are:

$$\begin{aligned} h_{111} &= 0 \\ h_{122} &= m_2 l_1 l_{c2} \sin(p_1 - p_2) + m_3 l_1 l_2 \sin(p_1 - p_2) \\ h_{133} &= m_3 l_1 l_{c3} \sin(p_1 - p_3) \\ h_{211} &= -h_{122} \\ h_{222} &= 0 \\ h_{233} &= m_3 l_2 l_{c3} \sin(p_2 - p_3) \\ h_{311} &= -h_{133} \\ h_{322} &= -h_{233} \\ h_{333} &= 0 \end{aligned} \tag{2.7}$$

The third term in Equation (2.1), representing gravity torques, is derived from the expression:

$$G_i = \sum_{j=1}^{3} m_j \mathbf{g}^T \mathbf{J}_{Li}^{(j)} \tag{2.8}$$

where $\mathbf{g}^T$ represents the transpose of the gravity vector and $\mathbf{J}_{Li}^{(j)}$ corresponds with the i-th column of $\mathbf{J}_L^{(j)}$ (given in Appendix A). The direction of gravitational acceleration is vertical, as indicated in Figure 2.3. In this case, however, its magnitude can take on one of two values:

Earth gravity ($\mathbf{g} = \begin{bmatrix} 0 & -g & 0 \end{bmatrix}^T = \begin{bmatrix} 0 & -9.807 & 0 \end{bmatrix}^T$ m/s^2)

or Mars gravity ($\mathbf{g} = \begin{bmatrix} 0 & -\frac{3}{8}g & 0 \end{bmatrix}^T = \begin{bmatrix} 0 & -3.678 & 0 \end{bmatrix}^T$ m/s^2).

Finally, the last term in Equation (2.1) is given by the expression:

$$\mathbf{Q} = \begin{bmatrix} \tau_1' \\ \tau_2' \\ \tau_3' \end{bmatrix} = \begin{bmatrix} \tau_1 - \tau_2 \\ \tau_2 - \tau_3 \\ \tau_3 \end{bmatrix} \tag{2.9}$$

where τ_i' represents the net torque (from all muscle groups) acting at joint i expressed in generalized coordinates, and τ_i represents the net torque at joint i expressed in relative coordinates.

All of the above equations were coded in a MATLAB (The Mathworks, Inc., Natick, MA) script (Appendix C). The simulation was carried out using the following procedure:

1. Set initial conditions
2. Apply control laws
3. Calculate joint accelerations
4. Integrate to obtain, in turn, joint velocities and joint positions

5. Calculate hip force from acceleration of center of mass of segment 3 (upper body)
6. Increment time and repeat until end of stance phase

The initial configuration of the system was set in accordance with configurations described in other studies (McMahon *et al.*, 1987; McMahon and Cheng, 1990; He *et al.*, 1991). The hip angle was set at 90 degrees (to the horizontal), the knee angle was set at 5 degrees less than the ankle angle, and the ankle angle itself was adjusted iteratively through successive simulation loops until the lowest point traced out by the locus of hip position was within ±1 cm of the horizontal location of the ankle. In other words, until the arc traced out by the hip was centered over the point of support (Figure 2.4). To obtain the initial joint velocities, it was assumed that the center of mass of the third segment was moving with a linear velocity, v_{c3}, and that the hip joint velocity was zero (following stabilization of the upper body during the initial heel strike). The velocities of the knee and ankle joint were thus uniquely determined through the inverse of the Jacobian matrix connecting the joint rotational velocities to the third segment's linear velocity:

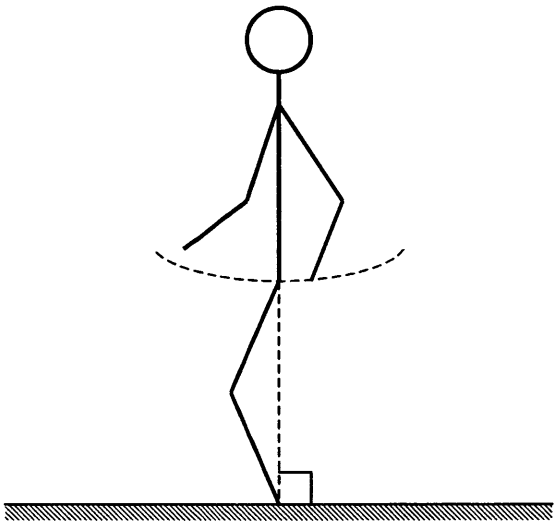

Figure 2.4: Hip locus centered over point of support.

$$\dot{\mathbf{p}} = (\mathbf{J}_L^{(3)})^{-1}\mathbf{v}_{c3} \tag{2.10}$$

To ensure that excessively high initial accelerations were avoided, and to simulate the effect of heel-strike shock-absorption provided by the human foot during locomotion, but without the added complexity of an additional segment, the initial linear velocity of the third segment's center of mass was provided with the transient function

$$\mathbf{v}_{c3} = (\mathbf{v}_{c3})_{max}\sin^2\left(\frac{t}{t_{max}}90°\right) \tag{2.11}$$

The t_{max} value was chosen to be 0.05 seconds to correspond with the duration of the heel-strike transient observed in other studies (McMahon *et al.*, 1987; He *et al.*, 1991) (transient heel-strike spike of magnitude 1,000–1,200 N lasting 0.04–0.05 seconds, both parameters independent of gravity level). In addition, to assess the sensitivity of hip joint loading on locomotion speed, the horizontal component of $(\mathbf{v}_{c3})_{max}$ was set at values of 2, 3, 4, 5, and 6 m/s in successive simulations in Earth gravity, and at values of 2, 3, and 4 m/s for Mars gravity, since it has been observed that humans are unlikely to run at speeds greater than 4 m/s in Mars gravity (Newman *et al.*, 1994; Wickman and Luna, 1996). It should further be noted that for both Earth and Mars, this range of speeds is consistent with running, rather than walking. Walking was not simulated since it presents a less severe loading condition for the hip and, in addition, it has been established that running (or at least loping) is a more efficient means of locomotion than walking in reduced gravity fields such as that on Mars (Newman *et al.*, 1994). The vertical component of $(\mathbf{v}_{c3})_{max}$ was set at a constant value of -0.78 m/s in accordance with McMahon and Cheng's (1990) finding that this value is relatively invariant.

Control laws were used to generate joint torques (representing the action of muscle forces) in response to the kinematic state of the system and drive it toward a desired future kinematic state. Several control laws have been previously formulated and are in common use. Some of these include: proportional, proportional plus derivative (PPD), impedance, proportional-integral-derivative (PID), adaptive, and optimal control. Two control laws were applied during the simulation. Both control laws make use of stiffness and damping terms and were chosen because models utilizing elasticity and damping components have successfully reproduced the gross mechanical properties of muscle contraction (Hollerbach, 1977; McMahon, 1984). The hip joint was controlled using a proportional plus derivative (PPD) control law:

$$\tau_3 = k_3(p_{3b} - p_3) - b_3\dot{p}_3 \tag{2.12}$$

The proportional and derivative constants, k_3 and b_3, were established through trial and error so that reasonable motions and torques were obtained at the hip (values are reported below). The ankle and knee joints were controlled in combination using an impedance control law (Asada & Slotine, 1986; Hogan, 1985). The impedance control law has the effect of causing the lower leg to act as if it were a linear spring connecting the hip joint directly to the ankle (see Figure 2.5). This control law was chosen for three reasons. Firstly, impedance control has been shown to be an effective means of simulating the passive and active properties of limbs actuated by muscles (Hogan, 1980). Secondly, several studies have found that modeling the lower leg as a linear spring produces reasonable results for locomotion kinematics and joint loading (Siegler *et al.*, 1982; McMahon *et al.*, 1987; McMahon and Cheng, 1990; Farley and Gonzalez, 1996; Viale *et al.*, 1998). Thirdly, it was desirable to be able to compare the results of this simulation to those reported in the literature, especially for hip force. This simulation

went a step further than those in which the human is modeled simply as a concentrated mass connected to the ground via a massless linear spring because the mass and inertia of the upper and lower leg were accounted for along with the inertia and displaced center of mass for the upper body.

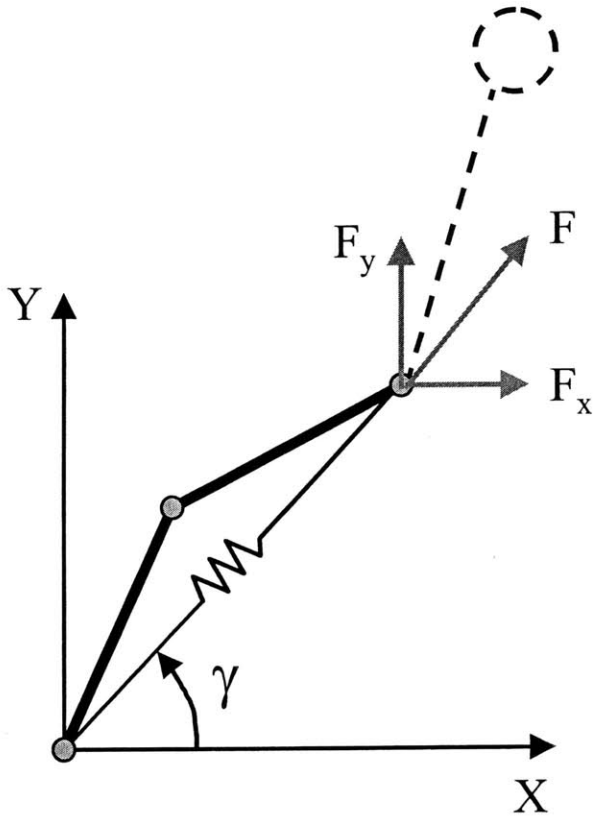

Figure 2.5: Impedance control of the ankle and knee joints causes the upper body to respond as if there were a virtual spring and damper connecting the hip directly to the ankle.

The mathematical expression of the impedance control law may be written:

$$\tau = \mathbf{G}_e - \mathbf{J}_h(\mathbf{K}_{\text{leg}}\mathbf{x}_e + \mathbf{B}_{\text{leg}}\dot{\mathbf{x}}_e) \tag{2.13}$$

where $\mathbf{G}$ is the estimated gravitational torque, $\mathbf{J}_h$ is the Jacobian matrix relating the ankle and knee angular velocities to the linear velocity at the hip (which is the same as the linear veloc-

ity of the center of mass of segment 3 when the trunk maintains a fixed orientation), $\mathbf{x}_e$ is the difference between the actual and desired distance between the hip and ankle, expressed as

$$\mathbf{x}_e = \mathbf{x} - \mathbf{x}_b \tag{2.14}$$

and similarly, $\dot{\mathbf{x}}_e$ is the difference between the actual and desired hip linear velocity. The coefficient matrices take on the following forms:

$$\mathbf{K}_{\text{leg}} = \begin{bmatrix} k_{\text{leg}}\cos\gamma & 0 \\ 0 & k_{\text{leg}}\sin\gamma \end{bmatrix} \tag{2.15}$$

and

$$\mathbf{B}_{\text{leg}} = \begin{bmatrix} b_{\text{leg}}\cos\gamma & 0 \\ 0 & b_{\text{leg}}\sin\gamma \end{bmatrix} \tag{2.16}$$

where γ is the angle between the horizontal and the line connecting the ankle and hip as indicated in Figure 2.5. The dependence on the angle of the leg was required so that the line of action of the spring and damper was always along the line connecting the ankle to the hip.

Joint accelerations were calculated by solving Equation (2.1) to yield:

$$\ddot{\mathbf{p}} = \mathbf{H}^{-1}(\mathbf{Q} - \mathbf{h}\dot{\mathbf{p}}_{sq} - \mathbf{G}) \tag{2.17}$$

where $\mathbf{Q}$ was updated to reflect the action of control torques.

At this point, the hip force, $\mathbf{f}_h$, was calculated using the following expression:

$$\mathbf{f}_h = m_3(\mathbf{g} - \mathbf{J}_L^{(3)}\ddot{\mathbf{p}}) \tag{2.18}$$

in which the linear acceleration of the center of mass of segment 3 was obtained from the joint angular accelerations through the jacobian matrix, $\mathbf{J}_L^{(3)}$.

Finally, as the last step in the simulation, numerical integration was performed using Euler's method to update the joint accelerations and velocities. The time step was chosen to be small enough (dt = 0.0001 sec) that intolerable numerical drift was avoided.

To ensure that the results of the simulation runs would be representative of the astronaut population, the mass properties and segment geometries were calculated for 5th percentile, 50th percentile, and 95th percentile adult males and females using the mass properties program GEBOD that uses regression equations based on data from 2,420 male and 1,905 US Air Force personnel (Baughman, 1983). Additional mass property parameters were calculated to account for the situation in which astronauts don a space suit and portable life support system (PLSS, worn as a backpack) to perform an EVA on Mars. The mass of the spacesuit was distributed proportionately amongst the three segments (according to original segment mass), while the mass of the PLSS was added to segment 3 alone. Furthermore, it was assumed that the mass of the spacesuit (29.5 kg) and PLSS (15 kg) would be the same for all six percentile cases. The values obtained from GEBOD and spreadsheet calculations are presented in Appendix B.

Control parameters for the simulation runs were set as follows. Through iteration, the hip joint values were set at

$$k_3 = 1000 \text{ N-m/rad}$$
$$b_3 = 100 \text{ N-m/rad/sec}$$

for all of the simulation runs. These values maintained the upper body in a fixed orientation (with respect to the ground reference frame) to within 1 degree, while producing torques well

below the threshold of human strength (approximately 200–300 N-m). For the impedance control parameters, it was found that the most realistic kinematics were obtained with the damping constant, b_{leg}, set to zero. Thus, in the final simulation runs, the leg acted simply as an undamped linear spring. To assess the impact of variation in leg spring stiffness, k_{leg} was set to values of 9, 11, 13 and 15 kN/m, chosen to agree with those values reported in the literature (McMahon *et al.*, 1987; McMahon and Cheng, 1990; Farley and Gonzalez, 1996; Viale *et al.*, 1998), for successive simulation runs using the male and female 50th percentile parameters. For the 5th and 95th percentile males and females, the leg spring stiffness was set at a constant value of 13 kN/m. The experimental design for the locomotion simulation runs is depicted in Figure 2.6. The two main categories were Earth gravity and Mars gravity. Mars

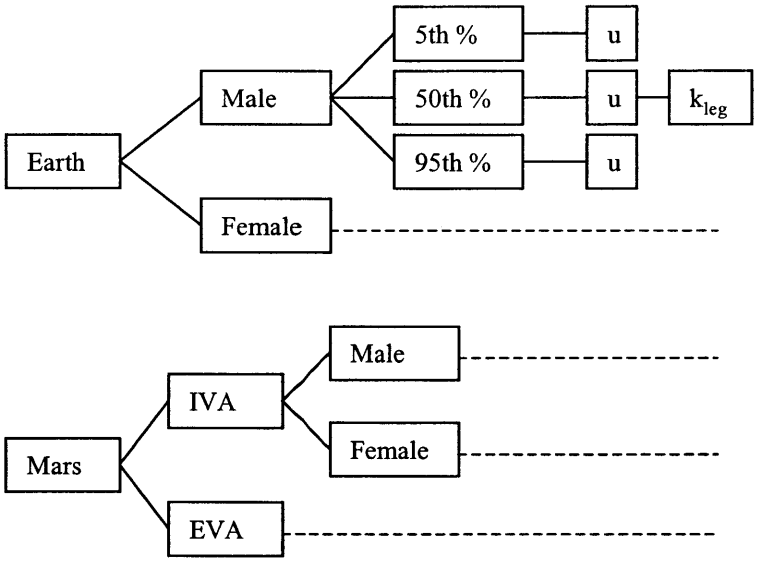

Figure 2.6: Schematic depicting experimental design for locomotion simulations.

was further divided into EVA and IVA. Each of these three groups were divided in turn by gender, body size percentile, and horizontal velocity (u). For the 50th percentile cases on Earth and in Mars EVA, additional permutations were performed for the range of leg spring stiffnesses (k).

2.2.2 Falls

As for the locomotion simulation, a three segment model was used for fall simulations (Figure 2.7). In this case, however, the lowest segment represented both lower legs combined, the second segment represented both upper legs combined, and the third segment represented the upper body, including trunk, head, and arms. Another significant difference from the locomotion model was that the system had five degrees of freedom to allow full three-dimensional motion, in contrast to the locomotion simulation in which only three degrees of freedom were required because the motion was restricted to a single plane. The fall model was based on van den Kroonenberg *et al.'s* (1995), but excluded some of their limitations. Their model had the hip location constrained to the frontal (y-z) plane and the trunk fixed at 30 degrees to the vertical so that only three degrees of freedom remained. The model used herein removed the limitations and thus retained all five degrees of freedom. As indicated in Figure 2.7 the degrees of freedom were: ankle inversion-eversion (q_1), ankle flexion-extension (q_2), knee flexion-extension (q_3), hip flexion-extension (q_4) and hip abduction-adduction (q_5). The ankle of the model was fixed to the ground which precludes the modeling of falls due to slipping. This was done to avoid the significantly greater complexity of modeling a dynamic system that is not anchored to the ground. Although this was a limitation, it is not anticipated that a fall due to slipping would significantly increase the load applied to the hip during impact since the same potential energy is involved in either case and since an anchored fall would likely increase the kinetic energy at impact (through centripetal acceleration around the ankle).

The added complexity in the equations of motion due to the additional degrees of freedom prompted the use of computational formulation. The software package used to accomplish the formulation was SD/FAST (Symbolic Dynamics, Mountain View, CA). SD/FAST takes input from a text file, called a 'system description' file, in which the geometry, mass properties,

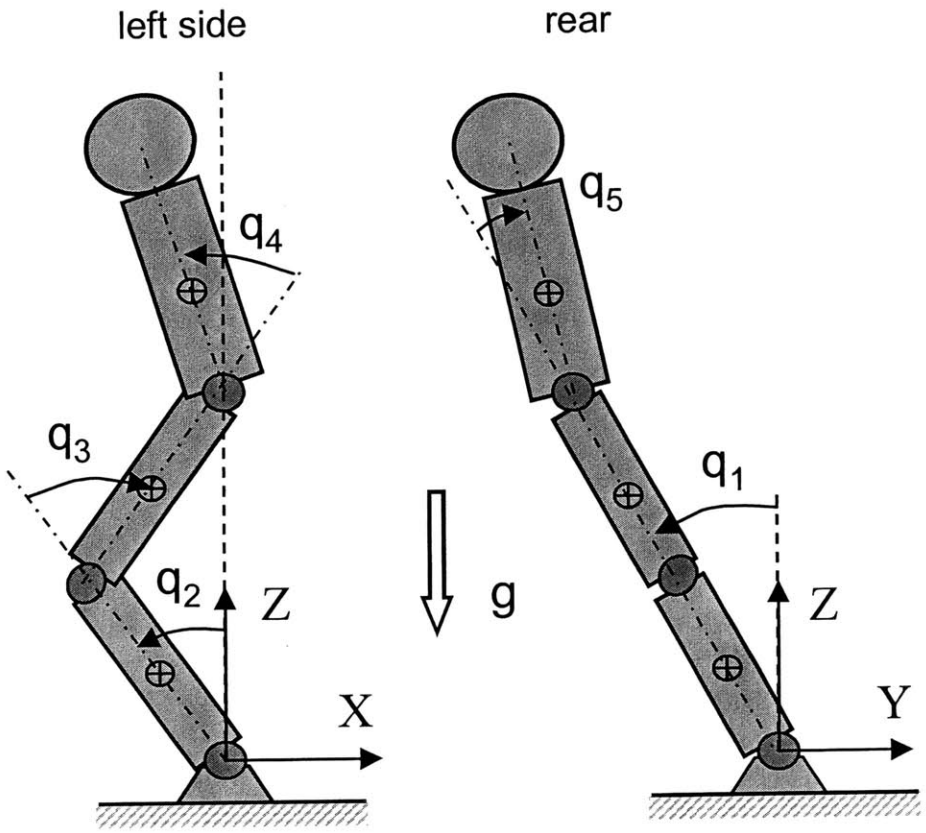

Figure 2.7: Three segment model used for simulation of human falling to the side.

connectivity, and gravity level are specified in a standard format. An example of a system description file for one of the simulation runs using parameters for a 50th percentile male is given in Appendix C. Once executed, SD/FAST formulates the equations of motion using Kane's method (Kane and Levinson, 1985) and represents them by means of subroutines. The user then writes additional code that calls these subroutines to initialize the positions and velocities of the joints, execute the time step loops, control the motion of the system through joint torques, and record the resulting kinematic and kinetic information (user code is presented in Appendix C).

The fall simulation was controlled in a similar manner to that of the locomotion simulation and according to the same justifications. Both degrees of freedom at the hip were controlled through PPD generated torques:

$$\begin{aligned} \tau_4 &= k_4(q_{4b} - q_4) - b_4\dot{q}_4 \\ \tau_5 &= k_5(q_{5b} - q_5) - b_5\dot{q}_5 \end{aligned} \tag{2.19}$$

In this case, the joint angles and velocities are represented by the variables, q_i and $\dot{q}_i$, respectively, to indicate that relative (rather than generalized) coordinates are used. The subscript 'b' indicates a "bias" or command angle (i.e., the angle toward which the joint torques push the joint). The ankle and the knee joint flexion-extension degrees of freedom were controlled together using impedance control, as presented in Equation (2.13) and Equation (2.14). In this case, however, the stiffness and damping matrices were independent of the overall leg angle. That is

$$\mathbf{K}_{\text{leg}} = \begin{bmatrix} k_{yz} & 0 \\ 0 & k_x \end{bmatrix} \tag{2.20}$$

and

$$\mathbf{B}_{\text{leg}} = \begin{bmatrix} b_{yz} & 0 \\ 0 & b_x \end{bmatrix} \tag{2.21}$$

where the subscripts yz and x refer to lines of action either parallel to the line connecting the ankle and hip (stays close to the yz plane) or perpendicular to the yz plane, respectively.

Ground impact was simulated using a simple spring-mass-damper model, as employed by both Robinovitch *et al.* (1991) and van den Kroonenberg *et al.* (1995). The restoring force was applied once the ankle eversion angle exceeded 90 degrees (thus bringing the hip into contact

with the ground) and was applied only at the hip, thus assuming that other parts of the leg and body did not come into contact with the ground before the hip, as has been found to be generally true in kinematic studies performed by van den Kroonenberg *et al.* (1996). Once the hip made contact with the ground, its initial location was recorded in three-dimensions. The soft tissue covering the hip was represented as a linear spring and dashpot model. As the tissue was compressed, the restoring force was calculated and applied opposite to the direction of displacement, according to the relation:

$$\mathbf{F}_r = -k_r\mathbf{dr} - b_r\dot{\mathbf{dr}} \tag{2.22}$$

where $\mathbf{dr}$ is the vector difference between the position of the hip during compression and the position of the hip at initial ground contact, k_r is the spring constant and b_r is the damping constant.

Several parameters were varied during successive simulation runs. Gravitational acceleration was set to either Earth gravity or Mars gravity. Mass properties and anthropometric data for males and females of the 5th, 50th, and 95th percentiles were derived using GEBOD and combined to produce the mass properties for the three segments (See Appendix B). For the Mars gravity simulations, two cases were again considered: intravehicular activity (IVA) and extravehicular activity (EVA), where the mass properties of the spacesuit were added to that of the astronaut. The initial positions and velocities for the joints were set to correspond with values chosen by van den Kroonenberg *et al.* (1995) based on their kinematics study. It was assumed that males have the same initial configuration as females. The 50th percentile values were obtained by interpolating between the values reported for 5th and 95th percentile subjects. Joint control parameters were varied iteratively until the final joint angles at fall impact were within a few degrees of the impact body configuration values previously reported (van

den Kroonenberg *et al.*, 1995). The spring stiffness values for the ground impact model were set to 90.4 kN/m for males and 71.1 kN/m for females falling in Earth gravity and during IVA on Mars. In contrast, for Mars EVA the stiffness was reduced by 20%, to 72.3 kN/m for males and 56.9 kN/m for females, to estimate the additional padding provided by a spacesuit. As a further evaluation of force attenuation provided by padding in the space suit or supplemental hip pads, the stiffness values were varied from 100% to 20% of the Earth / Mars IVA values for the simulations run on the 50th percentile male and female models. It was assumed, on the other hand, that the damping constant for ground impact would not be affected by the presence of a spacesuit, and thus the damping constants were fixed at 756 N/(m/s) for males, and 561 N/(m/s) for females (Robinovitch *et al.*, 1991).

Control parameters used in the fall simulation runs are given in Table 2.3. The parameters that exerted the greatest influence on the simulations were found to be the hip torsional stiff-

Table 2.3 Control parameters used in fall simulations.

Subject	k_5	k_4	b_4	k_x	b_x	k_{yz}	b_{yz}	k_r	b_r
F5E	8	500	10	5000	100	1120	100	71100	561
F50E	12	500	10	5000	100	1450	100	71100	561
F95E	16	700	10	5000	100	1650	100	71100	561
M5E	15	1000	10	5000	100	1700	100	90400	756
M50E	20	1200	10	5000	100	2050	100	90400	756
M95E	30	1400	10	5000	100	2320	100	90400	756
F5M	8	500	10	5000	100	1120	100	56900	561
F50M	12	500	10	5000	100	1200	100	56900	561
F95M	16	700	10	5000	100	1200	100	56900	561
M5M	15	1000	10	5000	100	1200	100	72300	756
M50M	20	1200	10	5000	100	1300	100	72300	756
M95M	20	1400	10	5000	100	1300	100	72300	756
F5MI	2	300	10	3000	100	450	50	71100	561
F50MI	4	300	10	3000	100	570	50	71100	561
F95MI	5	350	10	3000	100	620	50	71100	561
M5MI	3	400	10	3000	100	650	50	90400	756
M50MI	5	500	10	3000	100	750	50	90400	756
M95MI	6	600	10	3000	100	800	50	90400	756

Subject Label: (M=male, F=female)(percentile)(E=Earth, M=Mars EVA, MI=Mars IVA)

nesses (k_5 and k_4) and the y-z plane leg stiffness (k_{yz}). Some parameters required only minor modification, such as a reduction in the leg perpendicular stiffness (k_x) and in-plane damping (b_{yz}) for Mars IVA, or none at all. The ground impact model stiffness and damping values (k_r and b_r) were set in accordance with the previous study by Robinovitch, *et al.* (1991) as described in the methods section of this chapter.

The experimental design for the fall simulation runs is depicted in Figure 2.8. The same permutations were used as in the locomotion simulations up to the body size percentile level. For the 50th percentile cases of both males and females in the Mars EVA category, additional permutations were performed for the range of ground impact stiffnesses (k_{gnd}) to account for the uncertainty in force attenuation through the space suit fabric.

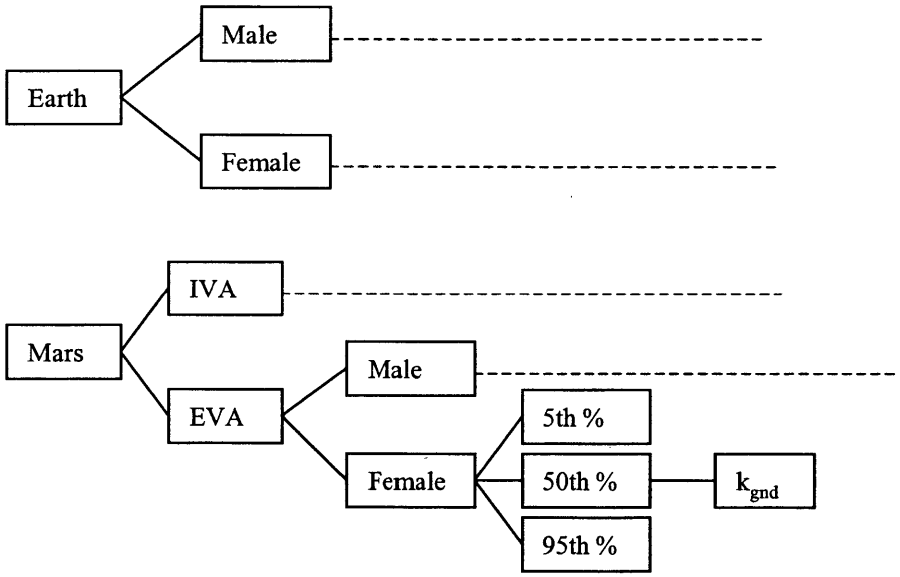

Figure 2.8: Schematic depicting experiment design for fall simulations

2.3 Results

2.3.1 Locomotion

A typical kinematic plot for the locomotion simulation, in this case a 50th percentile male running at 4 m/s in Earth gravity, is shown in Figure 2.9a. The plot depicts a 'stick-figure' representation of the three segment human model, as viewed from the astronaut's left side. Each figure is a snapshot of the model, taken at intervals of 0.05 seconds. The figure shows that during the locomotion simulation the upper body remained vertical, the knees flexed and extended, and the leg rotated around the ankle. With the assistance of the drawn arc, it is easy to see that the hip position dipped down slightly and then recovered as it translated forward. The Mars (EVA) locomotion stick-figure plot (Figure 2.9b) appears similar to the Earth case, except that it is noticeable that the leg started out at a slightly shallower angle to the horizontal at heel-strike, and the knee achieved a slightly greater degree of flexion.

Typical joint position and velocity plots for the locomotion simulations (in this case a 50th percentile male running at 4 m/s on Earth and during a Mars EVA) are shown in Figure 2.10. For this case the initial ankle angle (found through iteration) was 73 degrees, the knee angle 68 degrees, and the hip angle 90 degrees. The knee first flexed to about 45 degrees (relative to the lower leg) at mid-stance and then extended during the remainder of the stance phase, thus accounting for a shortening and extension of the virtual spring acting between the point of support and the hip. The ankle joint angle increased throughout the stance phase, initially increasing rapidly due to flexion at the knee, then increasing more gradually as the leg rotated around the point of support, and finally reached an angle of about 127 degrees at toe-off. The hip joint angle deviated less than 1 degree from its starting value of 90 degrees.

a)

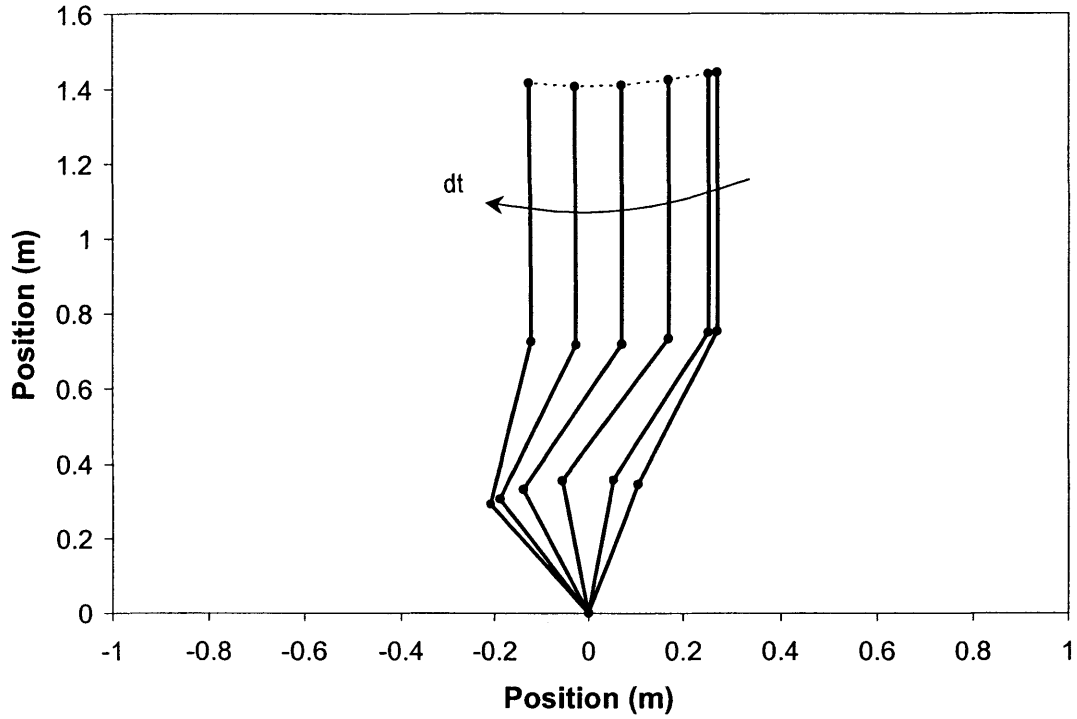

b)

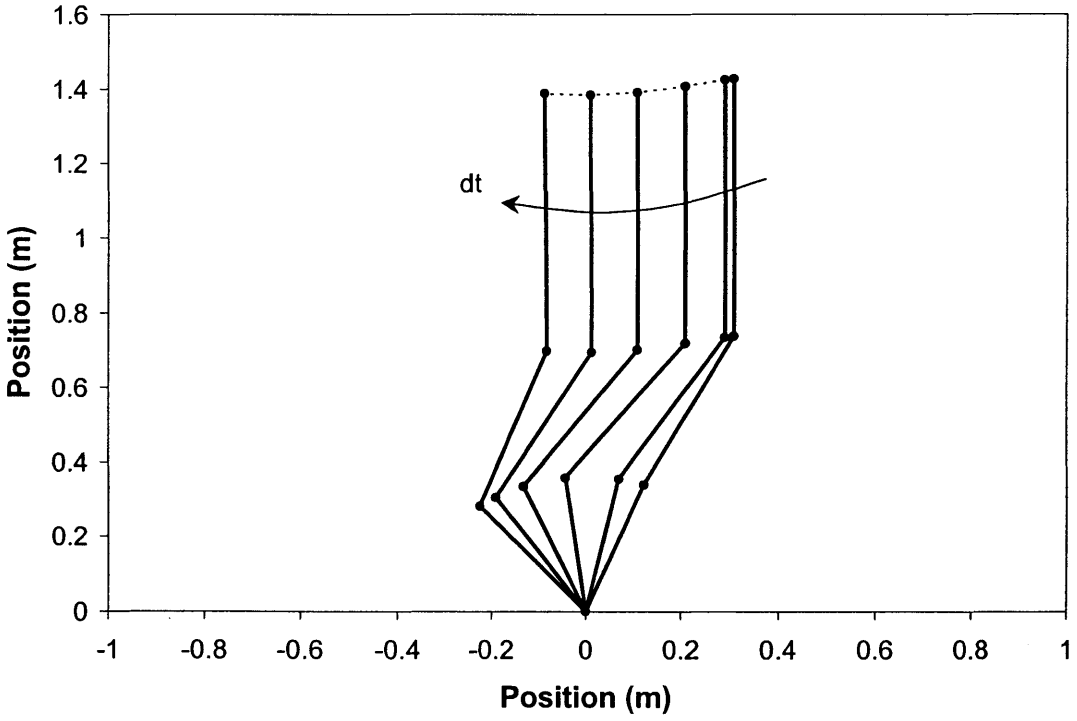

Figure 2.9: Kinematic ('stick-figure') plot for 50th percentile male running at 4 m/s in a) Earth gravity, and b) Mars gravity.

a)

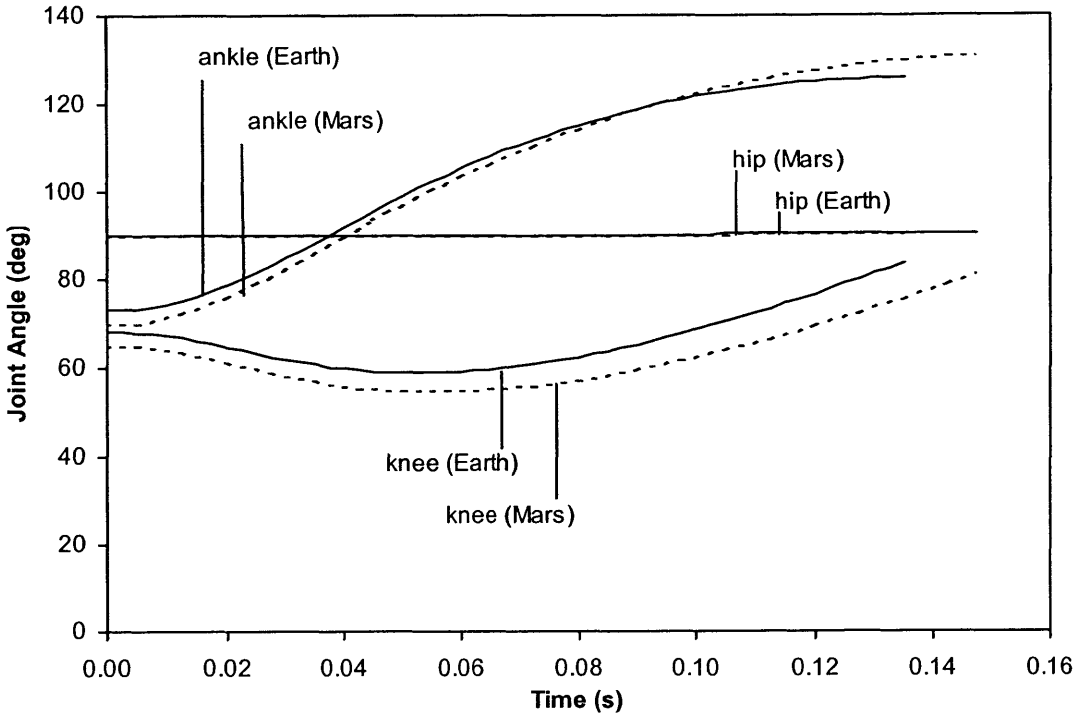

b)

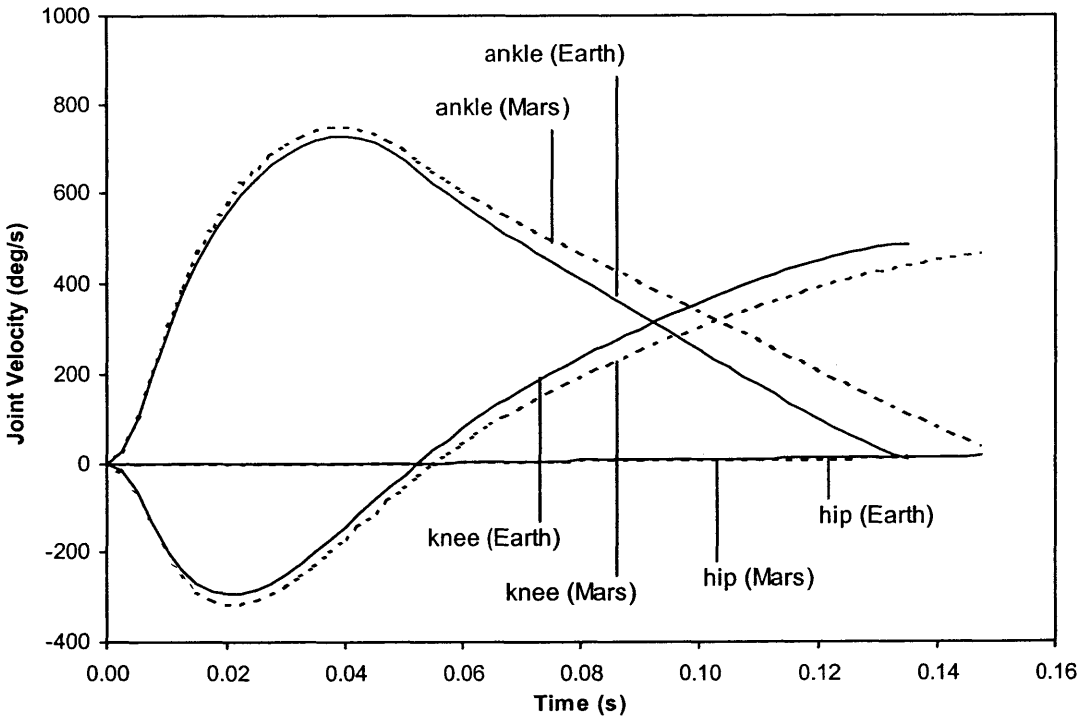

Figure 2.10: Plots of a) joint position, and b) joint velocity for a 50th percentile male running at 4 m/s in Earth gravity and Mars gravity (EVA).

The plot of joint velocities (Figure 2.10b) shows clearly how the most rapid change in the ankle and knee angles occurred during the first 0.02 to 0.04 seconds, corresponding with the initial flexion of the knee following heel-strike. While the angular velocity of the knee changed sign, indicating a switch from flexion to extension, the angular velocity of the ankle simply approached zero toward the end of the stance phase since the effect of leg rotation was almost exactly balanced by extension at the knee. For the Mars case, the ankle and knee joint achieved slightly higher velocities overall, particularly toward the end of the stance phase.

Joint accelerations are shown in Figure 2.11a. The acceleration started at zero and followed a smooth transition attributable to the transient function employed for the center of mass velocity of segment 3. The highest acceleration values occurred during the first 0.04 seconds, corresponding with flexion of the knee, compression of the virtual leg spring, and the increase in velocity of the segment 3 center of mass during the transient period. Interestingly, the Mars acceleration curves reached higher peaks than the Earth accelerations during the initial stance, but then dropped to below the Earth acceleration values for most of the remainder of the stance phase.

The plot of joint torque (Figure 2.11b) reveals that very little torque developed in any of the joints until well after the end of the transient period (0.05 seconds). The peak knee torques were approximately 200 N-m at around 0.08 seconds (Earth) and 300 N-m at around 0.09 seconds (Mars). The ankle torques reached relatively high values toward the end of the stance phase, as much as -400 N-m, demonstrating the effort required to maintain the leg spring stiffness as the leg neared full extension. By contrast, the hip torques were low, never reaching more than -35 N-m. The ankle and knee torques obtained for the Mars simulation achieved significantly higher magnitudes than the Earth case, particularly in the 0.08 to 0.09 sec time

a)

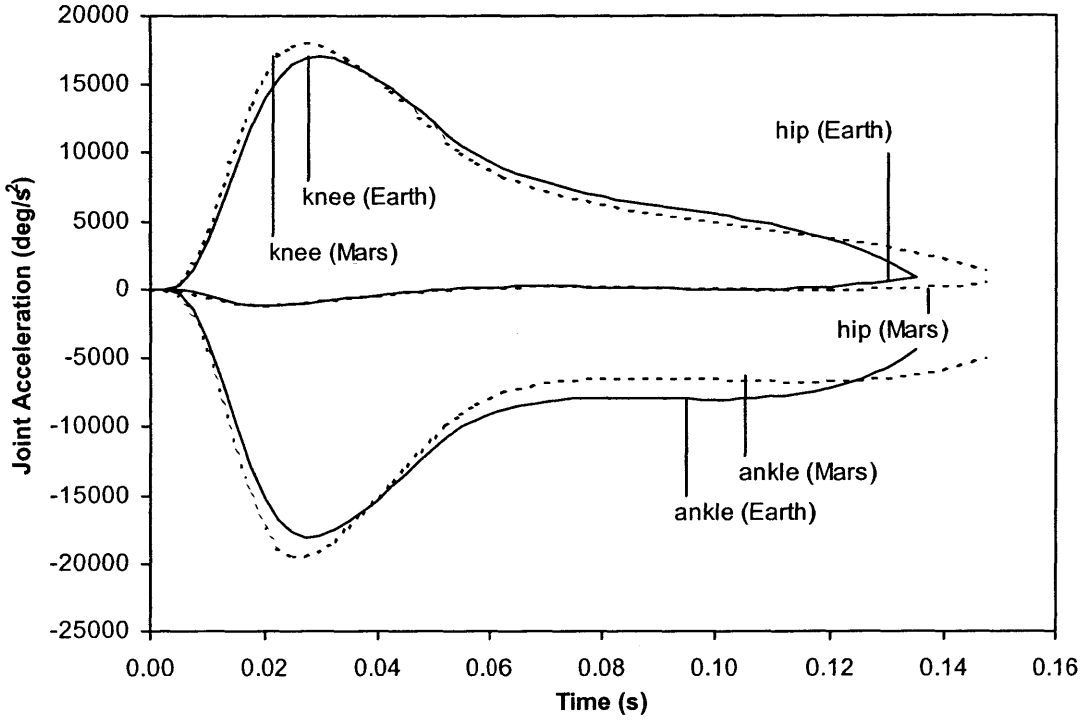

b)

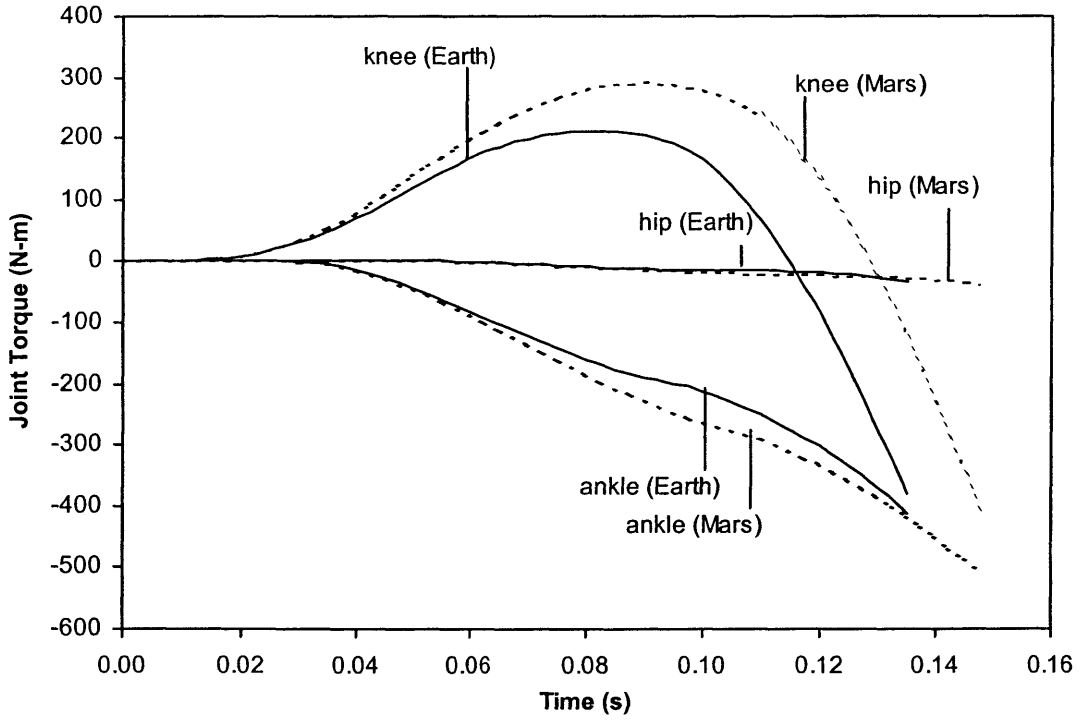

Figure 2.11: Time history plots of a) joint acceleration, and b) joint torque for a 50th percentile male running at 4 m/s in Earth gravity and Mars gravity (EVA).

frame, where the knee torque for Mars exceeded the Earth case by as much as 100 N-m. The reason for this is apparent after examining the next two plots (hip locus and hip joint force).

The hip locus plot (Figure 2.12a) confirms that the hip trajectory was centered over the point of support for both Earth and Mars simulation cases. The angle swept out by the leg was noticeably larger for the Mars gravity simulation, indicating a longer support period. Furthermore, the hip locus was slightly lower for the Mars case, indicating that the leg is compressed to a greater extent.

The greater amount of leg compression, observed in the hip locus plot, lead to a greater total hip force for the Mars EVA case (Figure 2.12b), since the leg was controlled as if it were a linear spring. This also explains the larger joint torques (Figure 2.11b) which were further magnified by the increased angular displacement of the ankle and knee joints (larger moment arms meant that more torque was required to achieve the same restoring force at the hip). The hip force was considered to be the force applied to the femoral head by the torso. A peak is seen in the horizontal component of force (x direction) for both cases during the heel-strike transient, as the leg spring line of action was at an angle to the vertical during initial compression. The horizontal force remained close to zero as the leg passed through 90 degrees and then increased as the toe-off point neared. The vertical component of hip force (y direction) started at a magnitude corresponding to upper body weight (since the transient function has the upper segment acceleration starting at zero), thereafter dropped off rapidly, and even became positive at around 0.02 seconds, then once again become increasingly negative, and reached a peak at about 0.085 seconds (Earth) or 0.095 seconds (Mars). The initial drop-off in hip force magnitude, and the positive swing, was due to the transient function causing the upper body (segment 3) to accelerate downwards at a higher rate than it would in free-fall (the upper leg actually pulled downward on segment 3 briefly, thus causing the upward force

a)

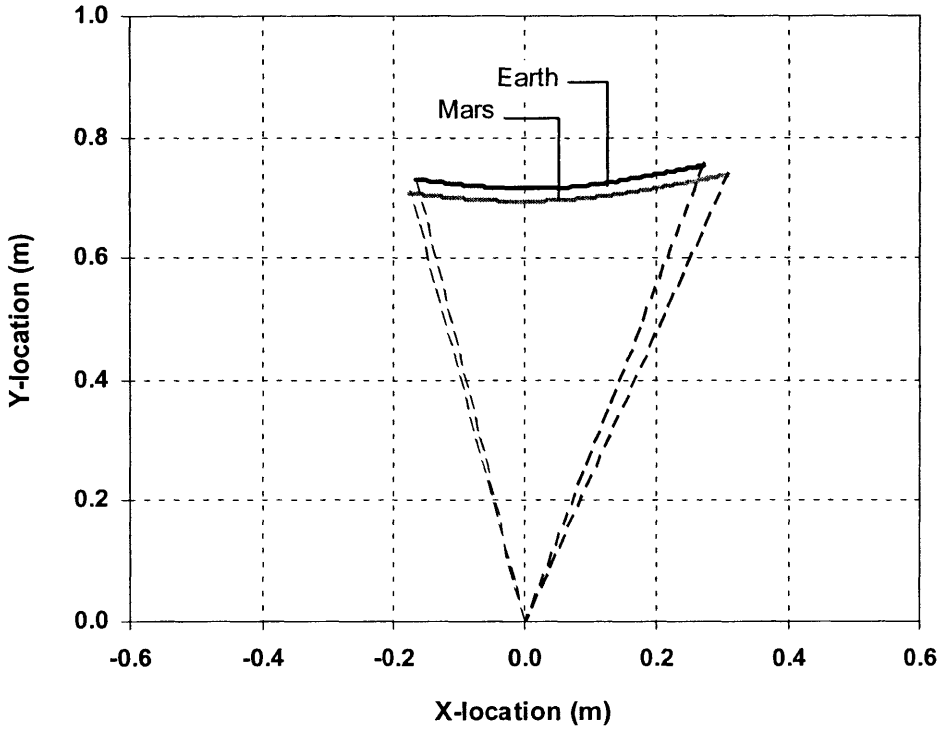

b)

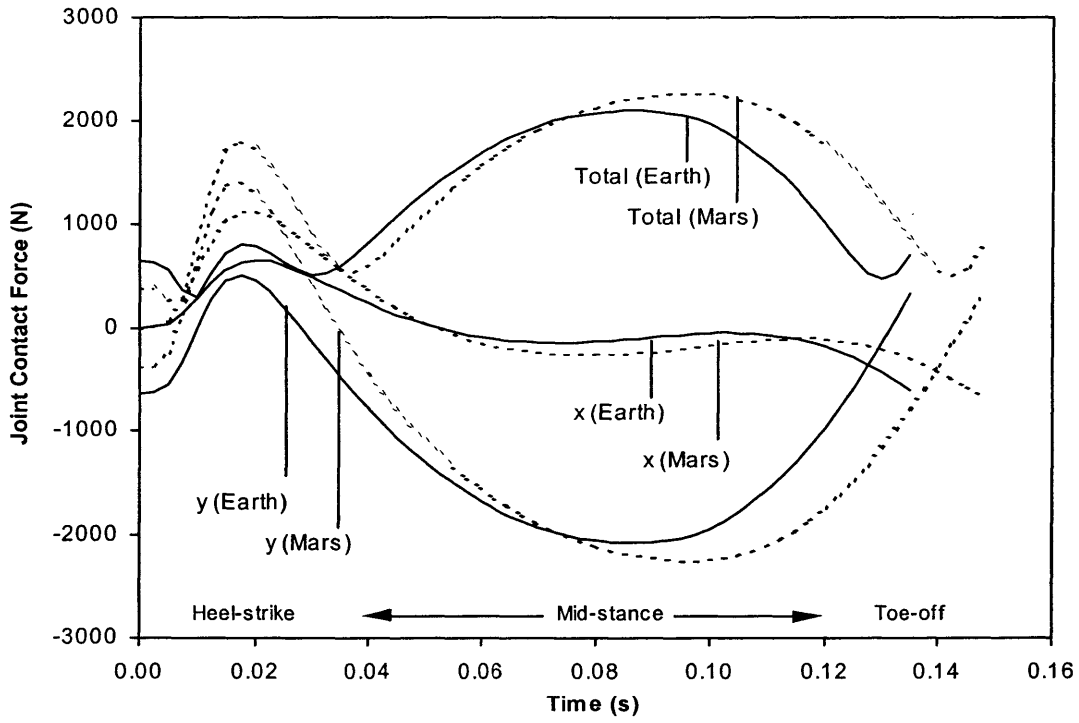

Figure 2.12: a) Hip locus plot, and b) time history plot of hip force, for a 50th percentile male running at 4 m/s in Earth gravity and Mars gravity (EVA).

applied to the hip joint by segment 3). The total force reached peaks of 2050 N (Earth) and 2300 N (Mars), both during mid-stance.

An important parameter for determining the stimulus for bone growth is the rate of change of force applied. A time history plot of the rate of change of total force applied to the hip of a 50th percentile male during locomotion in Earth gravity and Mars gravity is shown in Figure 2.13. The peak rates of change occurring during the heel-strike transient were 230 kN/s (Mars) and 190 kN/s (Earth), while the peak rates of change occurring during the remainder of the stance phase were +50 and -70 kN/s (Earth), and +60 and -70 kN/s (Mars).

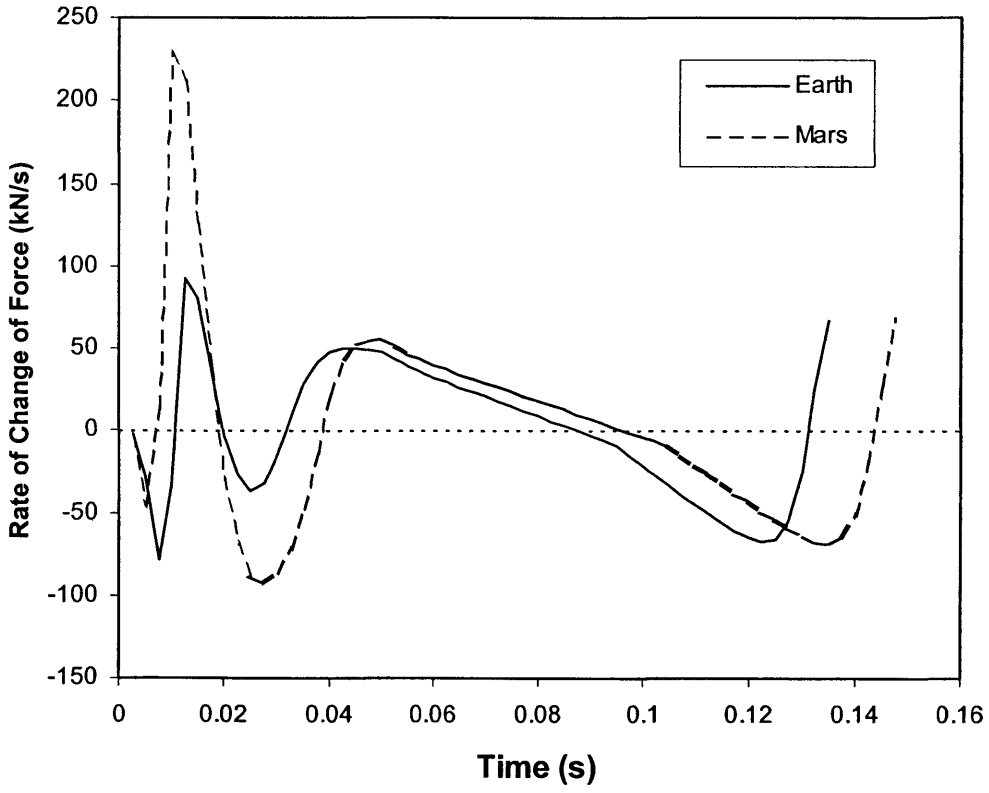

Figure 2.13: Time history plot of rate of change of force applied to the hip during locomotion on Earth and on Mars.

The sensitivity of peak hip force to variation in leg stiffness is depicted in Figure 2.14 (50th percentile male) and Figure 2.15 (50th percentile female). Peak force values are given in

Newtons (N) on the left vertical axis, and in Earth-equivalent body weights (EBW) on the right vertical axis. For the case of a male running in Earth gravity (Figure 2.14a), five curves are plotted, representing horizontal velocities (u) ranging from 2 to 6 m/s. The relationship between leg spring stiffness and predicted peak hip force was linear, with an average slope of 54 N/(kN/m) and a range of 47–60 N/(kN/m). For the case of a male running on Mars (Figure 2.14b), two sets of velocity curves are plotted, a range of 2–4 m/s for IVA and the same range for EVA. The relationship between peak hip force and leg stiffness was similar to that seen for the Earth case, with a slope of approximately 52 (47–60) N/(kN/m) for IVA and approximately 57 (52–68) N/(kN/m) for EVA.

For an average female subject, the slope of peak hip force vs leg stiffness was approximately 36 N/(kN/m) for both Earth and Mars IVA cases, but averaged about 53 N/(kN/m) for Mars EVA (Figure 2.15).

Increasing the horizontal velocity by 4 m/s (from 2 to 6 m/s) increased the peak hip force by approximately 700 N for a male running on Earth (Figure 2.16a), independent of leg stiffness (Figure 2.14a), a slope of 175 N/(m/s). For a male running on Mars (Figure 2.16b), the slopes were 160 N/(m/s), for IVA, and 212 N/(m/s) for EVA. Initial leg angle (measured as initial ankle angle, given that the leg is almost straight at heel-strike) decreased from about 80 degrees to about 68 degrees as the velocity increased from 2 to 6 m/s for a male running on Earth. In comparison, initial leg angle decreased from 81 to 74 degrees during Mars IVA, and from 78 to 70 degrees during Mars EVA, as velocity was increased from 2 to 4 m/s. Values for peak force obtained in other studies have been included in Figure 2.16a for reference and are discussed in the next section.

For females (Figure 2.17) the average slope of peak hip force vs horizontal velocity was 139 N/(m/s) for Earth, 128 N/(m/s) for Mars IVA and 190 N/(m/s) for Mars EVA. The initial

a)

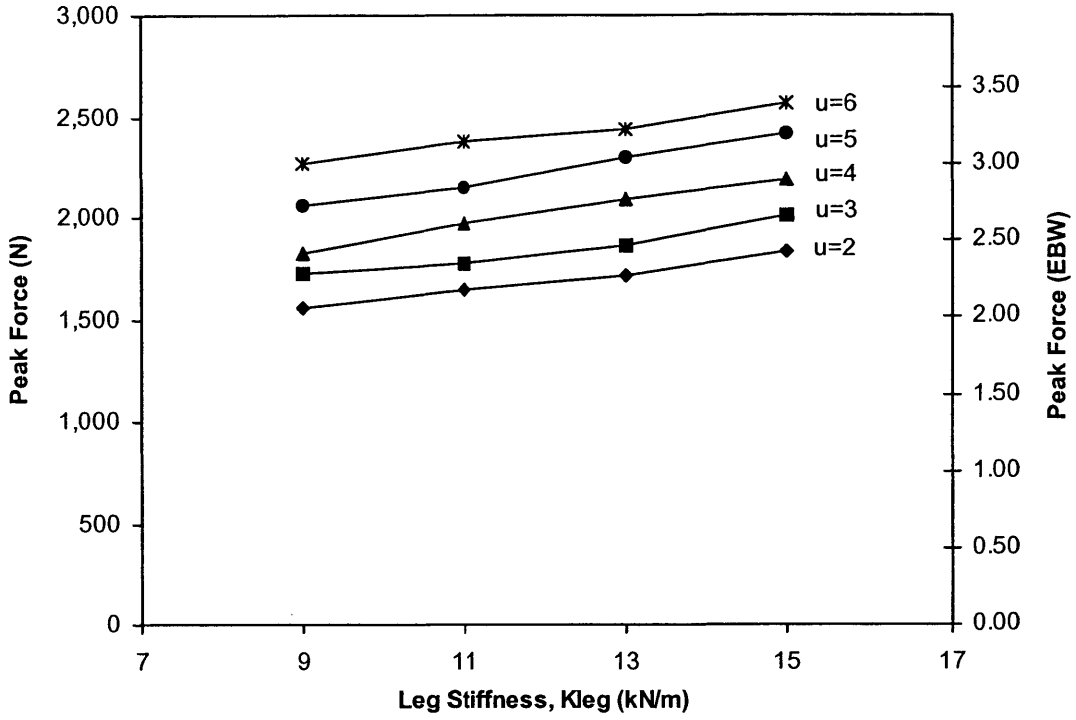

b)

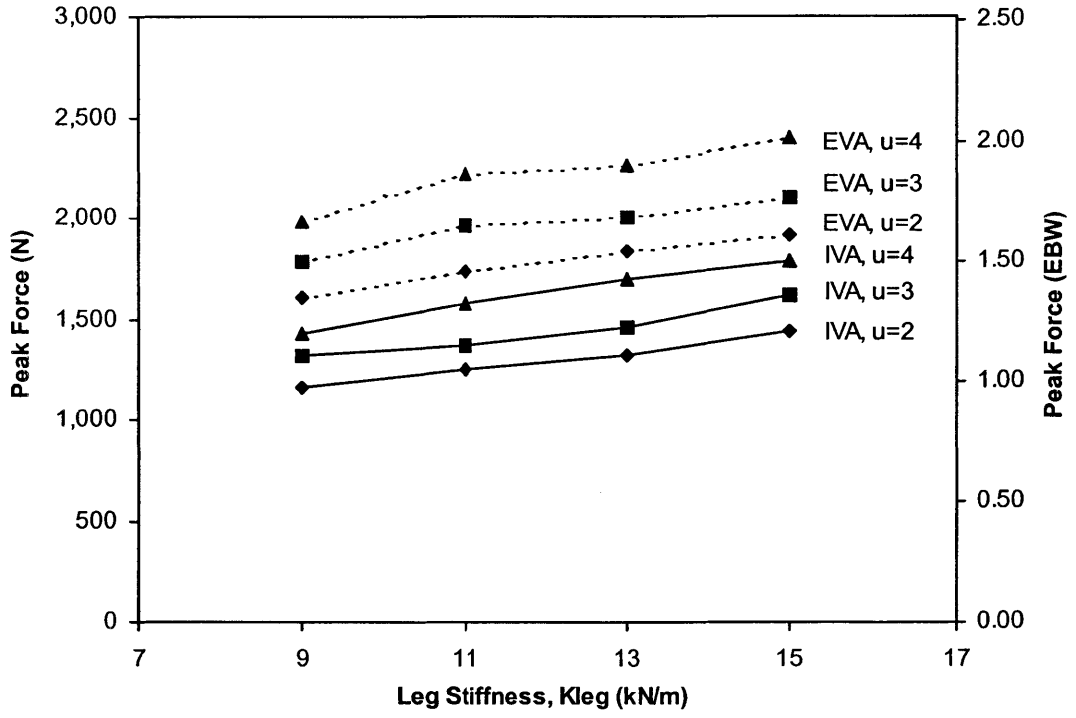

Figure 2.14: Peak hip force as a function of leg stiffness for a 50th percentile male running in a) Earth gravity, and b) Mars gravity.

a)

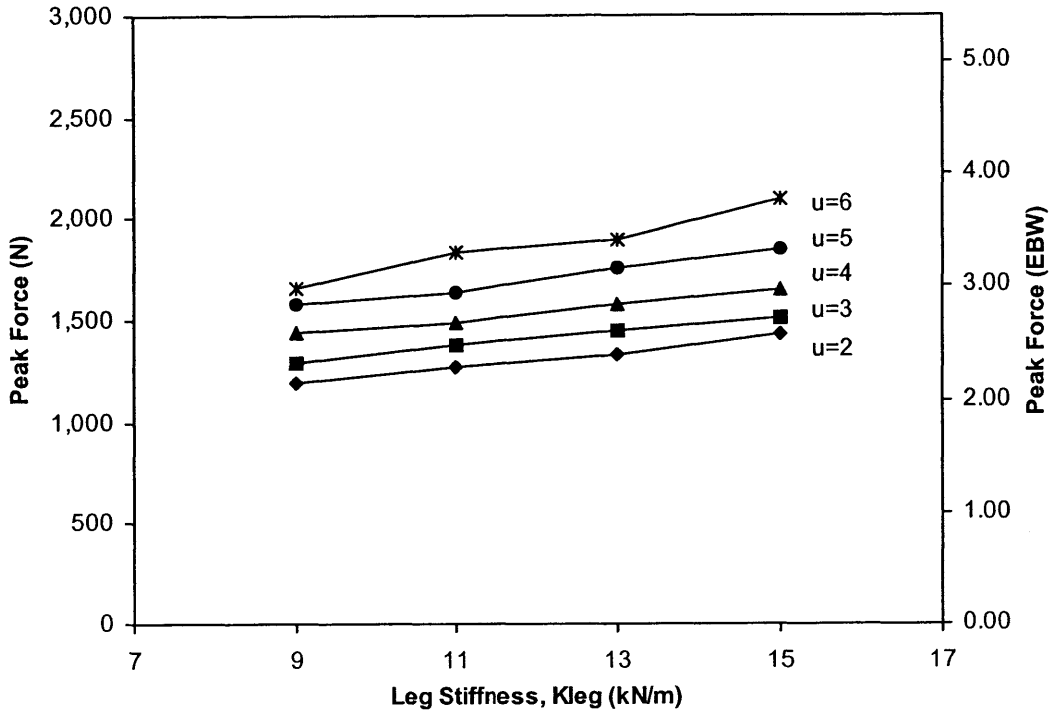

b)

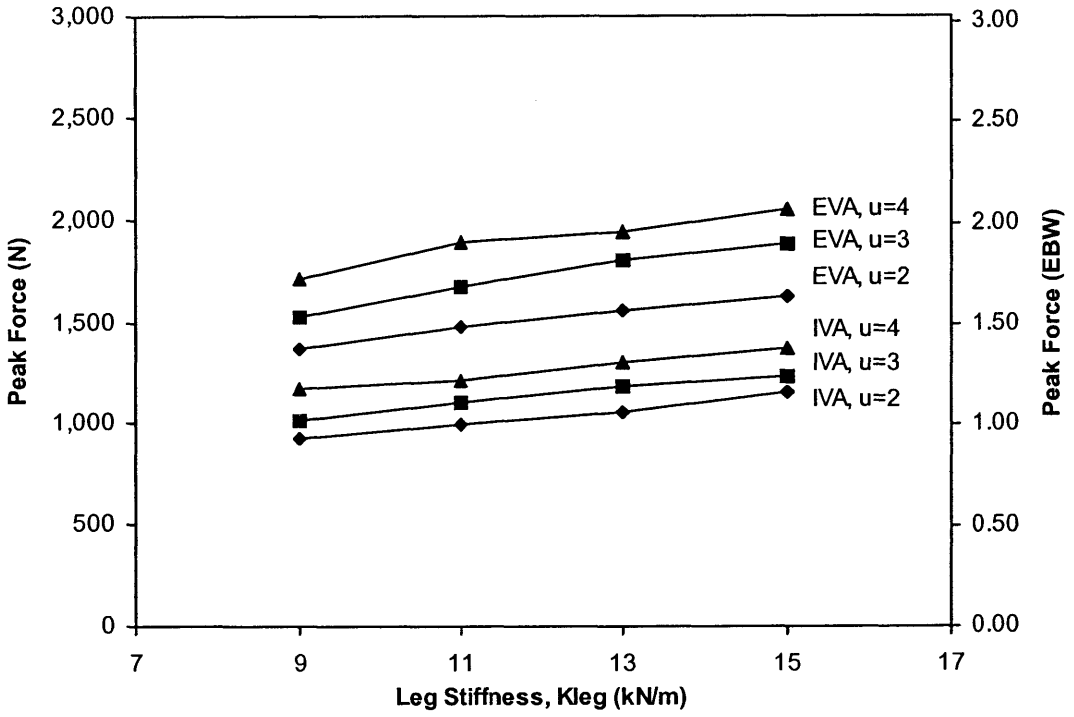

Figure 2.15: Peak hip force as a function of leg stiffness for a 50th percentile female running in a) Earth gravity, and b) Mars gravity.

a)

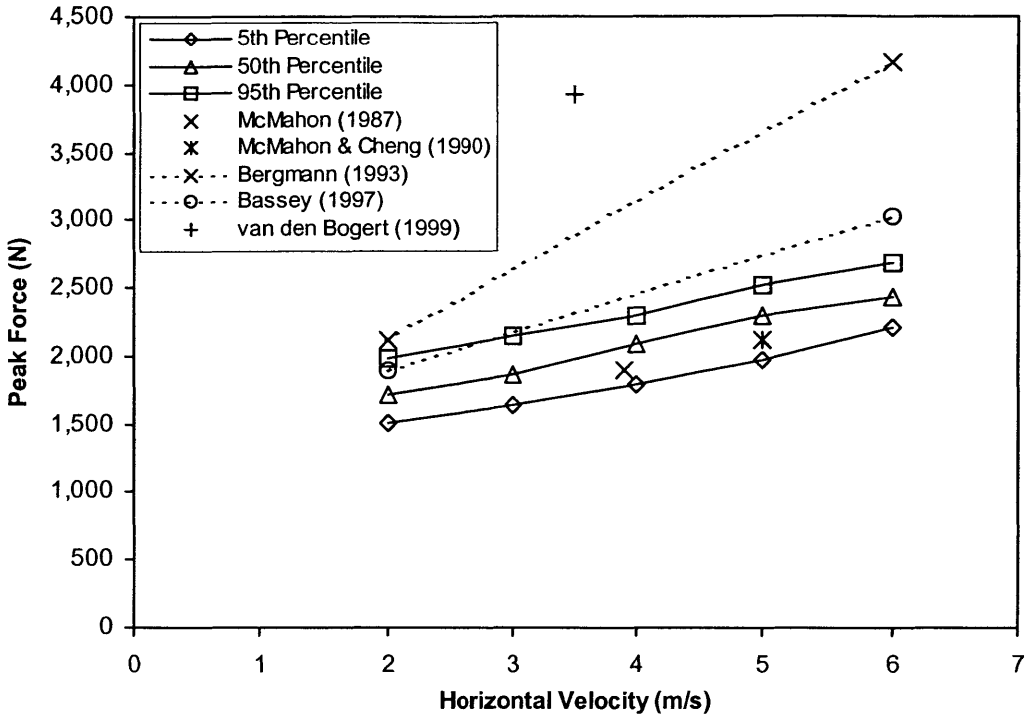

b)

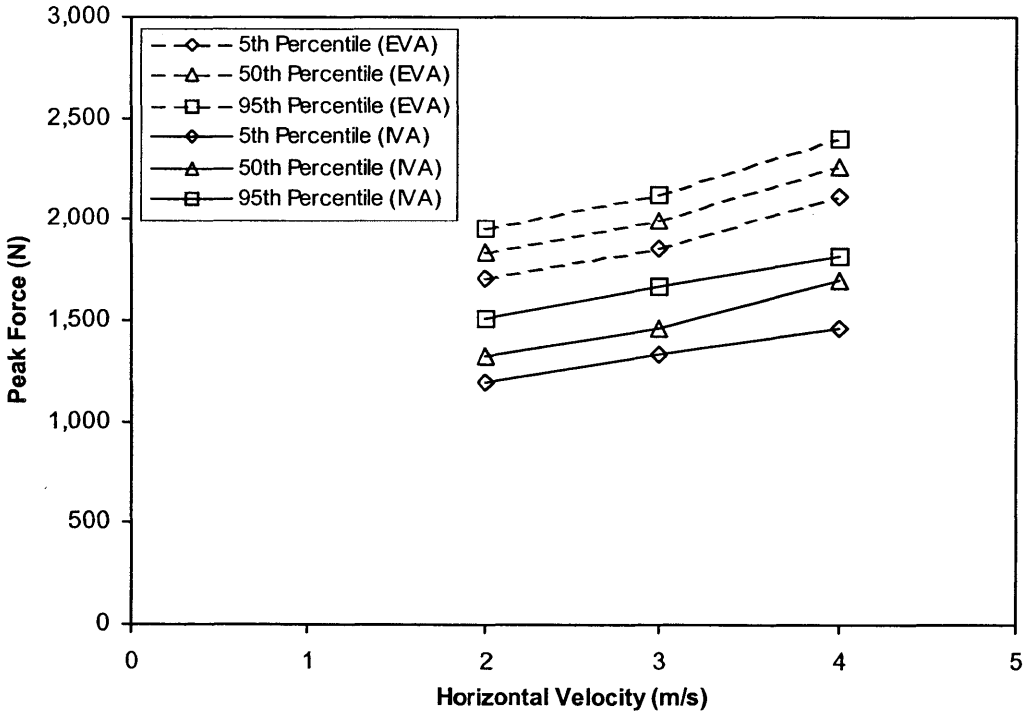

Figure 2.16: Peak hip force as a function of horizontal velocity for males running a) on Earth, and b) on Mars.

leg angle decreased from 82 to 70 degrees for the 2–6 m/s velocity range on Earth, from 82 to 75 degrees for Mars IVA, and from 79 to 71 degrees for Mars EVA, the Mars velocity range being only 2–4 m/s.

2.3.2 Falls

As in the locomotion simulation, the kinematic results of the fall simulations may be represented in terms of 'stick-figure' plots. In the fall simulations, however, both the x-z plane (sagittal plane, viewed from the subject's left side) and the y-z plane (frontal plane, viewed from behind the subject) are presented in order to capture the three-dimensional motion. The kinematics plots for the case of a 50th percentile male falling to the side on Earth and during a Mars EVA are presented in Figure 2.18. In both cases, each stick figure was captured at intervals of 0.05 seconds. The greater number of stick-figures (with smaller gaps) in the Mars case (Figure 2.18b) shows how the model fell more slowly in reduced gravity. In both cases, the sagittal plane projection reveals that the upper body maintained a near constant angle to the frontal plane while the hip location did not deviate far from the frontal plane. The frontal plane projections reveals how the hip abducted to the right side in response to the trunk's inertia, and the leg extended so that the model landed in a more extended configuration, particularly in Mars gravity. Immediately after hip impact the trunk's angle with respect to the horizontal was rapidly reduced.

Plots of joint position and joint velocity for a 50th percentile male falling in Earth gravity are shown in Figure 2.19. Ankle and knee flexion increased during the first 0.4 seconds, causing shortening of the leg-spring length. Thereafter the leg rapidly extended prior to impact. The hip flexion plot reveals some deviation from the initial angle with a reversal to baseline

a)

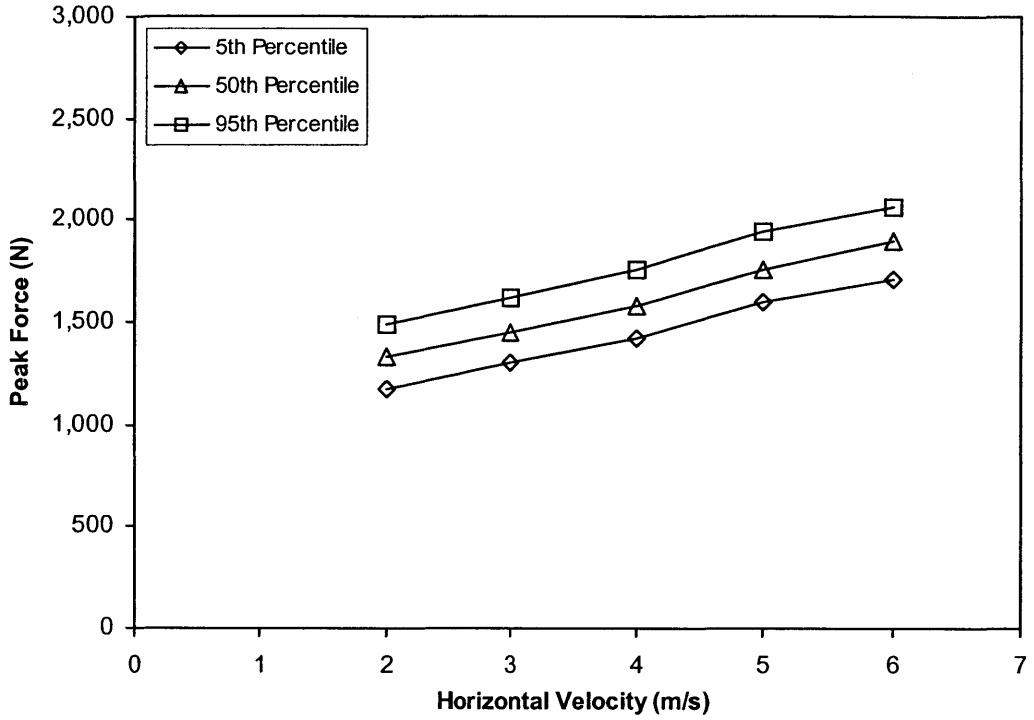

b)

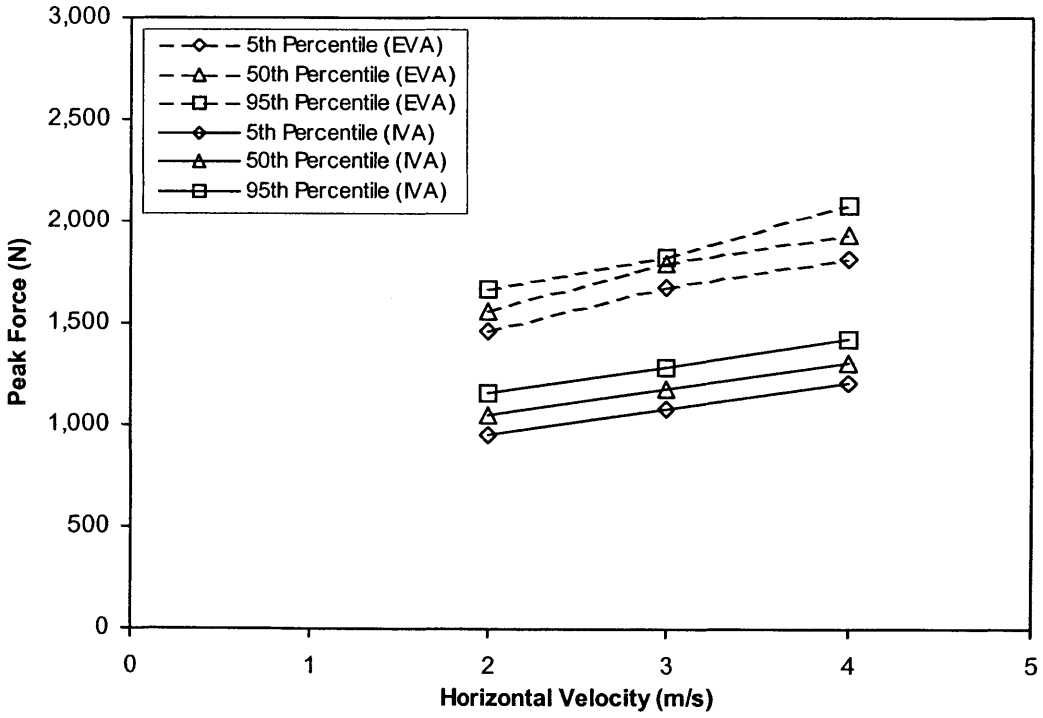

Figure 2.17: Peak hip force as a function of horizontal velocity for females running a) on Earth, and b) on Mars.

a) Earth gravity

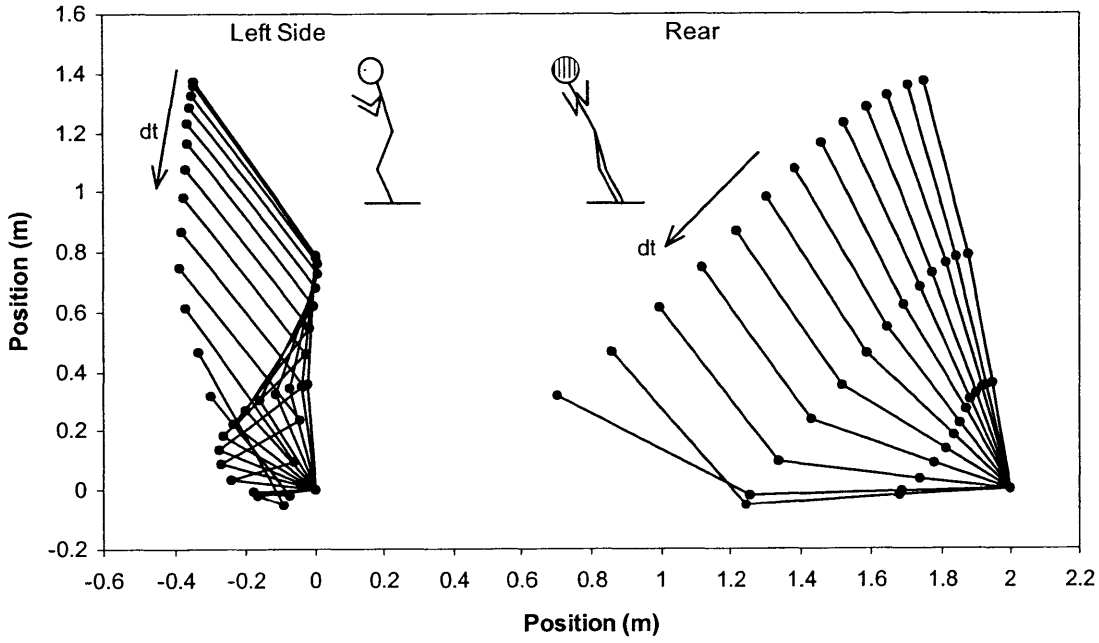

b) Mars gravity

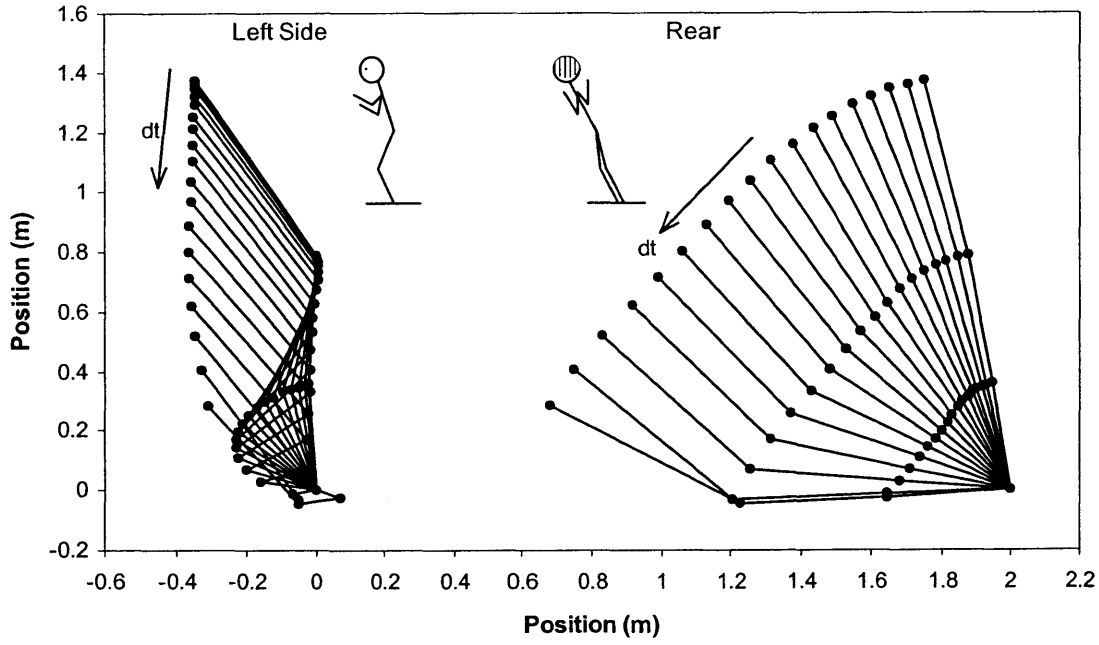

Figure 2.18: Kinematic ('stick-figure') plots for a 50th percentile male falling to the side in a) Earth gravity and b) Mars gravity (EVA case).

close to the time of impact. The hip abduction-adduction angle reached -50 degrees immediately before impact.

The plots of joint velocity (Figure 2.19b) are smooth and physiologically reasonable in magnitude. The maximum velocity reached before impact was approximately 700 deg/s for knee extension.

The plots of joint acceleration (Figure 2.20a) are smooth, continuous and of reasonable magnitude up until impact. Following impact, high accelerations were recorded due to the sudden changes, including reversals, in joint velocity.

In general, the joint torques (Figure 2.20b) were well within the limits of strength for an average male (200–300 N-m for most lower limb joints). A possible exception was the maximum torque of slightly over 300 N-m generated in ankle extension close to the time of impact.

Of principal interest in this study is the force applied to the greater trochanter during hip impact. A time history plot of these forces, generated in the case of a 50th percentile male simulation, is shown in Figure 2.21. The peak total force generated during impact in the Earth gravity case was about 7000 N, occurring at 0.56 seconds, with components of 1000 N (x or anterior-posterior direction), 3500 N (y or medial-lateral direction) and 6000 N (z or vertical direction).

Joint angles representing the body configuration at impact are presented in Table 2.4. In addition, example impact configurations for a 50th percentile male are shown in Figure 2.22. For the fall simulations occurring in Earth gravity, the configurations were controlled so that the joint angles at time of impact were within a few degrees of those reported by van den Kroonenberg *et al.* (1995) (second column in the top section). The knee angle deviated slightly from their value due to the fact that their simulation applied the simplifying assumption of equal upper and lower leg lengths. The hip flexion angle also differed slightly from

a)

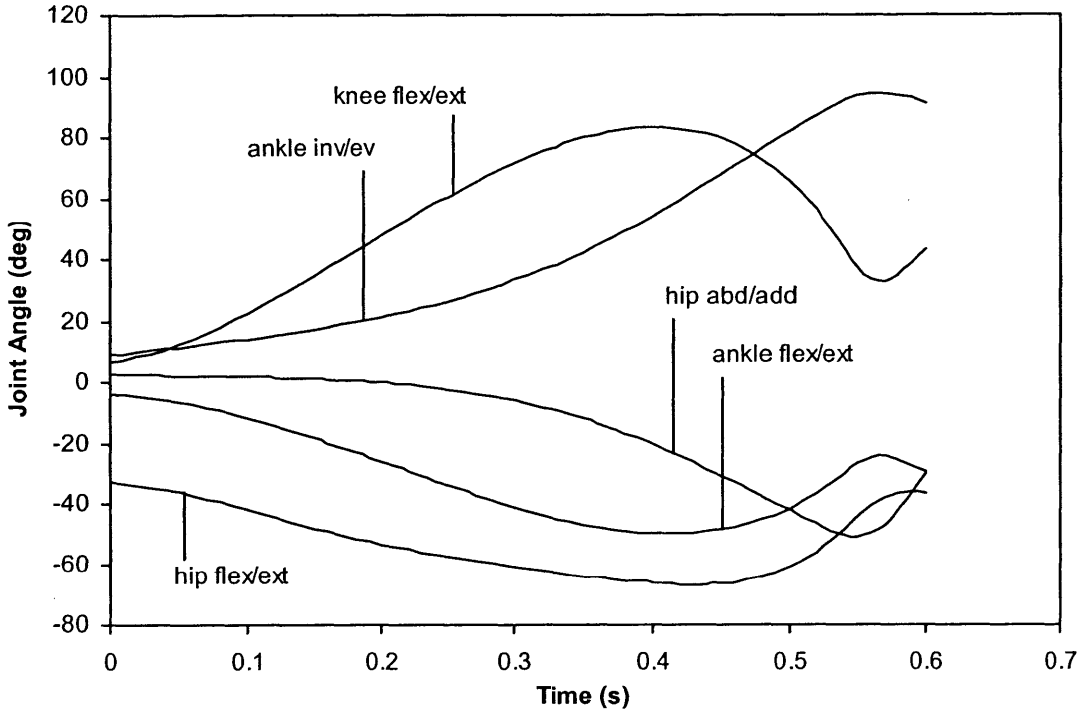

b)

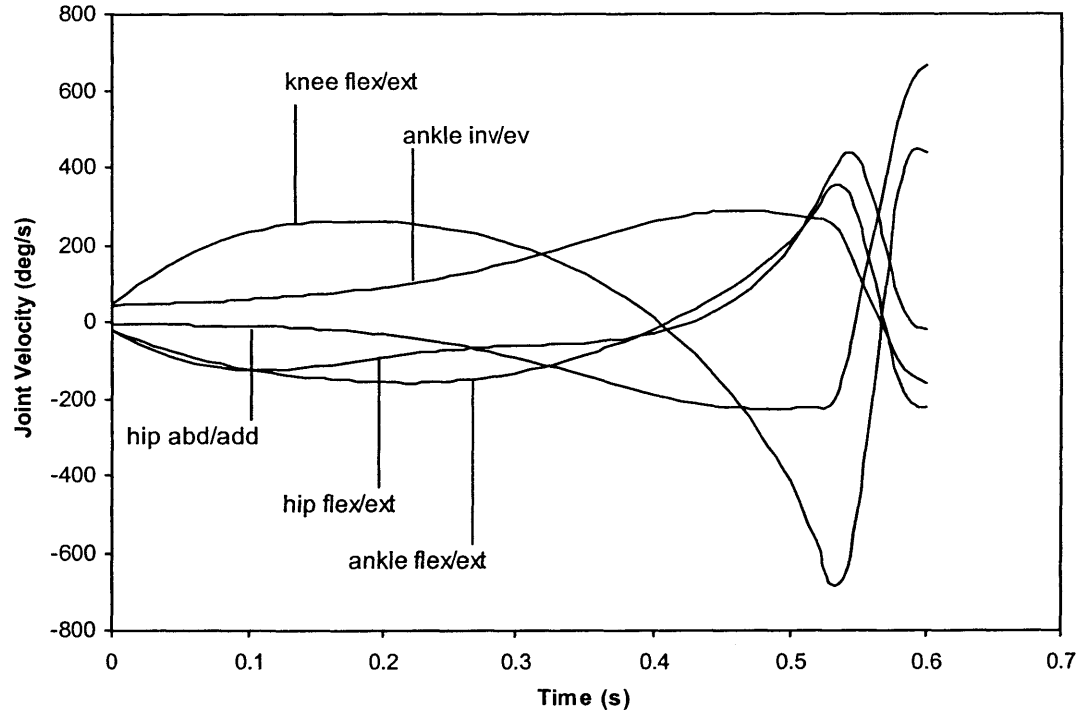

Figure 2.19: Plots of a) joint position and b) joint velocity for 50th percentile male falling in Earth gravity

a)

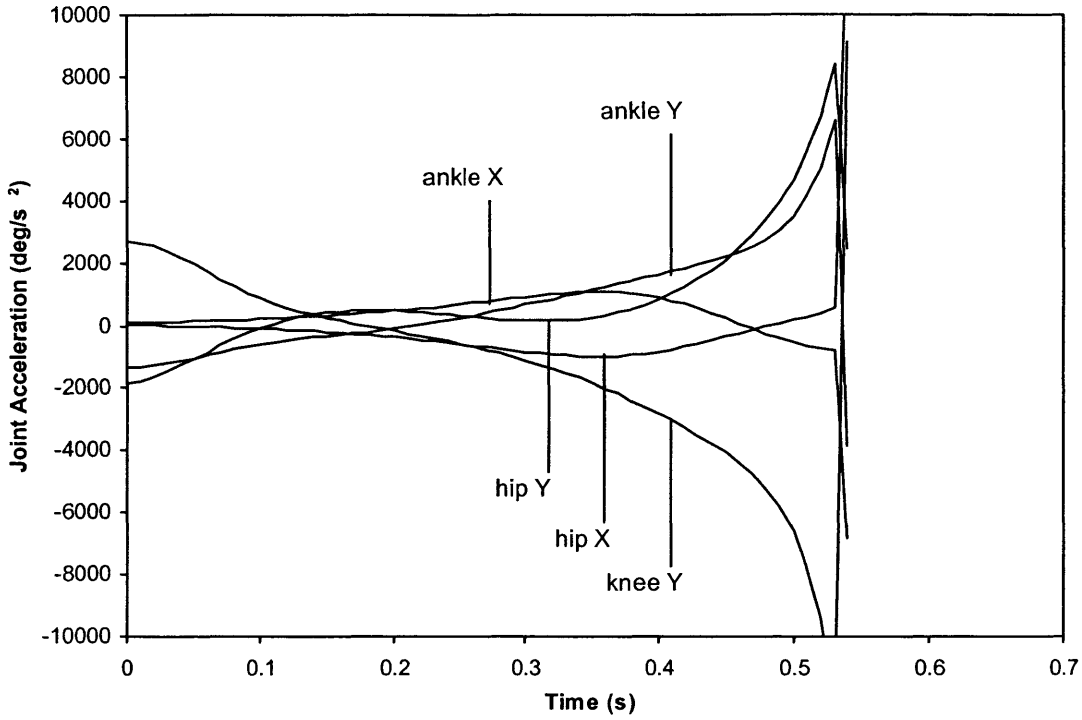

b)

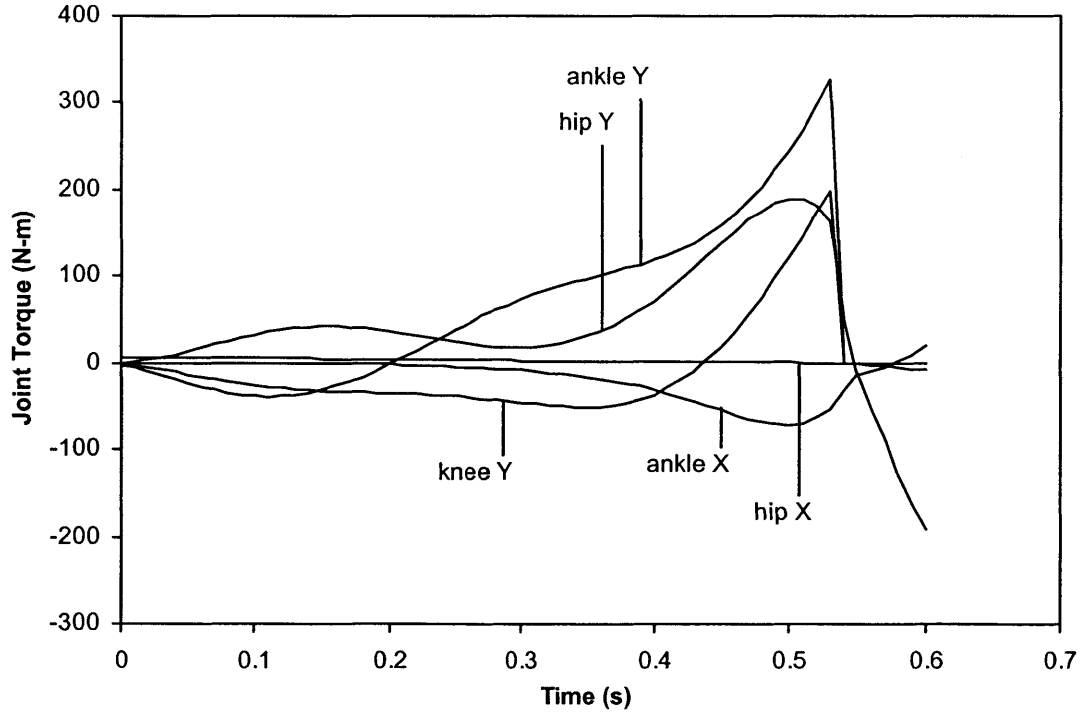

Figure 2.20: Plots of a) joint acceleration and b) joint torque for 50th percentile male falling in Earth gravity

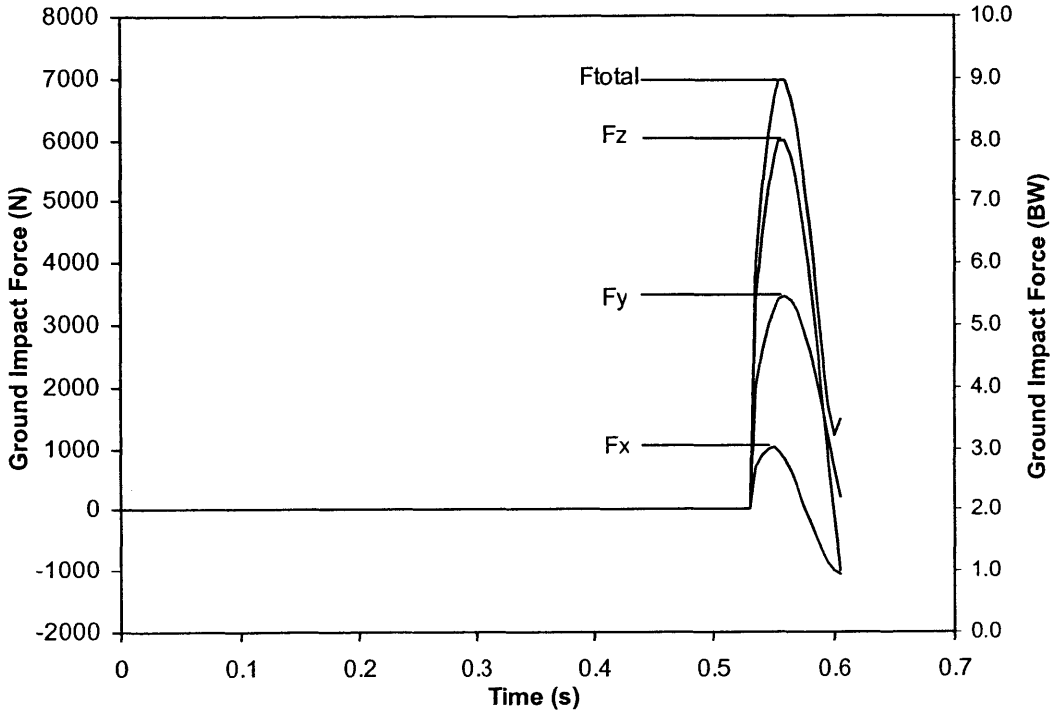

Figure 2.21: Plot of hip impact force for 50th percentile male following a fall to the side.

Table 2.4 Body configurations at time of hip impact. (vdK = van den Kroonenberg)

Angle	vdK Kinem	F5E	F50E	F95E	M5E	M50E	M95E
AnkleX	89.8	90.2	90.1	90.2	90.1	90.1	90.0
AnkleY	-33.8	-34.1	-33.8	-33.5	-33.1	-33.4	-33.4
KneeY	67.6	53.3	52.6	51.7	48.5	49.2	50.0
HipX	35.1	34.9	34.7	34.2	35.8	34.9	35.4
HipY	-30.0	-36.0	-38.3	-37.3	-36.3	-36.6	-36.9
Angle	Mars EVA	F5M	F50M	F95M	M5M	M50M	M95M
AnkleX	90.0	90.1	90.9	90.2	90.1	90.1	90.1
AnkleY	-15.0	-15.6	-15.9	-15.5	-17.8	-16.7	-16.3
KneeY	23.0	22.7	23.7	23.1	25.5	24.0	23.7
HipX	45.0	43.1	44.0	44.5	45.1	45.5	43.9
HipY	-30.0	-34.9	-35.0	-33.6	-33.4	-32.8	-32.7
Angle	Mars IVA	F5MI	F50MI	F95MI	M5MI	M50MI	M95MI
AnkleX	90.0	90.1	90.1	90.0	90.0	90.2	90.0
AnkleY	-20.0	-21.1	-20.8	-20.9	-20.4	-20.9	-20.9
KneeY	33.0	33.4	32.9	32.9	30.4	31.5	31.9
HipX	40.0	39.5	40.7	40.4	39.6	39.9	39.7
HipY	-30.0	-32.5	-33.5	-33.6	-34.7	-34.5	-34.3

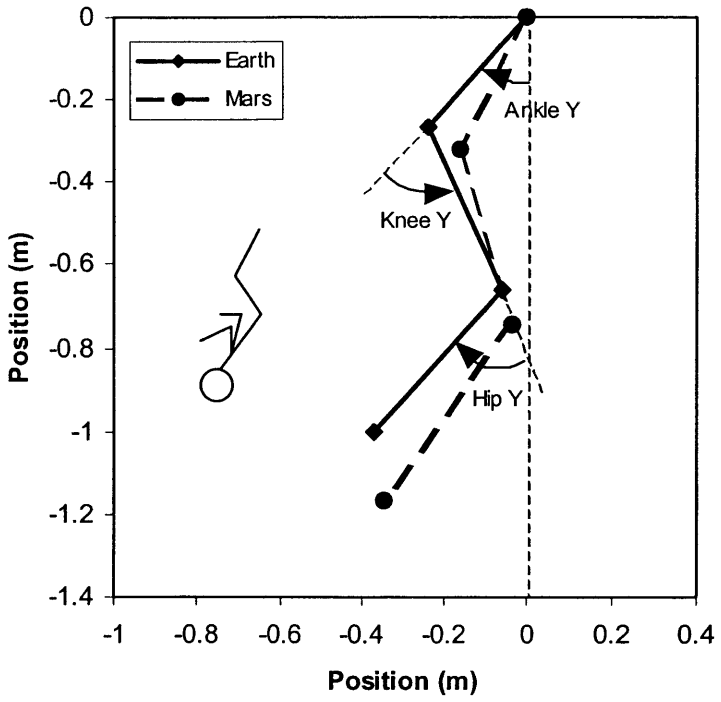

Figure 2.22: Body configurations at time of impact (viewed from above) for a 50th percentile male falling in Earth gravity and Mars gravity (EVA case). The relevant joint angles are indicated with respect to the Earth configuration.

their value since this degree of freedom was no longer fully constrained. For the Mars EVA and IVA cases, it was not possible to get the subjects to fall in the same configuration as the Earth gravity falls without the use of unrealistic control parameters. Instead, a 'natural' fall impact configuration was established through iteration (second column in lower two sections of Table 2.4), and the control parameters were adjusted for each simulation until the subject impacted with joint angles within a few degrees of the corresponding reference configuration.

The effect of variation of the ground impact model stiffness on the peak hip impact force generated in the case of 50th percentile male and female simulations of falls during Mars EVA are depicted in Figure 2.23. While the male and female curves have very similar slopes (42 N/(kN/m) for the male and 43 N/(kN/m) for the female), the force ranges differ notice-

ably. The peak impact forces range from about 2.1 to 5.1 kN for males, and from about 1.7 to 4.1 kN for females.

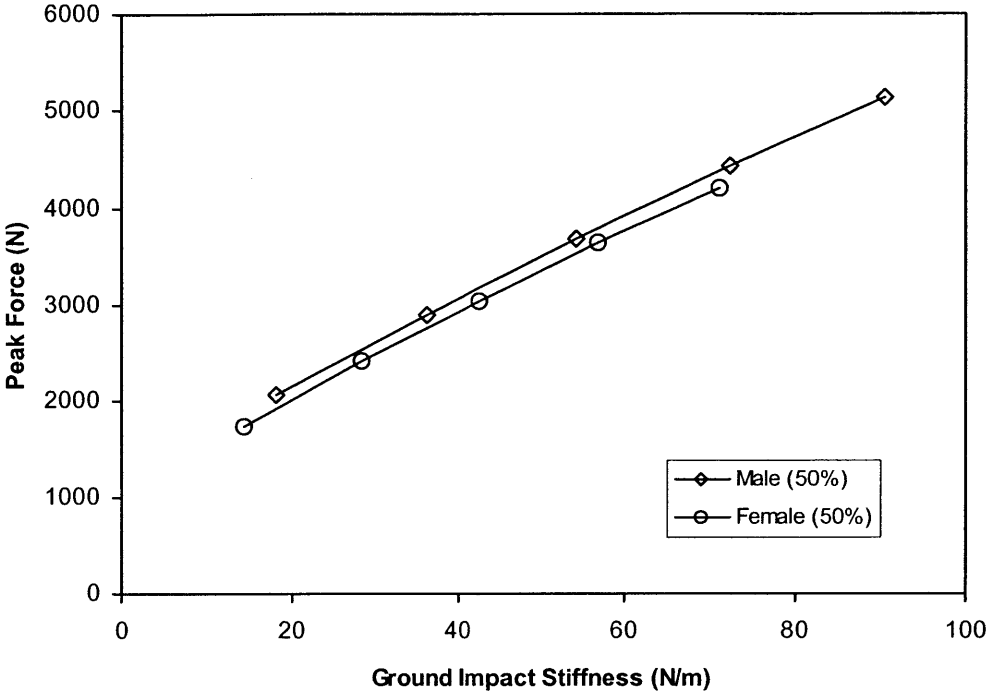

Figure 2.23: Peak hip impact force variation over the range of ground contact stiffnesses modeled.

Peak impact forces for 5th, 50th, and 95th percentile males ranged from about 5.8 to 8.3 kN for Earth, 3.7 to 5.2 kN for Mars IVA and 4.0 to 5.1 kN for Mars EVA (Figure 2.24). Comparing the peak impact forces for Mars EVA and IVA, note that EVA exceeds IVA for 5th percentile males, is approximately equal for 50th percentile males, while IVA slightly exceeds EVA for 95th percentile males. Values obtained by Robinovitch *et al.* (1995) and Parkkari *et al.* (1995) are included in the chart for reference and are discussed in the next section.

Peak impact forces for 5th, 50th, and 95th percentile females ranged from about 4.3 to 6.2 kN for Earth, 2.7 to 3.9 kN for Mars IVA and 3.2 to 4.2 kN for Mars EVA (Figure 2.25).

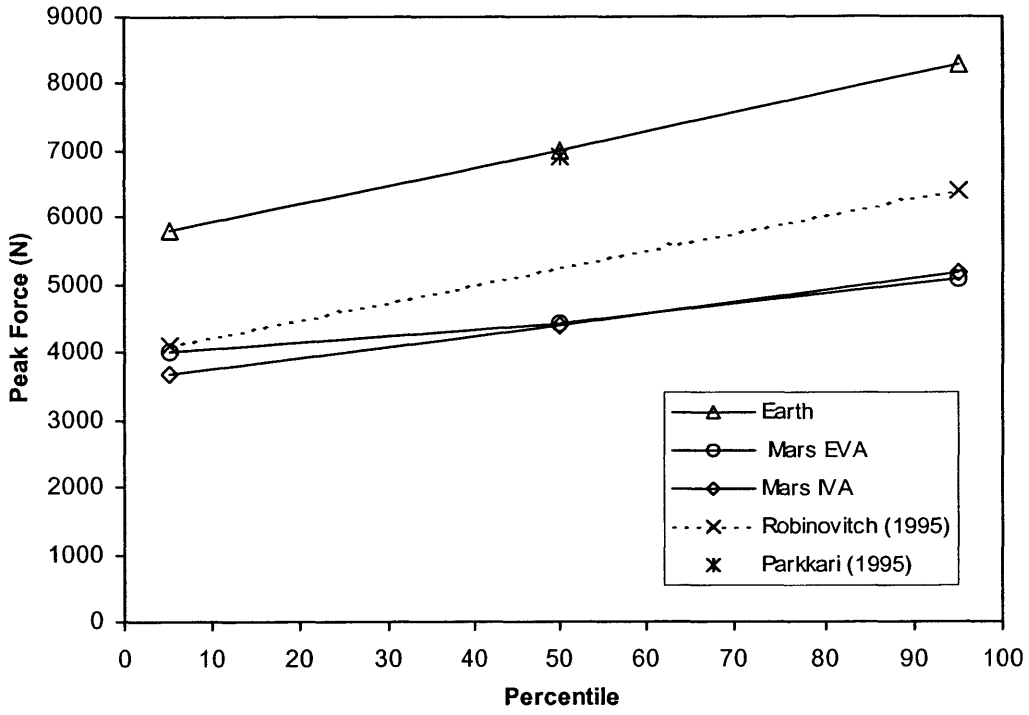

Figure 2.24: Peak force exerted on the hip during fall impact (males).

While the slope of the Mars EVA curve is less than that of the Mars IVA curve, the crossover effect observed for males does not occur. Values obtained by van den Kroonenberg *et al.* (1995, 1996) are included in the chart for reference and are discussed in the next section.

2.4 Discussion

The main purpose of the dynamics simulation studies described in this chapter was to establish values for the load applied to the proximal femur of astronauts during activities performed on Earth or in the reduced gravity of Mars. This computational modeling approach was prompted by the observation that little or no data exist on hip loading during activities performed in Mars gravity. An experimental approach was not considered practical given the

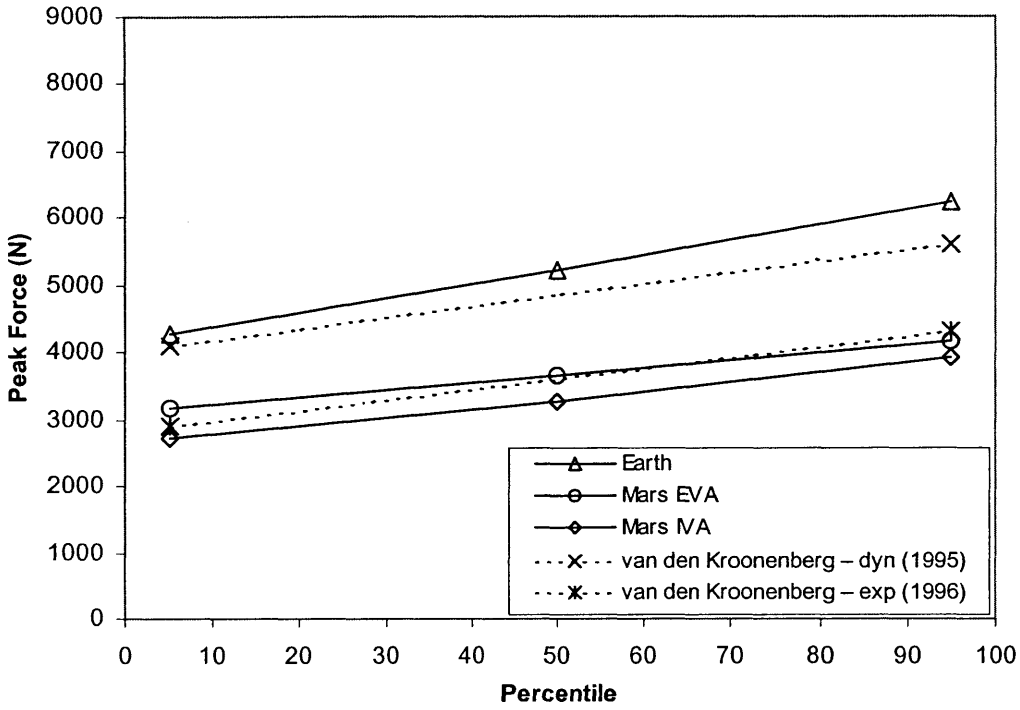

Figure 2.25: Peak force exerted on the hip during fall impact (females)

limitations of physical reduced gravity simulation devices and the requirement for invasive surgery to directly measure *in vivo* hip loading.

The first activity chosen for simulation, namely running, represents a normal activity that the astronaut would expect to perform either a short time after return to Earth or arrival to Mars. The second activity, a fall to the side that impacts the greater trochanter, represents a condition that is not expected under normal circumstances, but may be considered likely, given the finding that astronauts usually have some degree of neurovestibular (balance) and mobility impairments following a long-term space flight. These impairments may also be compounded by the astronaut's unfamiliarity with moving in reduced gravity (in the Mars IVA case) and the motion constraints of a space suit (during Mars EVA).

As mentioned earlier, the three segment distributed mass model was intended to achieve more realistic results than those obtained using simple lumped-mass-spring models. This type of simplification of the human body, however, still retains significant limitations. Modeling the leg as two segments excludes the effect of a foot. To compensate for this, the locomotion simulation employed a transient function intended to mimic the shock absorption provided by a foot during the initial heel-strike portion of the stance phase. While this transient function eliminated the unreasonably high accelerations and forces that the three segment model would otherwise produce at time zero, in some cases it produced the unrealistic result of a tensile force placed on the femur due to excessive downward acceleration of segment 3. Nevertheless, it is believed that this effect did not significantly alter the peak hip forces recorded in mid-stance, since this point was well beyond the end of the transient period. These limitations of the transient function do, however, disqualify the initial peaks observed in the plot of rate of change of applied force and only the peaks observed in the remainder of the stance period should be considered realistic. Since there appears to be no evidence in the literature that foot motion contributes to fall dynamics, this limitation was considered to be inconsequential for fall simulations. Grouping several body segments together to form the third segment in both models ignores the influence that motion of these segments might have on hip force. This may be more significant in the locomotion simulation than in the falling simulation since arm swings, and swinging the opposite leg might be expected to contribute additional downward force to the hip joint of the stance leg through centrifugal effects. Since the combined mass of the arms and suspended leg were still well below that of the trunk and head, the centrifugal effect was assumed to be negligible for the desired level of accuracy. For the fall simulation the arms are not expected to produce motions that would effect the hip force significantly. Grouping upper and lower legs from the left and right side together to form a single upper and

lower leg was not considered a significant limitation due to the fact that experimental studies have shown that humans generally keep these body segments locked together during falls (van den Kroonenberg *et al.*, 1996).

One limitation that may be worth accounting for, is the absence of the muscle force contribution to the joint reaction force. It has been shown that these muscle forces have the beneficial effect of redistributing stress in the proximal femur in such a way that the onset of fracture is postponed to a higher joint contact force (Nordin and Frankel, 1989; Rockwood *et al.*, 1991). The effects of muscle forces on failure load are further explored in the finite element analysis reported in subsequent chapters. Finally, it must be acknowledged that the method of choosing values for control parameters through trial and error is somewhat simplistic and may carry a penalty in terms of reducing the accuracy of the reported joint torques. Fortunately, most of the critical parameters (leg stiffness and damping, ground impact stiffness and damping) could be chosen based on values reported in studies specifically designed to define them, as mentioned in the methods section. Nevertheless, a more sophisticated approach to establishing control parameters, such as the use of optimal control, might be warranted in future studies, especially if such studies aim to produce reliable joint torque values.

The results of the locomotion simulations compare reasonably well with previous studies in terms of peak hip force. For instance, the peak hip force for an average male, running at 4 m/s was found to be about 2,100 N, or 2.8 times body weight. This is a little higher than the peak vertical force of 2.5 BW reported by McMahon *et al.* (1987) for a subject running at 3.9 m/s, but equal to the peak force of 2.8 BW reported by McMahon and Cheng (1990) for a subject running at 5 m/s. The value of 2.8 BW is toward the low end of the force ranges measured using implants, such as Bergmann *et al.* (1993) (2.8–5.5 BW) and Bassey *et al.* (1997) (2.5–4.0 BW), and considerably lower than the value of 5.2 BW reported by van den Bogert *et al.*

(1999) for a subject running at 3.5 m/s. This is understandable, however, given that the simulation results do not include the effects of muscle forces which generally add 1–2 BW to the *in vivo* joint reaction force during locomotion (Cheal *et al.*, 1992).

One result that at first appears to be at odds with the literature, is the observation of a larger hip locus sweep angle, and consequently a longer support period, for the case of locomotion during Mars EVA compared to Earth gravity locomotion. For instance, He *et al.* (1991) found that the leg angle with respect to the vertical decreased by approximately 5 degrees (indicating a shorter support period) as the gravity level was decreased from 1 G (Earth) to 0.38 G (Mars). Newman *et al.* (1994) found that ground contact time was independent of gravity level. Both of these studies examined subjects in a shirt-sleeve environment, however, and do not account for the additional mass of a spacesuit and backpack life-support unit. Given the same assumptions about horizontal and vertical velocity at heel-strike as those used by He *et al.*, it seems clear that larger sweep angle, and the longer support times, for the Mars EVA case, result from the additional leg compression required to reverse the increased downward momentum associated with the larger mass of segment 3.

The plot of rate of change of applied force during locomotion on Earth and Mars (Figure 2.13) has relevance to the issue of bone growth stimulation. It has been shown that osteogenesis is critically related to loading rate and load history (Carter, 1984). Furthermore, Strain rates of approximately 0.01–0.1 s^{-1} (Lanyon and Rubin, 1984; Mosley and Lanyon, 1998) and loading frequencies of approximately 10–30 Hz (al-Holou *et al.*, 1997; Qin *et al.*, 1998) have been shown to be optimal for inducing osteogenesis. To determine whether the loading rates calculated in the locomotion simulation are sufficient to induce osteogenesis or maintain bone mass would require an in-depth analysis of the strain rates in the proximal femur, and that is not the subject of this thesis. However, given that the magnitudes of the peak loading rates

during the mid-stance portion of locomotion (as mentioned above, the peaks during the heel-strike transient should be discounted) are similar for Earth locomotion and Mars EVA, and since the peak force magnitudes are also comparable, it is clear that skeletal loading similar to that experienced on Earth can be achieved during locomotion on Mars if appropriate weight is added, say in the form of a backpack. This is an encouraging result since there is evidence that bone mass can be maintained by relatively short bouts of treadmill exercise (Konieczynski, *et al.* 1998) and maintaining (or increasing) bone mass while on Mars would be an important step in preparing a crew for the long return journey to Earth and increased skeletal loading on arrival.

The values obtained for peak hip impact force during the fall simulations also compare favorably with other studies. The 7.0 kN value obtained for peak force in the case of a 50th percentile male falling on Earth is slightly higher than the range of 4.1 to 6.4 kN reported by Robinovitch *et al.* (1995b), but similar to the value of 6.9 kN reported by Parkkari *et al.* (1995). Also the peak impact forces of 4.3 kN, for a 5th percentile female falling in Earth gravity, and 6.2 kN, for a 95th percentile female falling in Earth gravity, compare well with the values of 4.1 kN and 5.6 kN obtained by van den Kroonenberg *et al.* (1995) in their dynamic simulations, but are a little higher than the corresponding values of 2.9 kN and 4.3 kN that they measured from experiment (van den Kroonenberg *et al.*, 1996).

Despite the fact that there appear to be no previous studies involving estimates or measurements of hip forces during activities performed in a Mars gravity environment, it seems natural to predict that the lower gravity level on Mars (3/8 G) would significantly lower the hip forces during both locomotion and falls. This was found to be true for IVA locomotion on Mars (peak force reduced by 19% for males and by 18% for females), IVA falls on Mars (peak force reduced by 37% for both males and females), and also for EVA falls (37% reduc-

tion for males and 30% reduction for females). However, the predicted peak hip forces were actually increased for EVA locomotion on Mars (increase of 8% for males and 22% for females). This increase in load is clearly a cause for concern if astronauts are expected to perform extravehicular activity shortly after arriving at Mars.

Although the simulation results from the Mars gravity cases are not easy validated directly, some confidence may be placed in the values based on the favorable correlations between the Earth gravity locomotion simulations and other studies. For hip impact, the predicted forces were a little high compared to the studies referenced for Earth gravity, and so the predicted fall impact forces in Mars gravity may also be a little higher than what would be found in reality.

An important aspect of the simulation results is that hip forces for Mars EVA are in general significantly greater than for Mars IVA for both locomotion and Falls. Clearly this is due to the added mass of the space suit, and more importantly, the backpack life support system. Since the backpack has a greater percentage of the mass, and is affixed to the upper body, it channels more of its inertia directly into loading at the hip. The implication is that designers of future space suits and PLSS's to be used for the exploration of Mars would be well advised to make every effort to reduce mass, especially in the backpack, so as to reduce the force that would be applied to the hip during locomotion and (potentially) falls. A concept that seems particularly attractive in this light, is the replacement of the backpack-style PLSS with a cart mounted PLSS that the astronaut wheels along with him as he moves around ("little red wagon" concept), thus removing part of the additional inertia that would be transferred into hip loading.

In conclusion, both the locomotion and fall simulations appear to have provided reasonable values for hip loading in comparison to other studies. Thus the hip force values may be

used with some confidence in calculating the factor of risk for fracture (Chapter 5), both in Earth gravity conditions and in Mars gravity conditions. Given the importance of muscle forces in locomotion (as demonstrated by the difference between simulation joint contact forces and implant measured joint contact forces), an estimate of the contribution of muscle forces to joint contact force will be used in calculating the factor of risk for fracture during locomotion (since muscle forces are used in calculating the failure load in locomotion — see Chapters 3 and 4).

2.5 References

al-Holou, N., Benghuzzi, H., and Forbes, K. (1997). "Development of a microcomputer-based system to monitor healing from injury." *Biomed Sci Instrum*, 34, 181-5.

Anonymous. "National Center for Health Statistics. Advance data from vital and health statistics: 1985 summary: national hospital discharge survey." *PHS*, Hyattsville, MD, 86-1250.

Asada, H., and Slotine, J.-J. E. (1986). *Robot Analysis and Control*, John Wiley & Sons, Inc., New York.

Bassey, E. J., Littlewood, J. J., and Taylor, S. J. (1997). "Relations between compressive axial forces in an instrumented massive femoral implant, ground reaction forces, and integrated electromyographs from vastus lateralis during various 'osteogenic' exercises." *J Biomech*, 30(3), 213-23.

Baughman, D. L. (1983). *Development of an Interactive computer program to produce body description Data*, Air Force Aerospace Medical Research Laboratory, Dayton, Report No. AFAMRL-TR-83-058.

Bergmann, G., Graichen, F., and Rohlmann, A. (1993). "Hip joint loading during walking and running, measured in two patients." *J Biomech*, 26(8), 969-90.

Carter, D. R. (1984). "Mechanical loading histories and cortical bone remodeling." *Calcif Tissue Int*, 36(Suppl 1), S19-24.

Cavagna, G. A., Willems, P. A., and Heglund, N. C. (1998). "Walking on Mars." *Nature*, 393(6), 636.

Cheal, E. J., Spector, M., and Hayes, W. C. (1992). "Role of loads and prosthesis material properties on the mechanics of the proximal femur after total hip arthoroplasty." *J Orthop Res*, 10(3), 405-422.

Crowninshield, R. D., Johnston, R. C., Andrews, J. G., and Brand, R. A. (1978). "A biomechanical investigation of the human hip." *J Biomechanics*, 11, 75-85.

Cummings, S. R., Black, D. M., and Nevitt, M. C. (1990). "Appendicular bone density and age predict hip fracture in women." *JAMA*, 263, 665-8.

Farley, C. T., and Gonzalez, O. (1996). "Leg stiffness and stride frequency in human running." *J Biomech*, 29(2), 181-6.

Farley, C. T., and McMahon, T. A. (1992). "Energetics of walking and running: insights from simulated reduced-gravity experiments." *J Appl Physiol*, 73(6), 2709-2712.

Ford, C. M., Keaveny, T. M., and Hayes, W. C. (1996). "The effect of impact direction on the structural capacity of the proximal femur during falls." *J Bone Min Res*, 11(3), 377-383.

Goh, J. C., Bose, K., and Das De, S. (1996). "Pattern of fall and bone mineral density measurement in hip fractures." *Ann Acad Med Singapore*, 25(6), 820-3.

Greenspan, S. L., Myers, E. R., Kiel, D. P., Parker, R. A., Hayes, W. C., and Resnick, N. M. (1998). "Fall direction, bone mineral density, and function: risk factors for hip fracture in frail nursing home elderly." *Am J Med*, 104(6), 539-45.

He, J. P., Kram, R., and McMahon, T. A. (1991). "Mechanics of running under simulated low gravity." *J Appl Physiol*, 71(3), 863-870.

Hedlund, R., and Lindgren, U. (1987). "Trauma type, age, and gender as determinants of hip fracture." *J Orthop Res*, 5, 242-6.

Hewes. (1968). "Analysis of self-locomotiove performance of lunar explorers based on experimental reduced-gravity studies." *Tech Note US Natl Aeronaut Space Adm*, 1-19.

Hewes, D. E. (1969). "Reduced-gravity simulators for studies of man's mobility in space and on the moon." *Hum Factors*, 11(5), 419-431.

Hogan, N. (1980). "Control of mechanical impedance of prosthetic joints." *Joint Automatic Control Conference*, San Francisco.

Hogan, N. (1985). "Impedance control: An approach to manipulation." *J Dyn Syst Meas Control*, 107.

Hollerbach, J. M. (1977). "The minimum energy movement for a spring muscle model." , Artificial Intelligence Laboratory, Massachusetts Institute of Technology, Cambridge, MA.

Kane, T. R. and Levinson, D. A. (1985) *DYNAMICS: Theory and Applications,* McGraw-Hill.

Konieczynski, D. D., Truty, M. J., and Biewener, A. A. (1998). "Evaluation of a bone's in vivo 24 -hour loading history for physical exercise compared with background loading." *J Orthop Res*, 16(1), 29-37.

Lanyon, L. E., and Rubin, C. T. (1984). "Static vs dynamic loads as an influence on bone remodelling." *J Biomech*, 17(12), 897-905.

Lauritzen, J. B., Petersen, M. M., and Lund, B. (1993). "Effect of external hip protectors on hip fractures." *Lancet*, 341(8836), 11-3.

Lauritzen. (1996). "[Prevention with hip protectors. Biomechanical aspects in falls and hip fractures]." *Nord Med*, 111(10), 340-3.

Lauritzen, J. B. (1997). "Hip fractures. Epidemiology, risk factors, falls, energy absorption, hip protectors, and prevention." *Dan Med Bull*, 44(2), 155-68.

Margaria, R. (1966). "Human locomotion on the earth and in subgravity." *Schweiz Z Sportmed*, 14(1), 159-167.

Margaria, R., and Cavagna, G. A. (1967). "Human locomotion on the moon surface." *Riv Med Aeronaut Spaz*, 30(4), 629-644.

McMahon. (1984). *Muscles, reflexes, and locomotion*, Princeton University Press, Princeton, NJ.

McMahon, T. A., Valiant, G., and Frederick, E. C. (1987). "Groucho running." *J Appl Physiol*, 62(6), 2326-2337.

McMahon, T. A., and Cheng, G. C. (1990). "The mechanics of running: how does stiffness couple with speed?" *J Biomech*, 23(Suppl 1), 65-78.

Mills, N. J. (1996). "The biomechanics of hip protectors." *Proc Inst Mech Eng [H]*, 210(4), 259-66.

Mochon, S., and McMahon, T. A. (1980). "Ballistic walking." *J Biomech*, 13(1), 49-57.

Mosley, J. R., and Lanyon, L. E. (1998). "Strain rate as a controlling influence on adaptive modeling in response to dynamic loading of the ulna in growing male rats." *Bone*, 23(4), 313-8.

Newman, D. J., Alexander, H. L., and Webbon, B. W. (1994). "Energetics and mechanics for partial gravity locomotion." *Aviat Space Environ Med*, 65(9), 815-823.

Nordin, M., and Frankel, V. H. (1989). *Basic biomechanics of the musculoskeletal system*, 2nd Ed., Lea & Febiger, Philadelphia.

Parkkari, J., Kannus, P., Heikkila, J., Poutala, J., Sievanen, H., and Vuori, I. (1995). "Energy-shunting external hip protector attenuates the peak femoral impact force below the theoretical facture threshold: an in vitro biomechanical study under falling conditions of the elderly." *J Bone Miner Res*, 10(10), 1437-42.

Parkkari, J., Kannus, P., Heikkila, J., Poutala, J., Heinonen, A., Sievanen, H., and Vuori, I. (1997). "Impact experiments of an external hip protector in young volunteers." *Calcif Tissue Int*, 60(4), 354-7.

Pinilla, Boardman, Bouxsein, Myers, and Hayes. (1996). "Impact direction from a fall influences the failure load of the proximal femur as much as age-related bone loss." *Calcified Tissue International*, 58, 231-235.

Qin, Y. X., Rubin, C. T., and McLeod, K. J. (1998). "Nonlinear dependence of loading intensity and cycle number in the maintenance of bone mass and morphology." *J Orthop Res*, 16(4), 482-9.

Robinovitch, S. N., Hayes, W. C., and McMahon, T. A. (1991). "Prediction of femoral impact forces in falls on the hip." *J Biomech Eng*, 113(4), 366-74.

Robinovitch, S. N., Hayes, W. C., and McMahon, T. A. (1995a). "Energy-shunting hip padding system attenuates femoral impact force in a simulated fall." *J Biomech Eng*, 117(4), 409-13.

Robinovitch, S. N., McMahon, T. A., and Hayes, W. C. (1995b). "Force attenuation in trochanteric soft tissues during impact from a fall." *J Orthop Res*, 13(6), 956-62.

Robinovitch, S. N., Hayes, W. C., and McMahon, T. A. (1997). "Distribution of contact force during impact to the hip." *Ann Biomed Eng*, 25(3), 499-508.

Robinovitch, S. N., Hayes, W. C., and McMahon, T. A. (1997). "Predicting the impact response of a nonlinear single-degree-of-freedom shock-absorbing system from the measured step response." *J Biomech Eng*, 119(3), 221-227.

Rockwood, C. A., Jr., Green, D. P., and Bucholz, R. W. (1991). *Rockwood and Green's Fractures in Adults, 3rd Ed.*, Lippincott, Philadelphia.

Schwartz, A. V., Kelsey, J. L., Sidney, S., and Grisso, J. A. (1998). "Characteristics of falls and risk of hip fracture in elderly men." *Osteoporos Int*, 8(3), 240-6.

Siegler, S., Seliktar, R., and Hyman, W. (1982). "Simulation of human gait with the aid of a simple mechanical model." *J Biomech*, 15(6), 415-425.

van den Bogert, A. J., Read, L., and Nigg, B. M. (1999). "An analysis of hip joint loading during walking, running and skiing." *Med Sci Sports Exerc*, 31(1), 131-42.

van den Kroonenberg, A. J., Hayes, W. C., and McMahon, T. A. (1995). "Dynamic models for sideways falls from standing height." *J Biomech Eng*, 117(3), 309-318.

van den Kroonenberg, A. J., Hayes, W. C., and McMahon, T. A. (1996). "Hip impact velocities and body configurations for voluntary falls from standing height." *J Biomech*, 29(6), 807-811.

Viale, F., Dalleau, G., Freychat, P., Lacour, J. R., and Belli, A. (1998). "Leg stiffness and foot orientations during running." *Foot Ankle Int*, 19(11), 761-5.

Wickman, L. A., and Luna, B. (1996). "Locomotion while load-carrying in reduced gravities." *Aviat Space Environ Med*, 67(10), 940-946.

CHAPTER 3

Estimation of Proximal Femur Failure Load During Locomotion and Falls Using Finite Element Analysis

Nothing is so strong as gentleness, and nothing is so gentle as real strength.

— Ralph W. Sockman

In general, two approaches have been used to assess the strength of the proximal femur and the associated fracture risk under various loading conditions: 1) Direct mechanical testing of cadaveric femora, and 2) Mathematical models of the proximal femur. This chapter discusses the relative merits of each and the motivation that led to the use of finite element modeling of bone, and in particular, the proximal femur. The ultimate motivation for using finite element analysis (FEA) in this thesis derives from the desire to model changes in femoral strength associated with space flight, which is discussed further in the chapter following this.

3.1 Background

Several previous studies have shown that the failure load of the proximal femur during *in vitro* mechanical testing correlates well with bone mineral density (BMD), bone mineral content (BMC), and other geometric and bone mineral parameters assessed using dual-energy x-ray absorptiometry (DXA) and computed tomography (CT). An indication of the degree of correlation is provided by the summary in Table 3.1. Clinically, however, it has been observed that a relatively modest increase in BMD results in a dramatic reduction in fracture incidence

Table 3.1 Correlations between *in vitro* bone strength and bone mineral parameters.

Study	Parameter	Correlation
Dalen *et al.*, 1976	Femoral neck BMC (DXA)	$r^2 = 0.79$
Hansson *et al.*, 1980	BMC (DXA)	$r^2 = 0.74$
Leichter *et al.*, 1982	bone mineral density (CT)	$r^2 = 0.76$
	bone mineral content (CT)	$r^2 = 0.67$
Alho *et al.*, 1988	Femoral neck cancellous bone density (CT)	$r^2 = 0.65$
Staffan *et al.*, 1989	Vertebral BMC (DXA)	$r^2 = 0.64$
Courtney *et al.*, 1994	Femoral neck c/s area (DXA)	$r^2 = 0.77$
	Femoral neck BMD (DXA)	$r^2 = 0.72$
Bouxsein *et al.*, 1995	Femoral neck BMD (DXA)	$r^2 = 0.79$
	Trochanteric BMD (DXA)	$r^2 = 0.81$
Courtney *et al.*, 1995	Femoral neck BMD (DXA)	$r^2 = 0.92$

(and *vice versa*) indicating that linear BMD versus strength correlations are not necessarily good predictors of fracture risk *in vivo*. This is due to the fact that body habitus factors, such as, body weight, subject height, muscle forces, etc., are not easily incorporated into a mechanical test methodology.

Some studies have sought to overcome the limitations of mechanical testing by using mathematical models of bone (either samples or whole bones). Mourtada *et al.* (1996) developed a two-dimensional curved-beam model based on DXA scans, and later showed through comparison with mechanical testing that failure load *in vitro* could also be predicted fairly accurately (Beck *et al.*, 1998).

In order to better model the complex geometry of bones such as the proximal femur, investigators have been using finite element analysis since 1972 (Huiskes and Chao, 1983). In addition to geometrical accuracy, FEA allows greater flexibility in the specification of boundary conditions and facilitates the variation of parameters of interest, such as density, muscle forces, and geometry, to assess their relative influence on strength. Some studies have used

two-dimensional models (Rohlmann *et al.*, 1980; Oonishi *et al.*, 1982; Testi *et al.*, 1999), but the majority of models have been three-dimensional, especially for the proximal femur.

A number of 3-D FEA studies have focussed on assessing and improving the accuracy of finite element model generation, and on automating the process (Table 3.2). In general, these

Table 3.2 Summary of FEA model generation techniques examined in various studies.

Study	FEA Method/Contribution	Conclusions
Basu *et al.*, 1985-86	Model derived from CT	
Keyak *et al.*, 1990, 1998	Automated geometry creation	
Viceconti *et al.*, 1999	Voxel-to-surface conversion	
Lengsfeld *et al.*, 1994, 1996	Automated meshing — hex. elements	
Viceconti *et al.*, 1998	Compared 4 AMG methods: mapped hex., tetrahedral, voxel, and surface-based hex. element definition	
Viceconti *et al.*, 1999	Unstructured hex. mesh from CT	
Keyak *et al.*, 1992	Effect of element size	Hex. elements should be no larger than 3mm on a side
Van der Sloten *et al.*, 1995	Influence of element distortion	Position of mid-side node and element skewness are most critical
Schmitt *et al.*, 1995	Algorithm to smooth edges of 3-D voxel models	
Lengsfeld *et al.*, 1998	Voxel-based and geometry-based methods have similar accuracy	
Oonishi and Hasegawa, 1982	Tested 4 material property schemes	Results very sensitive to scheme
Lotz *et al.*, 1991a, 1991b	Compared linear and non-linear material properties	Good agreement with in vitro test for yielding and load at fracture

Hex. = hexahedral (brick) elements

studies have found that voxel-based automatic mesh generation (AMG) and solid/surface geometry-based mesh generation have comparable accuracy, but that analysis results are very sensitive to element size, distortion, and material property assignment.

The main load cases that have been applied by investigators using finite element analysis include: (1) impact from a fall to the side (Lotz *et al.*, 1991b; Ford *et al.*, 1996a, 1996b; Oden *et al.*, 1999), (2) single-legged stationary stance (Lotz *et al.*, 1991b), (3) mid-stance during the gait cycle (Keyak *et al.*, 1990; Cheal *et al.*, 1992), (4) other phases of gait (heel-strike, toe-off)

(Savvidis *et al.*, 1991, Cheal *et al.*, 1992), (5) stair ascent (Cheal *et al.*, 1992), and (6) isometric contraction of various muscle groups (Cheal *et al.*, 1992).

A few investigators have specifically looked at the influence of muscle forces on stress in the proximal femur (Rohlmann *et al.*, 1981; Lengsfeld *et al.* 1996; Duda *et al.*, 1998). In particular, Duda *et al.* found that simplified load regimes incorporating only a few muscles produced differences in proximal femur strain as high as 26% compared to load regimes in which all thigh muscles were included. Also, Bassey *et al.* (1997) found that the hip forces measured by their instrumented implant *in vivo* were significantly related to muscle activity.

A particularly challenging aspect of finite element modeling of bone is the prediction of failure loads. Bone is a complex material resembling a composite engineering structure, but with the added complexity of local variations in material properties (e.g., modulus) and their principal directions. It has been modeled as either isotropic (simplest case) or to varying degrees of anisotropy (transversely isotropic, orthotropic). Several researchers have used a von Mises stress-based failure criterion to assess failure in the proximal femur (Lotz *et al.*, 1991a, 1991b; Ford et al., 1996). Cezayirlioglu *et al.* (1985) examined several failure criteria that have been used in composite materials and found that the Malmeisters-Tsai-Wu criterion was in best agreement with test data. Keyak *et al.* (1998) obtained relatively high correlations between their finite element model and mechanical tests of femora in the stance ($r^2 = 0.75$, linear regression) and fall configurations ($r^2 = 0.90$, non-linear regression). The methodology described in this chapter relies heavily on finite element failure analysis techniques developed by colleagues at the Orthopaedic Biomechanics Laboratory (Oden *et al.*, 1999; Selvitelli, 1997). Their work focussed on predicting the failure load of the proximal femur during a fall and the effect of local density changes on the failure load. They evaluated several failure criteria: maximum principal stress; maximum shear stress; von Mises; Raghava, Yeh and Caddell;

maximum principal strain; maximum stress; Hill; Hoffman; and Malmeisters-Tsai-Wu. The maximum principal strain failure criterion was shown to provide the best prediction of yield load in comparison with the four-point bending ($r^2 = 0.86$) and torsional mechanical tests of the cylindrical trabecular (cancellous) bone specimens (Oden and Selvitelli, 1998). The same criterion was also used to predict the failure behavior of 18 femora tested in a stance configuration and achieved a high degree of correlation ($r^2 = 0.87$, linear regression, slope ≈ 1) (Oden and Rosler, 1998).

3.2 Methods

3.2.1 Finite Element Model

The process of generating a three-dimensional finite element model from a QCT scan of a cadaveric proximal femur (based on technique developed by Oden *et al.* (1999)) is depicted in Figure 3.1. A proximal femur from a 36 y.o. male donor (chosen for being representative of a typical astronaut) was obtained post-mortem through the LifeLegacy Foundation (Tucson, AZ). The femur was harvested fresh and stored at -20° C. In the initial stage, the femur was thawed at room temperature, placed in a saline-filled sealed container, and scanned using peripheral QCT (pQCT, a higher resolution (0.1995 mm/pixel) capability than QCT; XCT3000, Norland Medical Systems, Fort Atkinson, Wisconsin). Scan slices were oriented perpendicular to the diaphyseal axis and spaced at intervals of 2 mm from the top of the head to 13.0 cm from the top of the head (65 slices), and then at intervals of 4 mm down to 21.0 cm from the top of the head (20 slices). All slices had a pixel scale of 0.1995 mm. The same femur was scanned, submerged in a saline-filled tub, using dual-energy x-ray absorptiometry

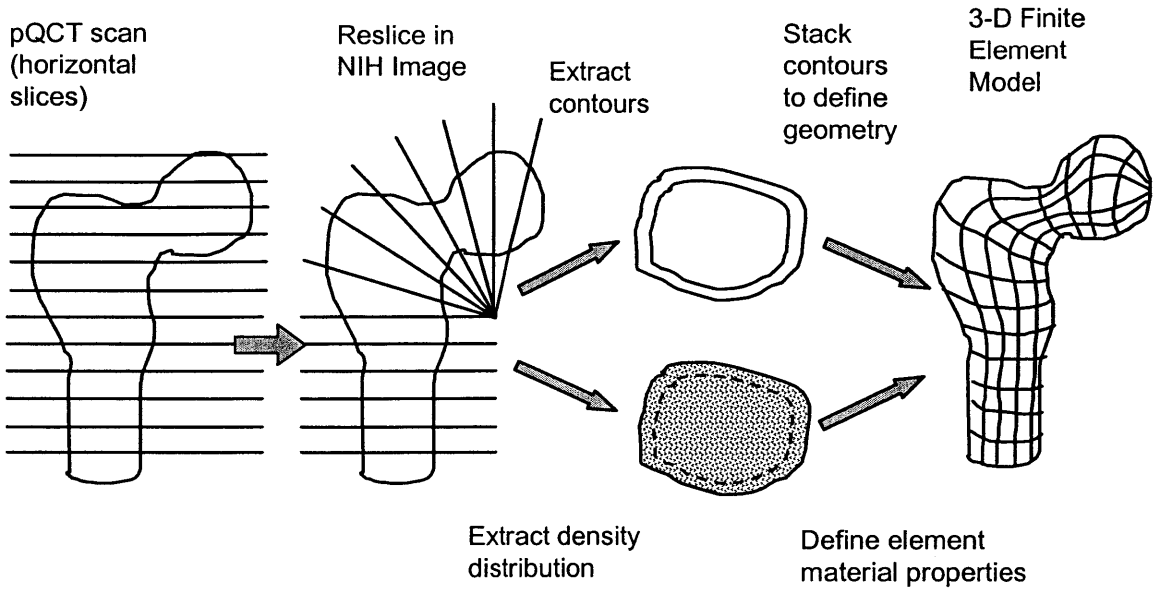

Figure 3.1: Process for generating a three-dimensional finite element model of the proximal femur through pQCT scans, based on techniques developed by Oden *et al.* (1999).

Table 3.3 Bone mineral density values obtained using a standard analysis program (Hologic) and custom software (Beck *et al.*, 1990; Mourtada *et al.*, 1996)

DXA Region	BMD (g/cm^2) (Hologic)	BMC (grams) (Hologic)	BMD (g/cm^2) (JHU)
Neck	0.753	4.07	0.825
Trochanteric	0.630	8.16	–
Intertrochanteric	1.040	22.48	0.844
Shaft	–	–	1.148

(DXA; QDR-2000plus, Hologic, Inc., Waltham, MA) and analyzed via a standard algorithm (Hologic, Inc., Waltham, MA), as well as a custom algorithm (Beck *et al.*, 1990; Mourtada *et al.*, 1996) to obtain regional BMD values. The values obtained using the two DXA analysis methods are given in Table 3.3.

In the next stage, the pQCT scans were processed in NIH Image (National Institutes of Health, Bethesda, MD) to obtain approximately 25 slices, with the slices in the intertrochanteric, neck, and head regions angled so as to follow the curvature of the neutral axis of the

femur. These slices (Figure 3.2a) are then thresholded (Figure 3.2b) to extract the outer (periosteal) and inner (endosteal) boundaries (Figure 3.2c).

a)

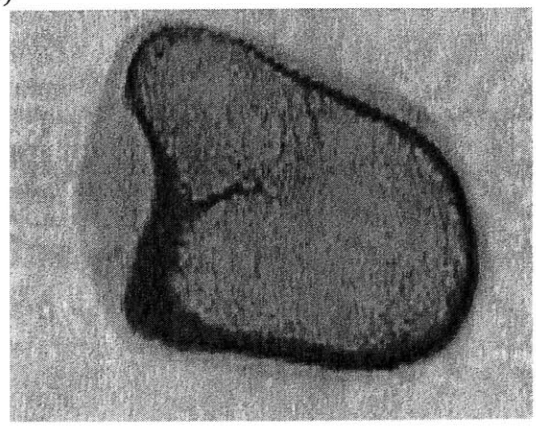

b)

c)

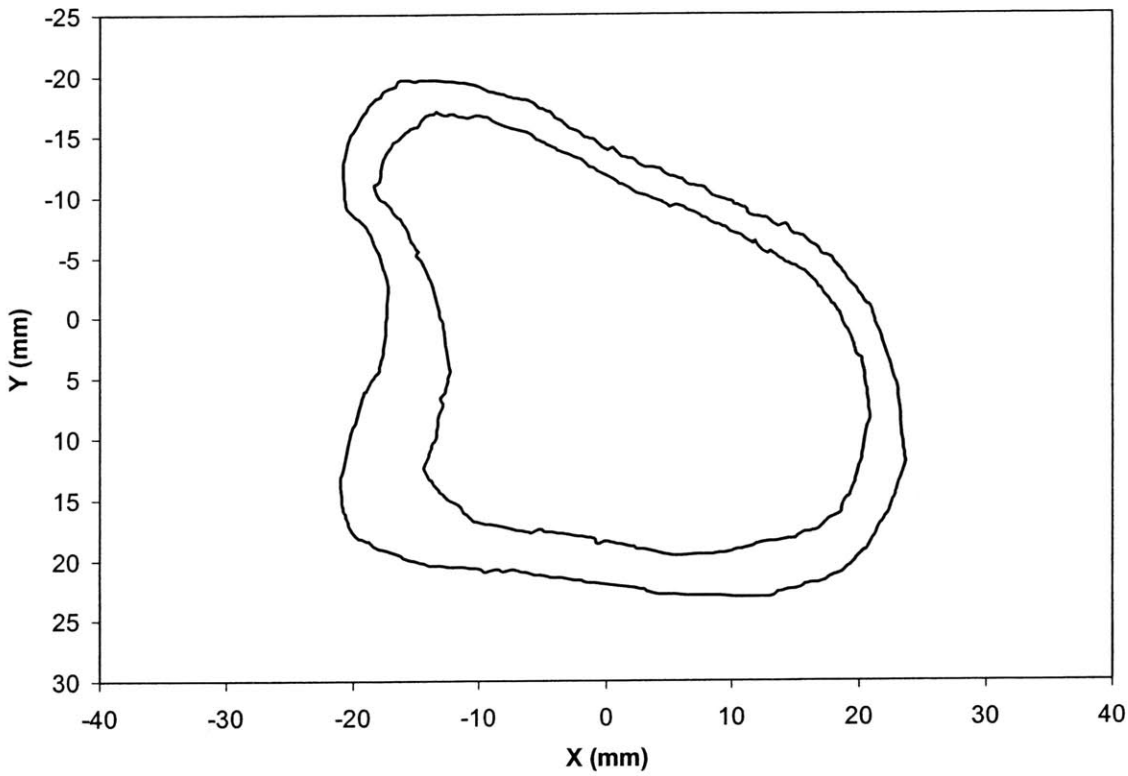

Figure 3.2: a) Sample femur slice after pQCT data has been processed in NIH Image (cuts through lesser trochanter at top left), b) thresholded slice, and c) boundaries extracted from thresholded slice.

The data obtained as described above, was used to create a geometric model (Figure 3.3) and a finite element model (Figure 3.4) of the femur in I-DEAS (Structural Dynamics

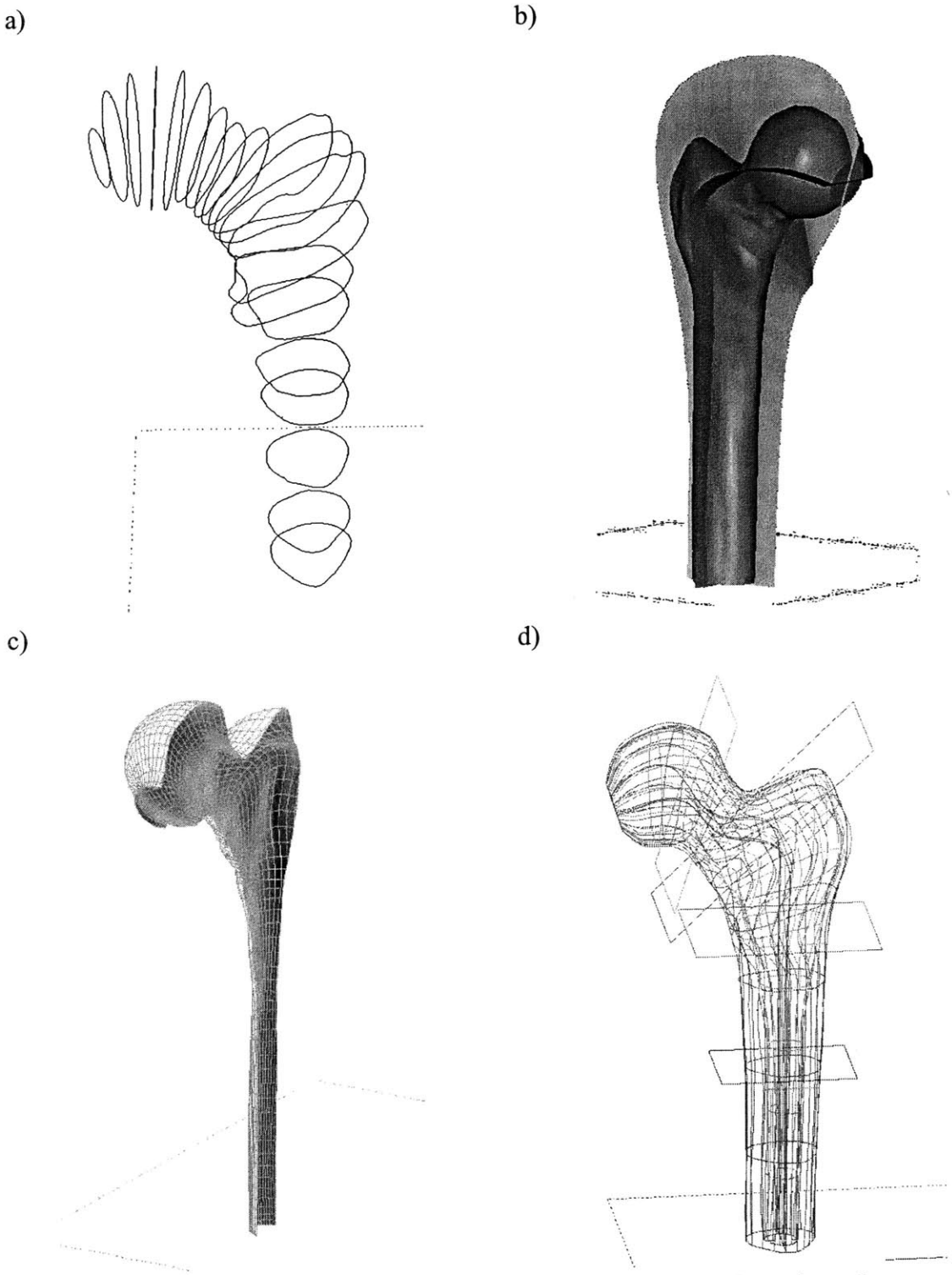

Figure 3.3: Creation of geometric femur model in I-DEAS. a) Outer boundary curves imported and stacked. b) Outer curves lofted to create total volume that is partitioned into quarters. c) Inner boundary curves imported and lofted to create surface that partitions total volume into cortical and cancellous regions. d) Using plane surfaces, the model is partitioned at four points along the length of the bone giving a final total of 40 volumes.

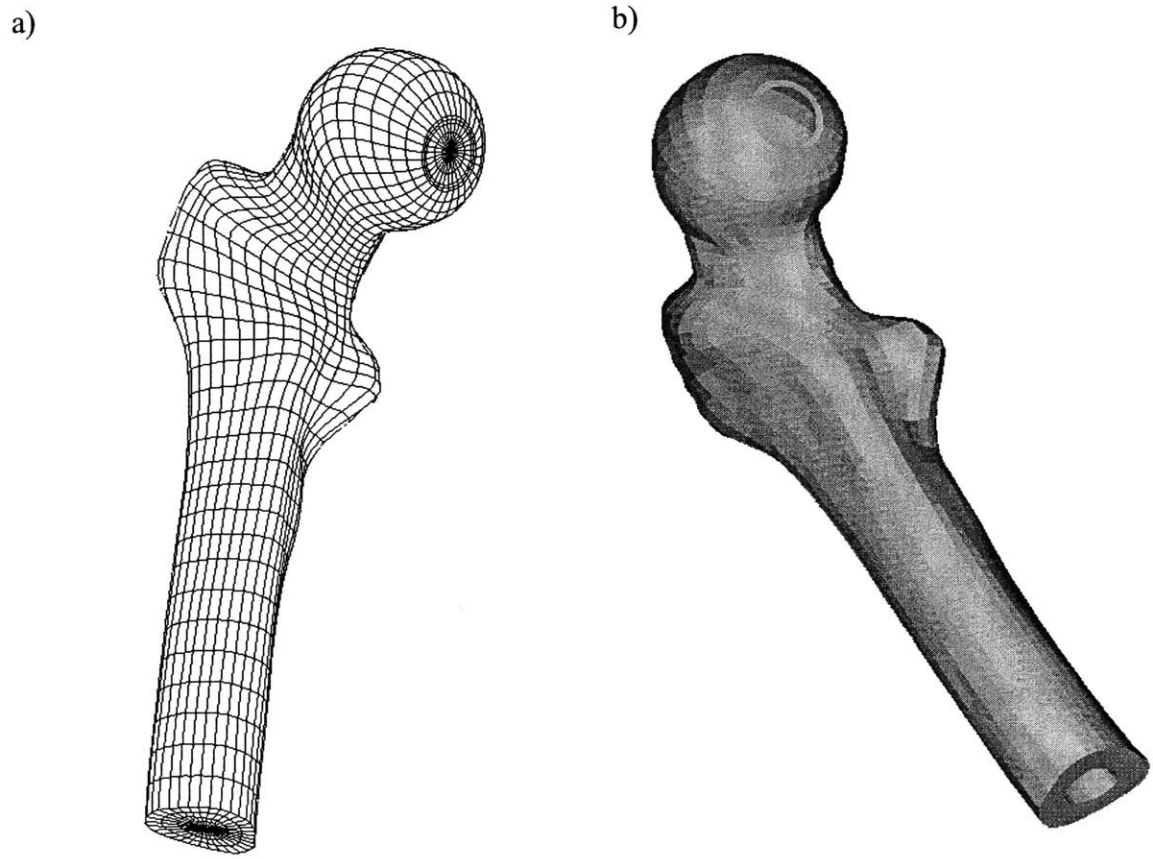

Figure 3.4: Conversion of geometric model into finite element model in I-DEAS. a) Complete model containing 6,400 elements and 25,164 nodes. b) The cortical shell was modeled and meshed as a separate volume.

Research Corporation (SDRC), Milford, OH). The first two steps in the generation of the model us the technique of Oden et al. (1999) and the remaining two steps involve extensions of their technique developed by the author. First, the x-y-z coordinates describing the outer boundaries were imported into I-DEAS and stacked in the appropriate relative positions (Figure 3.3a). Second, the outer boundary curves were lofted to create a surface enclosing the total volume of the bone. Straight lines aligned with x-z and y-z planes, and passing through the centre of each curve, were lofted to create two surfaces that were used, in turn, to partition the total volume into quarters (Figure 3.3b). Third, the inner boundary curves were imported into I-DEAS and lofted to create a surface that was used to partition the bone into cortical and cancellous regions, bringing the number of sub-volumes to 8 (Figure 3.3c). Fourth, plane surfaces

corresponding approximately with mid-diaphysis, diaphyseal-intertrochanteric transition, trochanteric-neck transition, and neck-head transition were used to partition the whole model into five lengthwise regions which resulted in a total of 40 sub-volumes in the model (Figure 3.3d).

The sub-volumes in the geometric model were meshed using mapped meshing to generate the finite element model of the femur (Figure 3.4a). A convergence study was previously conducted and showed that an element density numbering more than 2,500 elements would achieve sufficient accuracy (convergence to within 1% of the solution for an infinite number of elements). The final model contained 6,400 elements, the high number of elements being required to model the cortical and cancellous bone as separate regions. The thickness of the cortical shell (Figure 3.4b) was divided into two element layers while the distance between the endosteal boundary and the central axis was divided into three element layers. The majority of elements were 20-noded quadrilateral elements with 15-noded wedge elements emerging in the central layer due to the degeneracy of the central point. A preliminary ABAQUS (Hibbitt, Karrlson and Sorenson, Inc., Pawtucket, RI) input file was then exported from I-DEAS in preparation for the actual finite element analysis to be performed using ABAQUS.

The material properties for each element were established as follows. First, CT attenuation values (ρ_a) were converted to apparent density (ρ in g cm^{-3}) using the equation:

$$\rho = (1.495 \times 10^{-3})\rho_a - 0.341 \tag{3.1}$$

which was supplied by the manufacturer (Norland Medical Systems, Fort Atkinson, Wisconsin) based on their calibrations. A previously developed FORTRAN program called "finddens.f" (Oden, 1994; Selvitelli, 1997) was used to sample the density values from points lying within a 4 mm sided cube surrounding the centroid of each element. The cube dimension of 4

mm per side is based on limitations of the continuum assumption in cancellous bone, as described by Harrigan *et al.* (1988). The density value for a given element was then calculated from the average density of the sample points, in the case of cancellous elements, or the maximum density of the sample points, in the case of cortical elements. The densities of the elements in the two regions were assigned using two different schemes because this method provided the best discrimination between cortical and cancellous densities, and also produced the most accurate failure loads. Furthermore, it was reasoned that if the density was averaged for a cortical element with a portion of the sample points lying in the cancellous region, as often occurs with elements lying on the boundary of these two regions, then the cortical element is inappropriately weakened. Conversely, densities for cancellous elements were averaged so that these elements were not inappropriately strengthened. Finally, the apparent density for each element was written to a file along with the element number.

The material properties for each element were established using a FORTRAN program called "matmak.f", previously developed by Oden (1994) and modified by the author to accommodate a model with separate cortical and cancellous regions. This program first reads in the apparent density values of each element from a separate file and then uses the density value to calculate the element's modulus. All elements were assumed to be isotropic. Several material property relations were considered (Burstein *et al.*, 1972; Reilly *et al.*, 1974; Reilly and Burstein, 1975; Carter and Hayes, 1976, 1977; Goldstein, 1987; Ashman and Rho, 1988; Rice *et al.*, 1988) before settling on the following two relations for the femur model. The modulus values for cancellous elements were calculated from the relation (Ashman *et al.*, 1989):

$$E = (2.84\times10^{3})\rho^{1.07} \tag{3.2}$$

and the modulus values for cortical elements was calculated from the relation (Snyder and Schneider, 1991):

$$E = 21910\rho - 23500 \tag{3.3}$$

where E equals the Young's modulus in MPa and ρ equals the apparent density in g/cm^3. These two relations were chosen in preference to other relations in the literature for the following reasons: in both cases the authors used human bone tissue from the lower limb (tibia); the Ashman *et al.* relation showed a high degree of correlation with mechanical test (r^2 = 0.96); and the Snyder and Schneider relation was correlated to CT data (r = 0.55 for Young's modulus). The Poisson's ratio, υ, was set to 0.3 for all elements.

3.2.2 Boundary Conditions

For the locomotion case (mid-stance) (Figure 3.5), the direction of the joint contact vector was adopted from Cheal et al. (1992), with unit vector components of 0.35 (x, or medial-to-lateral axis), -0.05 (y, or posterior-to-anterior axis) and -0.93 (z, or distal-to-proximal axis). Since the y-component was only 5% of the z-component, it was neglected to simplify application of the boundary conditions. The femur model was rotated 20.6 degrees about the y-axis so that the joint contact load direction would be oriented in the global z direction. The nodes in the distal end of the femur were prevented from translating in the global x, y, and z directions. Constant muscle forces, consistent with the mid-stance condition (Cheal *et al.*, 1992), were applied throughout the analysis. The muscle insertion areas are shown in Figure 3.5 while the magnitudes and directions are given in Table 3.4. In the finite element model, the muscle forces were applied by dividing the total magnitude equally amongst the surface nodes lying in the insertion area for the particular muscle (or muscle group in the case of the iliop-

Table 3.4 Muscle forces applied during locomotion (mid-stance) loading condition.

Muscle Group	Magnitude (BW)	Med.-lat. (x)	Post.-ant. (y)	Dist.-prox. (z)
Gluteus medius	0.80	-0.67	0.18	0.72
Gluteus minimus	0.30	-0.78	0.21	0.59
Iliopsoas	1.30	-0.10	0.73	0.68

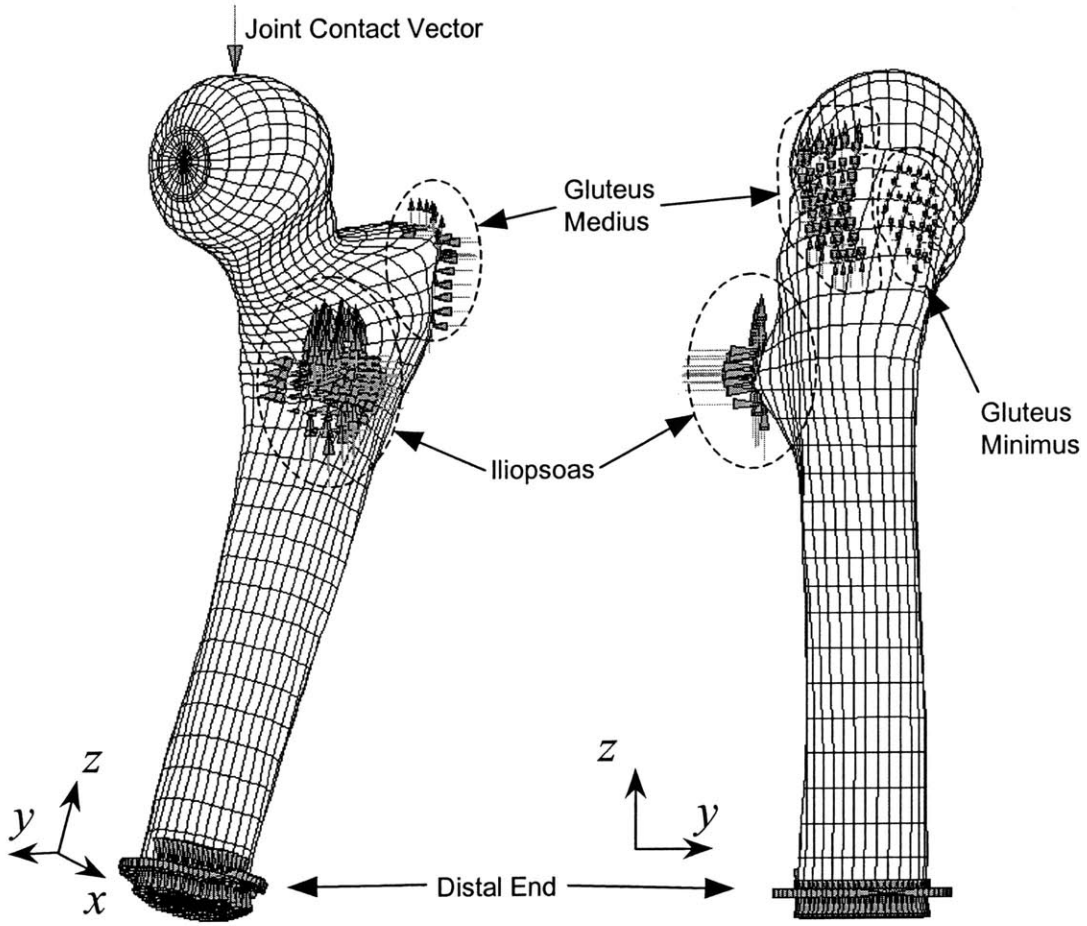

Figure 3.5: Boundary conditions for finite element analysis of locomotion (mid-stance) loading condition.

soas). The joint contact boundary condition was applied in the form of a ramp displacement from 0 to -6.0 mm applied to a group of 13 nodes at the top of the head (multiple nodes were selected to minimize distortion). A displacement boundary condition was chosen in preference to a force boundary condition for modeling joint contact because a ramped force boundary condition was incapable of indicating the point at which failure occurred (since failure is

defined as a decrease in reaction load with increasing displacement, and a ramp force cannot decrease by definition). A single node at the center of the head was fixed in the x and y directions to provide a reaction to the muscle forces, as would be provided by the acetabulum and pelvis. The total force applied to the femoral head was then calculated as the magnitude of the x and y reaction components at the center, and the z reaction component at the top of the head. To assess the influence that muscle forces have on the magnitude of the failure load in the mid-stance condition, an additional analysis was executed with the muscle forces excluded, but retaining the same displacement ramp to the top of the head as well as the other fixed displacement boundary conditions.

The boundary conditions for the fall loading are shown in Figure 3.6. The configuration of the femur was based on that described by Courtney *et al.* (1994). The femur was first inter-

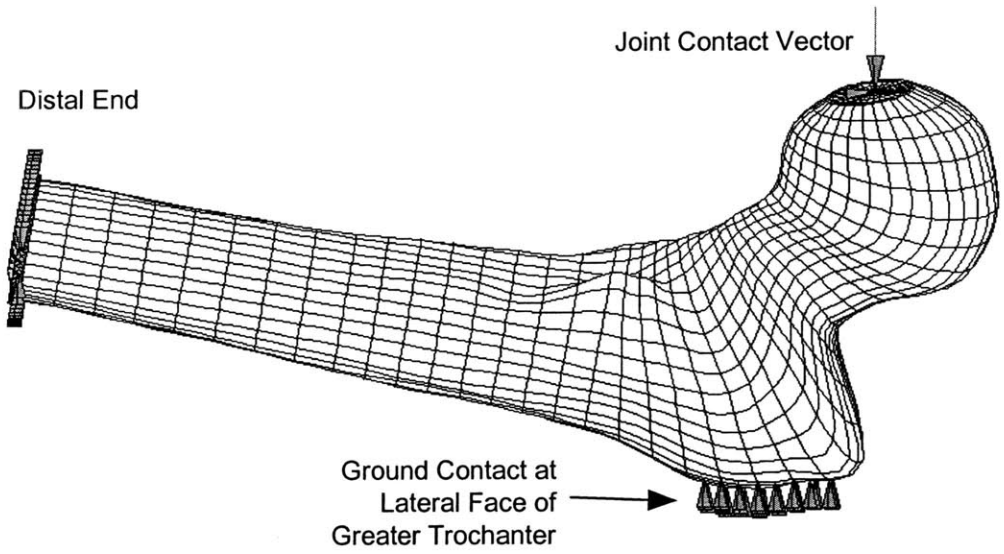

Figure 3.6: Boundary conditions for fall loading case.

nally rotated (foot would point inward) about the diaphyseal axis (z-axis) by an angle of 15 degrees, and then rotated about the global y-axis (see Figure 3.6) by an angle of 10 degrees. The nodes in the distal end were prevented from translating in the global x- or y-directions,

while the nodes in the contact area of the greater trochanter were prevented from translating in the x-direction. The displacement (x-direction) was applied equally amongst the nodes in the flat surface at the medial end of the head (distributed over several nodes to minimize local distortion) and these same nodes were prevented from translating in the z-direction.

3.2.3 Failure Criteria

The algorithm used to apply the failure criteria for individual elements as well as for the whole bone (based on algorithm used by Selvitelli (1997)) is depicted in Figure 3.7. An ele-

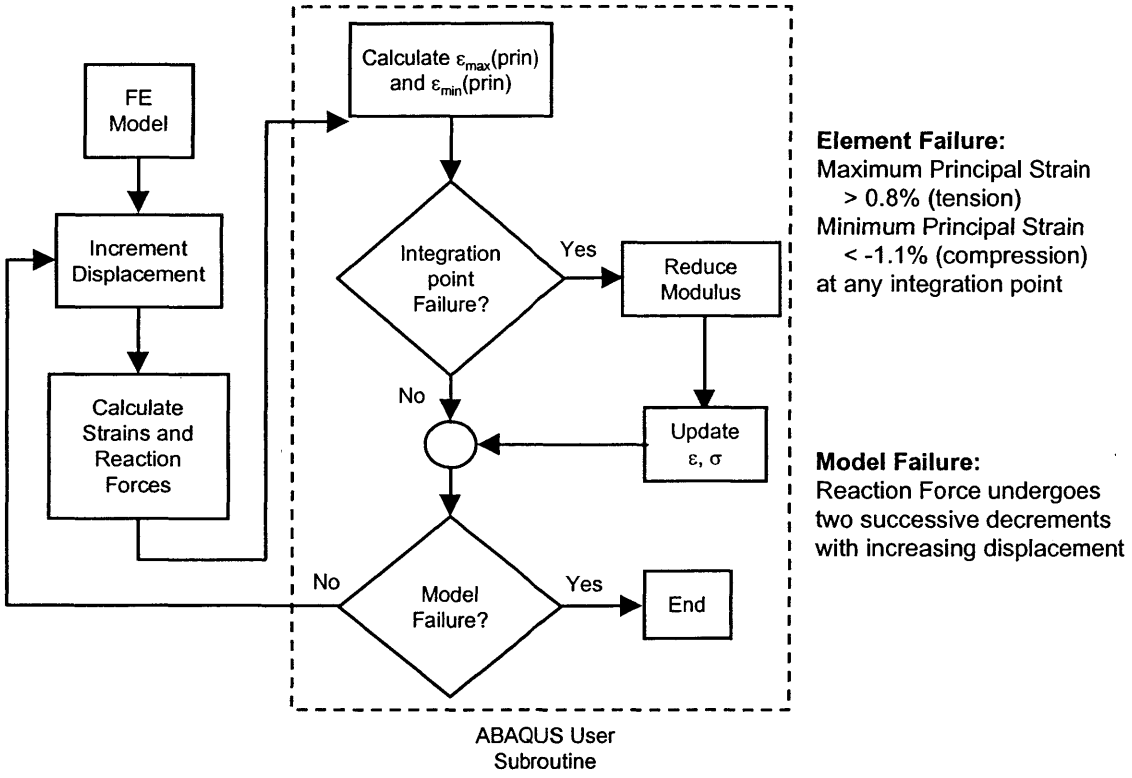

Figure 3.7: Flowchart depicting application of failure criteria for individual elements and whole bone through the use of a user subroutine included in the ABAQUS run (based on Selvitelli (1997)).

ment was considered to have failed if the maximum principal strain exceeded 0.8% (tension) or the minimum principal strain exceeded -1.1% (compression) at any of the element integration points. When this occurred, the modulus value for that integration point was reduced to

0.01 MPa, which simulated zero stiffness without causing a singularity. The stress and strain state was calculated at each increment, and thus accounted for the incremental effect of failed elements. When the reaction force at the displacement application nodes underwent two successive decrements with increasing displacement, the model was considered to have failed. The failure load was then taken to be the maximum force achieved during the analysis.

Application of the boundary conditions (restraints, displacements, and concentrated loads) at the discrete points associated with nodes tended to create unreasonably high stress concentrations in the immediate vicinity of these points of application. If these elements were allowed to fail, the relaxation effect would have reduced the stress in the natural stress concentration areas such as the femoral neck. To prevent this from happening, the elements directly associated with boundary condition application, or in close proximity to these areas, were protected from failure by assigning only a single material field to these elements in the ABAQUS input file. That is, if the principal strain exceeded a failure limit for the protected element, the modulus was kept unchanged.

3.2.4 Analysis

The final ABAQUS input file, including node and element definitions, material property cards and boundary conditions, was written out by the program "matmak". Analysis runs were then performed by executing ABAQUS. In general, a linear elastic analysis was performed first so that the model could be checked for errors relatively quickly. Once this was successfully completed, a failure analysis run was carried out. The displacement ramp was described in terms of virtual time. Control of the time increment durations was controlled automatically by ABAQUS, but with the following specified constraints: an initial time increment of 0.01 seconds, a maximum time increment of 0.04 seconds, and a minimum time increment of 0.001

seconds. The total time for the ramp displacement was 1.0 seconds. During each of the time increments, the displacement and reaction force at the displacement application node on the femoral head were recorded. In addition, the labels of any elements that failed during the increment were recorded.

3.3 Results

3.3.1 Mid-Stance Analysis

A load versus displacement plot for the baseline femur analyzed in a mid-stance load configuration (with muscle forces applied) is shown in Figure 3.8. In this case, the peak load

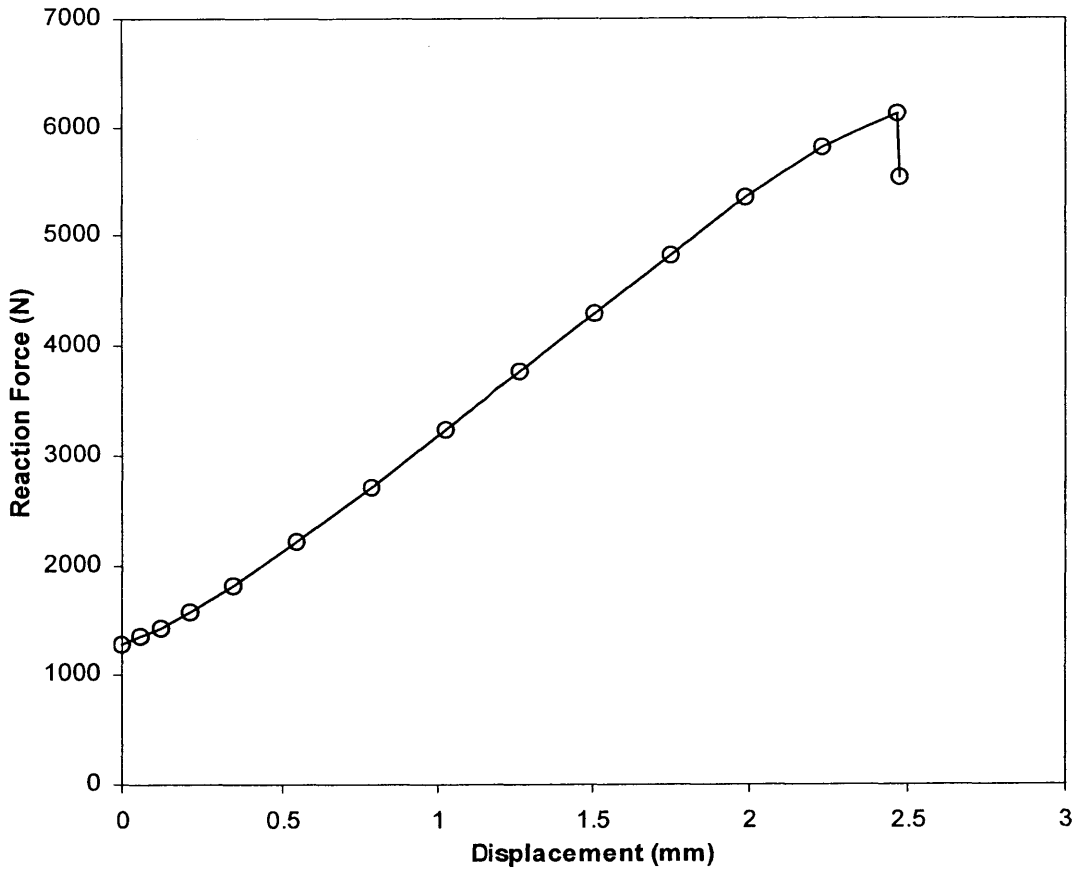

Figure 3.8: Load vs Displacement plot for baseline femur in mid-stance load configuration (muscle forces included).

achieved during the analysis, approximately 6,130 N, coincided with a displacement of about 2.5 mm. The stiffness of the femur in the mid-stance orientation was approximately 2,180 N/mm (2.2×10^6 N/m). The curve starts off with a non-zero preload of approximately 1,300 N due to the fact that the model was brought to equilibrium under the action of the applied muscle forces before the displacement was applied at the femoral head. During the first 0.5 mm of displacement, the slope of the curve increases, reflecting the decreasing fractional contribution of the muscle forces to the joint reaction force. As the displacement continued past the 2 mm point, the effects of yielding were increasingly apparent, finally leading to the catastrophic failure at 3 mm of displacement. The reaction force at the head drops off very rapidly due to the large increase in the number of failed elements during the last displacement increment.

A depiction of the deformed femur at the point of failure, along with the undeformed shape, is provided in Figure 3.9. It can be seen that the entire proximal femur experienced a buckling mode due to the combination of the clamped condition at the distal end and the node at the center of the head which is fixed in the x and y directions. The application of the prescribed displacement at the top of the head formed a slight indentation locally, but did not limit the downward displacement and rotation of the overall femoral head. The region of compression failure in the inferior surface of the neck, close to the subcapital margin was clearly visible. Regions of tensile failure were less easily identified, though.

A contour plot of the maximum principal strain is shown in Figure 3.10. Note that the highest values corresponded with regions of concentration of tensile strain. In this case, tensile strain concentrations were visible in both the superior and inferior portions of the neck surface, close to the point of transition to the head. A strain concentration was also clearly visible at the top of the head in the region where the joint contact load (displacement) was

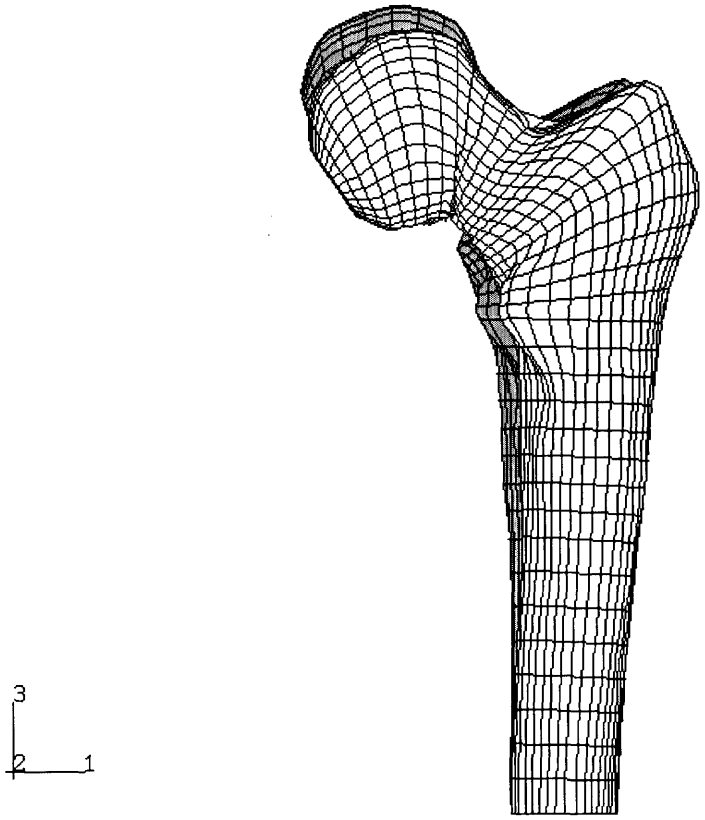

Figure 3.9: Mid-stance loading: Depiction of the deformed femur (white) at point of failure, superimposed on an image of the undeformed femur (grey). The 1, 2, and 3 directions indicated correspond with x, y, and z axes, respectively.

applied. The need to protect elements from undesirable local failure in this region was obvious.

As expected, the pattern of element failure (Figure 3.11) corresponded closely with the regions of greatest tensile strain. Element failure originated in the inferior portion of the neck, but quickly jumped to the superior surface of the neck, thereafter the area of failure propagated around the circumference of the neck and joined the two regions. This pattern of failure was consistent with a subcapital transcervical fracture.

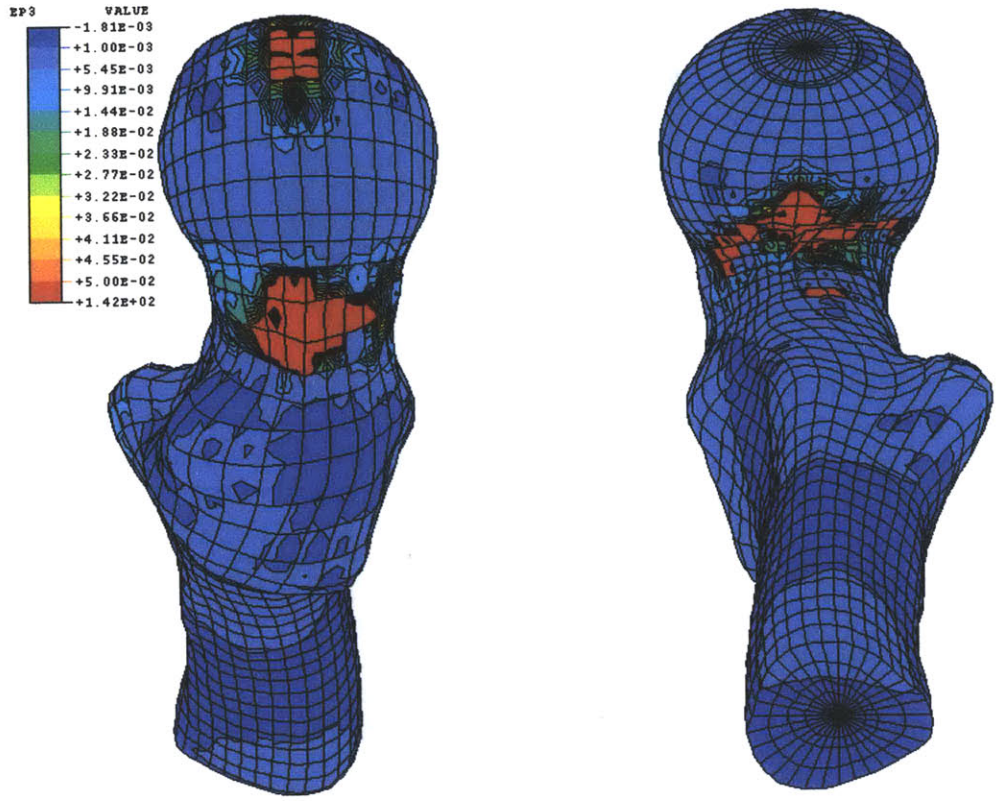

Figure 3.10: Mid-stance loading: Contour plot of maximum principal strain. The highest values correspond with areas of greatest tensile strain.

The load displacement curve for the case of mid-stance loading without muscle forces is shown in Figure 3.12. In this case the curve projects through the origin since the absence of muscle forces eliminates the preload experienced in the previous case that included muscle forces. Also due to the absence of muscle forces, the lower part of the curve is more linear than the previous case. The failure load in this case was approximately 4,880 N. The stiffness in the no muscle case (2254 N/mm) was slightly greater than the stiffness with the inclusion of muscles (2151 N/mm), but the difference was only 5%.

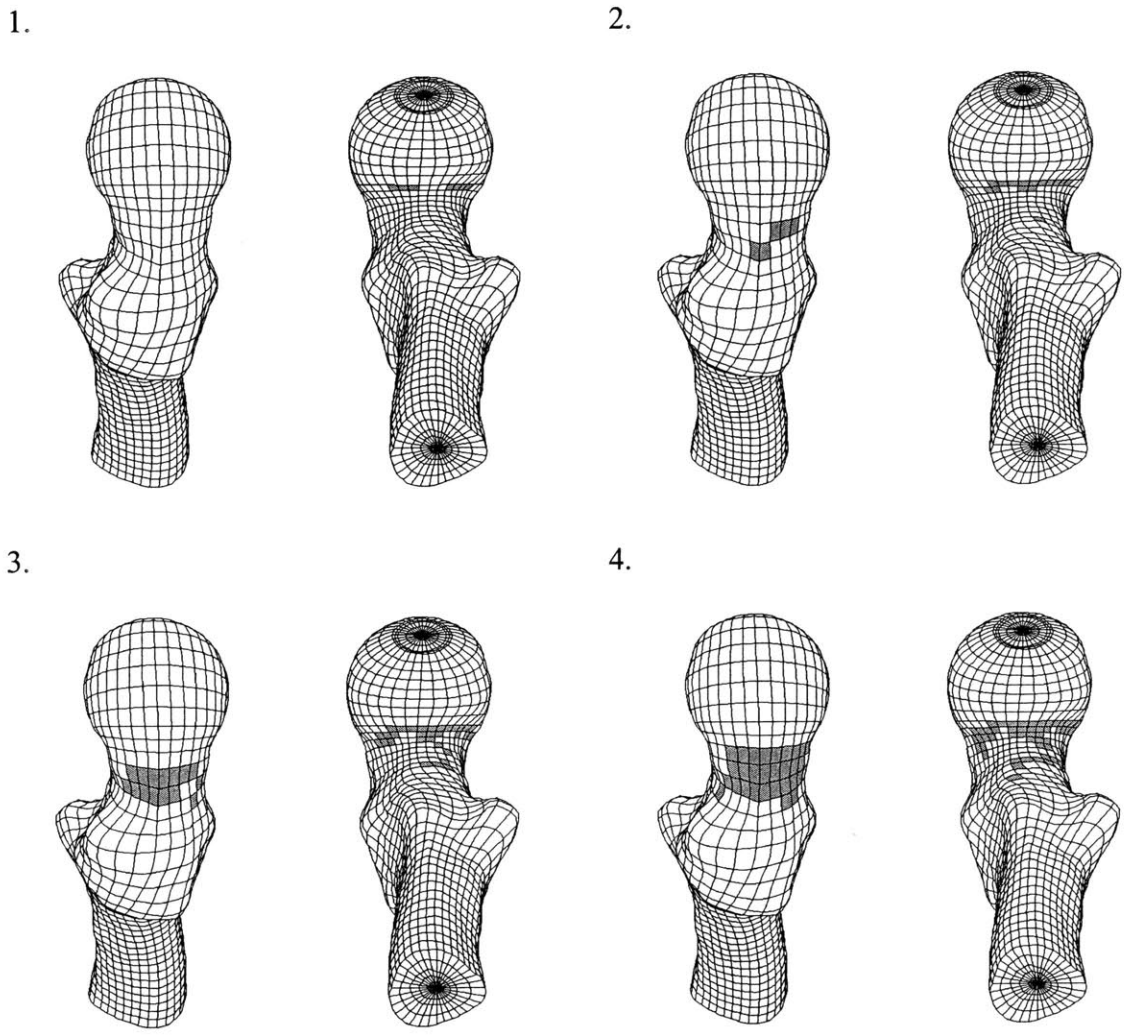

Figure 3.11: Mid-stance loading: Pattern of element failure in the proximal femur. Failed elements are indicated in grey. The failure sequence proceeds according to the numbered sequence, with the superior aspect of the femur presented on the left, and the inferior aspect on the right for each set.

3.3.2 Fall Loading Analysis

The load-displacement plot for the fall loading configuration is given in Figure 3.13. The peak load of approximately 4,390 N occurred at a displacement of about 1.2 mm at the joint contact node. The curve is observed to be highly linear in the lower portion, up until approximately 0.8 mm, and thereafter the effects of yielding become increasingly apparent. The analysis terminated after the first decrement in reaction force because the large number of failed

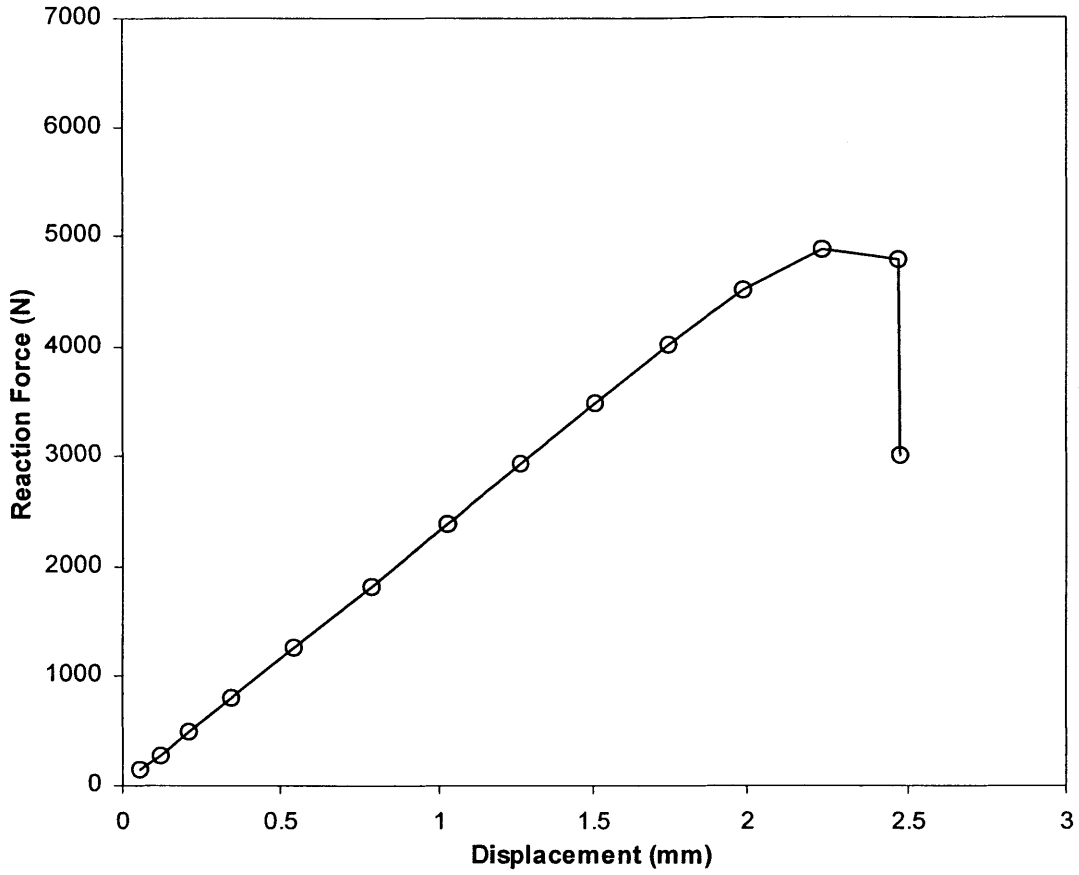

Figure 3.12: Load vs displacement plot for loading in the mid-stance configuration, but without the application of muscle forces.

elements created deformations that exceeded the capability of the equilibrium solver in ABAQUS.

The deformation of the femur caused by the fall loading is shown in Figure 3.14 along with a representation of the undeformed femur for reference. It is clear that the neck undergoes a significant amount of bending resulting in severe compression in the superior surface of the neck close to the junction between the neck and the greater trochanter. The deformation seen at the medial end of the head is a result of the fact that all of the nodes in the flat surface are prescribed with equal displacement in the z direction. Consequently, this surface is unable to rotate about the x and y directions and the local distortion occurs as a result.

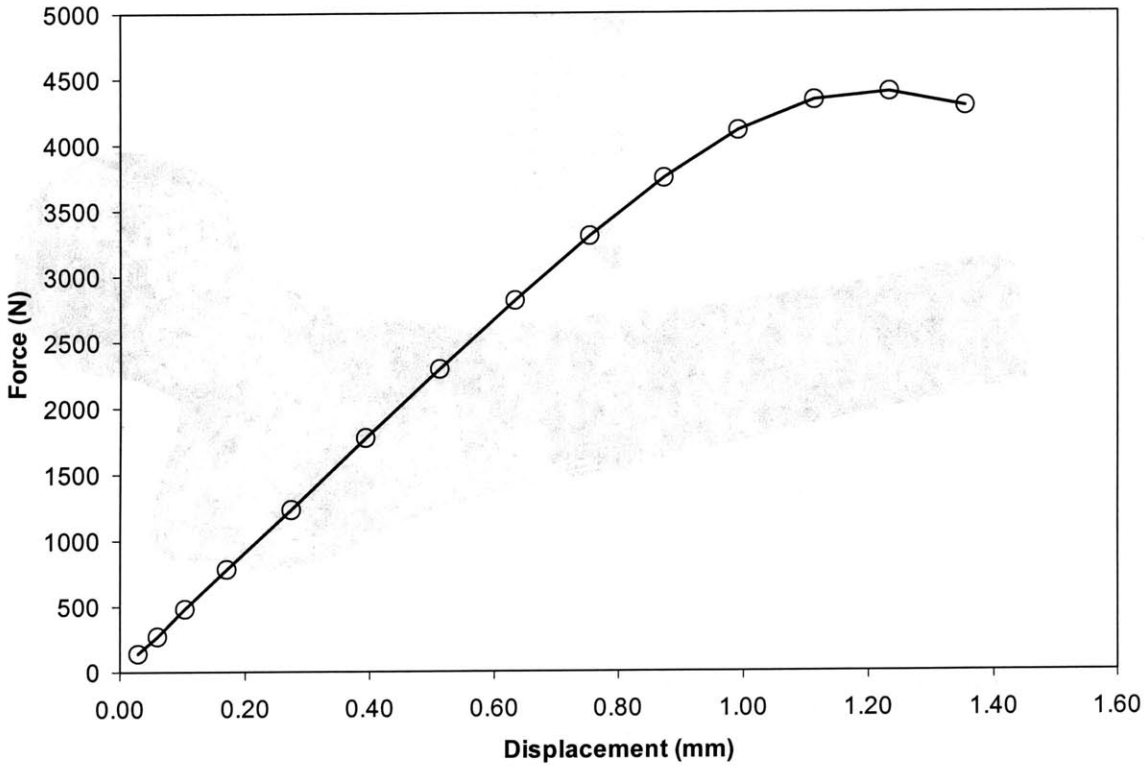

Figure 3.13: Load vs displacement plot for baseline femur in fall loading configuration.

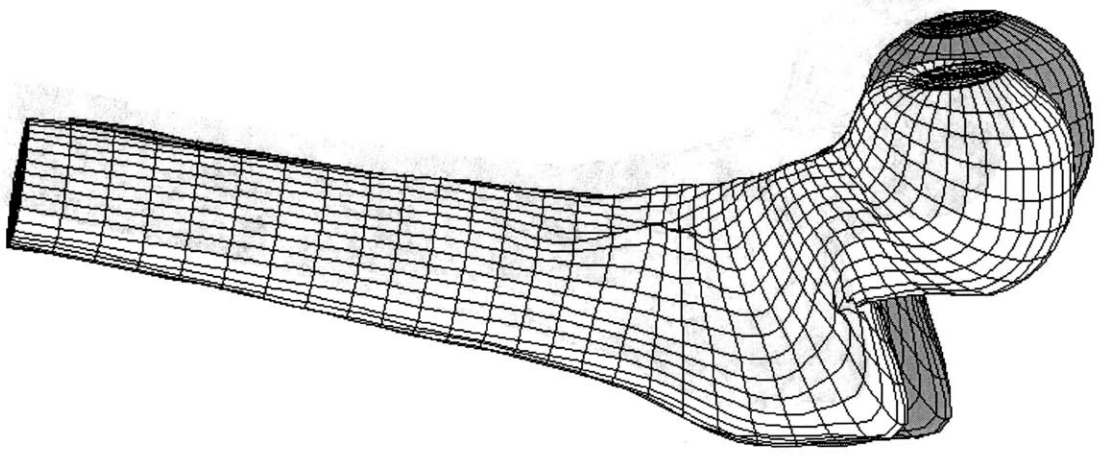

Figure 3.14: Fall loading: Depiction of the deformed femur (white) at point of failure, superimposed on an image of the undeformed femur (grey).

A contour plot of the minimum principal strain is shown in Figure 3.15. Note that the most negative values correspond with areas of greatest compression. A region of concentrated com-

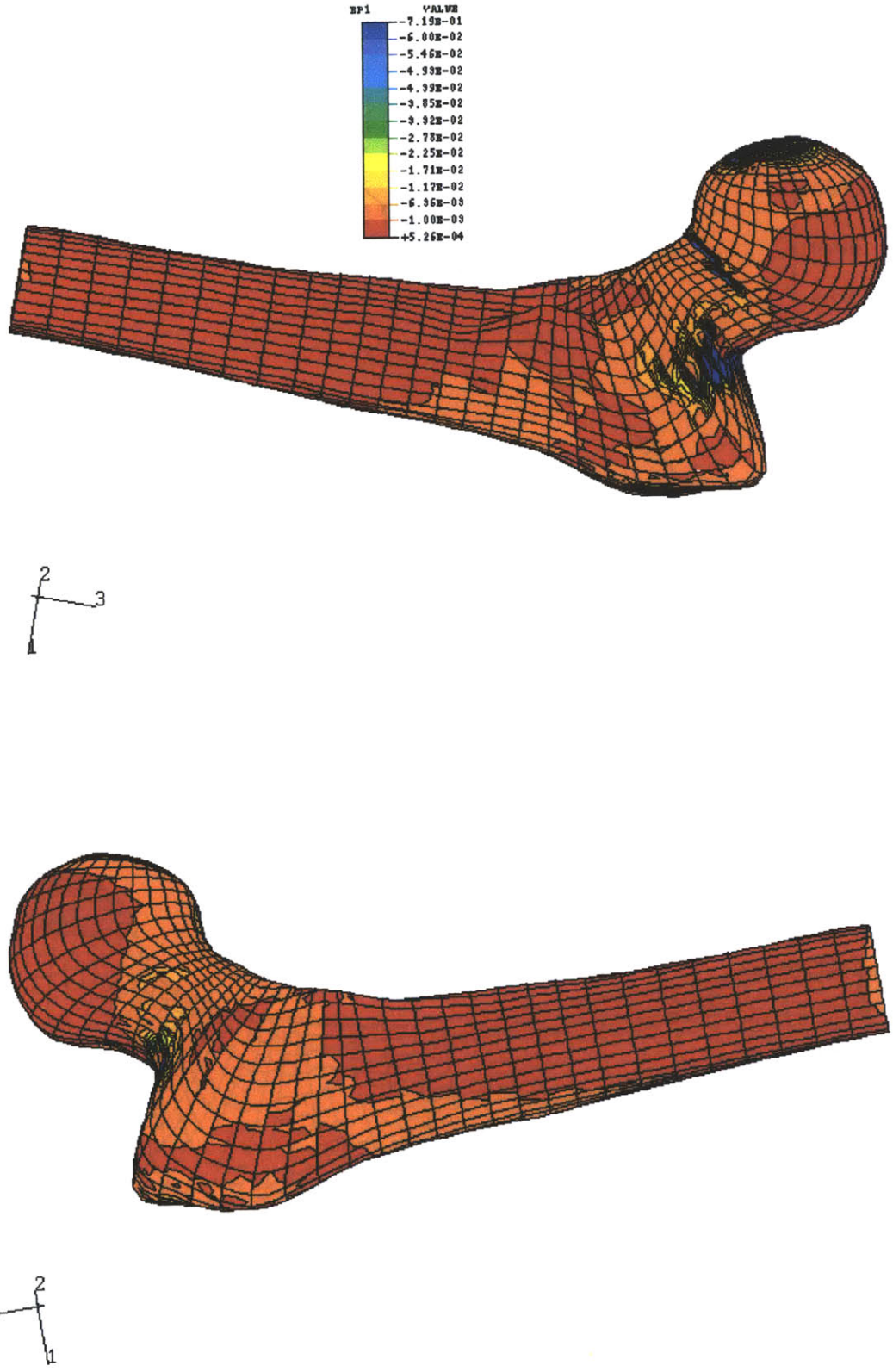

Figure 3.15: Fall loading: Contour plot of minimum principal strain. In this case, the highest negative values correspond with areas of greatest compression. The 1, 2, and 3 directions correspond with the x, y, and z axes, respectively.

pression is clearly visible in the superior surface of the neck (in the fall configuration depicted, this area corresponds with the part of the neck closer to the ground). The local strain concentrations caused by the displacement boundary condition on the medial end of the head is clearly noticeable, but the lateral end of the greater trochanter does not show much strain concentration indicating that the reaction loads are better distributed on that end. Not surprisingly, more elements required protection from the non-physiological strains at the medial end of the head (3-4 element layers) than at the greater trochanter contact area (1-2 element layers).

The pattern of element failure (Figure 3.16) is seen to correspond closely with the regions of concentration of compressive strain. Here, the failure pattern originates in the superior neck surface and a small line along the subcapital margin on the posterior side and thereafter expands around the neck circumference, also propagating to the posterior surface of the greater trochanter.

The largest failure load was obtained for the case of mid-stance with the inclusion of muscle forces (6,130 N), while the mid-stance case without muscle forces showed a marked reduction in failure load (4,880 N) (Figure 3.17). Thus the protective effect of the forces applied by the gluteus medius, gluteus minimus and iliopsoas muscles was responsible for an increase in strength of 1,250 N, or as much as 26%, over the loading condition without muscles. The lowest structural strength (4,390 N) was exhibited in the fall loading case.

3.4 Discussion

The finite element analysis presented in this chapter was aimed at assessing the strength of the proximal femur in its baseline condition, that is, for an astronaut on earth before departing

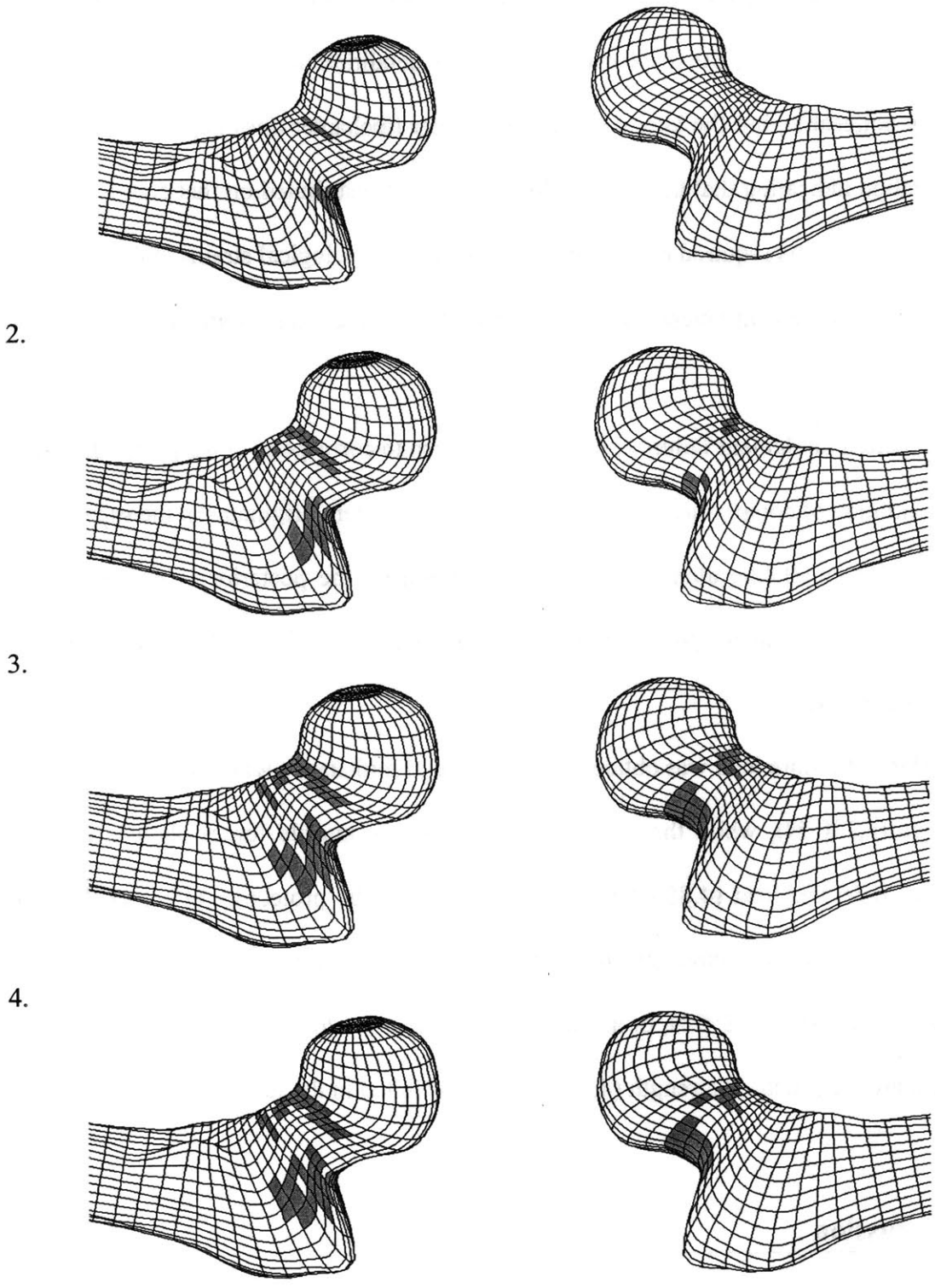

Figure 3.16: Fall loading: Pattern of element failure in the proximal femur. Failed elements are indicated in grey. The failure sequence proceeds from top to bottom, with the posterior aspect of the femur presented on the left, and the anterior aspect on the right.

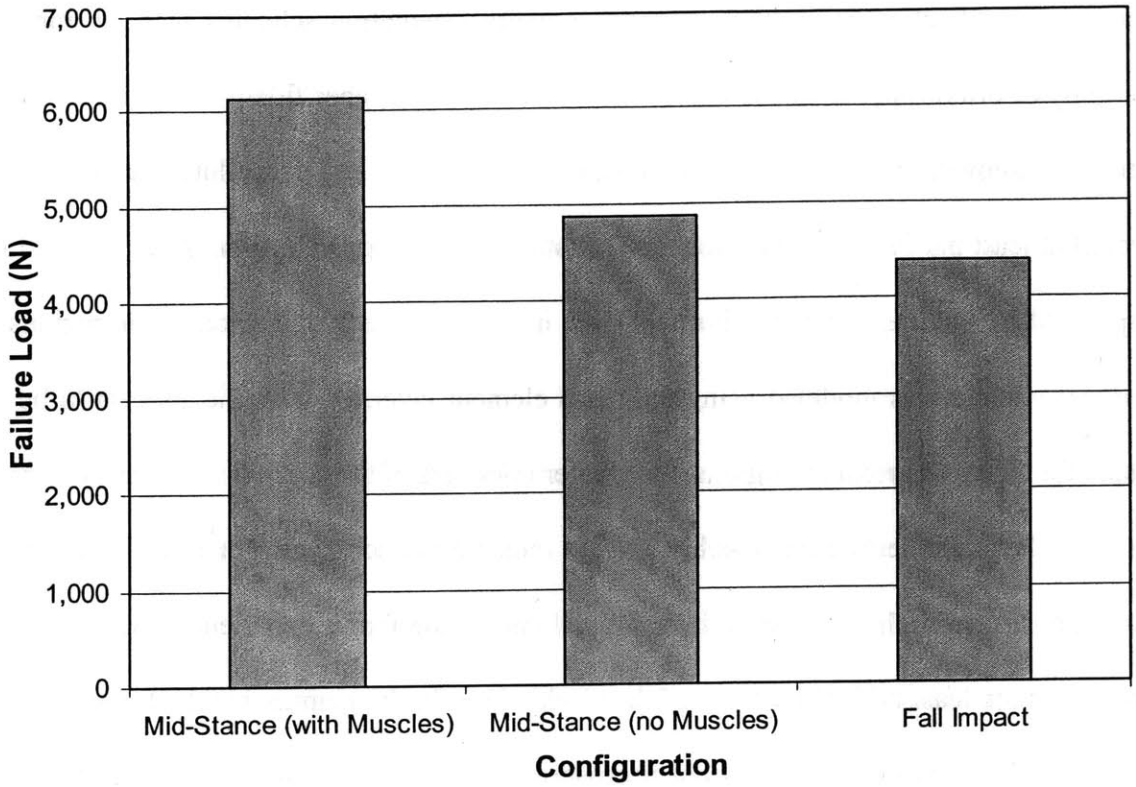

Figure 3.17: Comparison of failure loads for the three conditions analyzed for the baseline femora.

on a long-term space flight mission. While the structural consequences associated with the weightlessness experienced during spaceflight are presented in the chapter following this, it is possible to draw some preliminary conclusions about the strengths and limitations of the methodology employed.

It is important to acknowledge the limitations in the modelling approach. First, the proximal femur was modeled as a continuum, despite the fact that porous trabecular bone makes up the majority of its volume. While there are good models for the microstructure of cancellous bone (Gibson, 1985), it is not practical to apply them at the whole bone level. Fortunately, it has been found that the continuum assumption for trabecular bone still yields good agreement with experiment, provided that guidelines such as those set by Harrigan *et al.* (1988) are fol-

lowed (discussed in Methods section). Second, the use of isotropic material properties represents a simplification over other material property orientation schemes such as transverse isotropy or orthotropy. It was reasoned, however, that the higher fidelity of geometric representation allowed by pQCT and the separation of cortical and cancellous element regions would at least partially make up for the limitations of isotropy. Third, in order to avoid high aspect ratio elements in the thin cortical shell in the head, neck and trochanteric regions, the cortical volume was modeled using only two element layers. While this appears to be adequate for the more proximal regions, the greater thickness of the cortex in the diaphysis results in rather large elements with possibly a slight reduction in accuracy. Fortunately, the loading conditions were such that diaphysis and distal end of the femur experienced little stress and were thus the least critical portions of the model. Fourth, the manner in which muscle forces are applied at surface nodes was not necessarily a very accurate representation of the local interface. While the force components are a good representation of the overall muscle force, the actual muscles more likely wrap around the bone and thus more likely give rise to higher shear stresses in the points of insertion and a more complex distribution of force magnitude. Since the regions of peak strain, and consequently also element failure, were well removed from these local muscle insertion points, St. Venant's principle reassures that the net effect in the regions of peak strain should be the same. Finally, a few limitations are implicitly incorporated by the displacement boundary conditions. Specifically, the fixing of x and y displacements of the nodes in the distal end of the femur during fall loading eliminates rotational degrees of freedom at this end. *In vivo* conditions, by contrast, most likely allow some rotational compliance at the distal end of the femur. Clamping the distal end completely during the mid-stance simulation, when combined with zero displacement restrictions on the x and y degrees of freedom of the center of the head prevents the femur from assuming a more natural

configuration during loading. This boundary condition, however, was required in order to counter the torque on the femur due to the muscle forces. The requirement of equal displacement of the nodes in the head displacement region has the side-effect of restricting the rotational freedom of the head. Applying the displacement to a single node would have permitted rotation more freely, but would have resulted in extremely high stress concentrations close to the point of application.

More a point of uncertainty than a limitation relates to the use of the principal strain failure criteria in the model. As previously mentioned, this criterion was chosen based on the fact that it was found by Oden *et al.* (1999) to have the best correlation with their mechanical testing results. However, they only applied the criterion to trabecular bone and it is not clear how well it performs in relation to cortical bone. Nevertheless, its application to cortical bone, as well as trabecular bone, in this model was justified based on their success at predicting whole bone failure using the same criterion (Oden and Rosler, 1998). Another uncertainty stems from Kopperdahl and Keaveny's (1998) finding that while tensile yield strains are independent of apparent density, compressive yield strains appear to be linearly related to density. This indicates that the use of constant value strain limits for both tension and compression in the failure algorithm may be a limitation in the case of compression. However Kopperdahl and Keaveny acknowledge that the compression limit is approximately constant for narrow density ranges and it is not expected that a variable compression strain limit would have significantly affected the failure load of the model.

Despite these limitations, the modeling technique is believed to posses several strengths. The use of higher resolution pQCT image data; the use of a fine, tightly controlled mapped mesh; and the separation of cortical and cancellous regions permitted the creation of a model that is highly accurate in terms of reproducing the macroscopic geometry and density distribu-

tion of the actual femur. This accuracy was important to achieve, since without it the modelling of the subtle changes in geometry and the density changes associated with space flight would not be feasible. This capability is discussed further in the next chapter.

The failure loads obtained for the three loading conditions examined in this chapter may be compared with those reported elsewhere in the literature. The experimentally derived regression equation reported by Courtney *et al.* (1994, 1995) predicts a failure load during fall loading of approximately 6,000 N for a femur with a femoral neck BMD of 0.75 g/cm^2. The regression for a similar experimental study by Bouxsein *et al.* (1994) predicts a somewhat lower value of around 4,750 N for the same neck BMD. The failure load obtained in this chapter, for a model based on a femur with the same neck BMD and loading configuration as these two studies, about 4,390 N, is about 27% lower than the value predicted by Courtney *et al.*, but within 8% of the value predicted by Bouxsein *et al.* Other studies have obtained mean failure loads less than 4,000 N, but in a load configuration in which the load angle to the neck was 60 degrees (instead of 15 degrees) and the diaphysis angle to the horizontal was 30 degrees (instead of 10 degrees) (2110 N: Lotz *et al.*, 1990; 2933-3505 N: Weber *et al.*, 1992). The failure load obtained for the model in the mid-stance configuration (with muscle forces), 6,127 N, is quite a bit lower than the value of 7,233 N predicted by the regression equation of Beck *et al.* (1990), but closer to the mean value of 6,574 N obtained by Leichter *et al.* (1982) and somewhat higher than the median value of 5,490 N obtained by Alho *et al.* (1988). The failure load obtained for the model without muscle forces, 4,880 N, is still lower. It should be pointed out, however, that their stance configuration had the load vector aligned parallel to the diaphyseal axis and this would likely have produced a larger failure load than if the diaphysis had been inclined at an angle of 20.6 degrees.

An important observation yielded by the results in this chapter concerns the protective effect of muscle forces. As was seen, the application of muscle forces for the principal muscles active during the mid-stance phase of gait produced a 21% increase in the strength of the femur. Based on this result, we may predict that the reduction in muscle force due to space flight associated atrophy will be an important factor in determining the overall change in femoral strength due to weightlessness.

Another result that has bearing on space flight changes is the observation that the femoral breaking strength is significantly less in the fall configuration (39% less than mid-stance with muscles). Considering that the forces applied to the hip during a fall are much larger than those experienced during normal gait, it is not surprising that the vast majority (about 90%) of hip fractures are the result of a fall. This is also important in considering the risk of fracture during potential EVA on Mars, especially considering the reduced mobility and increased weight brought about by a space suit. These issues will be examined in much greater detail in the following two chapters.

3.5 References

Alho, A., Husby, T., and Hoiseth, A. (1988). "Bone mineral content and mechanical strength." *Clin Orthop Rel Res*, 227(2), 292-7.

Ashman, R. B., and Rho, J. Y. (1988). "Elastic modulus of trabecular bone material." *J Biomech*, 21(3), 177-181.

Ashman, R. B., Rho, J. Y., and Turner, C. H. (1989). "Anatomical variation of orthotropic elastic moduli of the proximal human tibia." *J Biomechanics*, 22(8/9), 895-900.

Bassey, E. J., Littlewood, J. J., and Taylor, S. J. (1997). "Relations between compressive axial forces in an instrumented massive femoral implant, ground reaction forces, and integrated electromyographs from vastus lateralis during various 'osteogenic' exercises." *J Biomech*, 30(3), 213-23.

Basu, P. K., Beall, A. G., Simmons, D. J., and Vannier, M. (1985-86). "3-D femoral stress analysis using CT scans and p-version FEM." *Biomater Med Devices Artif Organs*, 13(3-4), 163-86.

Beck, Mourtada, Ruff, Scott, J., and Kao. (1998). "Experimental testing of a dexa-derived curved beam model of the proximal femur." *Journal of Orthopaedic Research*, 16(3), 394-398.

Beck, S., Ruff, P., Warden, M., Scott Jr., M., and Rao, S. (1990). "Predicting femoral neck strength from bone mineral data a structural approach." *Investigative Radiology*, 25(1), 6-18.

Bouxsein, M. L., Courtney, A. C., and Hayes, W. C. (1994). "Ultrasound and densitometry of the calcaneus correlate with the failure loads of cadaveric femurs." *Calcif Tissue Int*, 56, 99-103.

Burstein, A. H., Currey, J. D., Frankel, V. H., and Reilly, D. T. (1972). "The ultimate properties of bone tissue: the effects of yielding." *J Biomech*, 5, 35-44.

Carter, D. R., and Hayes, W. C. (1976). "Bone compressive strength: the influence of density and strain rate." *Science*, 194, 1174-1175.

Carter, D. R., and Hayes, W. C. (1977). "The compressive behaviour of bone as a two-phase porous structure." *J Bone Jt Surg*, 59, 954-962.

Cezayirlioglu, H., Bahniuk, E., Davy, D. T., and Heiple, K. G. (1985). "Anisotropic yield behavior of bone under combined axial force and torque." *J Biomech*, 18(1), 61-9.

Cheal, E. J., Spector, M., and Hayes, W. C. (1992). "Role of loads and prosthesis material properties on the mechanics of the proximal femur after total hip arthoroplasty." *J Orthop Res*, 10(3), 405-422.

Courtney, A. C., Wachtel, E. F., Myers, E. R., and Hayes, W. C. (1995). "Age-related reductions in the strength of the femur tested in a fall loading configuration." *J Bone Joint Surg (Am)*, 77, 387-395.

Courtney, A. C., Wachtel, E. F., Myers, E. R., and Hayes, W. C. (1994). "Effects of loading rate on strength of the proximal femur." *Calcif Tissue Int*, 55, 53-58.

Dalen, N., Hellstrom, L., and Jacobson, B. (1976). "Bone mineral content and mechanical strength of the femoral neck." *Acta Orthop Scand*, 47, 503-508.

Duda, G. N., Heller, M., Albinger, J., Schultz, O., Schneider, E., and Claes, L. (1998). "Influence of muscle forces on femoral strain distribution." *J Biomech*, 31(9), 841-6.

Eriksson, S. A. V., Isberg, B. O., and Lindgren, J. U. (1989). "Prediction of vertebral strength by dual photon absorptiometry and quantitative computed tomography." *Calcif Tissue Int*, 44, 243-250.

Ford, C. M., Keaveny, T. M., and Hayes, W. C. (1996). "The effect of impact direction on the structural capacity of the proximal femur during falls." *J Bone Min Res*, 11(3), 377-383.

Gibson, L. J. (1985). "The mechanical behaviour of cancellous bone." *J Biomech*, 18(5), 317-28.

Goldstein, S. A. (1987). "The mechanical properties of trabecular bone: dependence of anatomic location and function." *J Biomechanics*, 20(11/12), 1055-1061.

Hansson, T., Roos, B., and Nachemson, A. (1980). "The bone mineral content and ultimate compressive strength of lumbar vertebrae." *Spine*, 5(1), 46-55.

Harrigan, T. P., Jasty, M., Mann, R. W., and Harris, W. H. (1988). "Limitations of the continuum assumption in cancellous bone." *J Biomechanics*, 21(4), 269-275.

Huiskes, R., and Chao, E. Y. (1983). "A survey of finite element analysis in orthopedic biomechanics: the first decade." *J Biomech*, 16(6), 385-409.

Keyak, J. H., Fourkas, M. G., Meagher, J. M., and Skinner, H. B. (1993). "Validation of an automated method of three-dimensional finite element modelling of bone." *J Biomed Eng*, 15(6), 505-9.

Keyak, J. H., Meagher, J. M., Skinner, H. B., and Mote, C. D., Jr. (1990). "Automated three-dimensional finite element modelling of bone: a new method." *J Biomed Eng*, 12(5), 389-97.

Keyak, J. H., Rossi, S. A., Jones, K. A., and Skinner, H. B. (1998). "Prediction of femoral fracture load using automated finite element modeling." *J Biomech*, 31(2), 125-33.

Keyak, J. H., and Skinner, H. B. (1992). "Three-dimensional finite element modelling of bone: effects of element size." *J Biomed Eng*, 14(6), 483-9.

Kopperdahl, D. L., and Keaveny, T. M. (1998). "Yield strain behavior of trabecular bone." *J Biomech*, 31(7), 601-8.

Leichter, I., Margulies, J. Y., Weinreb, A., Mizrahi, J., Robin, G. C., Conforty, B., Makin, M., and Bloch, B. (1982). "The relationship between bone density, mineral content, and mechanical strength in the femoral neck." *Clin Orthop Rel Res*, 163(3), 272-81.

Lengsfeld, M., Kaminsky, J., Merz, B., and Franke, R. P. (1994). "[Automatic generation of 3-D finite element codes of the human femur]." *Biomed Tech (Berl)*, 39((5)), 117-22.

Lengsfeld, M., Kaminsky, J., Merz, B., and Franke, R. P. (1996). "Sensitivity of femoral strain pattern analyses to resultant and muscle forces at the hip joint." *Med Eng Phys*, 18(1), 70-8.

Lengsfeld, M., Schmitt, J., Alter, P., Kaminsky, J., and Leppek, R. (1998). "Comparison of geometry-based and CT voxel-based finite element modelling and experimental validation." *Med Eng Phys*, 20(7), 515-22.

Lotz, J. C., Cheal, E. J., and Hayes, W. C. (1991a). "Fracture prediction for the proximal femur using finite element models: Part I: Linear analysis." *J Biomech Eng*, 113(4), 353-60.

Lotz, J. C., Cheal, E. J., and Hayes, W. C. (1991b). "Fracture prediction for the proximal femur using finite element models: Part II: Nonlinear analysis." *J Biomech Eng*, 113(4), 361-5.

Lotz, J. C., Cheal, E. J., and Hayes, W. C. (1995). "Stress distributions within the proximal femur during gait and falls: implications for osteoporotic fracture." *Osteoporos Int*, 5(4), 252-261.

Lotz, J. C., Gerhart, T. N., and Hayes, W. C. (1990). "Mechanical properties of trabecular bone from the proximal femur: a quantitative CT study." *J Comp Assist Tomog*, 14, 107-114.

Merz, B., Niederer, P., Muller, R., and Ruegsegger, P. (1996). "Automated finite element analysis of excised human femora based on precision -QCT." *J Biomech Eng*, 118(3), 387-90.

Mourtada, F. A., Beck, T. J., Hauser, D. L., Ruff, C. B., and Bao, G. (1996). "Curved beam model of the proximal femur for estimating stress using dual-energy x-ray absorptiometry derived structural geometry." *J Orthop Res*, 14(3), 483-492.

Oden, Z. M. (1994). "Computational prediction of functional adaptation in canine radii," Ph.D. Dissertation, Tulane University, New Orleans.

Oden, Z. M., and Rosler, D. M. (1998). "Finite element prediction of femoral failure load." *Ann Biomed Eng*, 26(S1), 78.

Oden, Z. M., and Selvitelli, D. M. (1998) "Modeling failure of trabecular bone." *Trans. 44th ORS*, 23:113.

Oden, Z. M., Selvitelli, D. M., and Bouxsein, M. L. (1999). "Effect of local density changes on the failure load of the proximal femur." *J Orthop Res*, Accepted 2/28/99.

Oonishi, H., and Hasegawa, T. (1982). "Two-dimensional finite element method analysis of the proximal end of the femur." *Nippon Seikeigeka Gakkai Zasshi*, 56(5), 431-7.

Pinilla, Boardman, Bouxsein, Myers, and Hayes. (1996). "Impact direction from a fall influences the failure load of the proximal femur as much as age-related bone loss." *Calcified Tissue International*, 58, 231-235.

Reilly, D. T., Burstein, A. H., and Frankel, V. H. (1974). "The elastic modulus for bone." *J Biomech*, 7, 271-275.

Reilly, D. T., and Burstein, A. H. (1975). "The elastic and ultimate properties of compact bone tissue." *J Biomech*, 393-405.

Rice, J. C., Cowin, S. C., and Bowman, J. A. (1988). "On the dependence of the elasticity and strength of cancellous bone on apparent density." *J Biomech*, 21(2), 155-168.

Rohlmann, A., Begmann, G., and Kolbel, R. (1980). "[Finite element analysis, its limitations and the relevance of its results to orthopaedic surgery as shown by simultaneous experimental measurements]." *Z Orthop*, 118(1), 122-31.

Rohlmann, A., Bergmann, G., and Kolbel, R. (1981). "[The stresses in femur]." *Z Orthop*, 119(2), 163-6.

Rohlmann, A., Mossner, U., Bergmann, G., and Kolbel, R. (1982). "Finite-element-analysis and experimental investigation of stresses in femur." *J Biomed Eng*, 4(3), 241-6.

Schmitt, J., Lengsfeld, M., Alter, P., and Leppek, R. (1995). "[Use of voxel-oriented femur models for stress analysis. Generation, calculation and validation of CT-based FEM models]." *Biomed Tech (Berl)*, 40(6), 175-81.

Selvitelli, D. M. (1997). "Finite element modeling of bone failure." M.S. Thesis, Dept. of Biomedical Engineering , Boston University, Boston.

Snyder, S. M., and Schneider, E. (1991). "Estimation of mechanical properties of cortical bone by computed tomography." *J Orthop Res*, 9, 422-431.

Taylor, M. E., Tanner, K. E., Freeman, M. A., and Yettram, A. L. (1996). "Stress and strain distribution within the intact femur: compression or bending." *Med Eng Phys*, 18(2), 122-31.

Testi, D., Viceconti, M., Baruffaldi, F., and Cappello, A. (1999). "Risk of fracture in elderly patients: a new predictive index based on bone mineral density and finite element analysis." *Comput Methods Programs Biomed*, 60(1), 23-33.

Van der Sloten, J., and Van der Perre, G. (1995). "The influence of geometrical distortions of three-dimensional finite elements, used to model proximal femoral bone." *Proc Inst Mech Eng [H]*, 209(1), 31-6.

Viceconti, M., Bellingeri, L., Cristofolini, L., and Toni, A. (1998). "A comparative study on different methods of automatic mesh generation of human femurs." *Med Eng Phys*, 20(1), 1-10.

Viceconti, M., Zannoni, C., Testi, D., and Capello, A. (1999a). "A new method for the automatic mesh generation of bone segments from CT data." *J Med Eng Tech*, 23(2), 77-81.

Viceconti, M., Zannoni, C., Testi, D., and Cappello, A. (1999b). "CT data sets surface extraction for biomechanical modeling of long bones." *Comput Methods Programs Biomed*, 59(3), 159-66.

Weber, T. G., Yang, K. H., Woo, R., and Fitzgerald, R. H. (1992). "Proximal femur strength: Correlation of the rate of loading and bone mineral density." *ASME Adv Bioeng*, 22, 111-114.

Zannoni, C., Mantovani, R., Viceconti, M. (1998). "Material properties assignment to finite element models of bone structures: a new method." *Med Eng Phys*, 20(10), 735-40.

CHAPTER 4

Modeling Structural Differences in the Proximal Femur Associated with Space Flight Adaptation and Gender

Make voyages. Attempt them. There's nothing else.
— Tennesee Williams

The previous chapter discussed modeling the structural properties of the proximal femur using three-dimensional finite element analysis. This chapter extends the modeling approach to account for the geometric and density changes observed in the proximal femur as a result of weightlessness during spaceflight. In particular, the intention was to determine the impact that combined endosteal absorption and decreased cancellous bone mineral density have on proximal femur strength. For the mid-stance loading condition the effect of muscle strength loss during space flight was also modeled in the analysis. In addition, an estimate of the failure load for mid-stance and falls in females was obtained through a scaling of the male finite element models.

4.1 Background

As mentioned in Chapter 1, there is considerable evidence that astronauts experience a loss of bone mineral density in critical weight-bearing areas as a result of the skeletal unloading associated with weightlessness. Oganov *et al.* (1992) reported that in 4.5 to 6 month stays on the Mir space station, cosmonauts lost as much as 14% of the bone mineral density in the

neck and trochanteric region. A 17 week bed rest study by LeBlanc *et al.* (1990) found that bone mineral density in the femoral neck decreased at a rate of 0.21 ± 0.05% per week while the density in the trochanteric region decreased at a rate of 0.27 ± 0.05% per week.

The space flight alterations modeled in this chapter are based on recent experimental data results obtained by Beck and Ruff (1999), whose analysis of BMD (areal bone mineral density, equal to the mass of bone mineral for a region divided by the region's projected area) from cosmonauts who spent several months in microgravity on Mir suggests a structural alteration in the proximal femur not specifically addressed in previous studies. In addition to overall density loss, it appears that thinning of the cortical shell occurs in the neck, trochanteric and diaphyseal regions. This thinning is reflected by an increase in average endosteal diameter (assumed to be due to endosteal absorption of bone by osteoclasts) at rates of 0.5%, 0.2%, and 0.3% per month for the diaphysis, trochanteric region, and neck, respectively, without any significant increase in average periosteal (outside) diameter (Figure 4.1). The same analysis found that the mean rates of BMD loss in the neck, trochanteric and diaphyseal regions were 1.3%, 1.4% and 0.8% per month, respectively, with very similar changes in section modulus. The minimum, mean and maximum values for rate of change of BMD and endosteal diameter are presented in Table 4.1. A summary of long term changes in BMD associated with weightlessness is provided in Table 4.2.

Not previously mentioned is that muscle strength decreases during space flight due to the reduced physical exertion required to move about in weightlessness (Kozlovskaia et al., 1984; Grogor'eva and Kozlovskaia, 1987). Muscle atrophy, reflected by a reduction in cross-sectional area, is accompanied by reduced neural drive and a general shift in fiber type from slow-twitch oxidative toward fast twitch glycolitic due to reduced load bearing in weightlessness (Desplanches, 1997). Reduction in muscle fiber cross-sectional area of as much as 11-

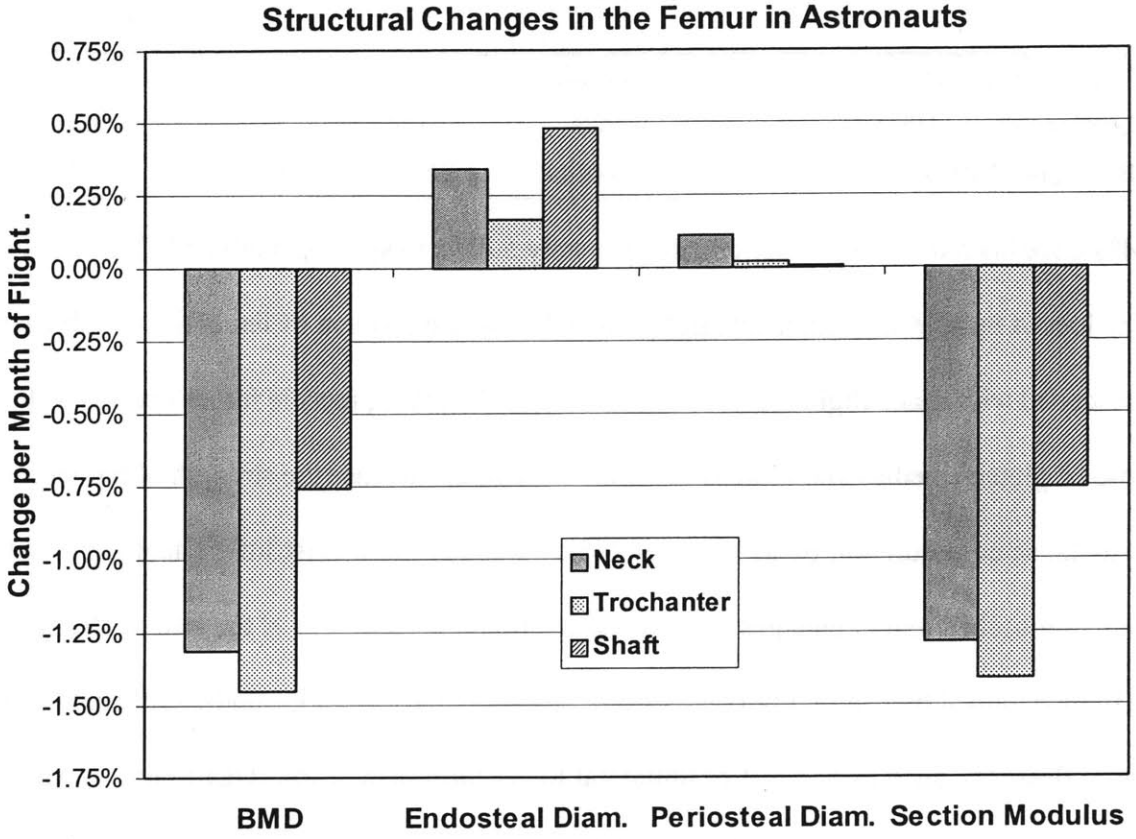

Figure 4.1: Values derived from DXA data on 20 cosmonauts, 7 with data from 2 flights, 27 flights total. BMD and Section Modulus exhibit approximately equal rates of change ranging from -0.75% to -1.50%. Most importantly, the rates of change in endosteal diameter are not offset by corresponding changes in the periosteal diameter, leading to a thinning of the cortical shell.
Source: Beck, T.J., Dept. of Radiology, Johns Hopkins University School of Medicine.

Table 4.1 Minimum, mean and maximum values for rate of change of BMD and endosteal diameter. Note: Maximum is negative for BMD and positive for endosteal diameter. Source: Beck, T.J., Dept. of Radiology, Johns Hopkins University School of Medicine

Parameter	Minimum (%/month)	Mean (%/month)	Maximum (%/month)
Neck BMD	1.7	-1.3	-3.8
Trochanteric BMD	0.2	-1.4	-3.6
Shaft BMD	0.0	-0.8	-1.6
Neck Endosteal Diam.	-2.5	0.3	2.7
Trochanteric Endosteal Diam.	-0.4	0.2	0.9
Shaft Endosteal Diam.	-1.7	0.5	1.8

Table 4.2 Comparison of studies assessing long term BMD losses in the femoral neck.

Study	Duration	BMD Loss	BMD Loss (%/week)
Oganov *et al.*, 1992	4.5–6 months	14% (neck)	0.54
LeBlanc *et al.*, 1990	17 weeks	3.6% (neck)	0.21
Beck and Ruff, 1999	4–10 months	1.25%/mnth (neck)	0.29

24% have been observed in astronauts after only 5 days in space (Booth and Criswell, 1997). The loss of muscle strength is integrally related to the assessment of femoral strength changes associated with space flight since, as was shown in Chapter 3, muscle forces exerted by the iliopsoas, gluteus medius and gluteus minimus are able to increase the strength of the femur in a mid-stance configuration by as much as 26%. Although there exist little quantitative data on human muscle strength changes in actual space flight, an estimate of the rate of strength loss may be obtained by examining results from various studies using ground-based analogues for weightlessness, such as bed rest or unilateral lower limb suspension (ULLS, performed using both humans and animals). LeBlanc *et al.* (1988) performed a 10 week bed rest study involving 5 weeks of ambulatory control and 5 weeks of complete horizontal bed rest and found that the maximal muscle strength of the plantar flexors (gastrocnemius and soleus) decreased by 26%. Dudley *et al.* (1989) examined the musculature of the knee and found an average decrease in the peak torque of 19% in the extensor muscle group following 30 days of 6 degree head-down bed rest (a popular simulation of the weightlessness of space flight). The strength of flexor muscles appeared to be unaffected. Berg *et al.* (1991) used 4 weeks of ULLS to examine changes in the quadriceps group of humans. They found that the peak torque decreased by 16–22%, while cross-sectional area decreased by 7%. Germain *et al.* (1995) found a slightly lower reduction (-10.3%) in the strength of the quadriceps during 28 days of head-down bed rest. Bamman *et al.* (1997, 1998) report that 14 days of bed rest reduced the one-repetition maximum strength of both the plantar flexors and knee extensors

by 9% and reduced concentric and eccentric strength in the same groups by 15-17%. Long-term effects were assessed by Koryak (1998, 1999) in a 120-day head-down bed rest study. The group of 6 male subjects (mean age 38 ± 2 years) exhibited a decrease in maximum voluntary contraction of 46% and a decrease in maximum strength of 34%. Furthermore, Antonutto *et al.* (1999) found that mean explosive power was reduced to 67% after 31 days, and to 45% after 180 days of space flight in the Mir space station. In general, 4-6 week bed rest studies have been found to decrease the strength of the quadriceps by 20-25% (Dudley *et al.*, 1992) and that of other muscles in the lower limb by as much as 40% (Bloomfield, 1997). The results of these studies, in terms of changes in muscle strength, are summarized in Table 4.3.

Table 4.3 Summary of muscle strength changes associated with unloading during space flight weightlessness and Earth-based analogs.

Condition/ Environment	Duration	Strength Change	Strength Change (%/week)	Muscle Group	Study
Bed Rest	10 wks	-26%	-2.6	plantar flexors	LeBlanc *et al.*, 1988
Bed Rest	30 days	-19%	-4.4	knee extensors	Dudley *et al.*,1989
ULLS	4 wks	-16% to -22%	-4.0 to -5.5	quadriceps	Berg *et al.*, 1991
Bed Rest	28 days	-10.3%	-2.6	quadriceps	Germain *et al.*, 1995
Bed Rest	14 days	-15% to -17%	-7.5 to -8.5	plantar flexors knee extensors	Bamman *et al.*, 1997, 1998
Bed Rest	120 days	-34% to -46%	-2.0 to -2.7		Koryak, 1998, 1999
Space Flight	180 days	-55%	-2.1		Antonutto et al., 1999

4.2 Methods

Femoral strength was assessed for three durations of exposure to weightlessness: 0 months (the baseline femur, already analyzed in Chapter 3), 6 months (representing a space station mission or a midpoint on the journey to Mars), and 12 months (representing arrival to Mars or a long duration space station mission). It should be emphasized that 12 months was not considered a realistic time for a return mission to Mars.

The method used herein to model the increase in endosteal diameter was as follows. The three-dimensional coordinates describing the endosteal surface curves (from CT slices processed in NIH Image) were read into a specifically written computer program (see Appendix D). The centroid for each curve was calculated and then used to determine the average radius

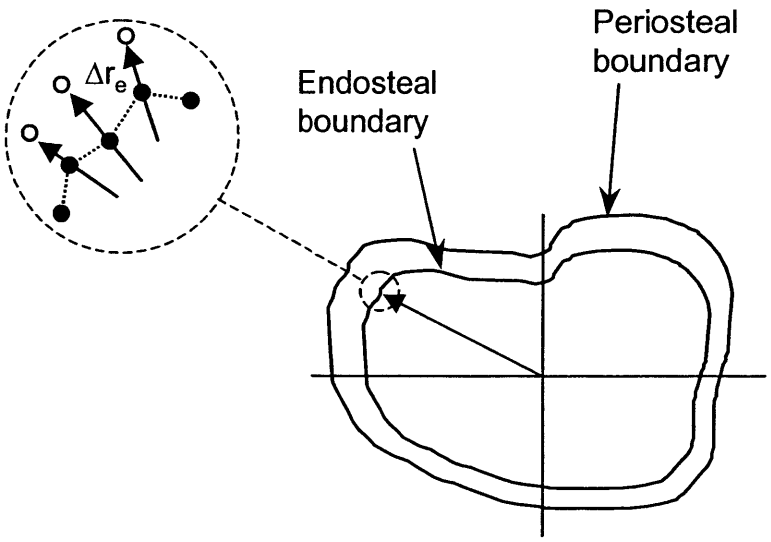

Figure 4.2: Method of increasing endosteal diameter to model space flight changes. (Described in text.)

to all the related points. Next, the values for endosteal radius expansion (mentioned above) were used to obtain the magnitude of point displacement, $|\Delta r_e|$, according to the relation:

$$|\Delta r_e| = (dr) n_m \bar{r} \tag{4.1}$$

where dr is the percent expansion per month, with the appropriate value used according to whether the curve was located in the diaphysis, the trochanteric region, or the neck, n_m is the number of months of weightlessness, and $\bar{r}$ is the average radius. No change in the curves for the endosteal surface of the femoral head was determined since no data were available for this region and since it is not expected that there would be a significant amount of endosteal absorption in the head given that stress is well distributed in the head during Earth gravity

loading and well below the levels attained in the neck and trochanteric regions. To complete the vector describing the point displacement, the direction was determined by bisecting the angle defined by the lines connecting the point in question to each of the neighboring points. In cases where the three points were in direct alignment, the bisecting angle was set at 90 degrees.

Once the new endosteal curves had been defined according to the duration of weightlessness, a modified finite element model was created in I-DEAS using the technique described in Chapter 3. The adjusted model was constructed to the point of mesh completion and element groups were defined in correspondence with the regions used in a standard DXA analysis, that is, head, neck, trochanteric (DXA "trochanteric" and "intertrochanteric" regions combined) and diaphysis. These element groups were further subdivided into cortical and medullary (cancellous or trabecular) groups (sub-volumes) using the endosteal surface partition (described in previous chapter) (Figure 4.3). The model was then exported to ABAQUS and analyzed to determine the location and volume of each element. In a separate FORTRAN program, the density, ρ_e, of each element in the neck cortex and trochanteric cortex groups was multiplied by the corresponding element volume, v_e, and then summed to produce the total bone mineral content (BMC, the mass of bone mineral in a region) for each of the two groups:

$$\begin{aligned} (\mathrm{BMC})_{\mathrm{nc}} &= \sum(\rho_e v_e)_{\mathrm{nc}} \\ (\mathrm{BMC})_{\mathrm{tc}} &= \sum(\rho_e v_e)_{\mathrm{tc}} \end{aligned} \tag{4.2}$$

where the subscripts 'nc' and 'tc' refer to the neck cortex and trochanteric cortex, respectively. The change in BMC (in grams) for the particular sub-volume was calculated by com-

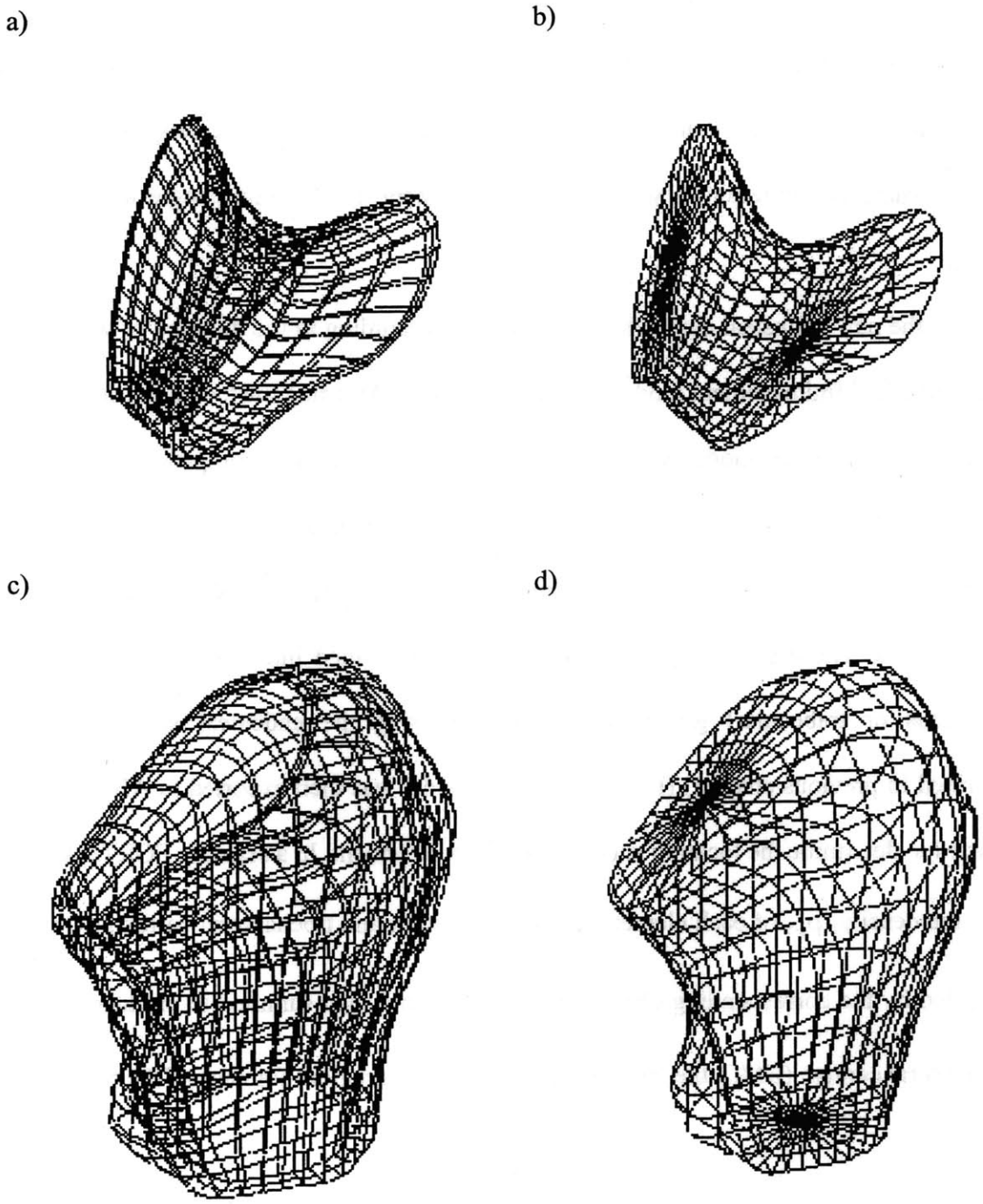

Figure 4.3: Cortical and medullary (cancellous) element sub-volumes defined for calculating changes in bone mineral content related to bone resorption at the endosteal surface. The four sub volumes shown are: a) neck cortex, b) neck medulla, c) trochanteric cortex, and d) trochanteric medulla.

paring the BMC at the given duration of weightlessness with the baseline (0 month) value. For instance, for the 12 month duration case, the ΔBMC was:

$$(\Delta BMC)_{nc12} = (BMC)_{nc12} - (BMC)_{nc0}$$
$$(\Delta BMC)_{tc12} = (BMC)_{tc12} - (BMC)_{tc0} \tag{4.3}$$

To get the total change in BMC (in grams) for a region (combined cortex and medulla), the ΔBMD reported by Beck and Ruff (Figure 4.1) was multiplied by the number of months and the projected area of the region, A_p:

$$(\Delta BMC)_n = (\Delta BMD)_n A_{np}$$
$$(\Delta BMC)_t = (\Delta BMD)_t A_{tp} \tag{4.4}$$

The change in BMC for the corresponding cortex sub-volume was then subtracted from the total BMC change and the result divided by the volume of the medulla group (after moving the endosteal boundary), V_m, to get the average density reduction for the elements in the particular sub-volume:

$$\Delta\bar{\rho}_{nm} = ((\Delta BMC)_n - (\Delta BMC)_{nc})/V_{nm}$$
$$\Delta\bar{\rho}_{tm} = ((\Delta BMC)_t - (\Delta BMC)_{tc})/V_{tm} \tag{4.5}$$

Finally, the average density was subtracted from all of the element densities in the corresponding medulla sub-volume and the resulting density used to calculate each elements modulus according to the relations given in Chapter 3.

The space flight related change in BMD for the diaphysis was modeled as an increase in endosteal diameter alone (since the medulla is largely void of cancellous bone in the diaphysis) and the densities of the elements in the medulla were not altered. In addition, no changes were modeled in the head region due to the lack of data from this region and the assumption that no significant changes in density occur.

The baseline muscle forces (given in Chapter 3) were reduced according to the duration of weightlessness as:

6 months: -40%

12 months: -60%

These values are intentionally conservative compared to the values reported in previous studies (for instance, Antonutto *et al.* (1999) reported a reduction in maximal explosive power of 55% after only 6 months) in order to avoid underestimating the strength of the femur in mid-stance loading, and to account for the fact that no studies have thus far given a value for muscle strength loss for space flight missions up to 12 months.

Given that a significant fraction of the astronaut corps are women, it was desirable to calculate failure loads applicable to women. Applied loads, already calculated in Chapter 2 for locomotion and falls in the female population, could then be combined with corresponding failure loads to obtain the factor of risk for hip fracture in the females (Chapter 5). Since the finite element model described in the last chapter was based on a male femur, a rough estimation of structural differences associated with gender was performed by scaling the male femur model. The scale factor was determined by comparing the lengths of the upper leg for males and females as provided by GEBOD for the dynamic analysis in Chapter 2. Using this approach, all three male finite element models (0 month, 6 month, and 12 month) were scaled by a factor of 0.977.

4.3 Results

Figure 4.4, Figure 4.5, and Figure 4.6 show the change in the endosteal boundary for the femoral neck, trochanteric region, and diaphysis, respectively, following 12 months of space-

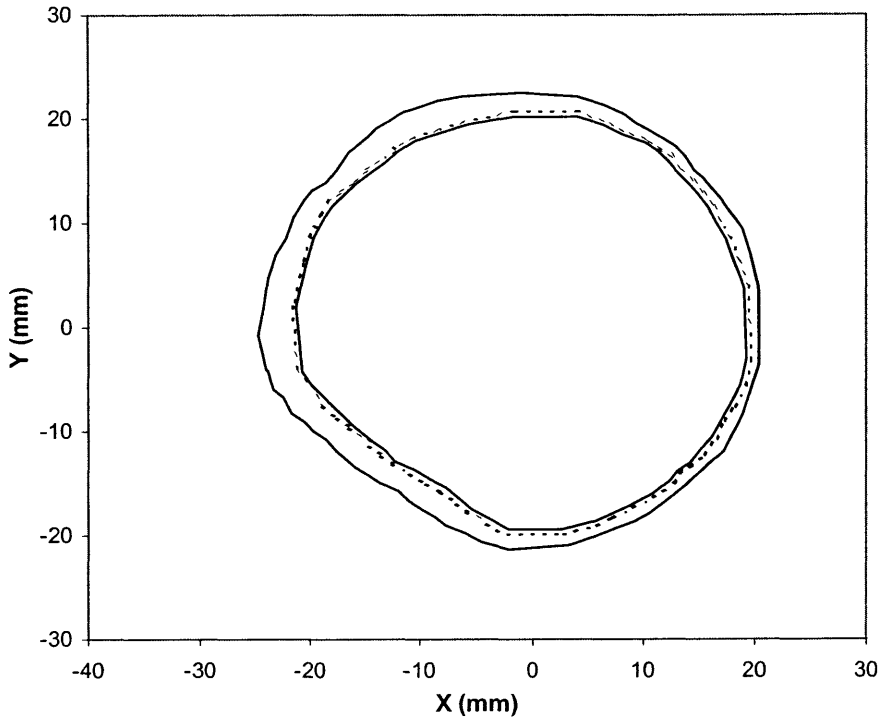

Figure 4.4: Space flight modified endosteal boundary in femoral neck.

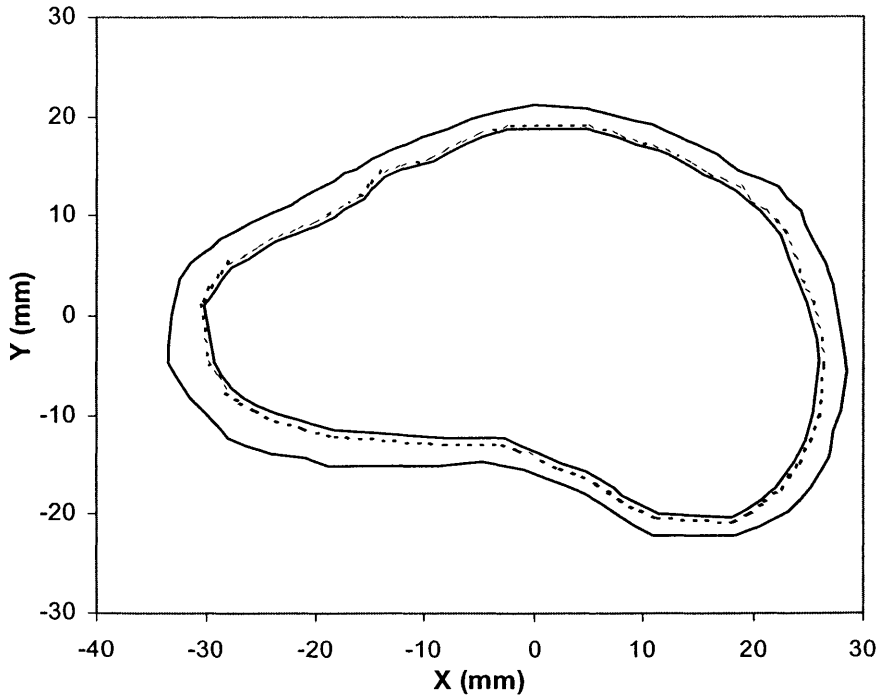

Figure 4.5: Space flight modified endosteal boundary in trochanteric region.

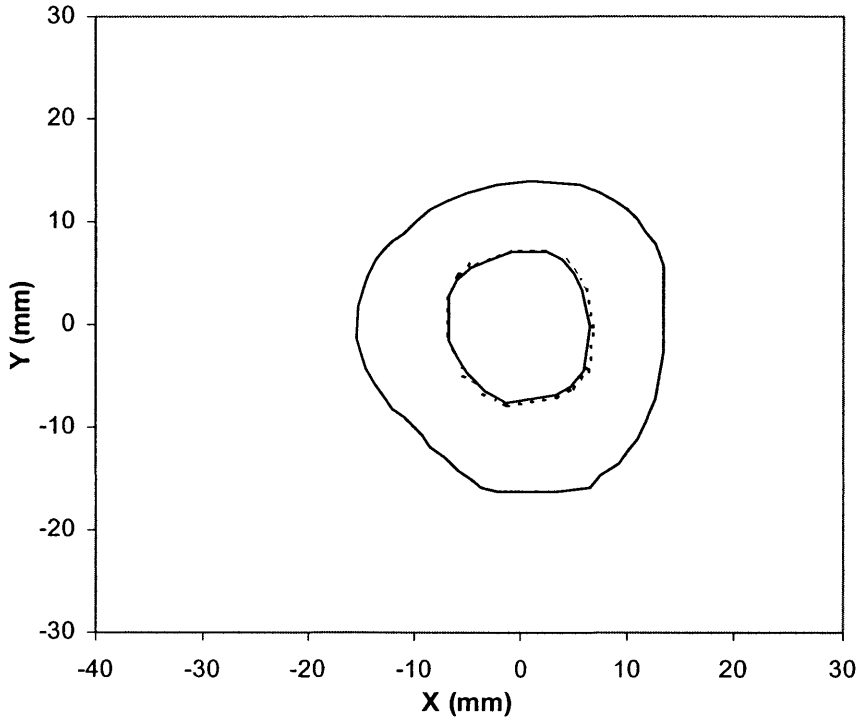

Figure 4.6: Space flight modified endosteal boundary in diaphysis.

flight. The changes in the trochanteric and neck regions, while not dramatic in terms of absolute displacement of the endosteal boundary, represent a significant fraction of the thickness of the cortical shell (5% to 20%, depending upon location along the circumference of the slice). The change in thickness of the cortical shell in the diaphysis (Figure 4.4c), however, was not very significant.

The changes in bone mineral content and the average density reduction for the medullary elements of the neck and trochanteric regions are given in Table 4.4 according to the two durations of weightlessness examined. The fraction of bone mineral content loss in the medulla (vs the BMC loss for the entire region) was 34% for the neck and 58% for the trochanteric region after 6 months of weightlessness; and 39% for the neck and 57% for the trochanteric region after 12 months of weightlessness. Geometric data for the femur models is included in Table 4.5.

Table 4.4 Changes in BMC and medullary element average density following 6 months and 12 months of weightlessness

Parameter	Trochanteric (6 months)	Neck (6 months)	Trochanteric (12 months)	Neck (12 months)
Change in BMC due to endosteal resorp. (g)	-1.12	-0.43	-2.30	-0.84
Total change in BMC (from areal BMD) (g)	-2.66	-0.69	-5.33	-1.39
Change in BMC for medulla (g)	-1.54	-0.26	-3.03	-0.54
Density change in medulla (g/cm^3)	-2.17E-02	-1.43E-02	-4.20E-02	-2.90E-02
Average Density Change for total region (g/cm^3)	-2.74E-02	-2.84E-02	-5.48E-02	-5.73E-02

Table 4.5 Geometric data for calculating medulla element density adjustment

Region	Volume (cm^3)	Projected Area (cm^2)
Neck Cortex (0 months)	6.32	–
Neck Medulla(0 months)	17.95	–
Troch. Cortex (0 months)	27.26	–
Troch. Medulla (0 months)	69.97	–
Neck Cortex (6 months)	5.93	–
Neck Medulla(6 months)	18.34	–
Troch. Cortex (6 months)	26.21	–
Troch. Medulla (6 months)	71.04	–
Neck Cortex (12 months)	5.51	–
Neck Medulla(12 months)	18.75	–
Troch. Cortex (12 months)	25.10	–
Troch. Medulla (12 months)	72.16	–
Total Neck	24.27	8.89
Total Trochanteric	97.24	30.62

A plot of reaction force versus displacement for the central node in the area of displacement application at the head is shown in Figure 4.7 for the case of mid-stance (male femur model). The three curves represent the reaction force at the head in the case of the baseline (0 month) femur, 12 months of spaceflight, and the baseline femur without muscle forces

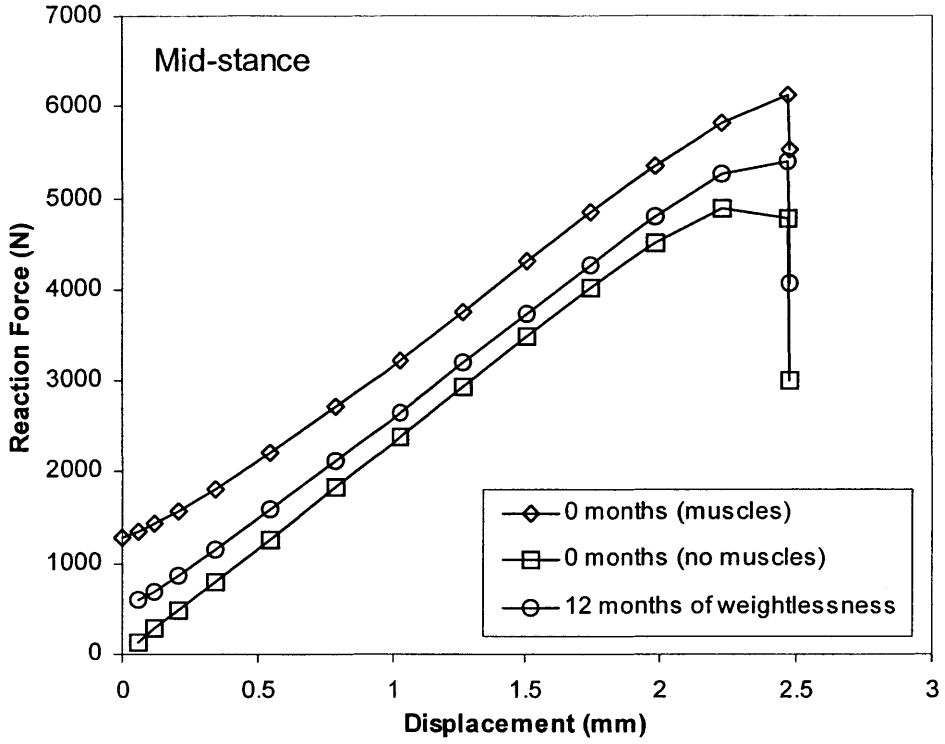

Figure 4.7: Reaction force versus displacement for mid-stance loading.

applied. The 0 and 12 month curves are observed to start out with an initial preloading (approximately 1,200 N and 500 N, respectively) due to the fact that the muscle forces were first ramped to their maximum levels before the displacement ramp at the head was applied (a 2 step analysis protocol). As mentioned in Chapter 3, the failure load was taken to be the peak reaction force achieved in each case. Examining the pre-flight versus post-flight plots (0 months versus 12 months), there was a 12% reduction in failure load (from 6,130 N to 5,390 N). The complete absence of muscle forces in the baseline model led to a 26% reduction in failure load. All three curves display the typically abrupt failure seen in the last increment due to the large number of elements failing.

The reaction force versus displacement curves for the 0 month and 12 month conditions in the fall loading configuration are compared in Figure 4.8 (male femur model). The failure

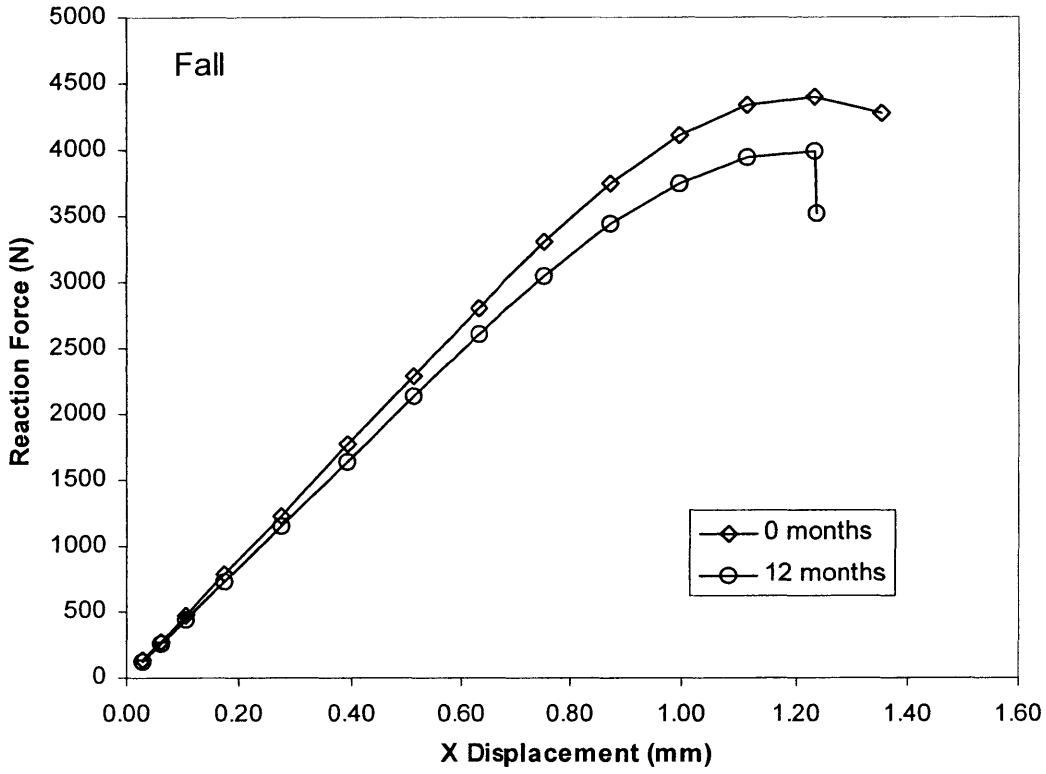

Figure 4.8: Reaction force versus displacement for fall loading.

load decreased by 9% in this case and both curves pass through (0,0) since no muscle forces were applied during fall loading.

A chart showing failure load versus duration of weightlessness for all mid-stance analyses is presented in Figure 4.9. The female values were approximately 4-5% below the corresponding male failure load values in all cases. The decline in femoral strength appears to be less during the second 6 months than during the first. This difference is almost certainly due to the fact that the muscle forces decline by 40% during the first 6 months, but only by 20% during the second 6 months, according to the model of muscle strength loss used.

The decline in femoral strength in a fall loading according to duration of weightlessness is shown in Figure 4.10. The decline in femoral strength in this case is clearly linear, and confirms the suspicion that the changing rate of strength decline in the mid-stance case is driven

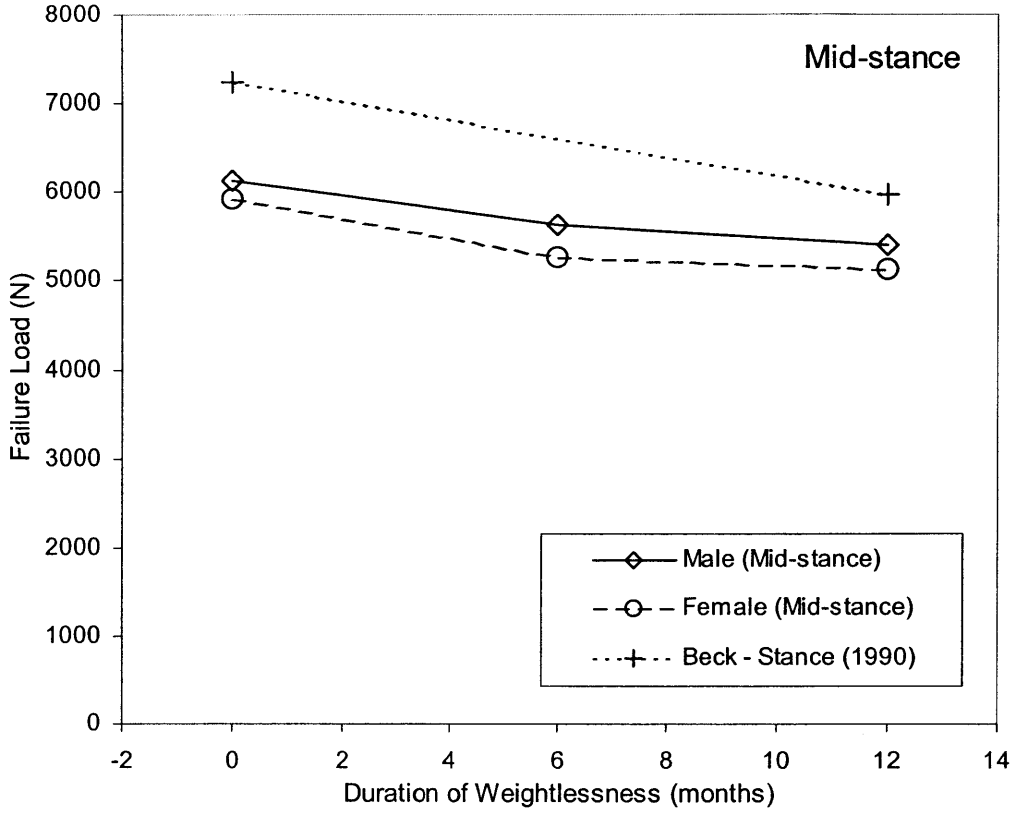

Figure 4.9: Failure load versus duration of weightlessness for all mid-stance analyses.

by the unequal rates of muscle strength decline (since muscle forces were not applied in the fall loading).

4.4 Discussion

The failure load values obtained in the mid-stance analyses were somewhat low compared to the results obtained by Beck *et al.* (1990) for mechanical test of femora with varying BMD levels (non-space flight). Furthermore, the mean age for the donors in their study was 65 years and thus the difference in failure may be greater if the model predictions are compared to specimens from donors of a comparable age (36 years). It should also be noted that, the over-

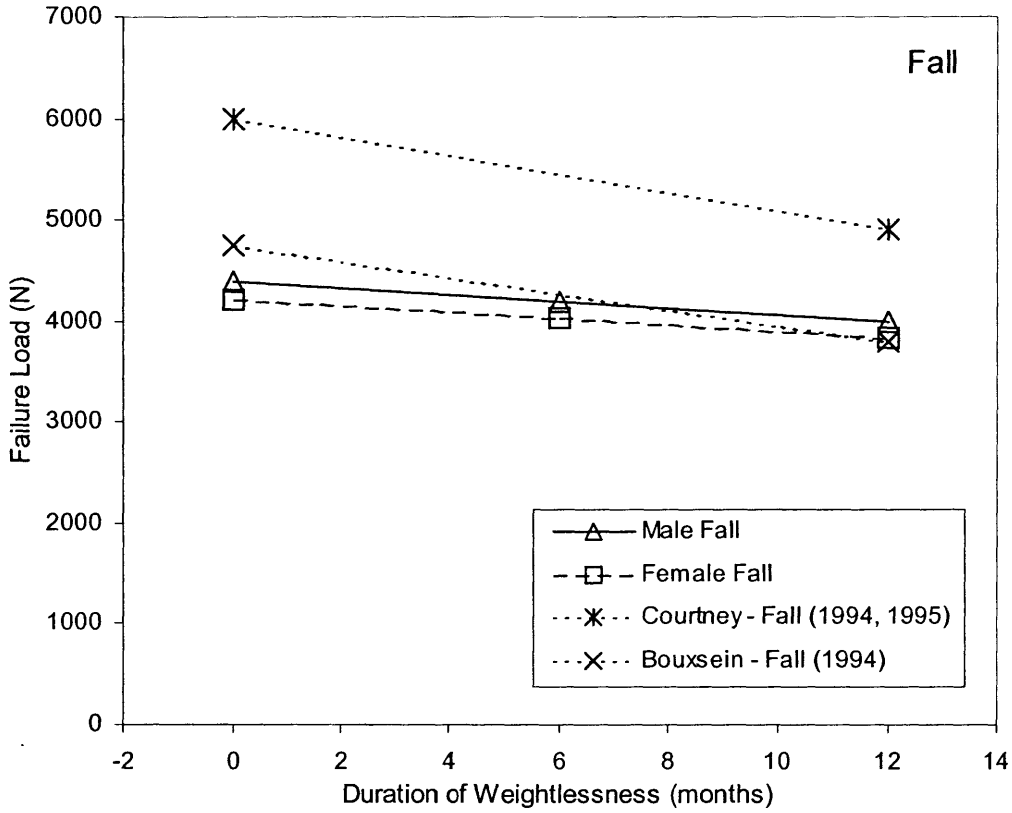

Figure 4.10: Decline in femoral strength in fall loading according to duration of weightlessness.

all rate of decline in femoral strength for the model over 12 months of space flight (1.0% per month) is markedly less than that predicted by Beck's correlation (1.5% per month). However, Beck *et al.*'s results represent cross-sectional differences in strength, as correlated to BMD, and do not necessarily reflect space flight longitudinal changes. In addition, the low values obtained from the model are less surprising, when one considers that the baseline BMD values for the femur on which all analyses herein are based were significantly below average for the age of the donor (36 year old male). In fact the value for femoral neck BMD at baseline (0.75 gm/cm^2) is just barely above the cutoff point for osteopenia according to the WHO diagnostic criteria (Looker *et al.*, 1995a, 1995b).

There was a relatively good correspondence between the fall failure load values and those obtained in the mechanical testing performed by Bouxsein *et al.* (1994) (neck BMD values for the model femur at baseline and after 12 months were substituted into the relevant regression equations to obtain the comparison curves). The values for the latter, however, were obtained from elderly donors (mean age of 76 years) and thus should be well below the values obtained from the model. This is clearly evident in comparing the same failure load values to those derived by Courtney *et al.* (1994, 1995) who carried out their testing on femora from young adult donors. As in the mid-stance results (Figure 4.9), there was a marked difference in the rate of decline in femoral strength for the model (0.8% per month) compared to the rate of decline in strength predicted by BMD correlations (1.5% per month for both Courtney et al., (1994,1995) and Bouxsein et al., (1994))

The principal contribution of the work described in this chapter is the development of a technique to accurately and explicitly model cortical and cancellous bone as separate volumes in a finite element model of the proximal femur. This type of explicit modeling of the cortical shell in the proximal femur has not been done before, previous finite element models having relied instead on a density threshold to distinguish between cortical and cancellous bone. A further strength of the finite element modeling technique discussed herein is that it facilitates adjustment of cortical shell geometry (expansion or contraction of endosteal and periosteal diameters). This ability has important application, not only in the analysis of strength changes associated with weightlessness in astronauts, but also in analyzing strength changes due to adjustments in cross-sectional geometry of the proximal femur in elderly individuals.

As mentioned previously, the desire to separate cortical and cancellous volumes in the proximal femur through an endosteal surface partition was prompted by the observation that bone loss in astronauts results in expansion of the endosteal diameter without expansion of the

subperiosteal diameter (Beck and Ruff, 1999). Studies by Ruff and Hayes (1984, 1988) and Beck *et al.* (1992, 1993) have shown that beyond the age of 50, an expansion in periosteal diameter occurs in men but is largely non-existent in women. This finding is believed to explain the markedly lower incidence of hip fracture in elderly males than in elderly females according to the following reasoning. Considering the femur as a hollow cylinder (for simplicity sake), the CSMI (I) is given by the relation:

$$I = \frac{\pi}{4}(R^4 - r^4) \tag{4.6}$$

where R is the outer radius, and r is the inner radius. Since radius is raised to the fourth power, a large increase in CSMI is obtained for a relatively small increase in average radius. Elementary beam theory predicts that stress, σ, is linearly related to the bending moment, M, at a given cross section:

$$\sigma = \frac{My}{I} \tag{4.7}$$

where y represents the distance from the neutral axis of the beam, therefore an increase in CSMI decreases the stress in the femur and thus increases the strength overall. In elderly females, R is constant while r increases, thus, decreasing the CSMI and increasing the stress in the bone leading to a further lowering of the structural capacity of the bone beyond that predicted by changes in density alone. Since a similar effect is believed to occur in astronauts, there is concern that the risk of fracture in this population is higher than that predicted by bone density alone.

The work described in this chapter was an attempt to gain insight into the impact that this geometric effect has on femoral strength changes in astronauts, and subsequently the impact

that it has on the factor of risk for hip fracture in astronauts. The techniques worked out were successful at modeling the geometric changes associated with endosteal expansion and the combined geometric and density changes produced a clear and consistent decline in femoral strength for both locomotion and fall loading conditions. The accuracy of the model at predicting the rate of strength loss associated with weightlessness was significantly limited by the lack of data on the three-dimensional distribution of density changes. In the absence of this information the only alternative was to use areal bone mineral density (BMD) data that provided only the total loss in bone mineral content (BMC) for given regions (neck and trochanteric). The change in BMC due to endosteal expansion was accounted for, but lacking three dimensional density data meant that the remaining portion of the BMC change could only be accounted for through a uniform reduction in density throughout the medulla portion of the region. This limitation is believed to be the primary reason why the models' predictions of the rate of decline in femoral strength with weightlessness were so much lower than the rates predicted by regression equations relating BMD to failure load in elderly femora. In support of this conclusion, recent analysis has shown that the strength of the proximal femur is highly sensitive to local differences in density change (Oden, 1999). Comparing the astronaut model to data from tests on elderly femora may have exaggerated the difference in rate of strength decline since it has been shown that elderly individuals experience an increased rate of strength decline (and an increased rate of fracture incidence) with age (and thus with changing BMD level) compared to younger individuals (such as in the astronaut population) (Cooper *et al.*, 1992). It is also worth pointing out that the maximum values in Table 4.1 indicate that some astronauts may experience rates of change in BMD and endosteal diameter of as much as 2–3 times the mean value that was used in the analysis (or more, in the case of neck endosteal diameter). The impact that these extreme rates of change would have on femoral

strength remains to be determined, but it is clear that much greater rates of strength loss are possible within the astronaut population.

Obtaining three-dimensional data on density distribution during bone changes associated with weightlessness appears to be the critical factor in improving the assessment of femoral strength changes related to spaceflight. There are currently plans to conduct QCT studies on the astronauts and cosmonauts who spend time on the International Space Station (Cann, 1998). In addition, a special portable DXA machine is being developed for the Space Station and it is anticipated that it will be capable of taking high-resolution multi-axial images of the proximal femur, thus offering another opportunity to reconstruct the three-dimensional distribution of density and the changes experienced during weightlessness.

Although the lack of three dimensional density distribution data is clearly the most significant limitation of the work discussed in this section, one additional limitation should be mentioned, namely, the use of a simple scale factor to derive female equivalent finite element models of the proximal femur from the models based on a male femur. The simple scaling could not account for differences of local geometry and density distribution that may exist between male and female femora. It was conducted simply to get a rough estimate of the strength values for female femora and to be able to use these values together with the values calculated for applied force (from the dynamics analysis in Chapter 2) to determine the factor of risk for fracture in female astronauts. The fact that the failure load values for the female models are likely less accurate than those for the male models should be borne in mind, especially when considering the factor of risk values presented in the next chapter. To improve the estimates of failure load in female femora, the analysis described in this and the last Chapters should be carried out again, but starting with a young adult female femur instead.

Despite these limitations, the modeling effort described in this chapter provides for the first time an assessment of the strength changes in the proximal femora of astronauts exposed to weightlessness that takes into account changes in three dimensional geometry while simultaneously estimating the effect of overall density reduction. It provides a valuable framework for future work that might exploit three-dimensional bone density information to obtain improvements in estimation of the rate of change of femoral strength during weightlessness.

4.5 References

Antonutto, Capelli, Girardis, Zamparo, and Prampero, d. (1999). "Effects of microgravity on maximal power of lower limbs during very short efforts in humans." *J Appl Physiol*, 86(1), 85-92.

Bamman, M. M., Hunter, G. R., Stevens, B. R., Guilliams, M. E., and Greenisen, M. C. (1997). "Resistance exercise prevents plantar flexor deconditioning during bed rest." *Med Sci Sports Exerc*, 29(11), 1462-8.

Bamman, M. M., Clarke, M. S., Feeback, D. L., Talmadge, R. J., Stevens, B. R., Lieberman, S. A., and Greenisen, M. C. (1998). "Impact of resistance exercise during bed rest on skeletal muscle sarcopenia and myosin isoform distribution." *J Appl Physiol*, 84(1), 157-63.

Beck, T.M. and Ruff, C.B. (1999). Personal communication.

Beck, T. J., Ruff, C. B., and Bissessur, K. (1993). "Age-related changes in femal femoral neck geometry: Implications for bone strength." *Calcified tissue*, 53(Suppl 1), S41-S46.

Beck, T. J., Ruff, C. B., Jr., W. W. S., Plato, C. C., Tobin, J. D., and Quan, C. A. (1992). "Sex differences in geometry of the femoral neck with aging: A structural analysis of bone mineral data." *Calcified Tissue International*, 50, 24-29.

Beck, S., Ruff, P., Warden, M., Scott Jr., M., and Rao, S. (1990). "Predicting femoral neck strength from bone mineral data a structural approach." *Investigative Radiology*, 25(1), 6-18.

Berg, H. E., Dudley, G. A., Haggmark, T., Ohlsen, H., and Tesch, P. A. (1991). "Effects of lower limb unloading on skeletal muscle mass and function in humans." *J Appl Physiol*, 70(4), 1882-5.

Bloomfield, S. A. (1997). "Changes in musculoskeletal structure and function with prolonged bed rest." *Med Sci Sports Exerc*, 29(2), 197-206.

Booth, F. W., and Criswell, D. S. (1997). "Molecular events underlying skeletal muscle atrophy and the development of effective countermeasures." *Int J Sports Med*, 18 Suppl(4), S265-9.Oganov, V. S., Grigor'ev, A. I., Voronin, L. I., Rakhmanov, A. S., Bakulin, A. V., Schneider, V. S., and LeBlanc, A. D. (1992). "[Bone mineral density in cosmonauts after flights lasting 4.5-6 months on the Mir orbital station]." *Aviakosm Ekolog Med*, 26(5-6), 20-24.

Bouxsein, M. L., Courtney, A. C., and Hayes, W. C. (1994). "Ultrasound and densitometry of the calcaneus correlate with the failure loads of cadaveric femurs." *Calcif Tissue Int*, 56, 99-103.

Cann, C. (1998) Personal Communication.

Cooper, C., Atkinson, E. J., O'Fallon, W. M., and Melton, L. J., 3d. (1992). "Incidence of clinically diagnosed vertebral fractures: a population-based study in Rochester,Minnesota, 1985-1989." *J Bone Miner Res*, 7(2), 221-7.

Courtney, A. C., Wachtel, E. F., Myers, E. R., and Hayes, W. C. (1994). "Effects of loading rate on strength of the proximal femur." *Calcif Tissue Int*, 55, 53-58.

Courtney, A. C., Wachtel, E. F., Myers, E. R., and Hayes, W. C. (1995). "Age-related reductions in the strength of the femur tested in a fall loading configuration." *J Bone Joint Surg (Am)*, 77, 387-395.

Desplanches, D. (1997). "Structural and functional adaptations of skeletal muscle to weightlessness." *Int J Sports Med*, 18 Suppl(4), S259-64.

Dudley, G. A., Duvoisin, M. R., Convertino, V. A., and Buchanan, P. (1989). "Alterations of the in vivo torque-velocity relationship of human skeletal muscle following 30 days of exposure to simulated microgravity." *Aviat Space Environ Med*, 60(7), 659-63.

Dudley, G. A., Hather, B. M., and Buchanan, P. (1992). "Skeletal muscle responses to unloading with special reference to man." *J Fla Med assoc*, 79(8), 525-9.

Germain, P., Guell, A., and Marini, J. F. (1995). "Muscle strength during bedrest with and without muscle exercise as a countermeasure." *Eur J Appl Physiol*, 71(4), 342-8.

Gigor'eva, L. S., and Kozlovskaia, I. B. (1987). "[Effects of weightlessness and hypokinesia on the velocity-strength properties of human muscles]." *Kosm Biol Aviakosm Med*, 21(1), 27-30.

Koryak, Y. A. (1998). "Influence of 120-days 6 degrees head-down tilt bed rest on the functional properties of the neuromuscular system in man." *Aviat Space Environ Med*, 69(8), 766-70.

Koryak, Y. A. (1999). "The effects of long-term simulated microgravity on neuromuscular performance in men and women." *Eu J Appl Physiol*, 79(2), 168-75.

Kozlovskaia, I. B., Grigor'eva, L. S., and Gevlich, G. I. (1984). "[Comparative analysis of the effects of weightlessness and its model on the velocity-strength properties and tonus of human skeletal muscles]." *Kosm Biol Aviakosm Med*, 18(6), 22-6.

LeBlanc, A., Gogia, P., Schneider, V., Krebs, J., Schonfeld, E., and Evans, H. (1988). "Calf muscle area and strength changes after five weeks of horizontal bed rest." *Am J Sports Med*, 16(6), 624-9.

LeBlanc, A. D., Schneider, V. S., Evans, H. J., Engelbretson, D. A., and Krebs, J. M. (1990). "Bone mineral loss and recovery after 17 weeks of bed rest." *J Bone Min Res*, 5(8), 843-850.

Looker, A. C., Johnston, J., C. C., Wahner, H. W., Dunn, W. L., Calvo, M. S., Harris, T. B., Heyse, S. P., and Lindsay, R. L. (1995a). "Prevalence of low femoral bone density in older U.S. women from NHANES III." *J Bone Min Res*, 10(5), 796-802.

Looker, A. C., Wahner, H. W., Dunn, W. L., Calvo, M. S., Harris, T. B., Heyse, S. P., Johnston, C. C., Jr., and Lindsay, R. L. (1995b). "Proximal femur bone mineral levels of U.S. adults." *Osteoporos Int*, 5(5), 389-409.

Oden, Z. M. (1999). Personal communication.

Ruff, C. B., and Hayes, W. C. (1984). "Age changes in geometry and mineral content of the lower limb bones." *Ann Biomed Eng*, 12, 573-84.

Ruff, C. B., and Hayes, W. C. (1988). "Sex differences in age-related remodeling of the femur and tibia." *J Orthop Res*, 6, 886-896.

Widrick, Knuth, Norenberg, Romatowski, Bain, Riley, Karhanek, Tappe, Trappe, Costill, and Fitts. (1999). "Effects of 17 day spaceflight on contractile properties of human soleus muscle fibres." *J Physiol (London)*, 516(3), 915-930.

CHAPTER 5 *Factor of Risk for Hip Fracture in Astronauts*

We must use time creatively, and forever realize that the time is always ripe to do right.

— Nelson Mandela

As pointed out earlier, to properly assess the risk of hip fracture it is necessary to consider additional factors besides bone mineral density. For instance, the body mass of the subject directly affects the load applied to the femoral head. Another factor independent of bone mineral density is the dissipation of the applied load into surrounding soft tissue during fall impact. Thus, to consider the case of astronauts performing activities on the surface of Mars, it was necessary to incorporate additional factors such as gravity level, and the mass and padding to the hip provided by a spacesuit worn during EVA. The purpose of this chapter is to combine the applied loading values calculated in Chapter 2 with the failure load values obtained in chapters 3 and 4 in order to derive an assessment of hip fracture risk for the range of activities and conditions considered.

5.1 Background

The majority of articles dealing with bone loss during space flight point out that decreasing bone mineral content is well correlated with bone strength and that as a consequence, astronauts are placed at increased risk of sustaining a fracture following a long-duration space

flight. It appears that none of these publications, however, provide any sort of quantitative assessment of the actual risk of fracture and few, if any, have examined other factors besides bone mineral density that contribute to fracture risk. Interestingly, one study has been carried out in which the prevalence of muskuloskeletal injury in the astronaut population as a whole was examined (Jennings and Bagian, 1996). They found that the incidence of orthopaedic injuries was surprisingly high for such a small adult population. During the period of 1987-95 there were a total of 26 fractures, 36 serious ligament, cartilage, or soft tissue injuries, and 28 orthopaedic surgical procedures in this adult group with a average size of 94 members (throughout the period). The study does not clearly delineate which fractures might have been related to bone loss during space flight, but does point out the need for better coordinated rehabilitation postflight. Given that the majority of U.S. Space Shuttle missions have been relatively short (approximately 2 weeks or less) compared to the time scale of bone loss, and considering that the astronaut population seems prone to injury due to high levels of physical activity and exercise training, it can certainly be expected that the prevalence of injury will rise once longer duration habitation missions are conducted to the International Space Station.

While factor of risk is a parameter that has long been used in traditional engineering disciplines, it is only relatively recently that it has been employed in orthopaedic research. Perhaps the earliest published use of this parameter in the field of orthopaedics was that in the book section by Hayes *et al.* (1991) and then in subsequent related articles (Hayes and Myers, 1994; Myers and Hayes, 1994). The utility of the factor of risk parameter (Φ is the popular symbol for factor of risk) is that it incorporates all of the relevant factors needed to assess fracture likelihood. By dividing the applied load by the failure load of the bone specimen (proximal femur in this case), a simple and universal parameter is obtained and one can immediately assess whether the likelihood of fracture is high (Φ close to 1.0, or greater than 1.0) or low

(Φ well below 1.0). In terms of flight operational issues, this type of information may be a great help to mission operations and training personnel since they can rapidly make decisions regarding the risk of fracture associated with a long-duration mission and make recommendations about the extent of countermeasures to be employed and precautions to be taken upon return to gravity (either on Earth or on the surface of Mars).

5.2 Methods

Applied force values (calculated in Chapter 2) and failure load values (determined in Chapters 3 and 4) were combined to produce factor of risk (Φ) values through the formula:

$$\Phi = \frac{F_{\text{applied}}}{F_{\text{fail}}} \tag{5.1}$$

Eight categories of risk were considered:

1. Mid-stance during locomotion (running) on Earth prior to space flight
2. Mid-stance during locomotion on Earth following 12 months of weightlessness
3. Mid-stance during IVA locomotion on Mars following 12 months of weightlessness
4. Mid-stance during EVA locomotion on Mars following 12 months of weightlessness
5. Fall loading on Earth prior to space flight
6. Fall loading on Earth following 12 months of weightlessness
7. Fall loading during IVA on Mars following 12 months of weightlessness
8. Fall loading during EVA on Mars following 12 months of weightlessness

Categories 2 and 6 do not represent a return mission to Mars, which would likely take at least two years in total (given current technology and mission plans), but rather represents the situation following an extended space station mission, or perhaps a future mission to the moon

and back. These two categories were included partly as a means of comparing fracture risk in Mars gravity with that in Earth gravity following 12 months of weightlessness.

Rather than simply calculating a single factor of risk for each category, a range of values were calculated in each case to represent (for males and females separately): 1) "best case" (lowest risk) conditions 2) an average adult under "typical" conditions, and 3) "worst case" conditions. The same failure load value, obtained in the finite element analysis of Chapters 3 and 4, was used for each of the three conditions. Variation of conditions came from the choice of parameters used in estimating the applied load through the dynamic analysis of Chapter 2. For the "best case" condition in mid-stance, the applied load associated with the lowest horizontal velocity (2 m/s) and a 5th percentile body size was used. For the "typical" condition in mid-stance, the applied load associated with a horizontal velocity of 4 m/s (for Earth) or 3 m/s (for Mars) and a 50th percentile body size was used. For the "worst case" condition in mid-stance, the applied load associated with a horizontal velocity of 6 m/s (for Earth) or 4m/s (for Mars) and a 95th percentile body size was used. The leg stiffness was assumed to be 13 kN/m in all categories, since this parameter was not varied for 5th and 95th percentile body sizes. In calculating the applied loading in each locomotion category, the contribution of muscle forces to the joint contact reaction force was added (with 60% reduction in magnitude for 12 months of weightlessness in the case of Mars). For the "best case", "typical", and "worst case" conditions associated with fall loading, the peak fall loads were taken for the 5th, 50th, and 95th percentile body sizes, respectively. For the Mars EVA fall loading, a 20% reduction in ground impact stiffness was incorporated to account for space suit padding.

To account for other combinations of parameters used in obtaining the applied loading, equations were derived in which these parameters can be substituted in order to arrive at more

generalized factor of risk values. The numerator and denominator of each factor of risk equation were obtained by performing a linear regression with respect to the relevant variables.

5.3 Results

A summary of the applied load, failure load, and factor of risk for each category and condition, and for each gender, is presented in Table 5.1. Factor of risk for hip fracture in males during locomotion (mid-stance) is presented graphically in Figure 5.1. There was a consistent trend between conditions with best and worst case values falling approximately 25% below and above the typical condition values, respectively. The most dangerous activity was locomotion in Earth gravity following a 12 month space flight mission where the factor of risk for the worst case condition came to within 13% of 1.0, indicating a significant chance of fracture. The fact that the risk factor for locomotion on Earth prior to weightlessness was already quite high (0.76) indicated that the femur used in the modeling was relatively weak, as observed previously. The factor of risk values for male locomotion in the Mars IVA and EVA categories were comparatively low, having a margin of safety of 40% or more for all conditions, indicating that locomotion on Mars following a 12 month spaceflight is relatively safe.

Factor of risk for fracture during locomotion (mid-stance) in females is presented in Figure 5.2. Similar trends to those observed for males were noted, with Earth gravity locomotion proving more risky than locomotion on Mars after a 12 month flight. The margin of safety was greater than for males, ranging from 31–74%, and thus it appears that locomotion is a relatively safe activity for females for all loading categories considered.

Factor of risk for fracture during fall loading in males is presented in Figure 5.3. The values were markedly higher than for locomotion, reaching as much as 2.08 for Earth gravity

Table 5.1 Applied load, failure load, and factor of risk for each category and condition. Applied and failure loads are expressed in Newtons (N).

	Males			Females		
Category	**Applied**	**Failure**	**F.O.Risk**	**Applied**	**Failure**	**F.O.Risk**
Best Case						
Stance, Earth, 0 m	2832	6127	0.46	2127	5925	0.36
Stance, Earth, 12 m	2832	5393	0.53	2127	5128	0.41
Stance, Mars IVA, 12 m	1719	5393	0.32	1333	5128	0.26
Stance, Mars EVA, 12 m	2236	5393	0.41	1846	5128	0.36
Fall, Earth, 0 m	5796	4390	1.32	4280	4208	1.02
Fall, Earth, 12 m	5796	3987	1.45	4280	3833	1.12
Fall, Mars IVA, 12 m	3674	3987	0.92	2710	3833	0.71
Fall, Mars EVA, 12 m	3997	3987	1.00	3164	3833	0.83
Typical						
Stance, Earth, 0 m	3752	6127	0.61	2796	5925	0.47
Stance, Earth, 12 m	3752	5393	0.70	2796	5128	0.55
Stance, Mars IVA, 12 m	2123	5393	0.39	1663	5128	0.32
Stance, Mars EVA, 12 m	2661	5393	0.49	2283	5128	0.45
Fall, Earth, 0 m	6988	4390	1.59	5211	4208	1.24
Fall, Earth, 12 m	6988	3987	1.75	5211	3833	1.36
Fall, Mars IVA, 12 m	4388	3987	1.10	3272	3833	0.85
Fall, Mars EVA, 12 m	4427	3987	1.11	3642	3833	0.95
Worst Case						
Stance, Earth, 0 m	4674	6127	0.76	3541	5925	0.60
Stance, Earth, 12 m	4674	5393	0.87	3541	5128	0.69
Stance, Mars IVA, 12 m	2619	5393	0.49	2009	5128	0.39
Stance, Mars EVA, 12 m	3201	5393	0.59	2669	5128	0.52
Fall, Earth, 0 m	8280	4390	1.89	6221	4208	1.48
Fall, Earth, 12 m	8280	3987	2.08	6221	3833	1.62
Fall, Mars IVA, 12 m	5171	3987	1.30	3905	3833	1.02
Fall, Mars EVA, 12 m	5074	3987	1.27	4162	3833	1.09

falls following 12 months of spaceflight. In addition, all of the conditions considered for a fall in Mars gravity IVA and EVA had a factor of risk close to (within 10%) or greater than 1.0, indicating that, unlike for locomotion, a fall on Mars following 12 months of weightlessness carries a high risk of hip fracture. Falls during IVA and EVA possessed approximately the same risk of fracture for matching conditions.

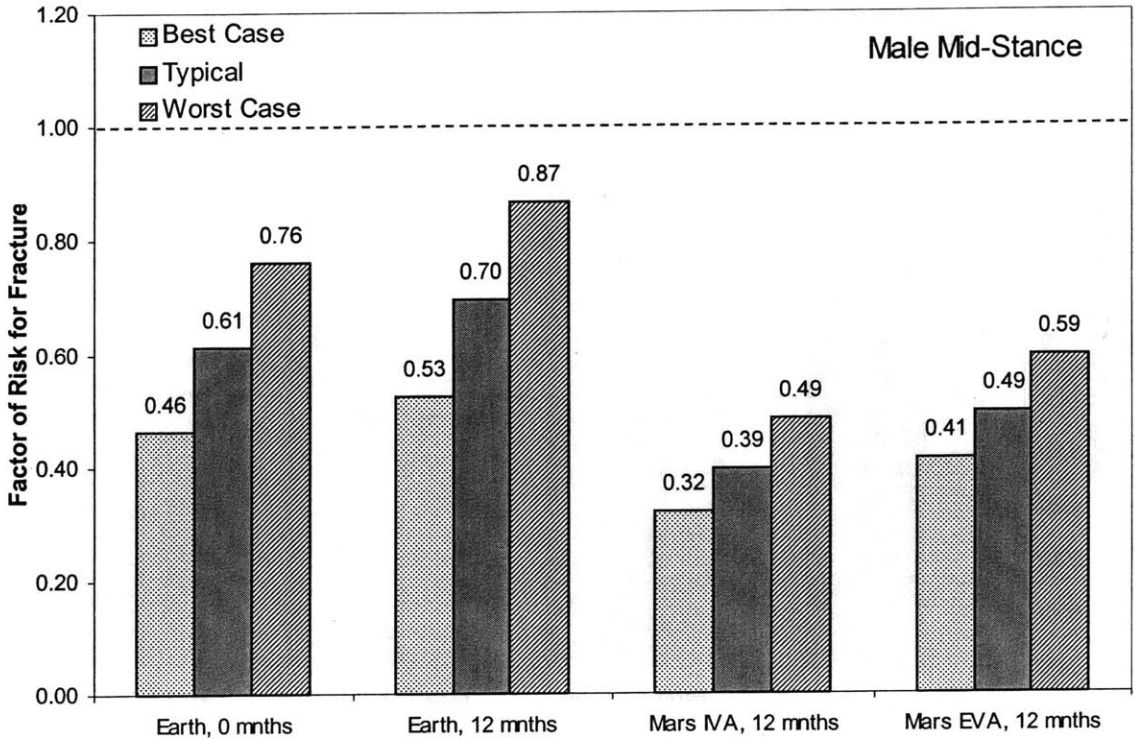

Figure 5.1: Factor of risk for hip fracture in males during mid-stance.

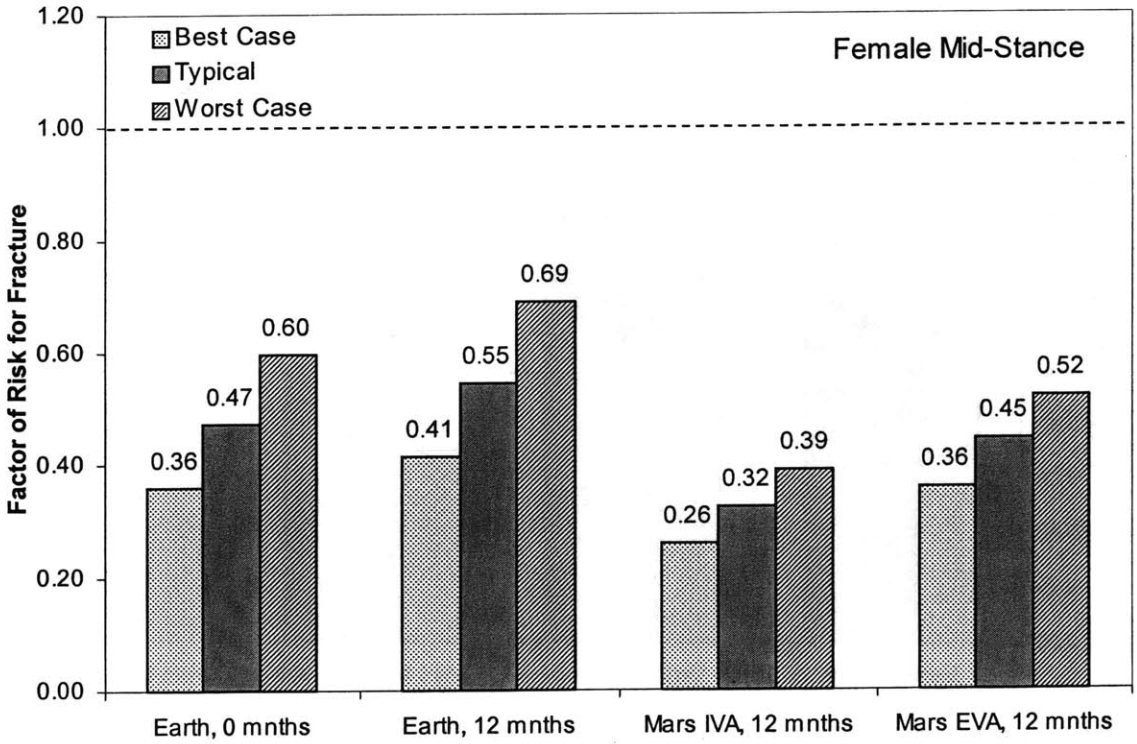

Figure 5.2: Factor of risk for hip fracture in females during mid-stance.

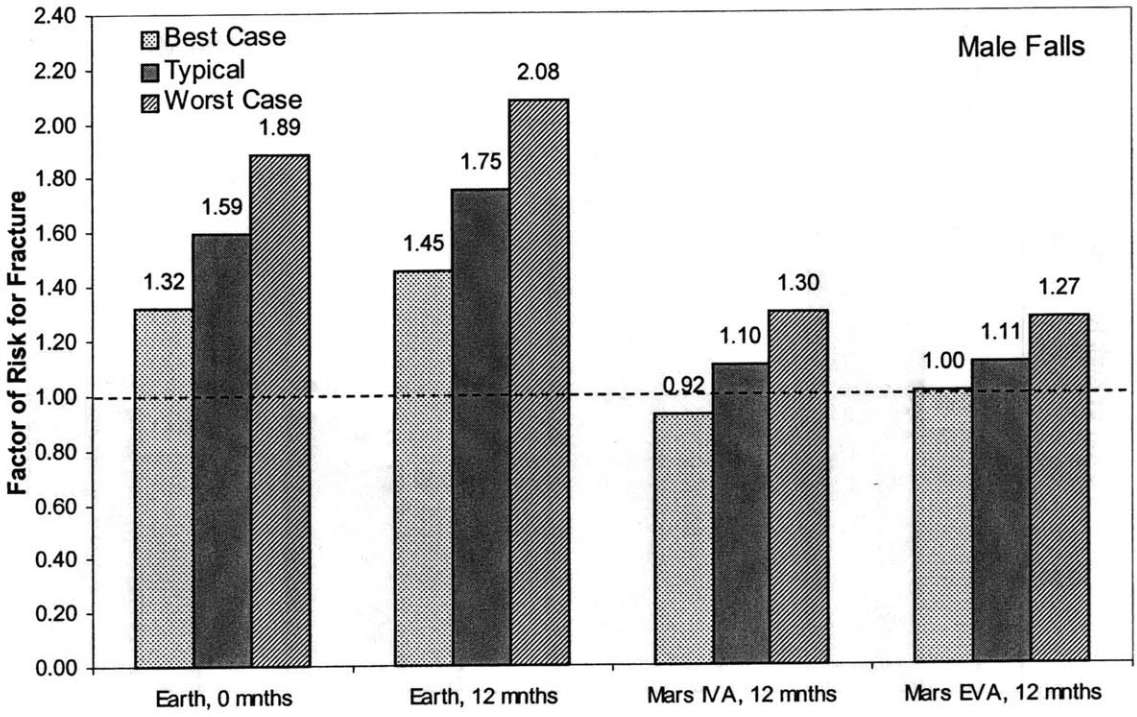

Figure 5.3: Factor of risk for hip fracture in males during fall loading.

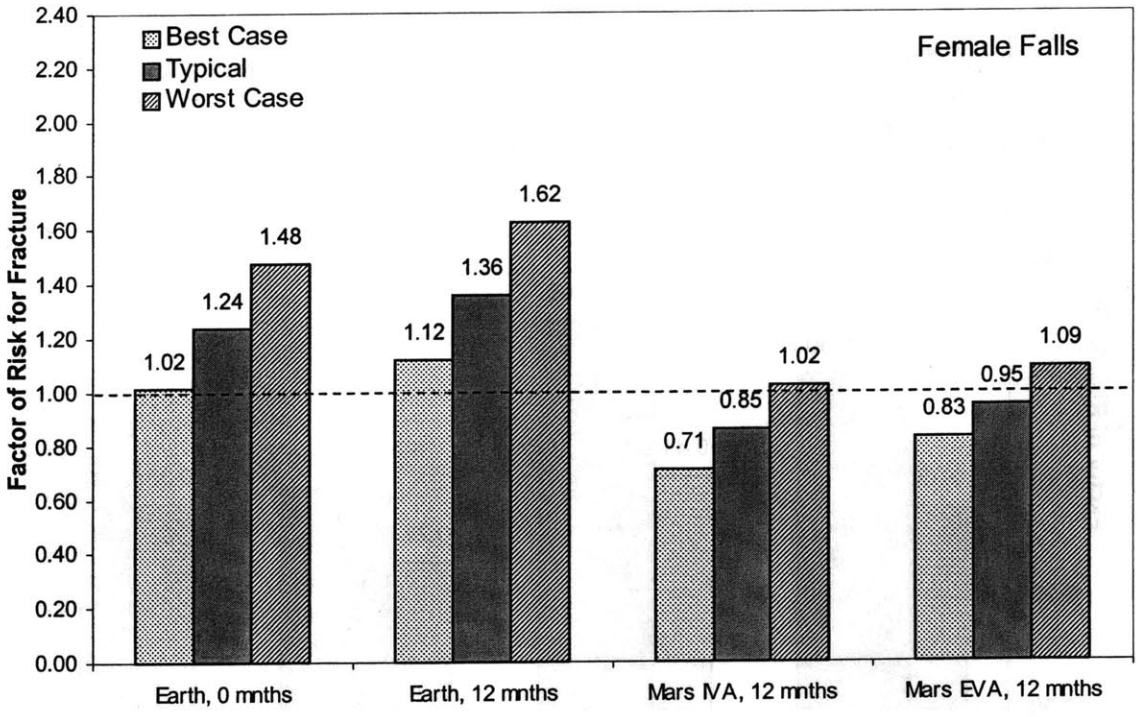

Figure 5.4: Factor of risk for hip fracture in females during fall loading.

Factor of risk for fracture during fall loading in females is presented in Figure 5.4. Similar trends to the male case were observed where falls on Earth had a markedly higher factor of risk than falls on Mars. Although the female factor of risk values were approximately 14–22% lower than the corresponding male values, the majority of values were still close to (within 10% of) 1.0, indicating that there is a high risk for fracture in females for all fall categories considered.

The equations derived for predicting factor of risk for fracture in both locomotion and falls are presented in Table 5.2. The linear regressions for the numerator and denominator expressions all yielded R^2 values of greater than 0.98, except for the denominators in the male and female locomotion case (which had R^2 values of 0.95 and 0.88, respectively).

Table 5.2 Equations for calculating factor of risk for hip fracture in males and females according to type of activity and gravitational environment. Note that m is the mass of the subject (kg), u is the horizontal velocity (m/s), and n is the number of months of weightlessness. Also note that the locomotion equations include the contribution of muscle forces.

Loading Condition	Male Factor of Risk	Female Factor of Risk
Locomotion (Earth)	$\frac{37.5m + 177.6u + 139.3}{6079 - 61.2n}$	$\frac{35.4m + 141.8u + 255.8}{5839 - 66.4n}$
Locomotion (Mars IVA)	$\frac{32.3m + 160.3u + 191.1}{6079 - 61.2n}$	$\frac{30.2m + 128u + 310.4}{5839 - 66.4n}$
Locomotion (Mars EVA)	$\frac{30.2m + 212.3u + 730.4}{6079 - 61.2n}$	$\frac{29.8m + 190.2u + 718.4}{5839 - 66.4n}$
Falls (Earth)	$\frac{79.1m + 923.4}{4392 - 33.6n}$	$\frac{79.9m + 721.4}{4211 - 31.25n}$
Falls (Mars IVA)	$\frac{47.6m + 737.7}{4392 - 33.6n}$	$\frac{49.2m + 515.3}{4211 - 31.25n}$
Falls (Mars EVA)	$\frac{34.3m + 1856.5}{4392 - 33.6n}$	$\frac{41.1m + 1334.1}{4211 - 31.25n}$

5.4 Discussion

Conclusions drawn from the results in this chapter should take into account the two most significant limitations of this study. The first major limitation is that the rate of decline in strength of the proximal femur with duration of weightlessness may have been underestimated by the finite element models. The second major limitation is that the female failure load values were based on finite element models that were simply scaled versions of their male counterparts. Both of these limitations have the capacity for reducing the accuracy of the values calculated for factor of risk for hip fracture.

It is also important to clarify the limited understanding of factor of risk as applied to orthopaedic fractures. Although factor of risk takes into account additional information besides bone mineral density in assessing fracture likelihood, its limitation lies in the extent to which the investigator is able to account for all of the parameters that influence both applied loading and failure load. From another viewpoint, the simplifications and assumptions used in deriving models to assess applied load and failure load can significantly alter the accuracy of factor of risk predictions of fracture. This is evident in the fact that factor of risk tends to underestimate the incidence of fracture observed in the elderly population.

Nevertheless, several general conclusions may be drawn based on the factor of risk results obtained. Fall impact clearly carries a higher risk of fracture than locomotion under all conditions. In fact, locomotion in Mars gravity, under both intravehicular and extravehicular (space suited) conditions, and for both male and female astronauts, appears to be a relatively safe activity (margin of safety of 40% or more), even right after a 12 month journey. However, locomotion in Earth gravity after a long duration space mission (such as a 12 month stay on the space station) is comparatively risky, especially in males (margin of safety of as low as 13%). In contrast to the relatively low risk of locomotion, falls carry a high risk of hip fracture

under all conditions. The highest risk of all is associated with a male astronaut falling in Earth gravity following a 12 month space mission. Unlike for locomotion, falls in Mars gravity also carry a high risk of hip fracture for both males and females. To compound this risk, the likelihood of initiating a fall is increased following space flight due to a compromised sense of balance (result of neurovestibular adaptation) and an increased susceptibility to fainting associated with orthostatic intolerance (low blood pressure upon standing associated with blood volume depletion). Furthermore, it has been shown that bone mass recovery upon return to Earth occurs at a markedly slower rate than loss during weightlessness (LeBlanc et al., 1990), so the astronaut may be at risk for an extended period. An obvious recommendation, given these circumstances, is that astronauts be encouraged to wear hip pads during physical activities for at least the first few weeks following a long-duration mission (both after arrival to Mars and upon return to Earth), since it has been shown that hip pads can reduce fall impact loading by as much as 65% (Robinovitch, 1995). In fact, it would even be wise to incorporate hip pads into future space suits for EVA on Mars. In counterbalance to this argument is the observation made in Chapter 2, that falls on Mars occur more slowly due to the reduced gravity and so astronauts have more time to react and break their fall.

Another important conclusion based on the results of this work is that muscle forces play a crucial role in the structural capacity of the proximal femur during the mid-stance phase of running. This demonstrates the interdependence of physiological systems and emphasizes the need to maintain muscle strength in addition to bone mineral density during long-duration space missions.

An interesting indication in the results of this chapter is that the risk of fracture during both locomotion and falls on Mars may be less than the risk of fracture when performing the same activities in Earth-gravity prior to space flight. This goes against the popular belief that

fracture risk would be increased under all circumstances following arrival at Mars, and may reflect the influence of additional factors besides bone mineral density (such as gravity level, and hip padding provided by a spacesuit) in determining fracture risk. On the other hand, as observed previously, the rate of strength decline of the proximal femur may have been underestimated by the finite element modeling technique due to lack of three-dimensional density information. In addition, it should be pointed out that the rates of BMD loss assessed for cosmonauts, and upon which the failure models in chapter 4 were based, were obtained under conditions in which the cosmonauts were required to perform exercises specifically designed to minimize bone loss. Poor compliance with exercise countermeasure protocols could also increase the rate of bone loss and consequently the rate of strength decline. A greater rate of strength decline during weightlessness could conceivably reverse the comparison between Earth and Mars, resulting in a higher risk of hip fracture during falls and locomotion in Mars gravity than during the same activities on Earth prior to space flight. The resolution of this uncertainty awaits the availability of three-dimensional densitometric scans of the proximal femur in astronauts or bed rest subjects experiencing bone density loss during skeletal unloading.

5.5 Recommendations for Future Work

At this stage there exists a great opportunity for extending the work presented in this thesis. Some suggestions for important contributions have already been mentioned, but these and others will be summarized here. The highest priority for future research should be to obtain data on the three-dimensional distribution of density changes in the proximal femur following space flight. These data would likely provide the greatest improvement in the accuracy of the

factor of risk predictions. Achieving this goal will require obtaining QCT or multi-axial DXA scans of the proximal femora of astronauts and/or bed rest patients immediately before and immediately after unweighting, and possibly also at one or two times during the period of unweighting. Such a study may take some time to arrange and it will also take at least several months to conduct the study and analyze the data thereafter. A more immediate possibility for improving fidelity of failure load predictions in women is to repeat the finite element analyses described in this thesis, but this time starting with the femur from a young adult female. Finally, it would be interesting to perform failure analyses that examine the effects of endosteal resorption and density reduction separately to gauge their relative contribution to strength loss.

5.6 References

Hayes, W. C., and Myers, E. R. (1994). "Biomechanics of age-related fracture risk." Osteoporosis: Etiology, diagnosis, and management, B. Riggs and L. Melton, eds., Raven Press, New York.

Hayes, W. C., Piazza, S. J., and Zysset, P. K. (1991). "Biomechanics of fracture risk prediction of the hip and spine by quantitative computed tomography." Radiologic Clinics of North America, D. I. Rosenthal, ed., W.B. Saunders Company, 1-18.

Jennings, R. T., and Bagian, J. P. (1996). "Muskuloskeletal injury review in the U.S. space program." *Aviat Space Environ Med*, 67(8), 762-6.

LeBlanc, A. D., Schneider, V. S., Evans, H. J., Engelbretson, D. A., and Krebs, J. M. (1990). "Bone mineral loss and recovery after 17 weeks of bed rest." *J Bone Min Res*, 5(8), 843-850.

Myers, E. R., and Hayes, W. C. (1994). "Age-related hip fractures." *Current Opinion in Orthop*, 5, 9-15.

Robinovitch, S. N., Hayes, W. C., and McMahon, T. A. (1995). "Energy-shunting hip padding system attenuates femoral impact force in a simulated fall." *J Biomech Eng*, 117(4), 409-13.

Appendix A

This appendix describes the jacobian matrices used in the formulation of the inertia tensor for the three segment model of human locomotion based on the Lagrangian formulation:

$$\mathbf{H}\ddot{\mathbf{p}} + \mathbf{h}\dot{\mathbf{p}}_{sq} + \mathbf{G} = \mathbf{Q} \tag{A.1}$$

which is described in the main text. Jacobian matrices, $\mathbf{J}_L{}^{(i)}$ and $\mathbf{J}_A{}^{(i)}$, provide the linear and angular velocities, respectively, of link i from the joint angular velocity vector:

$$\begin{aligned} \mathbf{v}_{ci} &= \mathbf{J}_L{}^{(i)}\dot{\mathbf{p}} \\ \omega_i &= \mathbf{J}_A{}^{(i)}\dot{\mathbf{p}} \end{aligned} \tag{A.2}$$

For the three segment system, the Jacobians are given by:

$$\begin{aligned} \mathbf{J}_A{}^{(1)} &= \begin{bmatrix} 1 & 0 & 0 \end{bmatrix} \\ \mathbf{J}_A{}^{(2)} &= \begin{bmatrix} 0 & 1 & 0 \end{bmatrix} \\ \mathbf{J}_A{}^{(3)} &= \begin{bmatrix} 0 & 0 & 1 \end{bmatrix} \\ \mathbf{J}_L{}^{(1)} &= \begin{bmatrix} -l_{c1}s_1 & 0 & 0 \\ l_{c1}c_1 & 0 & 0 \end{bmatrix} \\ \mathbf{J}_L{}^{(2)} &= \begin{bmatrix} -l_1 s_1 & -l_{c2}s_2 & 0 \\ l_1 c_1 & l_{c2}c_2 & 0 \end{bmatrix} \\ \mathbf{J}_L{}^{(3)} &= \begin{bmatrix} -l_1 s_1 & -l_2 s_2 & -l_{c3}s_3 \\ l_1 c_1 & l_2 c_2 & l_{c3}c_3 \end{bmatrix} \end{aligned} \tag{A.3}$$

where $c_i = \cos(p_i)$ and $s_i = \sin(p_i)$. Also, as mentioned in the main text, l_i represents the length of link i, and l_{ci} represents the distance from the inboard joint to the segments center of mass. The terms in the manipulator inertia tensor can now be found using the expression:

$$\mathbf{H} = \sum_{i=1}^{3} \left(m\mathbf{J}_L{}^{(i)T}\mathbf{J}_L{}^{(i)} + \mathbf{J}_A{}^{(i)}I_i\mathbf{J}_A{}^{(i)} \right) \tag{A.4}$$

The individual terms, H_{ij}, are given in the main text.

Appendix B

This appendix presents the mass properties and geometric data obtained from GEBOD for use in the three segment locomotion and fall simulations.

Notes:

1. Space suit mass was distributed proportionately amongst body segments (according to segment mass)

2. PLSS mass was added only to segment 3.

3. Moments of inertia for segments including space suit were scaled according to mass increase.

5th Percentile Female

Three Segment Model Parameters								body-to-jt	inb-to-body
	L1	0.32	LzCT*	0.14	LyUA*	0.13		0.17	0
	L2	0.40	LzUT*	0.29	LyLA*	0.13		0.21	0.15
	L3	0.61	LzN*	0.45				0.21	0.19
	L1CG	0.17	LzH*	0.6					
	L2CG	0.21	LzUA*	0.26	LzUL*	0.2			
	L3CG	0.21	LzLA*	0	LzLL*	0.56			
	M1	4.46	I1X	0.0398	I2X	0.1902		I3X	2.6198
	M2	12.39	I1Y	0.0398	I2Y	0.1902		I3Y	2.5131
	M3	27.51	I1Z	0.0045	I2Z	0.0268		I3Z	0.2052
	Mtotal	44.36							
*w.r.t LT CG									
	M1run	2.23	I1Yrun	0.01992					
	M2run	6.20	I2Yrun	0.09512					
	M3run	35.93	I3Yrun	3.5756					
MARS	Suit Mass**	29.51	PLSS IX	0.93	PLSS_CGx	0.22			
	PLSS Mass	15	PLSS IY	0.66	PLSS_Cgy	0			
** Suit is ILC "M-suit"			PLSS IZ	0.36	PLSS_CGz	0			
	M1Mars	7.43	I1XMars	0.0663	I2XMars	0.3168		I3XMars	6.7212
	M2Mars	20.64	I1YMars	0.0663	I2YMars	0.3168		I3YMars	6.9412
	M3Mars	60.80	I1ZMars	0.0075	I2ZMars	0.0446		I3ZMars	1.5396
	MtotalMars	88.87							
	M1runMars	3.72	I1YrunMars	0.0332					
	M2runMars	10.32	I2YrunMars	0.1584					
	M3runMars	74.84	I3YrunMars	8.8327					

50th Percentile Female

Three Segment Model Parameters							body-to-jt	inb-to-body
	L1	0.35	LzCT*	0.14	LyUA*	0.14	0.19	0
	L2	0.43	LzUT*	0.3	LyLA*	0.14	0.23	0.16
	L3	0.62	LzN*	0.46			0.21	0.20
	L1CG	0.19	LzH*	0.61				
	L2CG	0.23	LzUA*	0.28	LzUL*	0.21		
	L3CG	0.21	LzLA*	0	LzLL*	0.6		
	M1	5.67	I1X	0.0591	I2X	0.2953	I3X	3.2978
	M2	16.32	I1Y	0.0591	I2Y	0.2953	I3Y	3.1395
	M3	34.52	I1Z	0.0067	I2Z	0.0425	I3Z	0.3066
	Mtotal	56.52						
*w.r.t LT CG								
	M1run	2.84	I1Yrun	0.02956				
	M2run	8.16	I2Yrun	0.14764				
	M3run	45.52	I3Yrun	4.6975				
MARS	Suit Mass**	29.51	PLSS IX	0.93	PLSS_CGx	0.22		
	PLSS Mass	15	PLSS IY	0.66	PLSS_Cgy	0		
** Suit is ILC "M-suit"			PLSS IZ	0.36	PLSS_CGz	0		
	M1Mars	8.63	I1XMars	0.0900	I2XMars	0.4495	I3XMars	7.3827
	M2Mars	24.85	I1YMars	0.0900	I2YMars	0.4495	I3YMars	7.5290
	M3Mars	67.55	I1ZMars	0.0102	I2ZMars	0.0646	I3ZMars	1.6860
	MtotalMars	101.03						
	M1runMars	4.32	I1YrunMars	0.0450				
	M2runMars	12.42	I2YrunMars	0.2247				
	M3runMars	84.29	I3YrunMars	10.0843				

95th Percentile Female

Three Segment Model Parameters								body-to-jt	inb-to-body
	L1	0.38	LzCT*	0.15	LyUA*	0.14		0.2	0
	L2	0.47	LzUT*	0.32	LyLA*	0.14		0.25	0.18
	L3	0.64	LzN*	0.49				0.21	0.22
	L1CG	0.2	LzH*	0.64					
	L2CG	0.25	LzUA*	0.29	LzUL*	0.22			
	L3CG	0.21	LzLA*	-0.01	LzLL*	0.65			
	M1	6.87	I1X	0.0827	I2X	0.4293		I3X	4.2046
	M2	20.39	I1Y	0.0827	I2Y	0.4293		I3Y	4.0002
	M3	41.42	I1Z	0.0094	I2Z	0.0628		I3Z	0.4156
	Mtotal	68.68							
*w.r.t LT CG									
	M1run	3.44	I1Yrun	0.04135					
	M2run	10.19	I2Yrun	0.21463					
	M3run	55.05	I3Yrun	6.2010					
MARS	Suit Mass**	29.51	PLSS IX	0.93	PLSS_CGx	0.22			
	PLSS Mass	15	PLSS IY	0.66	PLSS_Cgy	0			
** Suit is ILC "M-suit"			PLSS IZ	0.36	PLSS_CGz	0			
	M1Mars	9.82	I1XMars	0.1182	I2XMars	0.6137		I3XMars	8.4636
	M2Mars	29.15	I1YMars	0.1182	I2YMars	0.6137		I3YMars	8.5534
	M3Mars	74.22	I1ZMars	0.0134	I2ZMars	0.0898		I3ZMars	1.8306
	MtotalMars	113.19							
	M1runMars	4.91	I1YrunMars	0.0591					
	M2runMars	14.57	I2YrunMars	0.3068					
	M3runMars	93.71	I3YrunMars	11.9408					

5th Percentile Male

Three Segment Model Parameters								body-to-jt	inb-to-body
	L1	0.33	LzCT*	0.13	LyUA*	0.15		0.18	0
	L2	0.41	LzUT*	0.32	LyLA*	0.15		0.22	0.15
	L3	0.68	LzN*	0.52				0.24	0.19
	L1CG	0.18	LzH*	0.68					
	L2CG	0.22	LzUA*	0.31	LzUL*	0.19			
	L3CG	0.24	LzLA*	0	LzLL*	0.56			
	M1	5.92	I1X	0.0568	I2X	0.2058		I3X	5.0690
	M2	12.77	I1Y	0.0568	I2Y	0.2058		I3Y	4.8298
	M3	42.70	I1Z	0.0072	I2Z	0.0258		I3Z	0.4296
	Mtotal	61.39							
*w.r.t LT CG									
	M1run	2.96	I1Yrun	0.02841					
	M2run	6.38	I2Yrun	0.1029					
	M3run	52.05	I3Yrun	6.1204					
MARS	Suit Mass**	29.51	PLSS IX	0.93	PLSS_CGx	0.22			
	PLSS Mass	15	PLSS IY	0.66	PLSS_Cgy	0			
** Suit is ILC "M-suit"			PLSS IZ	0.36	PLSS_CGz	0			
	M1Mars	8.77	I1XMars	0.0841	I2XMars	0.3047		I3XMars	10.2162
	M2Mars	18.90	I1YMars	0.0841	I2YMars	0.3047		I3YMars	10.2339
	M3Mars	78.23	I1ZMars	0.0107	I2ZMars	0.0383		I3ZMars	1.8729
	MtotalMars	105.90							
	M1runMars	4.39	I1YrunMars	0.0421					
	M2runMars	9.45	I2YrunMars	0.1524					
	M3runMars	92.06	I3YrunMars	12.2124					

50th Percentile Male

Three Segment Model Parameters								body-to-jt	inb-to-body
		L1	0.36	LzCT*	0.13	LyUA*	0.15	0.19	0
		L2	0.44	LzUT*	0.32	LyLA*	0.15	0.24	0.17
		L3	0.69	LzN*	0.53			0.24	0.20
		L1CG	0.19	LzH*	0.69				
		L2CG	0.24	LzUA*	0.31	LzUL*	0.2		
		L3CG	0.24	LzLA*	-0.02	LzLL*	0.61		
		M1	7.40	I1X	0.0822	I2X	0.3154	I3X	6.1262
		M2	16.62	I1Y	0.0822	I2Y	0.3154	I3Y	5.8123
		M3	53.07	I1Z	0.0104	I2Z	0.0400	I3Z	0.5984
		Mtotal	77.09						
*w.r.t LT CG									
		M1run	3.70	I1Yrun	0.04108				
		M2run	8.31	I2Yrun	0.15768				
		M3run	65.08	I3Yrun	7.7196				
MARS	Suit Mass**		29.51	PLSS IX	0.93	PLSS_CGx	0.22		
	PLSS Mass		15	PLSS IY	0.66	PLSS_Cgy	0		
** Suit is ILC "M-suit"				PLSS IZ	0.36	PLSS_CGz	0		
		M1Mars	10.23	I1XMars	0.1136	I2XMars	0.4361	I3XMars	11.1328
		M2Mars	22.98	I1YMars	0.1136	I2YMars	0.4361	I3YMars	11.0660
		M3Mars	88.39	I1ZMars	0.0143	I2ZMars	0.0553	I3ZMars	2.0827
		MtotalMars	121.60						
		M1runMars	5.11	I1YrunMars	0.0568				
		M2runMars	11.49	I2YrunMars	0.2180				
		M3runMars	104.99	I3YrunMars	13.8399				

95th Percentile Male

Three Segment Model Parameters									body-to-jt	inb-to-body
		L1	0.39	LzCT*	0.14	LyUA*	0.16		0.21	0
		L2	0.47	LzUT*	0.34	LyLA*	0.16		0.25	0.18
		L3	0.73	LzN*	0.57				0.24	0.22
		L1CG	0.21	LzH*	0.74					
		L2CG	0.25	LzUA*	0.33	LzUL*	0.21			
		L3CG	0.24	LzLA*	-0.02	LzLL*	0.64			
		M1	8.85	I1X	0.1128	I2X	0.4549	I3X	7.9621	
		M2	20.61	I1Y	0.1128	I2Y	0.4549	I3Y	7.5342	
		M3	63.34	I1Z	0.0141	I2Z	0.0582	I3Z	0.8314	
		Mtotal	92.81							
*w.r.t LT CG										
		M1run	4.43	I1Yrun	0.05638					
		M2run	10.31	I2Yrun	0.22745					
		M3run	78.07	I3Yrun	10.0860					
MARS	Suit Mass**		29.51	PLSS IX	0.93	PLSS_CGx	0.22			
	PLSS Mass		15	PLSS IY	0.66	PLSS_Cgy	0			
** Suit is ILC "M-suit"				PLSS IZ	0.36	PLSS_CGz	0			
		M1Mars	11.67	I1XMars	0.1486	I2XMars	0.5995	I3XMars	13.3095	
		M2Mars	27.17	I1YMars	0.1486	I2YMars	0.5995	I3YMars	13.1002	
		M3Mars	98.48	I1ZMars	0.0186	I2ZMars	0.0767	I3ZMars	2.3787	
		MtotalMars	137.32							
		M1runMars	5.84	I1YrunMars	0.0743					
		M2runMars	13.58	I2YrunMars	0.2998					
		M3runMars	117.90	I3YrunMars	16.6170					

Appendix C *Simulation Code*

This appendix presents the primary simulation code used in the locomotion and fall simulations. It includes: 1) the MATLAB script used for the locomotion simulations, 2) a sample system description file that is read by SD/FAST in formulating the equations of motion for a dynamic system (in this case, a 50th percentile male wearing a spacesuit for an EVA conducted on Mars), and 3) the C code used to run the fall simulation.

C.1 Locomotion Simulation MATLAB script

```
% MATLAB script for 3-segment planar model of a human to simulate dynamics
% of stance phase of gait

clear;
clf

% Define constants / initial values:

g = 9.807; % gravitational acceleration on Earth
%g = 0;% weightless
%g= g*3/8;% gravitational acceleration on Mars
gv = [0; g];% planar case
PI = acos(-1);
dtr = PI/180;
rtd = 180/PI;

on = 1;
off = 0;

% Flags and switches
trans = on;
min_flag = off;
last_run = off;

file_print = on;

kin_plot = on;
pos_plot = on;
vel_plot = off;
acc_plot = off;
trq_plot = off;
frc_plot = on;
loc_plot = on;

tpeak = 0.05;
dt = 0.0005;% coarse time step

nextplot = 250;% frequency of body config plots
```

```
iter_count = 1;
iter_max = 30;

% Start of parameters ----------

% Note: for MARS, don't forget to change "g"

% Start: 50% MALE (Earth) ==========

% Mass properties
m1 = 3.70;
m2 = 8.31;
m3 = 65.08;
I1 = .0411;
I2 = .1577;
I3 = 7.7196;

% Segment dimensions
l1 = .36;
l2 = .44;
l3 = .69;
lc1 = .19;
lc2 = .24;
lc3 = .24;

% End: ==========

% Control Parameters ----------
k1 = 0;% ankle joint stiffness
d1 = 0;% ankle joint damping
k2 = 200;% knee joint stiffness
d2 = 20;% knee joint damping
%k2 = 0;% knee joint stiffness
%d2 = 0;% knee joint damping
k3 = 1000;% hip joint stiffness
d3 = 100;% hip joint damping

kp = 13000;% Impedance Control: spring constant
%kd = 100;% Impedance Control: damping constant
kd = 0;% Impedance Control: damping constant

% End of parameters ----------

if file_print == on
  fid_kin = fopen('c:\Grant\PhD_Thesis\Run_data\kinem.dat','w');
end

% Initial velocities

%v3i = [-2.0; -0.78];% hip vel ( 7.2 km/h slow jog)
%v3i = [-3.0; -0.78];% hip vel (10.8 km/h jog)
v3i = [-4.0; -0.78];% hip vel (14.4 km/h moderate run)
%v3i = [-5.0; -0.78];% hip vel (18.0 km/h moderate run)
%v3i = [-6.0; -0.78];% hip vel (21.6 km/h fast run)

%v3i = [0; 0];% test case

%vc3i = [-2.0; -0.5];% initial velocity of upper body center of mass (slow run)
%vc3 = [0.0; 0.0];% initial velocity of upper body center of mass (test case)
```

```
p1 = 70*dtr; % Initial ankle angle (prior to iteration)
p1_deg = p1*rtd;

% Start of iteration loop for starting leg angle ----------

while ((min_flag == off) | (last_run == off)) & iter_count < iter_max

  clear min_hipx min_hipy min_step
  clear v3 v3x v3y
  clear p2 p3 p pd2 pd pdsq pdd
  clear time x xh x1 x2 x3
  clear p1rec p2rec p3rec pd1rec pd2rec pd3rec pdd1rec pdd2rec pdd3rec
  clear hipx hipy
  clear tau1 tau2 tau3 tau1rec tau2rec tau3rec
  clear f32 f32x f32y

  % Set values that need to be re-initialized during each iteration
  t = 0;
  step = 1;% step counter
  countplot = 1;% counter for body config plots

  if (min_flag == on)
    last_run = on;
  dt = 0.0001;% small time step
%dt = 0.0005;% small time step
%dt = 0.005;% small time step
  end

% Initial Joint Positions
% initial ankle angle set above
p2 = p1-5.0*dtr;% initial knee angle
p3 = 90*dtr;% initial hip angle

p = [p1; p2; p3];

s1 = sin(p1);
c1 = cos(p1);
s2 = sin(p2);
c2 = cos(p2);
s3 = sin(p3);
c3 = cos(p3);
c12 = cos(p1-p2);
c13 = cos(p1-p3);
c23 = cos(p2-p3);
s12 = sin(p1-p2);
s13 = sin(p1-p3);
s23 = sin(p2-p3);

p1b = 0;% desired ankle angle (for PPD control)
p2b = p2;% desired knee angle (for PPD control)
p3b = 90*dtr;% desired hip angle (for PPD control)

JL3 = [-l1*s1 -l2*s2 -lc3*s3; l1*c1 l2*c2 lc3*c3];
%vc3 = vc3i * (sin(t/tpeak*90*dtr))^2; % use sine-squared function for smooth buildup
%pd = JL3\vc3;% initial joint velocity = inverse of JL3, multiplied by vc3

JLh = [-l1*s1 -l2*s2; l1*c1 l2*c2]; % relates hip linear velocity to ankle and knee vel.
if (trans == on)
  v3 = v3i * (sin(t/tpeak*90*dtr))^2; % sine-squared function for smooth buildup
else
```

```
  v3 = v3i;
end
pd2 = JLh\v3;% initial joint velocity = inverse of JL2, multiplied by v3
pd = [pd2(1); pd2(2); 0];

v3b = [-3.0; 0.5]; % desired final velocity at hip (for Impedance Control)

pdsq = [pd(1)^2; pd(2)^2; pd(3)^2];

pdd = [0; 0; 0];% initial joint acceleration

tau1 = 0;
tau2 = 0;
tau3 = 0;

JL3d = [-l1*c1*pd(1) -l2*c2*pd(2) -lc3*c3*pd(3); -l1*s1*pd(1) -l2*s2*pd(2) -lc3*s3*pd(3)];
vc3d = JL3*pdd + JL3d*pd;
f32 = - m3*(gv + vc3d);% force on femur from upper body

x1 = [l1*c1 l1*s1];
x2 = [l2*c2 l2*s2];
x3 = [l3*c3 l3*s3];
x  = [0 0; x1; x1+x2; x1+x2+x3]; % positions of joints and head
xh = (x1 + x2)';

leg_init = sqrt(xh(1)^2 + xh(2)^2);
leg = leg_init;

% Record initial values

time(step) = t;
p1rec(step) = p(1)*rtd;
p2rec(step) = p(2)*rtd;
p3rec(step) = p(3)*rtd;
pd1rec(step) = pd(1)*rtd;
pd2rec(step) = pd(2)*rtd;
pd3rec(step) = pd(3)*rtd;
pdd1rec(step) = pdd(1)*rtd;
pdd2rec(step) = pdd(2)*rtd;
pdd3rec(step) = pdd(3)*rtd;

hipx(step) = xh(1);
hipy(step) = xh(2);

tau1rec(step) = tau1;
tau2rec(step) = tau2;
tau3rec(step) = tau3;

f32x(step) = f32(1);
f32y(step) = f32(2);

v3x(step)=v3(1);
v3y(step)=v3(2);
%v3x(step)=vc3(1);
%v3y(step)=vc3(2);

%for t = dt:dt:0.3
%for t = dt:dt:0.25
%for t = dt:dt:0.20
%for t = dt:dt:dt
```

```
if (min_flag == on) & (kin_plot == on)
  figure(1)
  clf
  set(1,'Color','white')
plot(x(:,1),x(:,2),'k-')
%title('Kinematics')
axis([-0.4 0.4 0 1.6])
axis equal
  text(x(4,1),x(4,2),'0')
  fig = gcbo;
  hold on
  if file_print == on
    fprintf(fid_kin,'%f\t%f\t%f\t%f\t%f\n',t,x(1,1),x(2,1),x(3,1),x(4,1));
    fprintf(fid_kin,'%f\t%f\t%f\t%f\t%f\n',t,x(1,2),x(2,2),x(3,2),x(4,2));
end
end

%while (leg <= leg_init)
while (f32y(step) <= 500) | (time < 0.1)

  t = t + dt;
  step = step + 1;

  H11 = m1*lc1^2 + I1 + m2*l1^2 + m3*l1^2;
  H12 = (m2*l1*lc2 + m3*l1*l2)*c12;
  H13 = m3*l1*lc3*c13;
  H21 = H12;
  H22 = m2*lc2^2 + I2 + m3*l2^2;
  H23 = m3*l2*lc3*c23;
  H31 = H13;
  H32 = H23;
  H33 = m3*lc3^2+I3;
  H = [H11 H12 H13; H21 H22 H23; H31 H32 H33];

  h111 = 0;
  h122 = m2*l1*lc2*s12 + m3*l1*l2*s12;
  h133 = m3*l1*lc3*s13;
  h211 = - m2*l1*lc2*s12 - m3*l1*l2*s12;
  h222 = 0;
  h233 = m3*l2*lc3*s23;
  h311 = - m3*l1*lc3*s13;
  h322 = - m3*l2*lc3*s23;
  h333 = 0;
  hm = [h111 h122 h133; h211 h222 h233; h311 h322 h333];

  p2b = p(1)-5.0*dtr;% desired knee angle: PPD control

  % Torques: Impedance Control

  gamma = asin(xh(2)/sqrt(xh(1)^2+xh(2)^2));
  xhb = leg_init*[cos(gamma); sin(gamma)];
  xdelta = xh - xhb;
  vdelta = v3 - v3b;
  Kmp = [kp*cos(gamma) 0; 0 kp*sin(gamma)];
  Kmd = [kd*cos(gamma) 0; 0 kd*sin(gamma)];
  tau = -JLh'*(Kmp*xdelta + Kmd*vdelta);
  tau1 = tau(1);
  tau2 = tau(2);
```

```
% Torques: Individual Joint PPD Control

  %tau1 = 0;% ankle torque
 %tau2 = k2*(p2b-p(2)) - d2*(pd(2)-pd(1));% knee torque (relative)
  tau3 = k3*(p3b-p(3)) - d3*(pd(3));% hip torque
 %tau2 = 0;
 %tau3 = 0;

  G1 = g*(m1*lc1 + m2*l1 + m3*l1)*c1;
  G2 = g*(m2*lc2 + m3*l2)*c2;
  G3 = g*m3*lc3*c3;

  G = [G1; G2; G3];

  Q = [tau1 - tau2; tau2 - tau3; tau3] + G;% Q in generalized coords
  % G-term counters gravity

  % Solve for accelerations

  B = Q-hm*pdsq-G;
  pdd = H\B;

  if (trans == on & t < tpeak)
    % prescribe motion of hip or seg 3 c.m.
    %vc3 = vc3i * (sin(t/tpeak*90*dtr))^2; % sine-squared function for smooth buildup
    %pd = JL3\vc3;% joint velocity = inverse of JL3, multiplied by vc3
    v3 = v3i * (sin(t/tpeak*90*dtr))^2; % sine-squared function for smooth buildup
pd2 = JLh\v3;% initial joint velocity = inverse of JL2, multiplied by v3
    pd = [pd2(1); pd2(2); 0];
    p = p + pd*dt;
  else
    % integrate
    pd = pd + pdd*dt;
    pd2 = [pd(1); pd(2)];
    p = p + pd*dt;
  end

  pdsq = [pd(1)^2; pd(2)^2; pd(3)^2];

  s1 = sin(p(1));
  c1 = cos(p(1));
  s2 = sin(p(2));
  c2 = cos(p(2));
  s3 = sin(p(3));
  c3 = cos(p(3));
  c12 = cos(p(1)-p(2));
  c13 = cos(p(1)-p(3));
  c23 = cos(p(2)-p(3));
  s12 = sin(p(1)-p(2));
  s13 = sin(p(1)-p(3));
  s23 = sin(p(2)-p(3));

  x1 = [l1*c1 l1*s1];
  x2 = [l2*c2 l2*s2];
  x3 = [l3*c3 l3*s3];
  x  = [0 0; x1; x1+x2; x1+x2+x3]; % positions of joints and head
  xh = (x1 + x2)';

  leg = sqrt(xh(1)^2 + xh(2)^2);
```

```
  if (min_flag == on) & (kin_plot == on)
  if countplot == nextplot
      countplot = 1;
    figure(1)
    plot(x(:,1),x(:,2),'k-')
      %gtext(num2str(step))
      if file_print == on
    fprintf(fid_kin,'%f\t%f\t%f\t%f\t%f\n',t,x(1,1),x(2,1),x(3,1),x(4,1));
    fprintf(fid_kin,'%f\t%f\t%f\t%f\t%f\n',t,x(1,2),x(2,2),x(3,2),x(4,2));
end
  end
  end

  JLh = [-l1*s1 -l2*s2; l1*c1 l2*c2]; % relates hip linear velocity to ankle and knee vel.
  v3 = JLh * pd2;
  JL3 = [-l1*s1 -l2*s2 -lc3*s3; l1*c1 l2*c2 lc3*c3];
  JL3d = [-l1*c1*pd(1) -l2*c2*pd(2) -lc3*c3*pd(3); -l1*s1*pd(1) -l2*s2*pd(2) -lc3*s3*pd(3)];
  vc3d = JL3*pdd + JL3d*pd;
  f32 = - m3*(gv + vc3d);% force on femur from upper body

  countplot = countplot + 1;

  % Record values

  time(step) = t;
  p1rec(step) = p(1)*rtd;
  p2rec(step) = p(2)*rtd;
  p3rec(step) = p(3)*rtd;
  pd1rec(step) = pd(1)*rtd;
  pd2rec(step) = pd(2)*rtd;
  pd3rec(step) = pd(3)*rtd;
  pdd1rec(step) = pdd(1)*rtd;
  pdd2rec(step) = pdd(2)*rtd;
  pdd3rec(step) = pdd(3)*rtd;

hipx(step) = xh(1);
hipy(step) = xh(2);

  tau1rec(step) = tau1;
  tau2rec(step) = tau2;
  tau3rec(step) = tau3;

  f32x(step) = f32(1);
  f32y(step) = f32(2);

v3x(step)=v3(1);
v3y(step)=v3(2);
%v3x(step)=vc3(1);
%v3y(step)=vc3(2);

end

[min_hipy,min_step] = min(hipy);
min_hipx = hipx(min_step);

fprintf('p1(t=0) = %3.0f\tmin_hipx = %5.4f\n',p1_deg,min_hipx);

if abs(min_hipx) < 0.01
  min_flag = on;
elseif min_hipx > 0.01
```

```
  p1 = p1 + 1*dtr;
  p1_deg = p1*rtd;
elseif min_hipx < -0.01
  p1 = p1 - 1*dtr;
  p1_deg = p1*rtd;
end

iter_count = iter_count + 1;

end

n = size(time);

for i = 1:n(2)
  f32mag(i) = sqrt(f32x(i)^2 + f32y(i)^2);
end

[f32max,j] = max(f32mag);
fprintf('Fmax = %5.0f N\tat t = %f sec\n',f32max,time(j));

text(x(4,1),x(4,2),num2str(t))

figure(1)
hold off

if pos_plot == on
figure(2)
plot(time,p1rec,time,p2rec,time,p3rec)
title('Joint Position')
legend('ankle','knee','hip')
end

if vel_plot == on
figure(3)
plot(time,pd1rec,time,pd2rec,time,pd3rec)
title('Joint Velocity')
legend('ankle','knee','hip')
end

if acc_plot == on
figure(4)
plot(time,pdd1rec,time,pdd2rec,time,pdd3rec)
title('Joint Acceleration')
  legend('ankle','knee','hip')
end

if trq_plot == on
figure(5)
plot(time,tau1rec,time,tau2rec,time,tau3rec)
title('Joint Torque')
legend('ankle','knee','hip')
end

if frc_plot == on
figure(6)
plot(time,f32x,time,f32y,time,f32mag)
title('Hip Force')
legend('X force','Y force','total force')
grid
%axis([0 0.2 -2000 2000])
```

```
end

if loc_plot == on
figure(7)
plot(hipx,hipy)
title('Hip Locus')
axis([-0.5 0.5 0 1])
axis equal
grid
end

%figure(8)
%plot(time,v3x,time,v3y)
%title('Hip Linear Velocity')
%legend('X velocity','Y velocity')

% Save data in files

if file_print == on
fid_pos = fopen('c:\Grant\PhD_Thesis\Run_data\jnt_pos.dat','w');
fid_vel = fopen('c:\Grant\PhD_Thesis\Run_data\jnt_vel.dat','w');
fid_acc = fopen('c:\Grant\PhD_Thesis\Run_data\jnt_acc.dat','w');
fid_trq = fopen('c:\Grant\PhD_Thesis\Run_data\jnt_trq.dat','w');
fid_frc = fopen('c:\Grant\PhD_Thesis\Run_data\hip_frc.dat','w');
  fid_loc = fopen('c:\Grant\PhD_Thesis\Run_data\hip_loc.dat','w');

for i=1:25:n(2)
    fprintf(fid_pos,'%f\t%f\t%f\t%f\n',time(i),p1rec(i),p2rec(i),p3rec(i));
    fprintf(fid_vel,'%f\t%f\t%f\t%f\n',time(i),pd1rec(i),pd2rec(i),pd3rec(i));
    fprintf(fid_acc,'%f\t%f\t%f\t%f\n',time(i),pdd1rec(i),pdd2rec(i),pdd3rec(i));
    fprintf(fid_trq,'%f\t%f\t%f\t%f\n',time(i),tau1rec(i),tau2rec(i),tau3rec(i));
    fprintf(fid_frc,'%f\t%f\t%f\t%f\n',time(i),f32x(i),f32y(i),f32mag(i));
    fprintf(fid_loc,'%f\t%f\t%f\n',time(i),hipx(i),hipy(i));
end

status = fclose(fid_pos);
status = fclose(fid_vel);
  status = fclose(fid_acc);
  status = fclose(fid_trq);
status = fclose(fid_frc);
  status = fclose(fid_loc);
  status = fclose(fid_kin);
end
```

C.2 Fall Simulation System Description File

```
# File: fall3seg.sd

# Author: Grant Schaffner          Original Script: March 30, 1999
#                                  Last Revision: June 6, 1999

# Units are SI (kg,m,sec)

#  Coord. System:  (Left Side)          (Back)        (Ref. Config)
#
#        (head)          o                o             o
```

```
#       trunk            \     ^ Z        |       ^ Z       |
#       u. leg           /     |           \     |        |
#       l. leg          \      -- > X        \    --> Y     |

#-------------------------------------------------
# Mass properties for 50% Male EVA from GEBOD program
#-------------------------------------------------

# Earth:
#gravity = 0 0 -9.807
# Mars:
gravity = 0 0 -3.678

#----- lower leg & ankle joint ----------------------------------
# For Mars: includes mass and inertia of space suit

body = lleg inb = $ground joint = ujoint
  mass = 10.23                    inertia = .1136 .1136 .0143
  bodytojoint = 0 0 -.19          inbtojoint = 0 0 0
  pin = 1 0 0
  pin = 0 1 0
#----- upper leg & knee joint -----------------------------------
# For Mars: includes mass and inertia of space suit

body = uleg inb = lleg joint = pin
  mass = 22.98                    inertia = .4361 .4361 .0553
  bodytojoint = 0 0 -.24          inbtojoint = 0 0 .17
  pin = 0 1 0

#----- trunk & hip joint ----------------------------------------
# Note: joint axes are specified in reverse order (first Y-dirn, then
# X-dirn) in order to simplify specification of prescribed motion.
# For Mars: includes mass and inertia of space suit and PLSS

body = trunk1 inb = uleg joint = ujoint
  mass = 88.39                    inertia = 11.1328 11.0660 2.0827
  bodytojoint = 0 0 -.24          inbtojoint = 0 0 .20
  pin = 0 1 0
  pin = 1 0 0
```

C.3 Fall Simulation C Code

```
/*****************************************************************************

Program: fall3seg (source = fall3seg.c)

Original Code : Grant Schaffner, March 31, 1999
Modifications:

Description: Simulation code for three segment model of human falling
        to side.

*****************************************************************************/

#include <stdio.h>
#include <math.h>

/* Bodies */
```

```
#define GND   -1
#define LLEG   0
#define ULEG   1
#define TRUNK  2

/* Joints */
#define ANK    0
#define KNE    1
#define HIP    2

/* State Variables */
#define NQ     5
#define NU     5
#define NEQ    (NQ+NU)
#define NJNT   3

/* Constraints */
#define NC     2
#define NLC    0

/* Integration Parameters */
/*#define DT 0.005*/ /* default time step */
#define DT 0.001 /* short time step */

#define TOL 1e-7
#define CTOL 1e-5

/* Number of simulation steps */

#define NSTEP 202
/*#define NSTEP 2*/ /* short diagnostic run */

/* Baumgarte stabilization constant ( for sdstab() )*/

#define A  20

/* Miscellaneous Constants */

#define OFF      0
#define ON       1

/* Segment Lengths */
/* 5% Female */
/*
#define L1  0.32
#define L2  0.40
#define L2CG_HIP 0.19
*/
/* 50% Female */
/*
#define L1  0.35
#define L2  0.43
#define L2CG_HIP 0.20
*/
/* 95% Female */
/*
#define L1  0.38
#define L2  0.47
#define L2CG_HIP 0.22
*/
```

```
/* 5% Male */
/*
#define L1  0.33
#define L2  0.41
#define L2CG_HIP 0.19
*/
/* 50% Male */

#define L1  0.36
#define L2  0.44
#define L2CG_HIP 0.20

/* 95% Female */
/*
#define L1  0.39
#define L2  0.47
#define L2CG_HIP 0.22
*/

/* Starting Values (all relative to vertical = generalized coords,
   except for Hip Y, which is referenced to the Y-Z plane. */

/* 5th Percentile Male and Female ----------------------------*/
/*
#define ANK_X_ST     8.24
#define ANK_Y_ST    -3.34
#define HIP_X_ST    11.40
#define HIP_Y_ST   -30.00

#define ANKV_X_ST    41.20
#define ANKV_Y_ST   -21.10
#define HIPV_X_ST    36.20
#define HIPV_Y_ST     0.00
*/
/* 50th Percentile Male and Female ----------------------------*/

#define ANK_X_ST     9.01
#define ANK_Y_ST    -3.74
#define HIP_X_ST    12.05
#define HIP_Y_ST   -30.00

#define ANKV_X_ST    44.05
#define ANKV_Y_ST   -22.30
#define HIPV_X_ST    36.70
#define HIPV_Y_ST     0.00

/* 95th Percentile Male and Female ----------------------------*/
/*
#define ANK_X_ST     9.78
#define ANK_Y_ST    -4.13
#define HIP_X_ST    12.70
#define HIP_Y_ST   -30.00

#define ANKV_X_ST    46.90
#define ANKV_Y_ST   -23.50
#define HIPV_X_ST    37.20
#define HIPV_Y_ST     0.00
*/
/* Joint Control Parameters */
```

```
#define BDAMP_ANK_X      0.0   /* N-m/(rad/sec) */
#define KROT_ANK_X       0.0   /* N-m/rad */
#define BIAS_ANK_X       0.0   /* desired position */
/*#define BDAMP_ANK_X     20.0 */  /* N-m/(rad/sec) */
/*#define KROT_ANK_X     200.0 */  /* N-m/rad */

#define BDAMP_ANK_Y      0.0   /* N-m/(rad/sec) */
#define KROT_ANK_Y       0.0   /* N-m/rad */
#define BIAS_ANK_Y       0.0   /* desired position */
/*#define BDAMP_ANK_Y     20.0 */  /* N-m/(rad/sec) */
/*#define KROT_ANK_Y     200.0 */  /* N-m/rad */

#define BDAMP_KNE      100.0   /* N-m/(rad/sec) */
#define KROT_KNE      1000.0   /* N-m/rad */
/*#define BIAS_KNE        0.0 */   /* desired position */

#define BDAMP_HIP_X      0.0   /* N-m/(rad/sec) */
#define KROT_HIP_X      20.0   /* N-m/rad */
#define BIAS_HIP_X      35.0   /* desired position (generalized coord) */
/*#define BDAMP_HIP_X     20.0*/   /* N-m/(rad/sec) */
/*#define KROT_HIP_X     200.0*/   /* N-m/rad */

/*#define BDAMP_HIP_Y      0.0 */  /* N-m/(rad/sec) */
/*#define KROT_HIP_Y       0.0 */  /* N-m/rad */
/*#define BIAS_HIP_Y       0.0 */  /* desired position (generalized coord) */
#define BDAMP_HIP_Y      10.0   /* N-m/(rad/sec) */
#define KROT_HIP_Y     1200.0   /* N-m/rad */
#define BIAS_HIP_Y      -30.0   /* desired position (generalized coord) */

/* Impedance Control Parameters */

#define KPX   5000.0
#define KDX    100.0
#define KPZ   1300.0
#define KDZ    100.0

/* Ground Contact Parameters */

/*#define KGND  90400.0*/  /* Earth / Mars 100% (Robinovitch et al., 1991) */
/*#define KGND  72320.0*/  /* Mars 80% */
/*#define KGND  54240.0*/  /* Mars 60% */
/*#define KGND  36160.0*/  /* Mars 40% */
#define KGND  18080.0  /* Mars 20% */
#define BGND    756.0  /* Damping constant (Robinovitch et al., 1991) */

/* Define external symbolic constants  */


/* Declare external variable types */
int step,jtcontrol[5],impcontrol,imp_start,imp_end,imp_flag;
double pi, dtr, rtd;
double accel[NU];
double hip_uleg[3], hip_pos[3], hip_start[3], hip_vel[3], hip_frc[3];
double l_init;

/* Joint data files */
char ankx[30]="ankx.dat",anky[30]="anky.dat",kne[30]="kne.dat",hipx[30]="hipx.dat",hipy[30]="hipy.dat";
FILE *ankx_ptr,*anky_ptr,*kne_ptr,*hipx_ptr,*hipy_ptr;
char hipp[30]="hipp.dat",hipv[30]="hipv.dat",hipf[30]="hipf.dat";
FILE *hipp_ptr,*hipv_ptr,*hipf_ptr;
```

```
char *dof[18] = {"Ankle X Pos","Ankle Y Pos","Knee Pos","Hip X Pos","Hip Y Pos",
        "Ankle X Vel","Ankle Y Vel","Knee Vel","Hip X Vel","Hip Y Vel"};

/* Function prototypes */

void printerrors(int nval, double array[]);

/* Declare External Functions */

/*-------------------------------------------------------------------------*/
/*                    Main program                                         */
/*-------------------------------------------------------------------------*/

main ()
{

 /* Declare variables local to main. */

 int i, lock[NU], fcnt, err;
 int j, flag;
 double t, y[NEQ], dy[NEQ], q[NQ], u[NU];
 double torque[NJNT][3],force[NJNT][3];
 double perrs[NC], verrs[NC], aerrs[NC];

 /* Reminder about external variables. */

 extern int step,jtcontrol[5],impcontrol;
 extern double pi, dtr, rtd;
 extern double accel[NU];
 extern double hip_uleg[3],hip_pos[3],hip_start[3],hip_vel[3],hip_frc[3];

 printf("\n  _____");
 printf("\n  |                                    |");
 printf("\n  |  Simulation of 3 segment fall      |");
 printf("\n  |____________________________________|\n\n");

 pi = acos(-1.0);
 dtr = pi/180.0;
 rtd = 180.0/pi;

 /* Set control swiches */

 jtcontrol[sdindx(ANK,0)] = OFF;  /* ankle X */
 jtcontrol[sdindx(ANK,1)] = OFF;  /* ankle Y */
 jtcontrol[sdindx(KNE,0)] = OFF;  /* knee */
 jtcontrol[sdindx(HIP,1)] = ON;  /* hip X, Note: axes reversed X=1 Y=0 */
 jtcontrol[sdindx(HIP,0)] = ON;  /* hip Y */

 impcontrol = ON; /* Impedance Control */

 /* Initialize flags */

 imp_start = OFF; /* Start of impact switch */
 imp_end = OFF;  /* End of impact switch */
 imp_flag = OFF;  /* Flag for printing state at impact only once */

 /* Open joint files */

 openfiles();
```

```
/* Optional data file headers - leave out to simplify MATLAB task? */

/*printhdrs();*/

/* Initialize simulation. */

sdinit();
sdprinterr(stdout);

printf("Simulation initialized.\n\n");

/* Set initial conditions. */

t = 0.0;
step = 0;

hip_uleg[0] = 0;  /* position of hip jt wrt upper leg */
hip_uleg[1] = 0;
hip_uleg[2] = L2CG_HIP;

hip_frc[0] = 0;
hip_frc[1] = 0;
hip_frc[2] = 0;

/*sdstab(2*A, A*A);*/ /* Activates Baumgarte integration stabilization */

initconds(t,y);

for (i=0 ; i < NU ; i++) dy[NU+i] = 0.0; /* sets accelerations to 0 */

sdstate(t,y,&y[NQ]);
sdprinterr(stdout);

/* printstate(t,y); */
printf("\nInitialized general coordinates:\n");
printgeneral(t,y);

printf("Kinematics Ready.\n\n");

sdderiv(dy,&dy);
sdprinterr(stdout);

/* call sdmotion once with dt = 0 to evaluate derivatives at t=0 */

sdmotion(&t,y,dy,0.0,CTOL,TOL,&flag,&err);
sdprinterr(stdout);
if(err != 0){
  printf("\a\n Problem with integrator at step %d! Error no.: %d\n\a\a\a",step,err);
  sdperr(perrs);
  printf("Position Errors:\n");
  printerrors(NC,perrs);
  sdverr(verrs);
  printf("Velocity Errors:\n");
  printerrors(NC,verrs);
  sdaerr(aerrs);
  printf("Acceleration Errors:\n");
  printerrors(NC,aerrs);
  exit();
 }
```

```
for (i = 0 ; i < NU ; i++) accel[i] = dy[NU+i];

printf("Kinematics Analysis.....");

flag = 0;

/* Kinematics Analysis Loop ########################################################## */

/*for(step = 1 ; step < NSTEP ; step++){*/

while(imp_end == OFF && t <= 2.0){

 sdreac(force,torque);

 printdata(t,y,dy,torque);

 /* Perform motion integration. */

 sdmotion(&t,y,dy,DT,CTOL,TOL,&flag,&err);
 sdprinterr(stdout);
 if(err != 0){
  printf("\a\n Problem with integrator at step %d! Error no.: %d\n\a\a\a",step,err);
  sdperr(perrs);
  printf("Position Errors:\n");
  printerrors(NC,perrs);
  sdverr(verrs);
  printf("Velocity Errors:\n");
  printerrors(NC,verrs);
  sdaerr(aerrs);
  printf("Acceleration Errors:\n");
  printerrors(NC,aerrs);
  exit();
 }
 for (i = 0 ; i < NU ; i++) accel[i] = dy[NU+i];

 if(hip_pos[2] > 0.0 && imp_start == ON){
  imp_end = ON;
 }

 if(imp_start == ON && imp_flag == OFF){
  imp_flag = ON;
  printf("\n\nGeneralized coords at initial impact:\n");
  printgeneral(t,y);
 }

}

/* Record beyond limit (ankle X > 90 deg) values */

sdreac(force,torque);

printdata(t,y,dy,torque);

printf("done.\n\n"); /* end of kinematics analysis */

/*printgeneral(t,y);*/

sdprinterr(stdout);

}
```

```
/*-------------------------------------------------------------------------*/
/*                      Functions                                          */
/*-------------------------------------------------------------------------*/

/*****************************************************************************
  openfiles

  This function opens all the kinematics and torque data files.
  *****************************************************************************/

openfiles()
{

  ankx_ptr = fopen(ankx,"w");
  if(ankx_ptr == NULL) {
            printf("Oops. Unable to open ankle X file. Exiting...\n");
            exit(-1);
            }

  anky_ptr = fopen(anky,"w");
  if(anky_ptr == NULL) {
            printf("Oops. Unable to open ankle Y file. Exiting...\n");
            exit(-1);
            }

  kne_ptr = fopen(kne,"w");
  if(kne_ptr == NULL) {
            printf("Oops. Unable to open knee file. Exiting...\n");
            exit(-1);
            }

  hipx_ptr = fopen(hipx,"w");
  if(hipx_ptr == NULL) {
            printf("Oops. Unable to open hip X file. Exiting...\n");
            exit(-1);
            }

  hipy_ptr = fopen(hipy,"w");
  if(hipy_ptr == NULL) {
            printf("Oops. Unable to open hip Y file. Exiting...\n");
            exit(-1);
            }

  hipp_ptr = fopen(hipp,"w");
  if(hipp_ptr == NULL) {
            printf("Oops. Unable to open hip pos file. Exiting...\n");
            exit(-1);
            }

  hipv_ptr = fopen(hipv,"w");
  if(hipv_ptr == NULL) {
            printf("Oops. Unable to open hip vel file. Exiting...\n");
            exit(-1);
            }

  hipf_ptr = fopen(hipf,"w");
  if(hipf_ptr == NULL) {
            printf("Oops. Unable to open hip force file. Exiting...\n");
```

```
            exit(-1);
            }

}

/*****************************************************************************

  printhdrs

  This function prints the first line (headers) of each output data file.

*****************************************************************************/

printhdrs()
{

  fprintf(ankx_ptr,"Time\t\tPosition\tVelocity\tAcceleration\tTorque\n");
  fprintf(anky_ptr,"Time\t\tPosition\tVelocity\tAcceleration\tTorque\n");
  fprintf(kne_ptr,"Time\t\tPosition\tVelocity\tAcceleration\tTorque\n");
  fprintf(hipx_ptr,"Time\t\tPosition\tVelocity\tAcceleration\tTorque\n");
  fprintf(hipy_ptr,"Time\t\tPosition\tVelocity\tAcceleration\tTorque\n");
  fprintf(hipp_ptr,"Time\t\tX Position\tY Position\tZ Position\n");
  fprintf(hipv_ptr,"Time\t\tX Velocity\tY Velocity\tZ Velocity\n");
  fprintf(hipf_ptr,"Time\t\tX Force\tY Force\tZ Force\n");

}

/*****************************************************************************

  printdata

  Prints data to files.

*****************************************************************************/

printdata(t,y,dy,trq)
double t, y[NEQ], dy[NEQ], trq[NJNT][3];
{

   fprintf(ankx_ptr,"%f\t%f\t%f\t%f\t%f\n",t,\
               y[sdindx(ANK,0)]*rtd,y[NQ+sdindx(ANK,0)]*rtd,dy[NU+sdindx(ANK,0)]*rtd,
               trq[ANK][0]);

   fprintf(anky_ptr,"%f\t%f\t%f\t%f\t%f\n",t,\
               y[sdindx(ANK,1)]*rtd,y[NQ+sdindx(ANK,1)]*rtd,dy[NU+sdindx(ANK,1)]*rtd,
               trq[ANK][1]);

   fprintf(kne_ptr,"%f\t%f\t%f\t%f\t%f\n",t,\
               y[sdindx(KNE,0)]*rtd,y[NQ+sdindx(KNE,0)]*rtd,dy[NU+sdindx(KNE,0)]*rtd,
               trq[KNE][1]); /* Note: trq[KNE][?] includes X, Y, and Z components */

   fprintf(hipx_ptr,"%f\t%f\t%f\t%f\t%f\n",t,\
               y[sdindx(HIP,1)]*rtd,y[NQ+sdindx(HIP,1)]*rtd,
               dy[NU+sdindx(HIP,1)]*rtd,trq[HIP][0]); /* Note: trq[][] in X,Y,Z order */

   fprintf(hipy_ptr,"%f\t%f\t%f\t%f\t%f\n",t,\
               y[sdindx(HIP,0)]*rtd,
               y[NQ+sdindx(HIP,0)]*rtd,dy[NU+sdindx(HIP,0)]*rtd,trq[HIP][1]);

   /* The following prints the joint data in pseudo-generalized coordinates */
```

```
  /*
  fprintf(hipx_ptr,"%f\t%f\t%f\t%f\t%f\n",t,\
                y[sdindx(HIP,1)]*rtd + y[sdindx(ANK,0)]*rtd,y[NQ+sdindx(HIP,1)]*rtd,
                dy[NU+sdindx(HIP,1)]*rtd,trq[HIP][0]);

  fprintf(hipy_ptr,"%f\t%f\t%f\t%f\t%f\n",t,\
                y[sdindx(HIP,0)]*rtd + y[sdindx(KNE,0)]*rtd + y[sdindx(ANK,1)]*rtd,
                y[NQ+sdindx(HIP,0)]*rtd,dy[NU+sdindx(HIP,0)]*rtd,trq[HIP][1]);
  */

  fprintf(hipp_ptr,"%f\t%f\t%f\t%f\n",t,hip_pos[0],hip_pos[1],hip_pos[2]);

  fprintf(hipv_ptr,"%f\t%f\t%f\t%f\n",t,hip_vel[0],hip_vel[1],hip_vel[2]);

  fprintf(hipf_ptr,"%f\t%f\t%f\t%f\n",t,hip_frc[0],hip_frc[1],hip_frc[2]);
}

/*****************************************************************************

  initconds

  This function sets up the initial conditions. The hand position is set to
  xstart, ystart values. This is referenced to the original position of the
  hand, with the arm hanging straight down. The x and y velocities of the
  hand are also set according to the value of omega (ang vel) value. Pass
  in y with an initial guess to control the assembly solution and improve
  convergence. On return, y should be a fully compatible state vector, unless
  an error is received.

*****************************************************************************/

initconds(t,y)
double t, y[];
{
  int i;
  double ankposX, ankposY, knepos, hipposX, hipposY;

  /* Setup initial conditions - positions and velocities */

  printf("Initial Conditions.....");

  /* Initial Configuration */

  for (i = 0 ; i < NEQ ; i++) y[i] = 0.0;
  for (i = 0 ; i < NU ; i++) accel[i] = 0.0;

  /* Note: Angles are measured as rotation of the segment coord. system
  relative to the inboard segment's coord. system. */

  ankposX = ANK_X_ST*dtr;      /* ankle X position */
  ankposY = ANK_Y_ST*dtr;      /* ankle Y position */
  knepos  = -ankposY-asin(L1/L2*sin(ankposY)); /* knee position */
  hipposY = HIP_Y_ST*dtr - knepos - ankposY;      /* hip Y position */
  hipposX = atan(cos(hipposY)*tan(HIP_X_ST*dtr-ankposX)); /* hip X position */

  y[sdindx(ANK,0)] = ankposX;
  y[sdindx(ANK,1)] = ankposY;
  y[sdindx(KNE,0)] = knepos;
  y[sdindx(HIP,1)] = hipposX;
  y[sdindx(HIP,0)] = hipposY;
```

```
 l_init = sqrt( L1*L1 + L2*L2 - 2*L1*L2*cos(180*dtr+knepos) );
 /* printf("\n\nl_init = %f\n\n",l_init);*/

 /* Initial Velocity */

 y[NQ+sdindx(ANK,0)] = ANKV_X_ST*dtr;
 y[NQ+sdindx(ANK,1)] = ANKV_Y_ST*dtr;
 y[NQ+sdindx(KNE,0)] = -2*ANKV_Y_ST*dtr;
 y[NQ+sdindx(HIP,1)] = HIPV_X_ST*dtr - ANKV_X_ST*dtr;
 y[NQ+sdindx(HIP,0)] = HIPV_Y_ST*dtr + 2*ANKV_Y_ST*dtr - ANKV_Y_ST*dtr;

 printf("done.\n\n"); /* end of initial conditions */

}

/**************************************************************************

 sdumotion

 If enabled, this function prescribes the motion of selected degrees-of-freedom.

**************************************************************************/

void sdumotion(t,q,u)
double t,q[NQ],u[NU];
{
 /*
 double ankYacc,kneacc,hipYacc,ankYvel,knevel,hipYvel,ankYpos,knepos,hipYpos;

 ankYacc = accel[sdindx(ANK,1)];
 kneacc = - 2*ankYacc;
 hipYacc = - ankYacc - kneacc;

 ankYvel = u[sdindx(ANK,1)];
 knevel = - 2*ankYvel;
 hipYvel = - ankYvel - knevel;

 ankYpos = q[sdindx(ANK,1)];
 knepos = - 2*ankYpos;
 hipYpos = - ankYpos - knepos;

 sdpresacc(KNE,0,kneacc);
 sdpresacc(HIP,0,hipYacc);
 */
 /* These next calls are only effective if sdstab() has been set */
 /* Reminder: sdprespos can be a function of time only */
 /*
  sdpresvel(KNE,0,knevel);
  sdpresvel(HIP,0,hipYvel);
 */

}

/**************************************************************************

  sduforce

  This routine computes and applies the forces acting in the system. It must
  always be included, when the Simplified Analysis Routines are used, because
```

```
  they will make calls to sduforce. This is the case even if the sdforce
  function is unused (empty).

*****************************************************************************/

void sduforce(t,q,u)
double t,q[NQ],u[NU];
{
 double trq[NQ],kne_des,knev_des,hipx_des,hipxv_des,hipy_des,hipyv_des;
 double q1,q2,qd1,qd2;
 double dx, dz; /* deviation from medial-lateral plane */
 double c1,c12,s1,s12;
 double J11, J12, J21, J22;  /* Jacobian Matrix Components*/
 double trq_p_anky,trq_d_anky,trq_p_kne,trq_d_kne;
 double hip_frc_uleg[3],trq_trunk[3];
 double hip_dx,hip_dy,hip_dz; /* ground penetration */
 double beta;

 /* Control of Lower Body Joints */

 /* ANKLE X */

 if(jtcontrol[sdindx(ANK,0)] == ON){
  trq[sdindx(ANK,0)] = - KROT_ANK_X*(q[sdindx(ANK,0)]-(BIAS_ANK_X)*dtr)
                - BDAMP_ANK_X*u[sdindx(ANK,0)];
  sdhinget(ANK,0,trq[sdindx(ANK,0)]);
 }

 /* ANKLE Y */

 if(jtcontrol[sdindx(ANK,1)] == ON){
  trq[sdindx(ANK,1)] = - KROT_ANK_Y*(q[sdindx(ANK,0)]-(BIAS_ANK_Y)*dtr)
                - BDAMP_ANK_Y*u[sdindx(ANK,0)];
  sdhinget(ANK,1,trq[sdindx(ANK,1)]);
 }

 /* KNEE */

 if(jtcontrol[sdindx(KNE,0)] == ON){
  kne_des = -2*q[sdindx(ANK,1)];
  knev_des = -2*u[sdindx(ANK,1)];
  trq[sdindx(KNE,0)] = - KROT_KNE*(q[sdindx(KNE,0)] - kne_des)
                - BDAMP_KNE*(u[sdindx(KNE,0)] - knev_des);
  sdhinget(KNE,0,trq[sdindx(KNE,0)]);
 }

 /* HIP X */

 if(jtcontrol[sdindx(HIP,1)] == ON){
  beta = q[sdindx(ANK,1)] + q[sdindx(KNE,0)] + q[sdindx(HIP,0)];
  hipx_des = atan(cos(beta)*tan(BIAS_HIP_X*dtr - q[sdindx(ANK,0)]));
  /*hipx_des = BIAS_HIP_X*dtr - q[sdindx(ANK,0)];*/
  hipxv_des = - u[sdindx(ANK,0)];
  trq[sdindx(HIP,1)] = - KROT_HIP_X*(q[sdindx(HIP,1)] - hipx_des)
                - BDAMP_HIP_X*(u[sdindx(HIP,1)] - hipxv_des);
  sdhinget(HIP,1,trq[sdindx(HIP,1)]);
 }

 /* HIP Y */
```

```
if(jtcontrol[sdindx(HIP,0)] == ON){
 hipy_des = BIAS_HIP_Y*dtr - q[sdindx(ANK,1)] - q[sdindx(KNE,0)];
 hipyv_des = - u[sdindx(ANK,1)] - u[sdindx(KNE,0)];
 trq[sdindx(HIP,0)] = - KROT_HIP_Y*(q[sdindx(HIP,0)] - hipy_des)
              - BDAMP_HIP_Y*(u[sdindx(HIP,0)] - hipyv_des);
 sdhinget(HIP,0,trq[sdindx(HIP,0)]);
}

/* Impedance Control Scheme */

if(impcontrol == ON && imp_start == OFF){

 q1 = q[sdindx(ANK,1)];
 q2 = q[sdindx(KNE,0)];
 qd1 = u[sdindx(ANK,1)];
 qd2 = u[sdindx(KNE,0)];

 s1 = sin(q1);
 c1 = cos(q1);
 s12 = sin(q1+q2);
 c12 = cos(q1+q2);

 dx = L1*s1 + L2*s12 - 0;
 dz = L1*c1 + L2*c12 - l_init;

 J11 = L1*c1 + L2*c12;
 J12 = L2*c12;
 J21 = -L1*s1 - L2*s12;
 J22 = -L2*s12;

 trq_p_anky = J11*KPX*dx + J21*KPZ*dz;
 trq_d_anky = KDX*(J11*J11*qd1+J11*J12*qd2) + KDZ*(J21*J21*qd1+J21*J22*qd2);
 trq_p_kne  = J12*KPX*dx + J22*KPZ*dz;
 trq_d_kne  = KDX*(J11*J12*qd1+J12*J12*qd2) + KDZ*(J21*J22*qd1+J22*J22*qd2);

 trq[sdindx(ANK,1)] = - (trq_p_anky + trq_d_anky); /* + trq[sdindx(HIP,0)]; */
 trq[sdindx(KNE,0)] = - (trq_p_kne + trq_d_kne); /* + trq[sdindx(HIP,0)]; */
 trq_trunk[0] = 0;
 trq_trunk[1] = - KROT_HIP_Y*(q[sdindx(HIP,0)] - hipy_des)
          - BDAMP_HIP_Y*(u[sdindx(HIP,0)] - hipyv_des);
 trq_trunk[2] = 0;
 sdhinget(ANK,1,trq[sdindx(ANK,1)]);
 sdhinget(KNE,0,trq[sdindx(KNE,0)]);
}

/* Ground reaction force during hip impact */

sdpos(ULEG,hip_uleg,hip_pos);
sdvel(ULEG,hip_uleg,hip_vel);
if(hip_pos[2] < 0.0){
 if(imp_start == OFF){
  imp_start = ON;
  hip_start[0] = hip_pos[0];
  hip_start[1] = hip_pos[1];
  hip_start[2] = hip_pos[2];
 }
 hip_dx = hip_pos[0] - hip_start[0];
 hip_dy = hip_pos[1] - hip_start[1];
 hip_dz = hip_pos[2] - hip_start[2];
```

```
  hip_frc[0] = - KGND*hip_dx - BGND*hip_vel[0];
  hip_frc[1] = - KGND*hip_dy - BGND*hip_vel[1];
  hip_frc[2] = - KGND*hip_dz - BGND*hip_vel[2];

  sdtrans(GND,hip_frc,ULEG,hip_frc_uleg);
  sdpointf(ULEG,hip_uleg,hip_frc_uleg);
 }
 else{
  hip_frc[0] = 0;
  hip_frc[1] = 0;
  hip_frc[2] = 0;
 }

}


/*************************************************************************

  printstate

  Prints out state array (positions and velocities of all dof).

*************************************************************************/

printstate(t,y)
double t,y[NEQ];
{
 int i;
 printf("time = %f\n",t);
 for (i = 0 ;  i< NQ ; i++) {
  /* Convert radians to degrees */
  printf("%s = %f\t\t%s = %f\n",dof[i],y[i]*rtd,dof[NQ+i],y[NQ+i]*rtd);
 }
 printf("\n");
}

/*************************************************************************

  printgeneral

  Prints out state in generalized coords (positions and velocities wrt vertical).

*************************************************************************/

printgeneral(t,y)
double t,y[NEQ];
{
 int i;
 double ankposX, ankposY, knepos, hipposX, hipposY, hipXchk;
 double r3[3];
 double q1, q2, q3, q4, q5;
 double beta;

 r3[0]=0;
 r3[1]=0;
 r3[2]=1;

 /*sdorient(TRUNK,r3);*/
 sdtrans(TRUNK,r3,GND,r3);
```

```
 q1 = y[sdindx(ANK,0)];
 q2 = y[sdindx(ANK,1)];      /* ankle Y position */
 q3 = y[sdindx(KNE,0)];      /* knee position */
 q4 = y[sdindx(HIP,0)];      /* hip Y position */
 q5 = y[sdindx(HIP,1)];

 beta = q2 + q3 + q4;

 ankposX = q1;
 ankposY = q2;
 knepos  = q3;
 hipposX = atan(tan(q5)/cos(beta)) + q1;   /* hip X position (in gnd frame) */
 hipXchk = atan(-r3[1]/r3[2]);             /* hip X position (in gnd frame) */
 hipposY = beta;                           /* hip Y position (wrt Y-Z plane) */

 printf("time = %f\n",t);
 printf("Ankle X Pos = %5.1f (90)\n",ankposX*rtd);
 printf("Ankle Y Pos = %5.1f (-33.8)\n",ankposY*rtd);
 printf("Knee  Y Pos = %5.1f\n",knepos*rtd);
 printf("Hip   X Pos = %5.1f (35.1)\n",hipposX*rtd);
 /*printf("Hip   X Pos = %5.1f (check)\n",hipXchk*rtd);*/
 printf("Hip   Y Pos = %5.1f (~ -30)\n",hipposY*rtd);
 printf("\n");
}

/*****************************************************************************

  printerrors

  Prints out an array of numbers.

*****************************************************************************/

void printerrors(int nval, double array[])
{
 int i;
 for (i = 0 ;  i< nval ; i++){
   if (array[i] > .0000001) printf("[%d] = %f\n", i, array[i]);
  }
 printf("\n");
}
```

Appendix D *Computer Code used to Modify Endosteal Boundaries and Cancellous Element Densities*

D.1 Modification of Endosteal Boundary Point Coordinates

```
 Program spaceadj
c**************************************************************************
c     Version: 1.0
c     Original Code by:  Grant Schaffner (6/26/99)
c     Description:  This program takes a series of point coordinates from files
c     defining curves. Each point is displaced outward along the angular
c     bisector defined by the two neighbouring points by an amount equal to a
c     certain percent increase in the average radius of the curve.
c**************************************************************************
parameter (maxpoints=1000)
parameter (dneck=0.0035) !  .35% dia. incr. per month (Neck)
parameter (dtroch=0.0020) ! .20% dia. incr. per month (Trochanteric)
parameter (dshaft=0.0050) ! .50% dia. incr. per month (Shaft)

character nfnam*40,tfile*80,pifile*80,pofile*80
character qifile*40,qofile*40
character ifnam*40,ofnam*40
real x(maxpoints), y(maxpoints), z(maxpoints) ! Original endosteal coords
real xcent(50),ycent(50),zcent(50),darea(50) ! Centroid coordinates for each slice
real ox(maxpoints), oy(maxpoints), oz(maxpoints) ! Outer coords
real dx(maxpoints), dy(maxpoints), dz(maxpoints)
real tx(maxpoints), ty(maxpoints), tz(maxpoints) ! Translated endost coords
real px(maxpoints), py(maxpoints), ptx(maxpoints), pty(maxpoints) ! Planar coords
real pox(maxpoints), poy(maxpoints)
real cox(maxpoints), coy(maxpoints), coz(maxpoints) ! Coordinates relative to centroid
creal ctx(maxpoints), cty(maxpoints), ctz(maxpoints)

real r(maxpoints), rmean
integer nfiles,tunit,piunit,pounit,qiunit,qounit,count
integer onpts

pi = acos(-1.0)
dtr = pi/180
rtd = 180/pi

write(6,*)'Input the no. of months of weightlessness:'
read(5,*)nmonths

open(unit=13,file='FORTNAMES_inn',status='old')
open(unit=14,file='FORTNAMES_out',status='old')

read(13,*) nfiles!THE TOTAL NUMBER OF FILES
read(14,*) ndummy

do 600 nslice=1,nfiles,1!Loop for total no. of slices
  xtot = 0
  ytot = 0
  ztot = 0
  rtot = 0

  read(13,9) ifnam
  read(14,9) ofnam
  nfnam = ifnam(10:16)
  write(6,*)'file = ',nfnam

c     Read inner boundary (endosteal) coords

  open(unit=100+nslice,file=ifnam,status='old')
  read(100+nslice,*)npts
c  write(6,*)'npts = ',npts

  do 100 i=1,npts
    read(100+nslice,*)x(i),y(i),z(i)
    xtot = xtot + x(i)
    ytot = ytot + y(i)
```

```
      ztot = ztot + z(i)
  100 continue

    close(100+nslice)

c     Read outer boundary (periosteal) coords

    open(unit=200+nslice,file=ofnam,status='old')
    read(200+nslice,*)onpts

    do 150 i=1,onpts
      read(200+nslice,*)ox(i),oy(i),oz(i)
  150 continue

    close(200+nslice)

c     Calculate centroid

    xc = xtot/npts
    yc = ytot/npts
    zc = ztot/npts

    xcent(nslice) = xc
    ycent(nslice) = yc
    zcent(nslice) = zc

c   write(6,*)'xc = ',xc
c   write(6,*)'yc = ',yc
c   write(6,*)'zc = ',zc

c     Determine average radius and distance of point from Y-axis
c     for endosteal boundary

    count = 0
    gtot = 0

    do 200 i=1,npts
      dx(i) = x(i) - xc
      dy(i) = y(i) - yc
      dz(i) = z(i) - zc
      r(i) = sqrt(dx(i)**2 + dy(i)**2 + dz(i)**2)
      rtot = rtot + r(i)
      if(dx(i) .ge. 0.1)then
  gtot = gtot + atan(dz(i)/dx(i))
  count = count + 1
      endif

c           Project points to 2-D plane with centroid
c           as origin and points located relative to centroid.

      px(i)  = sqrt(dx(i)**2 + dz(i)**2)
      if(x(i) .lt. xc)then
  px(i) = - px(i)
      endif
      py(i)  = dy(i)
  200 continue

    gamma = gtot/count! Angle of curve plane to horizontal
    gdeg = gamma * rtd

c   write(6,*)'Curve=',nslice,'  Angle to horiz=',gdeg

    rmean = rtot/npts

C     Calculate pt move distance according to region of femur

    if(nslice .ge. 21) then! head
      ptdisp = 0
    elseif(nslice .ge. 16) then ! neck
      ptdisp = rmean * nmonths * dneck/2
    elseif(nslice .ge. 10) then ! trochanter
      ptdisp = rmean * nmonths * dtroch/2
    else! shaft
      ptdisp = rmean * nmonths * dshaft/2
    endif

c   do 800 ki = 1,nmonths! Loop for changes during each month

    do 300 n = 1,npts-1

      if(n .eq. 1)then
  dx1 = px(npts-1) - px(1)
  dy1 = py(npts-1) - py(1)
```

```
    else
dx1 = px(n-1) - px(n)
dy1 = py(n-1) - py(n)
    endif

    dx2 = px(n+1) - px(n)
    dy2 = py(n+1) - py(n)

    ax1 = abs(dx1)
    ay1 = abs(dy1)
    ax2 = abs(dx2)
    ay2 = abs(dy2)

    if(ax1 .le. ay1 .and. ax1 .lt. 0.1)then
if(dy1 .gt. 0) then
  alpha = 90*dtr
else
  alpha = 270*dtr
endif
    elseif(ay1 .lt. 0.1)then
if(dx1 .gt. 0) then
  alpha = 0
else
  alpha = 180*dtr
endif
    elseif(ax1 .lt. 0.1 .and. ay1 .lt. 0.1)then
write(6,*)'Points too close together!!!'
write(6,*)'Curve=',nslice,' Point=',n
alpha = 0!???
    else
if(dx1 .gt. 0 .and. dy1 .gt. 0)then !1st quadrant
  alpha = atan(ay1/ax1)
elseif(dx1 .lt. 0 .and. dy1 .gt. 0)then !2nd quadrant
  alpha = 180*dtr - atan(ay1/ax1)
elseif(dx1 .lt. 0 .and. dy1 .lt. 0)then !3rd quadrant
  alpha = 180*dtr + atan(ay1/ax1)
else!4th quadrant
  alpha = 360*dtr - atan(ay1/ax1)
endif
    endif

    if(ax2 .le. ay2 .and. ax2 .lt. 0.1)then
if(dy2 .gt. 0) then
  beta = 90*dtr
else
  beta = 270*dtr
endif
    elseif(ay2 .lt. 0.1)then
if(dx2 .gt. 0) then
  beta = 0
else
  beta = 180*dtr
endif
    elseif(ax2 .lt. 0.1 .and. ay2 .lt. 0.1)then
write(6,*)'Points too close together!!!'
write(6,*)'Curve=',nslice,' Point=',n
q=180*dtr!???
    else
if(dx2 .gt. 0 .and. dy2 .gt. 0)then !1st quadrant
  beta = atan(ay2/ax2)
elseif(dx2 .lt. 0 .and. dy2 .gt. 0)then !2nd quadrant
  beta = 180*dtr - atan(ay2/ax2)
elseif(dx2 .lt. 0 .and. dy2 .lt. 0)then !3rd quadrant
  beta = 180*dtr + atan(ay2/ax2)
else!4th quadrant
  beta = 360*dtr - atan(ay2/ax2)
endif
    endif

    theta = (alpha+beta)/2

    deltax = ptdisp*cos(theta)
    deltay = ptdisp*sin(theta)

    tapx = px(n) + deltax
    tapy = py(n) + deltay
    tarad = sqrt(tapx**2+tapy**2)

    tbpx = px(n) - deltax
    tbpy = py(n) - deltay
    tbrad = sqrt(tbpx**2+tbpy**2)

    if(tarad .ge. tbrad)then
```

```
ptx(n) = tapx
pty(n) = tapy
   else
ptx(n) = tbpx
pty(n) = tbpy
   endif

c     Convert back to 3-D coordinates:

   tx(n) = xc + ptx(n)*cos(gamma)
   ty(n) = yc + pty(n)
   tz(n) = zc + ptx(n)*sin(gamma)

300  continue

 ptx(npts) = ptx(1)
 pty(npts) = pty(1)

 tx(npts) = tx(1)
 ty(npts) = ty(1)
 tz(npts) = tz(1)

c     NOTE: fort.* file in FORT_inn directory is overwritten !!

 tunit = 100+nslice
 tfile = ifnam! Same directory and filename
 open(unit=tunit,file=tfile,status='unknown')
 write(tunit,*)npts

 do 400 i=1,npts
   write(tunit,*)tx(i),ty(i),tz(i)! new point coordinates
400  continue

 close(tunit)

c     Write out coordinates for projected points:

 piunit = 500+nslice
 pifile = 'pi/pi'//nfnam(6:7)//'.dat'
 open(unit=piunit,file=pifile,status='unknown')
 write(piunit,*)npts

 do 500 i=1,npts
c     Project translated endosteal boundary back to plane (double check):
c    ctx(i) = tx(i) - xc
c    cty(i) = ty(i) - yc
c    ctz(i) = tz(i) - zc
c    ptx(i) = sqrt(ctx(i)**2 + ctz(i)**2)
c    if(tx(i) .lt. xc)then
c ptx(i) = - ptx(i)
c    endif
c    pty(i) = cty(i)

   write(piunit,*)px(i),py(i),ptx(i),pty(i)
500  continue

 close(500+nslice)

c     Project outer coordinate points to plane
 pounit = 600+nslice
 pofile = 'po/po'//nfnam(6:7)//'.dat'
 open(unit=pounit,file=pofile,status='unknown')
 write(pounit,*)onpts

 do 550 i=1,onpts
   cox(i) = ox(i) - xc
   coy(i) = oy(i) - yc
   coz(i) = oz(i) - zc
   pox(i)  = sqrt(cox(i)**2 + coz(i)**2)
   if(ox(i) .lt. xc)then
pox(i) = - pox(i)
   endif
   poy(i)  = coy(i)

   write(pounit,*)pox(i),poy(i)
550  continue

 close(600+nslice)

c     Write out 3-d coordinates for orig., translated & outer curves
c     for MATLAB check

 qiunit = 700+nslice
```

```
 qifile = 'qi/qi'//nfnam(6:7)//'.dat'
 open(unit=qiunit,file=qifile,status='unknown')
 write(qiunit,*)npts

 do 650 i=1,npts
   write(qiunit,*)x(i),y(i),z(i),tx(i),ty(i),tz(i)
650  continue

 close(700+nslice)

 qounit = 800+nslice
 qofile = 'qo/qo'//nfnam(6:7)//'.dat'
 open(unit=qounit,file=qofile,status='unknown')
 write(qounit,*)onpts

 do 700 i=1,onpts
   write(qounit,*)ox(i),oy(i),oz(i)
700  continue

 close(800+nslice)

c     Calculate change in endosteal area for each curve

 circum = 0

 do 750 i=1,npts-1
   ptdist = sqrt((px(i+1)-px(i))**2 + (py(i+1)-py(i))**2)
   circum = circum + ptdist
750  continue

 darea(nslice)=circum*ptdisp
c  write(6,*)'slice ',nslice,'  delta area = ',darea(nslice)

c 800  continue

 600continue! End of loop for each slice

 close(13)

 9format(a)

 999stop
 end
```

D.2 Modification of Cancellous Element Densities

```
Program densadj
c     ************************************************************************
c     Version: 1.0
c     Original Code by:  Grant Schaffner (8/9/99)
c     Description:  This program reads in element volumes and densities from
c     two sets of files (preflight model and postflight model). It then
c     calculates the bone mineral mass loss from the change in cortical volume
c     in the trochanteric and neck regions. It then subtracts this bone mineral
c     mass loss from the total mass loss (estimated from areal BMD (DXA)) and
c     then adjusts the medullary element densities in the trochanteric and
c     neck regions to account for the remainder of the loss.
c     ************************************************************************

      parameter (id0=6400)     ! No of elements 0 month model
      parameter (idn=6400)     ! No of elements n month model
      parameter (tc0s=897)     ! Troch cort start element
      parameter (tc0f=1600)    ! Troch cort finish element
      parameter (nc0s=1601)    ! Neck cort start element
      parameter (nc0f=2048)    ! Neck cort finish element
      parameter (tm0s=3905)    ! Troch med start element
      parameter (tm0f=4960)    ! Troch med finish element
      parameter (nm0s=4961)    ! Neck med start element
      parameter (nm0f=5632)    ! Neck med finish element
      parameter (tcns=897)     ! Troch cort start element
      parameter (tcnf=1600)    ! Troch cort finish element
      parameter (ncns=1601)    ! Neck cort start element
      parameter (ncnf=2048)    ! Neck cort finish element
      parameter (tmns=3905)    ! Troch med start element
      parameter (tmnf=4960)    ! Troch med finish element
      parameter (nmns=4961)    ! Neck med start element
      parameter (nmnf=5632)    ! Neck med finish element
      parameter (dbmdt=-0.0145) ! % Change in troch areal bmd per month
```

```
      parameter (dbmdn=-0.0130) ! % Change in neck areal bmd per month
      parameter (areat=30.62)   ! Proj c/s area of troch (cm^2)
      parameter (arean=8.89)    ! Proj c/s area of neck (cm^2)

      character vtc0file*40,vtm0file*40,vnc0file*40,vnm0file*40
      character vtcnfile*40,vtmnfile*40,vncnfile*40,vnmnfile*40
      character d0file*40,dpfile*40,dnfile*40,chng*2
      integer d0,dp,dn,tc0,tm0,nc0,nm0,tcn,tmn,ncn,nmn
      real eldens0(id0),eldensn(idn)
      real tc0mass,tcnmass,nc0mass,ncnmass,months
      real tm0vol,tmnvol,nm0vol,nmnvol
    real tc0vol,tcnvol,nc0vol,ncnvol

      write(6,*)'How many months of weightlessness?'
      read(5,*)months

      vtc0file = 'vtc0.dat'
      vtm0file = 'vtm0.dat'
      vnc0file = 'vnc0.dat'
      vnm0file = 'vnm0.dat'
      d0file   = 'dens_0.dat'

      if(months.lt.6.1.and.months.gt.5.9)then
        vtcnfile = 'vtc6.dat'
        vtmnfile = 'vtm6.dat'
        vncnfile = 'vnc6.dat'
        vnmnfile = 'vnm6.dat'
        dpfile   = 'dens_6_preadj.dat'
        dnfile   = 'dens_6.dat'
      endif

      if(months.lt.12.1.and.months.gt.11.9)then
        vtcnfile = 'vtc12.dat'
        vtmnfile = 'vtm12.dat'
        vncnfile = 'vnc12.dat'
        vnmnfile = 'vnm12.dat'
        dpfile   = 'dens_12_preadj.dat'
        dnfile   = 'dens_12.dat'
      endif

      write(6,*)'n month files:'
      write(6,*)'vtcnfile = ',vtcnfile
      write(6,*)'vtmnfile = ',vtmnfile
      write(6,*)'vncnfile = ',vncnfile
      write(6,*)'vnmnfile = ',vnmnfile
      write(6,*)'dpfile = ',dpfile
      write(6,*)'dnfile = ',dnfile

      write(6,*)'Change the n month filenames (y/n)?'
      read(5,*)chng
      if(chng.eq.'y'.or.chng.eq.'Y')then
        write(6,*)'New vtcnfile:'
        read(5,*)vtcnfile
        write(6,*)'New vtmnfile:'
        read(5,*)vtmnfile
        write(6,*)'New vncnfile:'
        read(5,*)vncnfile
        write(6,*)'New vnmnfile:'
        read(5,*)vnmnfile
        write(6,*)'New dpfile:'
        read(5,*)dpfile
        write(6,*)'New dnfile:'
        read(5,*)dnfile
      endif

      d0  = 10
      tc0 = 20
      tm0 = 30
      nc0 = 40
      nm0 = 50
      dp  = 110
      tcn = 120
      tmn = 130
      ncn = 140
      nmn = 150
      dn  = 160

      open(unit=d0, file=d0file,status='old')
      open(unit=tc0,file=vtc0file,status='unknown')
      open(unit=nc0,file=vnc0file,status='unknown')
    open(unit=tm0,file=vtm0file,status='unknown')
    open(unit=nm0,file=vnm0file,status='unknown')
      open(unit=dp, file=dpfile,status='old')
```

```
      open(unit=tcn,file=vtcnfile,status='unknown')
      open(unit=ncn,file=vncnfile,status='unknown')
      open(unit=tmn,file=vtmnfile,status='unknown')
      open(unit=nmn,file=vnmnfile,status='unknown')
      open(unit=dn, file=dnfile,status='unknown')

      read(tc0,*)itc0
      read(nc0,*)inc0
      read(tcn,*)itcn
      read(ncn,*)incn
  read(tm0,*)itm0
  read(nm0,*)inm0
      read(tmn,*)itmn
      read(nmn,*)inmn


      do 100 i = 1,id0
        read(d0,*)nel,dens
        eldens0(nel) = dens
  100 continue

      do 200 i = 1,idn
        read(dp,*)nel,dens    ! Read densities from preadj file
        eldensn(nel) = dens   ! Use of eldensn is correct
  200 continue

      close(d0)
      close(dp)

c     Note: vol is converted from mm^3 to cm^3 below

      do 300 i = 1,itc0
        read(tc0,*)nel,vol
        tc0mass = tc0mass + eldens0(nel)*vol/1000
    tc0vol = tc0vol + vol/1000
  300 continue

      do 400 i = 1,inc0
        read(nc0,*)nel,vol
        nc0mass = nc0mass + eldens0(nel)*vol/1000
    nc0vol = nc0vol + vol/1000
  400 continue

      do 500 i = 1,itcn
        read(tcn,*)nel,vol
        tcnmass = tcnmass + eldensn(nel)*vol/1000
    tcnvol = tcnvol + vol/1000
  500 continue

      do 600 i = 1,incn
        read(ncn,*)nel,vol
        ncnmass = ncnmass + eldensn(nel)*vol/1000
    ncnvol = ncnvol + vol/1000
  600 continue

  do 550 i = 1,itm0
        read(tm0,*)nel,vol
        tm0vol = tm0vol + vol/1000
  550 continue

      do 650 i = 1,inm0
        read(nm0,*)nel,vol
        nm0vol = nm0vol + vol/1000
  650continue


      do 700 i = 1,itmn
        read(tmn,*)nel,vol
        tmnvol = tmnvol + vol/1000
  700 continue

      do 800 i = 1,inmn
        read(nmn,*)nel,vol
        nmnvol = nmnvol + vol/1000
  800continue

  cReport volumes:

  write(6,*)'Region Volumes (cm^3)'
  write(6,*)'=========================='
  write(6,*)'0 month values:'
  write(6,*)'---------------'
  write(6,*)'Neck Cortex   = ',nc0vol
```

```
write(6,*)'Neck Medulla  = ',nm0vol
write(6,*)'Troch Cortex  = ',tc0vol
write(6,*)'Troch Medulla = ',tm0vol
write(6,*)' '
write(6,*)months,'month values:'
write(6,*)'----------'
write(6,*)'Neck Cortex   = ',ncnvol
write(6,*)'Neck Medulla  = ',nmnvol
write(6,*)'Troch Cortex  = ',tcnvol
write(6,*)'Troch Medulla = ',tmnvol
write(6,*)' '

c   Calculate change in bone mineral mass due to cortical
c   volume loss (endosteal absorption) in each region

    dtcmass = tcnmass - tc0mass
    dncmass = ncnmass - nc0mass

    write(6,*)' '
    write(6,*)'Change in BMC due to endosteal absorption:'
    write(6,*)'Troch:  ',dtcmass
    write(6,*)'Neck:   ',dncmass
    write(6,*)' '

c   Calculate total change in bone mineral mass according
c   to areal BMD change (DXA) in each region

    dtmass = dbmdt*months*areat
    dnmass = dbmdn*months*arean

    write(6,*)'Total Change in BMC (from areal BMD):'
    write(6,*)'Troch:  ',dtmass
    write(6,*)'Neck:   ',dnmass
    write(6,*)' '

c   Subtract loss of bone mineral mass due to endosteal
c   absorption to get loss of mass in medulla

    dtmmass = dtmass - dtcmass
    dnmmass = dnmass - dncmass

    write(6,*)'Change in BMC for medulla:'
    write(6,*)'Troch:  ',dtmmass
    write(6,*)'Neck:   ',dnmmass
    write(6,*)' '

c   Divide by final medulla volume of region to get change
c   in density of elements in medulla

    ddenstm = dtmmass/tmnvol
    ddensnm = dnmmass/nmnvol

    write(6,*)'Density change in medulla:'
    write(6,*)'Troch:  ',ddenstm
    write(6,*)'Neck:   ',ddensnm
    write(6,*)' '

c   Adjust densities and save in new file

    do 900 nel = tmns,tmnf
      eldensn(nel) = eldensn(nel) + ddenstm
900 continue

    do 1000 nel = nmns,nmnf
      eldensn(nel) = eldensn(nel) + ddensnm
1000 continue

    do 1100 nel = 1,idn
      write(dn,*)nel,eldensn(nel)
1100 continue

    close(tc0)
    close(nc0)
    close(tm0)
    close(nm0)
    close(tcn)
    close(ncn)
    close(tmn)
    close(nmn)
    close(dn)

    stop
    end
```